UNIVERSITÉ DE GENÈVE
Département de physique nucléaire et corpusculaire

FACULTÉ DES SCIENCES
Professeur Alain Blondel

Search for Excited Electron Production Using Di-Electron + Photon Signature and Search for New Heavy Neutral Gauge Boson Using Di-Electron Signature with ATLAS at $\sqrt{s} = 7$ TeV

THÈSE

présentée à la Faculté des Sciences de l'Université de Genève
pour obtenir le grade de Docteur ès sciences, mention physique

par

Ahmed Aly Abdelalim Aly

d'Égypte

Thèse N° 4373

GENÈVE
Atelier d'impression ReproMail
2011

UNIVERSITÉ DE GENÈVE

FACULTÉ DES SCIENCES

Doctorat ès sciences
Mention physique

Thèse de *Monsieur Ahmed Aly ABDELALIM ALY*

intitulée :

"Search for Excited Electron Production Using Di-Electron + Photon Signature and Search for New Heavy Neutral Gauge Boson Using Di-Electron Signature with ATLAS at $\sqrt{s}$ = 7 TeV"

La Faculté des sciences, sur le préavis de Messieurs A. BLONDEL, professeur ordinaire et directeur de thèse (Département de physique nucléaire et corpusculaire), M. POHL, professeur ordinaire (Département de physique nucléaire et corpusculaire), G. IACOBUCCI, professeur ordinaire (Département de physique nucléaire et corpusculaire), J.-P. REVOL, docteur (CERN – Genève, Suisse), et Monsieur D. FORTIN, docteur (ATLAS Group – TRIUMF – Vancouver, Canada), autorise l'impression de la présente thèse, sans exprimer d'opinion sur les propositions qui y sont énoncées.

Genève, le 22 novembre 2011

Thèse - 4373 -

Le Doyen, Jean-Marc **TRISCONE**

N.B. - La thèse doit porter la déclaration précédente et remplir les conditions énumérées dans les "Informations relatives aux thèses de doctorat à l'Université de Genève".

Abstract

The ATLAS detector has been used to search for excited or exotic electrons (e^*) decaying to $e\gamma$ as well as heavy neutral gauge bosons (Z') decaying to e^+e^-. For the Z' search, results are based on pp collisions at $\sqrt{s} = 7$ TeV corresponding to an integrated luminosity of about 39 pb^{-1} of 2010 data. No statistically significant excess above the Standard Model processes is observed. Upper limits at 95% confidence level are set on the cross section times branching ratio of narrow Z' resonances decaying to electrons as a function of the resonance mass. These limits allow to set a lower mass limits on the Sequential Standard Model and on E6-motivated Z' models.

For the e^* search, results are based on a dataset of 2 fb^{-1} of `ATLAS` 2011 data. In the case of single e^* production an oppositely charged electron is also produced in association with the e^* yielding a $e^+e^-\gamma$ final state. The discovery of e^* would be a first indication of lepton compositeness. No statistically significant excess above the Standard Model processes is observed. Upper limits at 95% confidence level are set on the cross section times branching ratio of $pp \to ee^* \to e^+e^-\gamma$. Again these limits allow to set a lower mass limit on e^*. In the special case where $\Lambda = m_e^*$, masses below 1.8 TeV are excluded.

Acknowledgements

First, I would like to thank a lot my supervisor, Prof. Alain Blondel, for his guidance, understanding, kindness, and before all of these, giving me the chance to run my PhD in the wonderful University of Geneva. Also, I would like to particularly thank Bertrand Martin for his help and support most of the time whatever my problem was he was always available and ready to find a solution and answer my questions. Last but not least, I would like to thank Jean-Pierre Revol for his help and his invitation for me to visit CERN for the first time, hence introducing me to my supervisor.

Dedicated to the Memory of ...
my Mother 1946–2009
my Father 1946–2010

Résumé

Dans cette thèse, le détecteur ATLAS a été utilisé pour rechercher des électrons excités ou exotiques (e^*) se désintégrant en $e\gamma$ ainsi que des bosons de jauge neutres massifs (Z') dans le canal de désintégration e^+e^-. Les résultats basés sur des collisions pp à $\sqrt{s} = 7$ TeV correspondant à une luminosité intégrée d'environ 39 pb^{-1} pour les données collectées en 2010 et 2 fb^{-1} pour les données 2011 sont présentés. Dans le modèle e^* considéré, un électron de charge opposée est également produit en association avec l'électron excité, donnant pour signature $e^+e^-\gamma$ dans l'état final. La découverte du e^* serait une première indication de sous-structure des leptons. Aucun excès statistiquement significatif au-dessus des prédictions du Modèle Standard n'est observé. Des limites supérieure à 95 % de niveau de confiance sont fixées sur les sections efficaces de production $\sigma(pp \to ee^* \to e^+e^-\gamma)$ ainsi que sur la production de résonances Z' se désintégrant en électrons, en fonction de la masse de résonance. Ces limites permettent de fixer une limite inférieure sur la masse du e^* ainsi que sur la masse du boson Z' dans le cadre du modèle séquentiel standard ou de modèles E6.

La thèse est composée de huit chapitres et une annexe. Le chapitre 1 donne une brève introduction et résume rapidement le contenu de cette thèse. Le chapitre 2 est une introduction au modèle standard de la physique des particules et souligne ses insuffisances actuelles. Il commence par une section dédiée aux particules élémentaires. Le formalisme mathématique est introduit dans la section suivante: aspects classiques de la théorie des champs, puis la quantification des champs, ainsi que les principaux aspects de la théorie électrofaible (EW) et la chromodynamique quantique (QCD). A la fin du chapitre 2, les insuffisances actuelles de ce cadre théorique sont évoquées et quelques candidats possibles de théories au-delà du Modèle Standard (BSM) sont donnés.

Le chapitre 3 décrit brièvement les modèles étudiés dans ce manuscrit donnant des états finaux à deux électrons ou deux électrons et un photon. Tout d'abord, certains modèles prédisant l'existence d'un boson Z' sont présentés, et les résultats récents des détecteurs `CDF` et `D0` installés auprès de l'accélérateur `Tevatron` du laboratoire Fermi sont également fournis. La section suivante présente l'électron excité dont l'existence est prédite par les modèles composites: le lagrangien effectif est introduit, puis les recherches précédentes d'électrons excités sont exposées, incluant les résultats des accélérateurs `DESY`, `LEP`, `Tevatron`, ainsi que le dernier résultat de la collaboration `CMS`.

Le chapitre 4 présente le Large Hadron Collider `LHC` et le détecteur `ATLAS`. La première section passe en revue le `LHC` et ses principales composantes, et donne un aperçu des autres expériences du LHC (`CMS`, `ALICE`, `LHCb`, `LHCf` et `TOTEM`). Ce chapitre contient une section consacrée à la Worldwide LHC Computing Grid (WLCG) qui est utilisée pour stocker et analyser l'énorme quantité de données recueillies par les différentes expériences du `LHC`. Dans la section 4.2, les aspects importants du détecteur `ATLAS` sont expliqués, notamment la définition du système de coordonnées utilisé, les différents sous-détecteurs, la mesure de luminosité, le système de déclenchement, et le système d'acquisition des données (DAQ).

Le chapitre 5 présente la simulation Monte Carlo dans `ATLAS`. La chaîne complète de simulation est décrite dans la section 5.1, de la génération d'événements et la simulation

de la réponse du détecteur au format des données utilisées dans cette analyse. Les échantillons Monte Carlo de signal et de bruit de fond utilisés tout au long de cette analyse sont également présentés dans ce chapitre.

Le chapitre 6 présente la définition des électrons et les photons dans l'expérience ATLAS, ainsi que leur algorithme de reconstruction. Dans la section 6.2, l'identification des électrons et des photons ayant pour but un meilleur rejet du bruit de fond est expliquée. Les critères d'identification des électrons et des photons sont nombreux, afin de couvrir un large éventail de besoins pour les analyses de physique. Ce chapitre comprend également deux études sur l'estimation dans les données de la probabilité pour un jet de satisfaire les critères d'identification d'un électron ou d'un photon.

Au chapitre 7, l'analyse des données 2010 est exposée. Une première analyse des données d'ATLAS est effectuée, à travers la recherche de bosons de jauge lourds neutres (Z') dans les données enregistrées en 2010 (environ 39 pb^{-1}). Une limite supérieure à 95% de niveau de confiance est établie sur la section efficace de production de boson Z', dans le cadre de plusieurs modèles. Ces résultats ont été publiés par la collaboration ATLAS au printemps 2010.

Le chapitre 8 présente enfin la recherche d'électrons excités dans les données collectées en 2011 par le détecteur ATLAS jusqu'au mois d'août (2,05 fb^{-1}). Ce chapitre commence par une section sur les données de collision, la liste des périodes de prise de données utilisée dans l'analyse, le format des données, les composantes du système de déclenchement utilisées, et la luminosité intégrée (la quantité de données) correspondant à chaque période. Dans la section 8.2 sont résumés les corrections et facteurs d'échelle appliqués à la simulation pour mieux reproduire les données, ainsi que les techniques d'analyse permettant de prendre en compte les défaillances matérielles dans le détecteur. Puis dans la section 8.3, la méthode d'analyse, la sélection des objets et des événements est mise en place. Les données sont comparées aux prédictions du Modèle Standard, en se basant à la fois sur la simulation Monte Carlo et sur des méthodes d'estimation de bruit de fond à partir des données. Les incertitudes systématiques sont également détaillées dans ce chapitre. Pour conclure, dans la section 8.9.3, les limites sur la section efficace de production et sur la masse des électrons excités sont données, incluant une brève discussion sur le concept de limite Bayésienne.

Table of Contents

List of Figures

List of Tables

1
Introduction

Woohoo! writing this introduction is the last step towards a Ph.D. In my case it means becoming an experimental particle physicist. In 2009, an outstanding occured: the Large Hadron Collider (LHC), located in Geneva, Switzerland, was able to reproduce the conditions that prevailed in the very early Universe. On the 23rd of November 2009, at 22 min past 2 pm, the first pp collision candidate at 900 GeV center of mass energy was seen in the ATLAS detector, one of the four main experiments at the LHC. This event carried the hopes and dreams of grand discoveries for all particle physicists all over the world. Since that day, many hundreds of billions of collisions have been recorded and are as we speak under strict scrutiny, employing thousands of students and researchers worldwide.

The first year of collision was mainly aimed at rediscovering the Standard Model (SM): remeasuring the well known parameters with even higher precision, and understanding the detector response to the new energy regime. The most important thing is to understand all what we observe. During 2010, ATLAS collected about 39 pb^{-1} of data, while during 2011 it gathered about 5 fb^{-1}. With this vast amount of data we can start looking at physics beyond the Standard Model and maybe writing an end for the story of the Higgs boson. After the discovery of the top quark (t) by CDF and D0 collaborations in 1995 and the third neutrino (ν_τ) by the DONUT[1] collaboration in 2000, the Higgs boson remains the only unobserved Standard Model particle. The Higgs boson is the cornerstone of the Standard Model, and if it does not exist, a new theory has to take the place of one of the most well known and well tested theories.

Whether the Higgs boson exists or not, the Standard Model is not the final theory that describes our universe, as it does not incorporate the physics of general relativity, such as gravitation and dark energy. The theory does not contain any viable dark matter particle that possesses all of the required properties deduced from observational cosmology. It also does not correctly account for neutrino oscillations (and their non-zero masses). Although the Standard Model is theoretically self-consistent, it has several apparently unnatural properties giving rise to puzzles like the strong CP problem and the hierarchy problem. It is believed to be correct in the electroweak energy regime, but still only an approximation. Many Beyond Standard Model (BSM) theories have been developed over the last century. Some of these theories absorb the Standard Model,

[1] DONUT (Direct Observation of the NU Tau) was an experiment at Fermilab dedicated to the search for tau neutrino interactions.

making it appear as a part of a bigger picture, and some others are standalone. The goal of LHC is to explore the energy frontiers and to dig deeper into the true nature of our Universe.

Some BSM theories predict the existence of a massive electrically neutral gauge boson (Z'). Searching for Z' is one goal of this thesis. Another BSM theory is the so-called compositeness model which assumes that both leptons and quarks are not elementary particles but have constituents known as preons. Preons are postulated to be "point-like" particles, conceived to be subcomponents of quarks and leptons. The word was coined by Jogesh Pati and Abdus Salam in 1974.

This thesis consists of eight chapters and one appendix. Chapter 2 gives a brief introduction to the Standard Model of Particle Physics and its current shortcomings. Section 2.1 summarizes the 17 SM elementary particles: 12 fermions, 4 vector bosons, and 1 scalar boson. In addition these particles have charge conjugated partners or antiparticles. The mathematical formalism of the SM is introduced in section 2.2. This section starts with Classical Field Theory Lagrangian aspect then followed with a quantized Lagrangian. It also summaries very briefly the main aspects both Electroweak (EW) and Quantum Chromodynamics (QCD) models. At the end of this chapter, section 2.3 lists the current shortcomings of the SM. A few possible candidates of BSM theories are given in section 2.4.

Chapter 3 describes briefly the models that we are interested in with 2 electrons or 2 electrons and a photon in the final state. Section 3.1 introduces some models that predict the existence of the Z' and provides the most recent results from the two TEVATRON detectors CDF and D0, in the context of Z' searches. Section 3.2 introduces the excited electron (e^*) predicted by the compositeness model: in sub-section 3.2.1 the effective Lagrangian is introduced and sub-section 3.2.2 summarizes the previous searches for e^*. Results from DESY, LEP, TEVATRON accelerators as well as the latest result from the CMS collaboration.

Chapter 4 introduces the LHC accelerator and the ATLAS detector. In section 4.1, the LHC and its main components are demonstrated with a brief summary of the LHC experiments given in sub-section 4.1.2. Sub-section 4.1.3 is devoted to the Worldwide LHC Computing Grid (WLCG) which is used to store and to analyze the huge amount of data collected by the different LHC experiments. In section 4.2, an overview is provided as well as important aspects of the ATLAS detector, specifically the definition of the coordinate system used, the different sub-detectors, the luminosity measurement, and the concept of triggers and the Data AcQuisition (DAQ).

Chapter 5 summarizes the Monte Carlo simulation in ATLAS. The full simulation chain starting from event generation and detector response simulation up to the data format used in this analysis is explained briefly in section 5.1. The Monte Carlo signals and background samples used through out this analysis are also introduced in this chapter, in sections 5.2, 5.3, and 5.4.

Chapter 6 introduces the electron and photon reconstruction in ATLAS. In section 6.2 the electron and photon identification are introduced for further background rejection. There are different quality cuts in order to cover a wide range of physics and analysis needs. This chapter ends with section 6.5 on estimating the rate a jet can fake a photon.

In chapter 7, a first look at real data, the search for heavy neutral gauge bosons (Z') with the 2010 data-set (about 39 pb^{-1}) is summarized. A 95% C.L. upper limit on Z' (in various BSM physics models) cross-section times branching ratio is also obtained which was published in the spring of 2011. Tables 7.7 and 7.8 summarizes these limits.

Chapter 8 introduces the excited electron search using a large fraction of the 2011 data (2.05 fb^{-1}). This chapter starts with a section on the collision data, the good run lists that were used in the analysis as well as the data format, the trigger stream, and the integrated luminosity (the amount of data) corresponding to each trigger period. In section 8.2 the corrections and scale factors, needed for the Monte Carlo to model the data the hardware problems in the detector, are summarized. Then in section 8.3 the analysis method, objects and event selections are described. A section on background estimation with different methods to estimate backgrounds from Monte Carlo as well as data-driven methods, also the systematic uncertainties are estimated through out these sections. Then a section on signal efficiency is given. Section 8.9.1 summarize the final data yield as well as the background expectations. At the end, in section 8.9.3, the limit on cross-section as well as on excited electron mass are given with a brief introduction on Bayesian limits with counting experiment.

2
The Standard Model of Particle Physics

Today, the Standard Model of Particle Physics (SM) describes beautifully three of the four known fundamental interactions - the electromagnetic, the weak (those two unified to the so called electroweak) and the strong forces - and the elementary particles that comprise our universe. It has been tested many times by many experiments so far and the results are consistent with the predictions of the SM, although there are some unexplained (unanswered) phenomena (questions). The fourth interaction, the gravitational force, acting on all massive particles, is not included in the SM.

2.1 The Standard Model

In the context of the SM, strong and electroweak forces are described via the exchange of 12 gauge bosons, eight colored massless gluons (g) for the strong force, one massless photon (γ) for the electromagnetic force, and three massive gauge bosons for the weak force ($W^{\pm}$, Z), see table 2.1.

Table 2.1: The gauge bosons (spin 1) that mediate the strong (g), electromagnetic (γ) and the weak ($W^{\pm}$ and Z) interactions.

Particle	**Mass (GeV)**	**El. Charge (e)**	**Full width (GeV)**
gluon (g)	0	0	-
photon (γ)	$< 1 \times 10^{-24}$	$< 5 \times 10^{-30}$	-
W boson ($W^{\pm}$)	80.4	± 1	2.085
Z boson (Z)	91.19	0	2.495

In the SM, the matter particles are the six quarks and the six leptons with their corresponding antiparticles. There are three generations of quarks and leptons. Each generation is a more massive copy of the former. This brings the question of: why Nature copies itself in such a manner? Why are there exactly three generations of matter particles? A summary of the fundamental particles of the Standard Model can be found in table 2.2.

[1]The Standard Model assumes that neutrinos are massless. However, several contemporary experiments prove that neutrinos oscillate between their flavour states, which could not happen if all were massless.

Table 2.2: The fundamental matter particles (fermions, spin 1/2) of the Standard Model. In addition, there are antiparticles for all these fermions, that have the same properties as their respective particles, but with reversed quantum numbers (like charge and color).

Family	**Particle**	**Mass [GeV][13]**	**El. Charge [e]**	**Mean Life [13]**
Leptons	electron (e^-)	0.511×10^{-3}	-1	$> 4.6 \times 10^{26}\ yr$
	electron neutrino (ν_e)	$< 2 \times 10^{-6}$	0	$> 15.4\ s/eV^1$
	muon (μ^-)	0.1057	-1	$2.197 \times 10^{-6}\ s$
	muon neutrino (ν_μ)	$< 0.19 \times 10^{-3}$	0	$> 15.4\ s/eV^1$
	tau (τ^-)	1.777	-1	$2.91 \times 10^{-13}\ s$
	tau neutrino (ν_τ)	$< 18.2 \times 10^{-3}$	0	$> 15.4\ s/eV^1$
Quarks	up (u)	1.5 to 3.3×10^{-3}	$+2/3$	-
	down (d)	3.5 to 6.0×10^{-3}	$-1/3$	-
	strange (s)	104×10^{-3}	$-1/3$	-
	charm (c)	1.27	$+2/3$	-
	beauty (b)	4.20	$-1/3$	-
	top (t)	172.5	$+2/3$	$0.5 \times 10^{-24}\ s$

In 1961 Sheldon Glashow [14] managed to combine the electromagnetic and weak interactions into the so-called electroweak interaction. Later, in 1967, Steven Weinberg [15] and Abdus Salam incorporated the Higgs mechanism into the electroweak theory, making the standard electroweak theory as we know it today (also known as the Glashow-Weinberg-Salam model). The first observations of neutral current interactions was made with the Gargamelle bubble chamber (now on display at CERN Microcosm museum) at CERN, in 1973 [16]. The discovery of the W and Z bosons[2] did not come until the upgraded Super Proton Synchrotron (SPS) was operational, colliding protons with anti-protons at unprecedented energies, making the resonances directly observable for the very first time.

2.2 Theoretical Aspects

Technically, quantum field theory (QFT) provides the mathematical framework for the SM, in which a Lagrangian, a scalar quantity describing the theory, controls the dynamics and kinematics of the theory. Each kind of particle is described in terms of a dynamical field that pervades space-time. The first successful QFT was Quantum ElectroDynamics (QED) developed from the 1920s to 1940s.

2.2.1 Classical Field Theory

The Lagrangian is given by the difference of the kinetic and potential energy, $L = T - V$. It is a function of the generalized coordinates q_i and their time derivatives $\dot{q}_i$. An important property of the Lagrangian is that conservation laws can easily be read off from it. For example, if the Lagrangian L depends on the time-derivative $\dot{q}_i$ of a generalized coordinate, but not on q_i itself, then the generalized momentum (kown as the *conjugate momentum*),

$$p_i \equiv \frac{\partial L}{\partial \dot{q}_i} \tag{2.1}$$

[2]W and Z bosons discovered by UA1 and UA2 collaborations, in 1983.

is a conserved quantity. When the constraints on the system are time dependent, the Lagrangian also depends on the time t:

$$L(q, \dot{q}, t) = T(q, \dot{q}, t) - V(q, t) \tag{2.2}$$

The number of generalized coordinates equals the number of degrees of freedom of the system. If the Lagrangian of a system is known, then the equations of motion of the system may be obtained by a direct substitution of the Lagrangian into the EulerLagrange equation, which is a particular family of partial differential equations;

$$\frac{d}{dt}\frac{\partial L}{\partial \dot{q}_i} = \frac{\partial L}{\partial \dot{q}_i} \tag{2.3}$$

In field theory, the fields $\phi_j(x^\mu), j = 1, 2, ..., N$, are independent variables, and the Lagrangian L is exchanged with the Lagrangian density $\mathcal{L}$ (also, usually known as the Lagrangian), which is the difference of the kinetic energy density and the potential energy density, $\mathcal{L} = \mathcal{T} - \mathcal{V}$. Now, the conjugate momenta are called the *conjugate fields*

$$\pi_j(x^\mu) \equiv \frac{\partial \mathcal{L}}{\partial \dot{\phi}_j} \tag{2.4}$$

and the Euler-Lagrange equations becomes:

$$\frac{\partial \mathcal{L}}{\partial \phi_j} = \partial_\alpha\left(\frac{\partial \mathcal{L}}{\partial(\partial_\alpha \phi_j)}\right) \quad , \qquad \partial_\alpha = \frac{\partial}{\partial x^\alpha} \tag{2.5}$$

2.2.2 Quantum Field Theory

To move from classical to quantized fields, the *generalized coordinates* and *conjugate momentum* are interpreted as operators and are subjected to canonical commutation relations (also called equal time commutators, E.T.C.)

$$[\phi_j(x_\mu), \pi_k(x'_\mu)] = i\hbar\delta_{jk}\delta(x_\mu - x'_\mu) \quad , \quad x^0 = y^0 \tag{2.6}$$

$$[\phi_i(x_\mu), \phi_j(x'_\mu)] = [\pi_i(x_\mu), \pi_j(x'_\mu)] = 0 \quad , \quad x^0 = y^0 \tag{2.7}$$

These operators act on a Hilbert space, the usual arena of Quantum Mechanics. The fields have quanta with the well-defined properties of the classical particle. The interaction between these particles can now be described by other fields whose quanta are different particles (force carrying bosons). With this formalism one can explore a new range of phenomena, like decaying particles, and vacuum fluctuations, all what we need is to find the right Lagrangian.

As mentioned above the first successful QFT was QED, but it will not be mentioned here and the next sections will cover Electroweak theory, Quantum Chromodynamics (for strong interactions) and the Higgs mechanism (that introduces mass terms into the Lagrangian).

2.2.3 Electroweak Model (EW)

Experiments [17] have shown that the weak force acts on left-handed particles only, leaving the right-handed particles untouched. The chirality (handedness) of a particle is dependent mathematically on whether the particle transforms in a right- or left-handed representation of the Poincaré group [18]. Due to the fact that fields with different chiralities have different transformation properties, the free lepton Lagrangian can be written in an asymmetric way, with the left-handed fields grouped in a doublet and the right-handed fields in singlets:

$$\mathcal{L}_0 = i[\overline{\Psi}_l^L(x)\partial\!\!\!/\Psi_l^L(x) + \overline{\psi}_l^R(x)\partial\!\!\!/\psi_l^R(x) + \overline{\psi}_{\nu l}^R(x)\partial\!\!\!/\psi_{\nu l}^R(x)] \tag{2.8}$$

where

$$\partial\!\!\!/ \equiv \gamma^\mu \partial_\mu \quad , \qquad \Psi_l^L(x) = \begin{pmatrix} \psi_{\nu l}^L(x) \\ \psi_l^L(x) \end{pmatrix} \tag{2.9}$$

$\mathcal{L}_0$ is required to be invariant under $SU(2)_L$ and $U(1)_Y$ transformations, where $U(1)_Y$ is the symmetry group that describes QED, Y is a conserved quantity called the weak hypercharge (to be explained later this section), L is lepton number, and γ^μ are the Dirac matrices.

- local phase transformations:

The local $SU(2)_L$ phase transformations are:

$$\begin{aligned} \Psi_l^L(x) \to \Psi_l^{L'}(x) &= e^{\frac{1}{2}ig\omega_j(x)\tau_j}\Psi_l^L(x) \quad , \\ \overline{\Psi}_l^L(x) \to \overline{\Psi}_l^{L'}(x) &= \overline{\Psi}_l^L(x)e^{-\frac{1}{2}ig\omega_j(x)\tau_j} \end{aligned} \tag{2.10}$$

where τ_j are the Pauli matrices that are the generators of $SU(2)_L$, $\omega_j(x), j = 1, 2, 3$ are three real differentiable functions of x and g is a real constant. Every right-handed lepton field is defined to be invariant under any $SU(2)_L$ transformation. Unfortunately, the free lepton Lagrangian, equation (2.8), is not invariant under these transformations. To make it invariant require several modifications. First, the ordinary derivatives $\partial\Psi_l^L(x)$ are replaced by the *covariant derivatives*;

$$\partial^\mu\Psi_l^L(x) \to D^\mu\Psi_l^L(x) \equiv [\partial^\mu + \frac{1}{2}ig\tau_j W_j^\mu(x)]\Psi_l^L(x) \tag{2.11}$$

where $W_j^\mu(x)$ are three gauge fields, instead of one field $A_\mu(x)$ in QED, one for each $SU(2)_L$ generator.

Then the Lagrangian of free particle, in terms of the *covariant derivative*, becomes:

$$\tilde{\mathcal{L}}_0 = i[\overline{\Psi}_l^L(x)D\!\!\!\!/\,\Psi_l^L(x) + \overline{\psi}_l^R(x)\partial\!\!\!/\psi_l^R(x) + \overline{\psi}_{\nu l}^R(x)\partial\!\!\!/\psi_{\nu l}^R(x)] \tag{2.12}$$

The second step is to require that the *covariant derivatives* and the gauge fields transform in the same way, this is done by making the field transform as

$$\begin{aligned} W_i^\mu(x) &\rightarrow W_i^{\mu'}(x) = W_i^\mu(x) + \delta W_i^\mu(x) \\ &\equiv W_i^\mu(x) - \partial^\mu \omega_i(x) - g\epsilon_{ijk}(x) W_k^\mu(x) \end{aligned} \tag{2.13}$$

for an infinitesimal $\epsilon_{ijk}(x)$. Hence,

$$D^\mu \Psi_l^L(x) \rightarrow e^{\frac{1}{2}ig\tau_j\omega_j(x)} D^\mu \Psi_l^L(x) \tag{2.14}$$

this leads to $SU(2)_L$ invariance [18]. The Lagrangian must be invariant under $U(1)$ local phase transformation;

$$\begin{aligned} \psi(x) \rightarrow \psi'(x) &= e^{ig'Yf(x)}\psi(x) \quad , \\ \overline{\psi}(x) \rightarrow \overline{\psi}'(x) &= \overline{\psi}(x) e^{-ig'Yf(x)} \end{aligned} \tag{2.15}$$

if the the ordinary derivatives are replaced by *covariant derivatives*;

$$\partial^\mu \psi(x) \rightarrow D^\mu \psi(x) = [\partial^\mu + ig'YB^\mu(x)]\psi(x) \tag{2.16}$$

where $B^\mu(x)$ is the real gauge field for QED that transforms as;

$$B^\mu(x) \rightarrow B^{\mu'}(x) = B^\mu(x) - \partial^\mu f(x) \tag{2.17}$$

In terms of *covariant derivatives*, equation (2.11) and (2.16), the Lagrangian, equation (2.8), could be written as;

$$\mathcal{L} = i[\overline{\Psi}_l^L(x) \not{D} \Psi_l^L(x) + \overline{\psi}_l^R(x) \not{D} \psi_l^R(x) + \overline{\psi}_{\nu l}^R(x) \not{D} \psi_{\nu l}^R(x)] \tag{2.18}$$

where,

$$\begin{aligned} D^\mu \Psi_l^L(x) &= [\partial^\mu + \frac{1}{2} ig\tau_j W_j^\mu(x) - \frac{1}{2} ig' B^\mu(x)]\Psi_l^L(x) \quad , \\ D^\mu \psi_l^R(x) &= [\partial^\mu - ig' B^\mu(x)]\psi_l^R(x) \quad , \\ D^\mu \psi_{\nu l}^R(x) &= \partial^\mu \psi_{\mu l}^R(x) \end{aligned} \tag{2.19}$$

The Lagrangian is said to be gauge-invariant under $SU(2)_L \otimes U(1)_Y$ by defining the fields $W_j^\mu(x)$ and $B^\mu(x)$ to be invariant under $U(1)_Y$ and $SU(2)_L$ gauge transformations respectively.

- global phase transformations:

The global phase $SU(2)_L$ transformations

$$\begin{aligned} \Psi_l^L(x) \rightarrow \Psi_l^{L'}(x) &= e^{\frac{1}{2}ig\omega_j(x)\tau_j}\Psi_l^L(x) \quad , \\ \overline{\Psi}_l^L(x) \rightarrow \overline{\Psi}_l^{L'}(x) &= \overline{\Psi}_l^L(x) e^{-\frac{1}{2}ig\omega_j(x)\tau_j} \end{aligned} \tag{2.20}$$

which is similar to the case of local transformation but now the positional dependance $g\omega_j(x)$ are three real numbers with the index $j = 1, 2, 3$. The free lepton Lagrangian, equation (2.8), is invariant when the right handed fields are defined as invariant under the global transformations, equation (2.20).

Having these symmetries in hand, according to Noether's theorem we must have conserved quantities.

- ***weak isospin currents:***

For each one of the three conserved weak isospin currents;

$$J_k^\mu(x) = \frac{1}{2}\overline{\Psi}_l^L(x)\gamma^\mu\tau_k\Psi_l^L(x) \quad , \qquad k = 1, 2, 3. \tag{2.21}$$

there is a conserved quantity, known as *weak isospin charge*, thus we have three of them:

$$I_k^W = \int J_k^0(x)\ d^3x = \frac{1}{2}\int \Psi_l^{L\dagger}(x)\tau_k\Psi_l^L(x)\ d^3x \quad , \qquad k = 1, 2, 3. \tag{2.22}$$

one interesting quantity is the conserved current $J_3^\mu(x)$:

$$\begin{aligned} J_3^\mu(x) &= \frac{1}{2}(\overline{\psi}_{\nu l}^L(x)\overline{\psi}_l^L(x))\gamma^\mu \begin{pmatrix} 1 & 0 \\ 0 & -1 \end{pmatrix} \begin{pmatrix} \psi_{\nu l}^L(x) \\ \psi_l^L(x) \end{pmatrix} \\ &= \frac{1}{2}(\overline{\psi}_{\nu l}^L(x)\gamma^\mu\psi_{\nu l}^L(x) - \overline{\psi}_l^L(x)\gamma^\mu\psi_l^L(x)) \end{aligned} \tag{2.23}$$

this is the neutral current which couples either to charged leptons or to neutral neutrinos. One can also define the so-called weak hypercharge current J_Y^μ as:

$$J_Y^\mu(x) = \frac{1}{e}s^\mu(x) - J_3^\mu(x) = -\frac{1}{2}\overline{\Psi}_l^L(x)\gamma^\mu\Psi_l^L(x) - \overline{\psi}_l^R(x)\gamma^\mu\psi_l^R(x) \tag{2.24}$$

and its conserved charge is the so-called weak hypercharge Y:

$$Y = \int J_Y^0(x)\ \ d^3x \tag{2.25}$$

that is related to the electric charge Q and the weak isocharge I_3^W through the relation;

$$Y = \frac{1}{e}Q - I_3^W \tag{2.26}$$

Now we can rewrite the Lagrangian in equation (2.18) in terms of the weak isospin and the weak hypercharge currents as:

$$\begin{aligned} \mathcal{L} = \mathcal{L}_0 &+ i[\overline{\Psi}_l^L(x)\gamma_\mu\left(\partial^\mu + ig\tau_j W_j^\mu(x) - \frac{1}{2}ig'B^\mu(x)\right)\Psi_l^L(x) \\ &+ \overline{\psi}_l^R\gamma_\mu\left(\partial_\mu - ig'B^\mu(x)\right)\psi_l^R + \overline{\psi}_{\nu l}^R\gamma_\mu\partial^\mu\psi_{\nu l}^R] \\ = \mathcal{L}_0 &- gJ_i^\mu(x)W_{j\mu}(x) - g'J_Y^\mu(x)B_\mu(x) \end{aligned}$$

$$\mathcal{L} \equiv \mathcal{L}_0 + \mathcal{L}_I \tag{2.27}$$

where $\mathcal{L}_I$ is the interaction Lagrangian. The first two terms (see figure (2.1)) of the interaction Lagrangian could be written in the form:

$$-g\sum_{i=1}^{2} J_i^{\mu}(x)W_{i\mu}(x) = \frac{-g}{2\sqrt{2}}[J^{\mu\dagger}(x)W_{\mu}(x) + J^{\mu}(x)W_{\mu}^{\dagger}(x)] \tag{2.28}$$

where J_i^{μ} are the charged leptonic current that according to experimental data must have a V-A structure:

$$\begin{aligned} J_{\mu}(x) &= \sum_l \overline{\psi}_l(x)\gamma_{\mu}(1-\gamma_5)\psi_{\nu l}(x) \\ J_{\mu}^{\dagger}(x) &= \sum_l \overline{\psi}_{\nu l}(x)\gamma_{\mu}(1-\gamma_5)\psi_l(x) \end{aligned} \tag{2.29}$$

and $W_{\mu}(x)$ is a new, non-hermitian, gauge field;

$$W_{\mu}(x) = \frac{1}{\sqrt{2}}[W_{1\mu}(x) - iW_{2\mu}(x)] \tag{2.30}$$

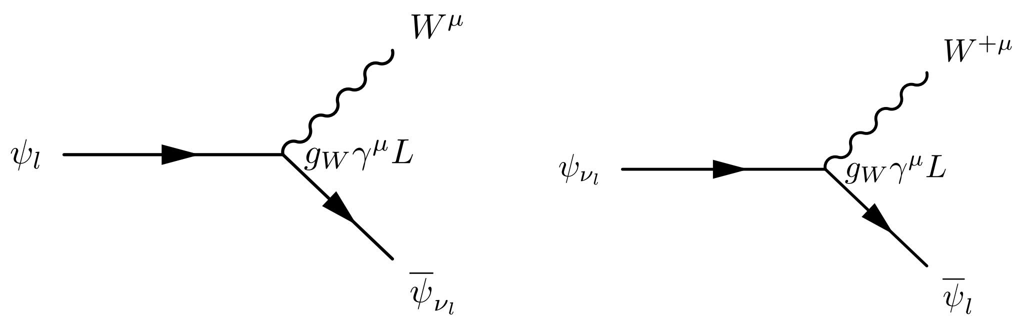

Figure 2.1: Feynman diagrams corresponding to equation (2.28), where $g_W = \frac{g}{2\sqrt{2}}$.

- *weak mixing angle* θ_W:

Gauge fields $W_{3\mu}$ and $B_{\mu}(x)$ can be written as linear combinations of the electromagnetic fields $A_{\mu}(x)$ and of the neutral current gauge field $Z_{\mu}(x)$:

$$\begin{aligned} W_{3\mu}(x) &= \cos\theta_W Z_{\mu}(x) + \sin\theta_W A_{\mu}(x) \\ B_{\mu}(x) &= -\sin\theta_W Z_{\mu}(x) + \cos\theta_W A_{\mu}(x) \end{aligned}$$

In this sense we can mix weak and electromagnetic interactions. They decouple when $\theta_W = 0$ but experimental data shows that this is not the case and $\theta_W \simeq 30^o$. Now we can write the last two terms of equation (2.27) as a function of the weak hypercharge current J_Y^{μ}:

$$\begin{aligned} -J_3^{\mu}(x)W_{\mu}^3(x) &- g'J_Y^{\mu}(x)B_{\mu}(x) \\ &= -\frac{g'}{e}s^{\mu}(x)[\sin\theta_W Z_{\mu}(x) + \cos\theta_W A_{\mu}(x)] \\ &- J_3^{\mu}(x)(g[\cos\theta_W Z_{\mu}(x) + \sin\theta_W A_{\mu}(x)] \\ &- g'[-\sin\theta_W Z_{\mu}(x) + \cos\theta_W A_{\mu}(x)]) \end{aligned} \tag{2.31}$$

Now the interaction Lagrangian takes the following form:

$$\mathcal{L}_I = -s^\mu(x)A_\mu(x) - \frac{g}{2\sqrt{2}}[J^{\mu\dagger}(x)W_\mu(x) + J^\mu(x)W_\mu^\dagger(x)]$$
$$-\frac{g}{\cos\theta_W}[J_3^\mu(x) - \frac{1}{e}\sin^2\theta_W s^\mu(x)]Z_\mu(x) \tag{2.32}$$

This is the $SU(2)_L \otimes U(1)_Y$ gauge-invariant interaction Lagrangian that Glashow presented in 1961, in which the first term is the electromagnetic current coupling to the photon field, the second term represents the charged current and its quanta, $W(x)$ and $W^\dagger(x)$, are interpreted as the physical $W^\pm$ vector bosons, and the last term is for the neutral current and its quanta $Z_\mu(x)$ is the physical boson Z^0. Still one problem is that $W^\pm$ and Z^0 are massless so far.

For the quark sector the EW interactions look the same as in the case of leptons. In this case the up-type (u,c,t) quarks play the neutrino's role and down-type (d,s,b) quarks play the lepton's (e,μ,τ) role. Quarks can move from one generation to another, thus the vertex factors involving quarks carry an additional factor to take into account the probability of quarks mixing. These probabilities are expressed by the Cabibbo-Kobayashi-Maskawa (CKM) matrix, equation (2.33), [13] in which the probability of a quark to transform from flavor i to flavor j is equal to $|V_{ij}|^2$:

$$V_{CKM} = \begin{pmatrix} |V_{ud}| & |V_{us}| & |V_{ub}| \\ |V_{cd}| & |V_{cs}| & |V_{cb}| \\ |V_{td}| & |V_{ts}| & |V_{tb}| \end{pmatrix} = \begin{pmatrix} 0.974 & 0.226 & 0.004 \\ 0.230 & 1.04 & 0.041 \\ 0.008 & 0.039 & 0.77 \end{pmatrix} \tag{2.33}$$

2.2.4 Quantum Chromodynamics (QCD)

In addition to EW interactions, quarks have also strong interactions, which are described by the so called Quantum Chromodynamics theory (QCD). QCD is a special kind of quantum field theory called non-abelian gauge theory. QCD enjoys two peculiar properties:

- ***Confinement*:** it means that the force between quarks does not diminish as they are separated. Because of this, it would take an infinite amount of energy to separate two quarks; they are forever bound into hadrons such as the proton and the neutron. Although analytically unproven, confinement is widely believed to be true because it explains the consistent failure of free quark searches.
- ***Asymptotic freedom*:** which means that at very high-energy, quarks and gluons (the strong force boson) interact very weakly. This prediction of QCD was first discovered in the early 1970s by David Politzer and by Frank Wilczek and David Gross. For this work they were awarded the 2004 Nobel Prize in Physics.

There is no known phase-transition line separating these two properties; confinement is dominant at low-energy scales, but as energy increases, asymptotic freedom becomes dominant. QCD defines a new quantum number for quarks and gluons, the color charge, which can be red, green or blue for a quark and anti-red, anti-green or anti-blue for a anti-quark. Therefore, there are three versions of each quark (anti-quark) flavor which are grouped in a triplet that belongs to the fundamental representation (**3**) (to the complex conjugate representation (**3***)):

$$\psi_q \equiv \begin{pmatrix} \psi_{q1} \\ \psi_{q2} \\ \psi_{q3} \end{pmatrix}, \qquad \overline{\psi}_q \equiv \begin{pmatrix} \overline{\psi}_{\overline{q}1} \\ \overline{\psi}_{\overline{q}2} \\ \overline{\psi}_{\overline{q}3} \end{pmatrix} \tag{2.34}$$

where the three indices "1", "2" and "3" in the quark triplet are usually identified with the three colors. Only colorless (white) particles can be found in free state that's why quarks must confine inside a hadron. The Lagrangian that describes the strong force is assumed to be invariant under $SU(3)_C$ transformations because there are three versions of each quark. The symmetry group $SU(3)_C$ has 8 generators (the so called Gell-Mann matrices, λ_a), and therefore the gluon corresponds to an octet of fields, belonging to the adjoint representation (**8**), and can be written as:

$$\mathbf{A}_\mu = A^a_\mu \lambda_a \tag{2.35}$$

Gluons have a combination of two color charges (one of red, green or blue and one of anti-red, anti-green and anti-blue) in a superposition of states, λ_a. All other particles have no color charge (colorless or white). The free-quark QCD Lagrangian is:

$$\mathcal{L}^0_{QCD} = \overline{\psi}_q(\gamma^\mu i\partial_\mu - m_q)\psi_q \tag{2.36}$$

As in the case of EW, the ordinary derivative ∂_μ is replaced with the covariant derivative D_μ to make the free quark Lagrangian invariant under $SU(3)_C$ transformation:

$$\partial^\mu \psi_q(x) \to D^\mu \psi_q(x) = [\partial^\mu + ig_s t^a G^{\mu,a}(x)]\psi_q(x) \tag{2.37}$$

where g_s is the strong coupling constant, $G^{\mu,a}(x)$ are the 8 gauge fields, and t^a are the 8 group generators:

$$t^a \equiv \frac{1}{2}\lambda^a \tag{2.38}$$

With this replacement the Lagrangian becomes:

$$\mathcal{L} = \overline{\psi}_q(x)(\gamma^\mu i\partial_\mu - m_q)\psi_q(x) - g_s j^a_\mu(x) G^{\mu,a}(x) \tag{2.39}$$

where the $j^a_\mu(x) \equiv \overline{\psi}_q(x)\gamma^\mu t^a \psi_q(x)$ is the conserved color-octet current and the corresponding conserved quantity is color charge. This Lagrangian gives us a QCD basic vertex, see figure (2.2).

Since gluons themselves carry color charge, they participate in strong interactions and are able to emit/absorb other gluons. The interaction Lagrangian corresponding to this is:

$$\mathcal{L}_G = -\frac{1}{4}G^a_{\mu\nu}(x)G^{\mu\nu,a}(x), \qquad G^a_{\mu\nu}(x) \equiv F^a_{\mu\nu} - g_s f^{abc} G^b_\mu G^c_\nu \tag{2.40}$$

where $F^a_{\mu\nu} \equiv \partial_\mu G^a_\nu - \partial_\nu G^a_\mu$ and $[t^a, t^b] = i f^{abc} t^c$. That's what causes the non-abelian nature of $SU(3)_C$ group, leading to 3- and 4-gluon vertices in figure (2.3). This gluon self-interaction causes the *asymptotic freedom*: as quarks come closer to each other, the chromodynamic binding force between them weakens. Conversely, as the distance between quarks increases, the binding force strengthens. The color field becomes stressed,

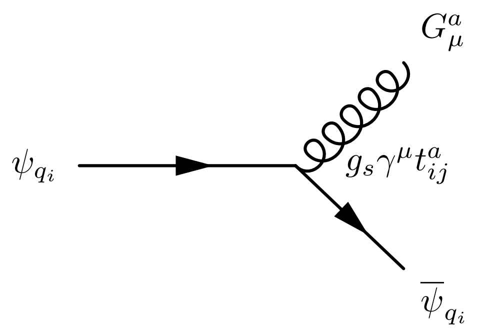

Figure 2.2: Feynman diagram corresponding to equation (2.39), the first QCD basic vertex.

much as an elastic band is stressed when stretched, and more gluons of appropriate color are spontaneously created to strengthen the field. Above a certain energy threshold, pairs of quarks and antiquarks are created. These pairs bind with the quarks being separated, causing new hadrons to form. This explains *color confinement*. This process of hadronization occurs before quarks formed in a high energy collision are able to interact in any other way. The only exception is the top quark, which decays before it hadronizes [19].

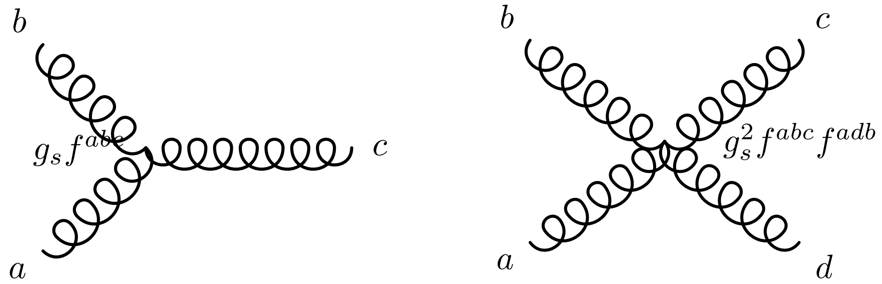

Figure 2.3: Feynman diagrams of 3- and 4-gluon vertices.

The complete Lagrangian of strong interactions is:

$$\begin{aligned}\mathcal{L}_{QCD} &= \overline{\psi}_q(x)(\gamma^\mu i\partial_\mu - m_q)\psi_q(x) - g_s j_\mu^a(x) G^{\mu,a}(x) \\ &+ F_{\mu\nu}^a F^{a,\mu\nu} - 2g_s F_{\mu\nu}^a f^{abc} G^{b,\mu} G^{c,\nu} + (g_s)^2 f^{abc} f^{adh} G_\mu^b G_\nu^c G^{d,\mu} G^{h,\nu} \end{aligned} \tag{2.41}$$

2.2.5 The Standard Electroweak Theory

In the SM, the Higgs mechanism is used to give masses to fermions as well as bosons, including the photon. But we know this is not the case for photon. To overcome this, the combination of spontaneous symmetry breaking for $SU(2)_L \otimes U(1)_Y$ in conjunction with the Higgs mechanism is used to give masses (proportional to the vacuum expectation value of the Higgs field) to fermions (through Yukawa coupling between the Higgs field and massless fermions) and to Z^0 and $W^\pm$ bosons while keeping the $U(1)_Y$ symmetry exact and therefore leaving the photon massless. This introduces a scalar field with a non-zero vacuum expection value, the Higgs field that is not invariant under the $SU(2)_L \otimes U(1)_Y$ transformation. The minimal $\phi(x)$ field is a doublet:

$$\Phi(x) = \begin{pmatrix} \phi_a(x) \\ \phi_b(x) \end{pmatrix} \tag{2.42}$$

where $\phi_a(x)$ and $\phi_b(x)$ are scalar fields. For simplicity we will consider only the electroweak Lagrangian for leptonic and bosonic parts and not the quark's part, $\mathcal{L} = \mathcal{L}^L + \mathcal{L}^B$. We can define a Higgs part, $\mathcal{L}^H$, in the Lagrangian:

$$\begin{aligned} \mathcal{L}^H &= [D^\mu \Phi(x)]^\dagger [D_\mu \Phi(x)] - \mu^2 \Phi^\dagger(x)\Phi(x) - \lambda[\Phi^\dagger(x)\Phi(x)]^2 \\ D^\mu \Phi(x) &= [\partial^\mu + \frac{1}{2} i g \tau_j W_j^\mu(x) + i g' Y B^\mu(x)]\Phi(x) \end{aligned} \tag{2.43}$$

This part of Lagrangian is invariant under $SU(2)_L \otimes U(1)_Y$, see for example [18]. The Higgs field Φ_0 of vacuum state:

$$\Phi_0 = \begin{pmatrix} 0 \\ \nu/\sqrt{2} \end{pmatrix} \quad , \qquad \nu = \sqrt{-\mu^2/\lambda} \tag{2.44}$$

(where $\lambda > 0$ and $\mu^2 > 0$) is not invariant under $SU(2)_L \otimes U(1)_Y$ transformation, and invariant under $U(1)_Y$ transformation alone as the photon is massless. In terms of deviations from the vacuum field the Higgs field:

$$\Phi(x) = \frac{1}{\sqrt{2}} \begin{pmatrix} \eta_1(x) + i\eta_2(x) \\ \nu + \sigma(x) + i\eta_3(x) \end{pmatrix} \tag{2.45}$$

The Higgs part of the Lagrangian could be written as a function of the real fields $\sigma(x)$, $\eta_i(x)$, $i = 1, 2, 3$. Knowing that the three η_i fields are unphysical, $\Phi(x)$ in case of a specific transformation, first $SU(2)_L$ then a $U(1)_Y$ transformation, the so-called unitary gauge, could be written as:

$$\Phi(x) = \frac{1}{\sqrt{2}} \begin{pmatrix} 0 \\ \nu + \sigma(x) \end{pmatrix} \tag{2.46}$$

where the fourth field $\sigma(x)$ will give on quantization a massive, electrically neutral and spin zero boson, the Higgs boson. Adding to the Lagrangian the fermion masses by adding the gauge invariant term $\mathcal{L}^{FH}$:

$$\mathcal{L} = \mathcal{L}^L + \mathcal{L}^B + \mathcal{L}^H + \mathcal{L}^{FH} \tag{2.47}$$

Here I will write only the lepton part as the quark part is identical:

$$\begin{aligned} \mathcal{L}^{LH} = \; -g_l \quad & [\overline{\Psi}_l^L(x)\psi_l^R(x)\Phi(x)] + \Phi^\dagger(x)\overline{\psi}_l^R(x)\Psi_l^L(x)] - \\ g_{\nu_l} \quad & [\Psi_l^L(x)\psi_{\nu_l}^R(x)\overline{\Phi}(x)] + \overline{\Phi}^\dagger(x)\overline{\psi}_{\nu_l}^R(x)\Psi_l^L(x)] \end{aligned} \tag{2.48}$$

where g_l and g_{ν_l} are dimensionless coupling constants and $\overline{\Phi}(x) = -i[\Phi^\dagger(x)\tau_2]^T$. After transformation (not shown here) one finds the SM predictions for $W^\pm$ and Z^0 bosons masses are;

$$M_W = \frac{1}{\sin\theta_W}\sqrt{\frac{\alpha\pi}{G\sqrt{2}}} \qquad\qquad M_Z = \frac{2}{\sin 2\theta_W}\sqrt{\frac{\alpha\pi}{G\sqrt{2}}} \tag{2.49}$$

where $\alpha \simeq 1/137$ is the so-called fine structure constant (the coupling constant characterizing the strength of the electromagnetic interaction) and $G \simeq 1.166 \times 10^{-5}$ is the Fermi constant. The prediction for the masses to the first perturbative order is $M_W = 76.9$ GeV and $M_Z = 87.9$ GeV. When using higher order perturbation theory, $M_W = 79.8 \pm 0.8$ GeV and $M_Z = 90.8 \pm 0.6$ GeV. The experimental values (see table 2.1) are $M_W = 80.398 \pm 0.025$ GeV and $M_Z = 91.1876 \pm 0.0021$ GeV [13] that is in good agreement with the SM predictions. Unfortunately, the fermions masses (the Higgs mass) are (is) function of the free parameters g (μ), where $M_l = \nu g/\sqrt{2}$ ($M_H = \sqrt{2\mu^2}$), therefore there is no prediction from the theory.

2.3 Current Shortcomings of the Standard Model

Although the SM is one of the most successful and thoroughly tested theories in physics, it cannot be the final answer. Many unsolved mysteries seem to require concepts and mechanisms that go beyond our present knowledge. In this section, a list of some examples of the SM shortcomings is given:

- ***Unification problem*:** in SM, there is no real unification between the electroweak and strong interactions, they are treated in parallel. The three coupling constants associated with the three gauge groups in the SM, are running with the energy available for interaction. It is believed that they should unify at some scale, unfortunately this is not the case for SM. This led theories to attempt to unify the strong and electroweak interactions in the so-called *Grand-Unified Theories*.

- ***Gravity*:** SM describes both the strong and electroweak forces but it does not tell us anything about the fourth fundamental force, gravity. This led theories to attempt to unify the strong and electroweak with gravity, *Theories of Everything*.

- ***Neutrino masses*:** experiments show that a neutrino created with a specific lepton flavor (ν_e, ν_μ or ν_τ) can later be measured to have a different flavor. Moreover the probability of measuring a particular flavor for a neutrino varies periodically as it propagates. This neutrino oscillation phenomena between different flavors is not possible if neutrinos have zero masses as assumed in the SM.

- ***Dark matter and Dark energy*:** astronomy and cosmology tell us that only about 4% of our universe is made of ordinary matter, the rest is the so-called Dark Matter (23%) and Dark Energy 73%. The SM does not have candidate for dark matter and does not explain dark energy.

- ***Baryon asymmetry*:** antiparticles are produced in any environment with a sufficiently high temperature (mean particle energy must be greater than the pair production threshold). During the period of baryogenesis, when the universe was extremely hot and dense, matter and antimatter were continually produced and annihilated. The presence of remaining matter, and absence of detectable remaining antimatter, is attributed to violation of the CP-symmetry relating matter and antimatter. The exact mechanism of this violation during baryogenesis remains a mystery and CP-violation incorporated in the CKM matrix is indeed not enough.

- ***The Higgs potential***[20]**:**

$$V_{Higgs} = V_0 - \mu^2\phi^\dagger\phi + \lambda(\phi^\dagger\phi)^2 + [\overline{\Psi}_{Li}Y_{ij}\Psi_{Rj}\phi + h.c.] \tag{2.50}$$

  where V_0 is the vacuum energy which is the constant term in the expression. Its magnitude ($\langle V_0\rangle \simeq (2\times10^{-3}\ eV)^4$) is a real puzzle, since it is off by orders and orders of magnitude with respect to what one could expect. The fine-tuning of the Higgs boson mass is a second problem, related to the fact that this parameter receives very large contributions from radiative corrections of either sign in the theory. Also the shape of the Higgs potential V depends on the value of the parameter λ and of the Higgs mass, and in some cases it develops an instability (the vacuum is not the vacuum anymore because there is no minimum for some values). And then there is the puzzle of why the Yukawa couplings of the Higgs to fermion fields are so widely different (the coupling to the top quark is of order unity, those to neutrinos are tiny).

- ***Hierarchy problem*****:** one could ask why the gravity energy scale (or Planck Mass, M_{Pl}) and the electroweak energy scale (M_{EW}) are so different: 10^{19} GeV compared to 246 GeV, respectively [21].

- ***Fermion generations and their masses*****:** the SM does not explain why there are three generations of leptons and quarks. Why does Nature need the two other generations? Why the fermions masses span over many orders of magnitude?

- ***Free parameters*****:** there are 19 free parameters in the SM that must be determined by experiments. These are:
  - ***lepton masses*****:** M_e, M_μ and M_τ.
  - ***quark masses*****:** M_u, M_c, M_t, M_d, M_s and M_b.
  - ***CKM matrix parameters*****:** θ_{12}, θ_{13}, θ_{23} and δ.
  - ***U(1), SU(2), and SU(3) gauge couplings*****:** g_1, g_2, and g_3.
  - ***QCD vacuum angle*****:** θ_{QCD}.
  - ***Higgs quadratic coupling*****:** μ.
  - ***Higgs self-coupling strength*****:** λ.

2.4 Physics Beyond the Standard Model (BSM)

Theorists have proposed several possible extensions for the SM, some possible candidates are listed below.

- ***Supersymmetry (SUSY)*****:** is a symmetry that relates every SM elementary particle to its so-called superpartner. The superpartner differs from its SM partner by half a unit of spin. In a theory with unbroken supersymmetry, for every type of boson there exists a corresponding type of fermion with the same mass and internal quantum numbers, and vice-versa. Since the superpartners of the SM particles have not been observed, supersymmetry, if it exists, must be a broken symmetry, allowing the superparticles to be heavier than the corresponding Standard Model particles. If supersymmetry exists close to the TeV energy scale, it allows for a solution of the hierarchy problem of the SM: the fact that the Higgs boson mass is subject to quantum corrections which (barring extremely fine-tuned cancellations among independent contributions) would make it so large as to undermine the internal consistency of the theory. In supersymmetric theories, on the other hand, the contributions to the quantum corrections coming from Standard Model particles are naturally canceled by the contributions of the corresponding superpartners. Another attractive feature of TeV-scale supersymmetry is the fact that it allows for the high-energy unification of the strong interactions and electroweak interactions. Models that conserve the so-called R-parity (new quantum number offered by SUSY in which all SM particles have R-parity $= 1$ while their superpartners have R-parity $= -1$) provide a candidate for Dark Matter. Moreover, it also introduces a natural mechanism for electroweak symmetry breaking. SUSY is also a feature of most versions of the so-called string theory, though it can exist in Nature even if string theory is incorrect.

- ***Extra dimensions*:** there are many models for extra dimensions some models are listed here:
  - ***The ADD model*:** also known as the model with large extra dimensions, it introduces a possible scenario to explain the weakness of gravity relative to the other forces. This theory requires that the fields of the SM are confined to a four-dimensional brane, while gravity propagates in several additional spatial dimensions that are large compared to the Planck scale. The theory thus offers a solution to the hierarchy problem. The theory also offers a Dark Matter candidate since the graviton can travel in all the spatial dimensions, giving rise to several Kaluza-Klein resonances on the four-dimensional brane.
  - ***Warped extra dimensions*:** it predicts one extra dimension that is highly curved and the production of the so-called Randall-Sundrum (RS) gravitons [22]. Such models require two fine tunings; one for the value of the bulk cosmological constant and the other for the brane tensions. There are two popular models. The first, called RS1, has a finite size for the extra dimension with two branes, one at each end. The second, RS2, is similar to the first, but one brane has been placed infinitely far away, so that there is only one brane left in the model.

  If the Higgs boson is not found, then other models may be possible candidates: technicolor models, Compositeness, ...

- ***Compositeness model*:** leptons and quarks may not be fundamental particles, but rather an agglomeration of smaller constituents called preons. The constituents could be 3 fermions or a fermion and a boson. These features are visible above a characteristic energy scale Λ below which quarks/leptons appear point like. Λ characterizes both the strength of preon coupling and physical range of the compositeness scale. Compositeness model can address some of the SM shortcomings like;
  - ***Mass hierarchy*:** compositeness model can naturally solve the observed mass hierarchy that appear in the three fermion generations.
  - ***three generations*:** this could be explained in a way similar to the presence of isotopes in atomic physics.
  - ***free parameters*:** it may explain parameters such as particle mass, electric charge, and color charge. It also can effectively minimize the Particle Zoo! to a lower number of fundamental particles.

  This model will be discussed in some more detail in chapter three.

3

Selected Models with Di-Electron and Di-Electron+Photon Final States

The SM describes quite accurately physics near the electroweak symmetry breaking scale ($\sim$ 246 GeV). Due to its shortcomings (some of them are already mentioned at the end of chapter 2), the SM is believed to be a "low energy" approximation to a more fundamental theory. Moreover, the SM cannot be valid at energies above the Planck scale ($\sim 10^{19}$ GeV)[21], where gravity can no longer be ignored. In this chapter, some of the Beyond Standard Model (BSM) candidates with di-electron and di-electron+photon final states are mentioned. More explicitly, this chapter is divided into two sections. In section 3.1 some models predicting one or more Z' are mentioned as well as `TEVATRON` limits on Z' while in section (3.2) the compositeness model with excited electron (e^*) as an example is discussed and the current limits on e^* reviewed.

3.1 New Neutral Weak Gauge Boson

The existence of new weak gauge bosons is predicted in many BSM theories. These new gauge bosons are usually named Z' for electrically neutral boson and W' for charged one. Some of such models are considered below:

- ***Sequential Standard Model (SSM)*** **[23]:** It is a higher energy copy of the SM with weak gauge bosons similar to those of the SM but heavier. This model is not gauge invariant and thus not a realistic model, but it is used as benchmark for Z' searches since in this model Z' has the same couplings to fermions as the SM Z boson. If this type of Z' exists, it will decay to usual SM fermion anti-fermion pairs.

- ***Grand-Unification*** E_6 ***models*****:** These models involve breaking the E_6 group into $SU(5)$ and two additional $U(1)$ groups, inducing two new neutral gauge bosons, Z'_ψ and Z'_χ [24, 25]. Their lowest mass linear combination is considered a Z' candidate:

$$\begin{aligned} E_6 \rightarrow SO(10) \otimes U(1)_\psi &\rightarrow SU(5) \otimes U(1)_\chi \otimes U(1)_\psi \rightarrow SM \otimes U(1)_{\theta_{E_6}} \\ Z'(\theta_{E_6}) &= Z'_\psi \cos\theta_{E_6} + Z'_\chi \sin\theta_{E_6} \end{aligned} \tag{3.1}$$

  where $0 \leq \theta_{E_6} < \pi$ is the mixing angle between the two $U(1)$. There are 6 well justified states Z'_S, Z'_N, Z'_ψ, Z'_χ, Z'_η, and Z'_I, each corresponding to a different value of θ_{E_6}, where $\chi(\theta_{E_6} = 0)$, $\psi(\theta_{E_6} = \pi/2)$, $\eta(\theta_{E_6} = \pi - \arctan\sqrt{5/3} \sim 0.71\pi)$, inert model $I(\theta_{E_6} = \arctan\sqrt{3/5} \sim 0.21\pi)$, the neutral-$N$ model ($\theta_{E_6} = \arctan\sqrt{15} \sim 0.42\pi$), and the secluded sector model, $S(\theta_{E_6} = \arctan\sqrt{15}/9 \sim 0.13\pi)$.

We assume that the resonance is narrow, such that it is not much wider than the mass resolution of the electromagnetic calorimeter. Table 3.1 displays the Z' intrinsic width of the considered models. For any E_6 model, the width is in any case predicted to be roughly between 0.5% and 1.25% [26].

Table 3.1: Intrinsic width relative to the Z' mass, and $Z' \to e^+e^-$ branching ratio at $m_{Z'} = 1$ TeV of the considered Z' models.

Model	Z'_{SSM}	Z'_ψ	Z'_{N}	Z'_η	Z'_I	Z'_{S}	Z'_χ
Width [%]	3.1	0.6	0.7	0.7	1.1	1.2	1.2
BR($Z' \to e^+e^-$) [%]	3.1	4.5	5.5	3.7	6.6	6.5	6.0

3.1.1 Previous searches for Z' at the TEVATRON

The TEVATRON is a $p\bar{p}$ collider working at $E_{\mathrm{cm}} = 1.96$ TeV. It has searched for Z' directly by looking for its resonances (for example dilepton invariant mass). It hosts two general purpose detectors D0 and CDF. At the TEVATRON, no excess above the SM predictions were observed. The latest observed upper limits from the D0 experiment on the production cross section multiplied by the branching ratio for the process $p\bar{p} \to Z' \to ee$ as a function of the mass hypothesis under the assumption that the observed dielectron invariant mass spectrum arises only from the backgrounds are shown in figure 3.1(a) [1]. This analysis is based on 5.4 fb^{-1} of data. The CDF collaboration did an equivalent analysis in the muon channel based on 4.6 fb^{-1} of data [2]. The observed mass limits given by D0 and CDF collaborations are summarized in table 3.2. Figure 3.1(b) shows the CDF cross section times branching ratio upper limits in the muon channel as a function of the dimuon invariant mass.

Table 3.2: The D0 and CDF observed lower mass limits for various Z' bosons [1, 2].

Model	Observed Lower Mass Limit (GeV)	
	D0	CDF
Z'_{SSM}	1023	1071
Z'_η	923	938
Z'_χ	903	930
Z'_ψ	891	917
Z'_N	874	900
Z'_S	822	858
Z'_I	772	817

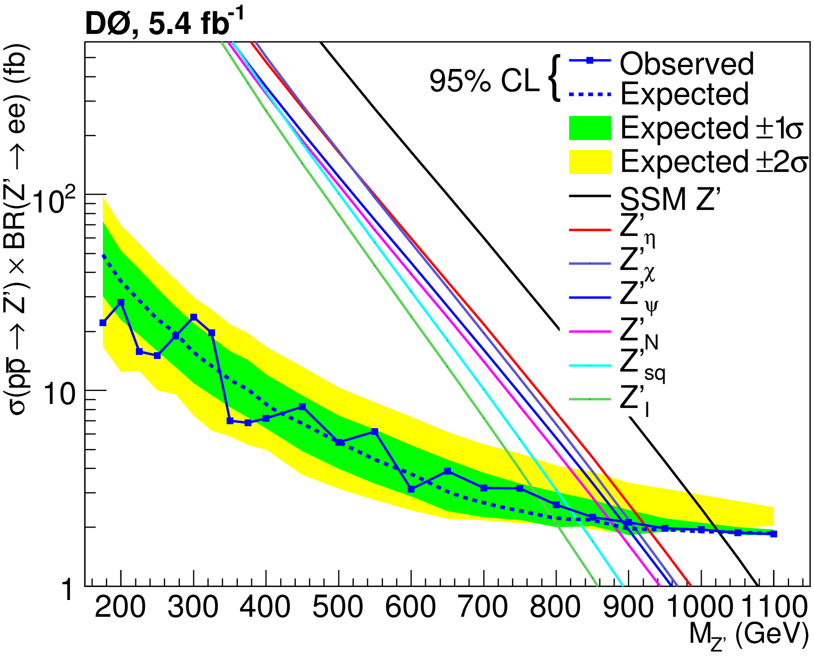

(a) D0

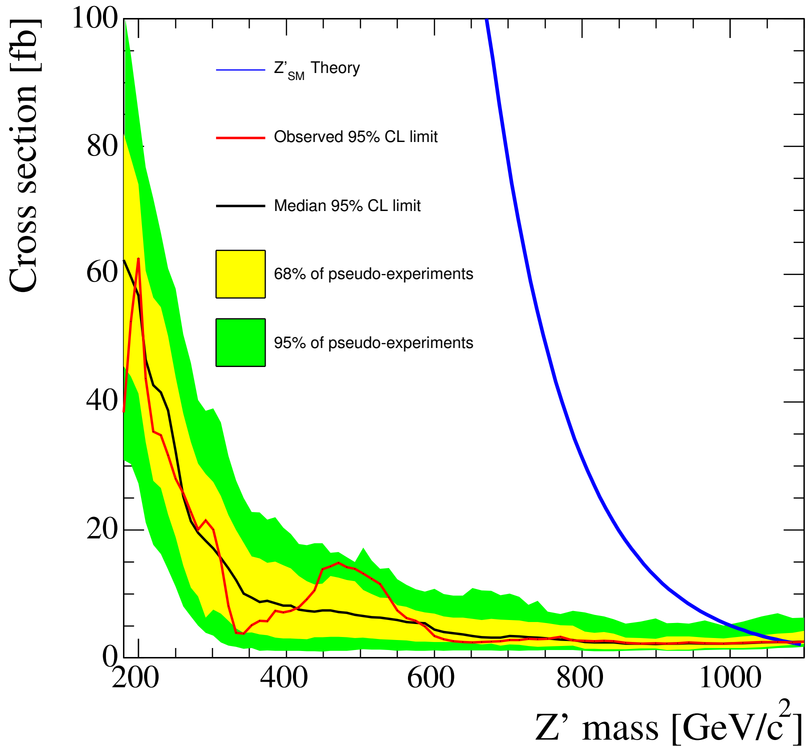

(b) CDF

Figure 3.1: The D0 (a) upper limits on $\sigma(p\bar{p} \to Z') \times BR(Z' \to ee)$ and the CDF (b) upper limits on $\sigma(p\bar{p} \to Z') \times BR(Z' \to \mu\mu)$ as a function of Z' mass. The median expected limits are shown with the ± 1 and ± 2 σ bands [1, 2].

3.2 Excited Electrons

The hierarchical structure of the quarks and leptons $SU(2)$ doublets in the SM could indicate that the quarks and leptons have a substructure. The so-called compositeness model assumes that quarks and leptons are bound states of three fermions or of a fermion and a boson. The supposed constituents are called preons. At the scale of the constituent binding energies Λ, a new strong interaction among quarks and leptons should appear. This would give a large spectrum of excited states [27, 28, 29, 3].

3.2.1 Effective Lagrangian

In phenomenological models, it is assumed that any theory of compositeness at large mass scale must have a low energy limit that preserves the symmetries of the SM. If quarks and leptons are composite, the strong forces binding their constituents induce flavor-diagonal contact interactions, which have significant effects at subprocess energies well below Λ [27]. Contact interactions between quarks and leptons may appear as the low energy limit of the exchange of heavy particles. At sufficiently high energies excited fermions could be produced directly. According to the model we consider [27], they should form weak iso-doublets and carry electromagnetic charges similar to those of the ordinary fermions. Excited leptons are assumed to have spin and isospin $\frac{1}{2}$ to limit the number of parameters. In the current study, CompHEP[1][30] is used to generate excited electron signal samples. Pythia[31] Monte-Carlo generator is also used. Since in Pythia the excited electron is only produced via contact interactions and decays only via gauge mediated interactions, the next two subsections will mention this particular case, i.e production via contact interaction and decay via gauge mediated interactions. Actually, CompHEP is used to generate signal samples to handle the e^* production/decay spin correlation which is not well modeled in Pythia, see Appendix A. There are a few processes already implemented in CompHEP , including the SM processes. To implement the e^* production/decay models in CompHEP, LanHEP [32] is used to write the Feynman rules in CompHEP format using the model Lagrangian as an input.

3.2.1.1 Production of excited electrons via contact interactions

Excited electrons may couple to ordinary quarks via contact interactions resulting from preon interactions. For energies below the compositeness scale Λ, these interactions can be described by an effective four-fermion Lagrangian [27]:

$$\mathcal{L}_{CI} = \frac{g^2}{2\Lambda^2} j^\mu j_\mu \tag{3.2}$$

where j_μ is the fermion current

$$j_\mu = \eta_L \overline{f}_L \gamma_\mu f_L + \eta'_L \overline{f}^*_L \gamma_\mu f^*_L + \eta''_L \overline{f}^*_L \gamma_\mu f_L + (L \to R) + h.c. \tag{3.3}$$

with f, f^* being the SM and excited fermions respectively. The arbitrary coupling constant is chosen such that $g^2 = 4\pi$. Only the left-handed currents are considered, $\eta_L = \eta'_L = \eta''_L = 1$, while the right-handed currents are neglected for simplicity, $\eta_R = \eta'_R = \eta''_R = 0$.

At LHC, excited electrons can be produced either singly $q\overline{q} \to e\overline{e}^*$ $(e^*\overline{e})$, figure 3.2(a), or in pairs $q\overline{q} \to e^*\overline{e}^*$, figure 3.2(b), through contact interactions. Since $e^*\overline{e^*}$ pair production

[1] CompHEP is a Monte Carlo program that evaluates the Feynman rules, calculates the matrix elements squared, generates events, and calculates the cross-sections at leading order from a given input Lagrangian.

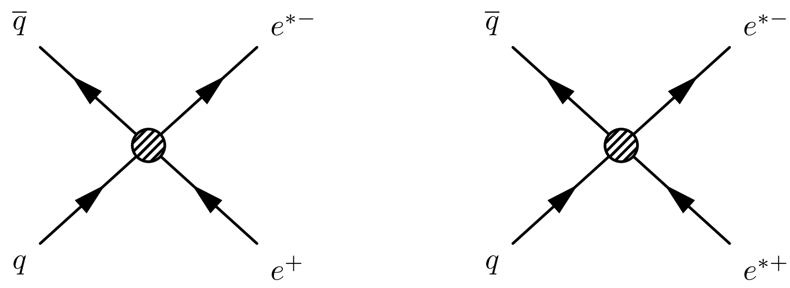

(a) e^* single production (b) e^* pair production

Figure 3.2: Contact interactions of excited electrons (e^*) with quarks (q) and electrons (e).

requires larger centre of mass energy than single $e\bar{e}^*$ production, it is less favored, see figure 3.3 [3]. Thus, we will consider only the case of single production. In case of single e^* production ($q\bar{q} \to e^* e$), the effective Lagrangian, equation (3.2), is reduced to:

$$\mathcal{L}_{CI} = \frac{g^2}{2\Lambda^2}(\bar{q}_L \gamma^\mu q_L)(\bar{e}^*_L \gamma_\mu e_L) + h.c. \tag{3.4}$$

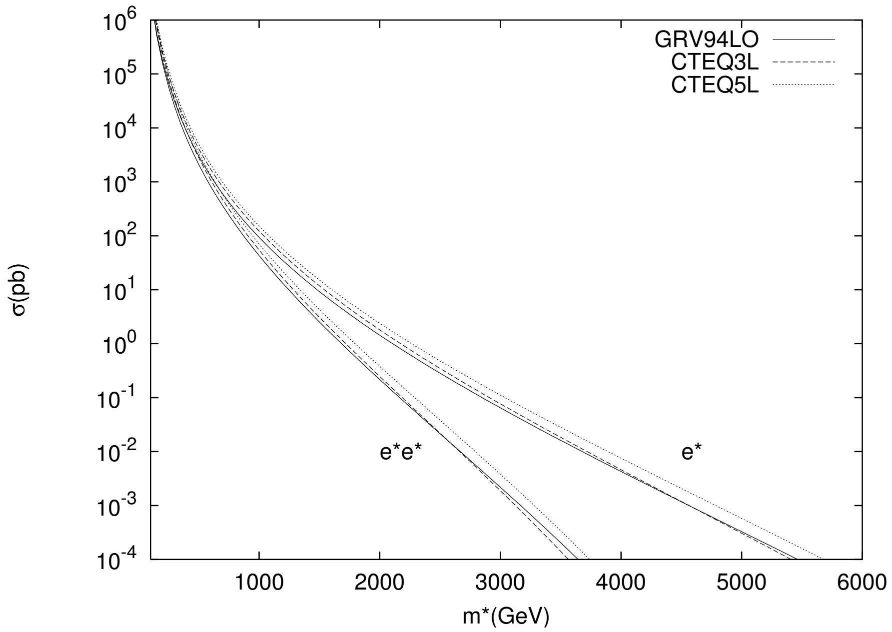

Figure 3.3: Cross sections for single and pair production of excited electrons through contact interactions at LHC ($\sqrt{s} = 14$ TeV, $\Lambda = m_{e^*}$) calculated using different PDFs [3].

The parton level cross sections for single excited electron production through contact interactions are given by [27]:

$$\widehat{\sigma}(q\bar{q} \to e\bar{e}^*, e^*\bar{e}) = \frac{\pi}{6\widehat{s}}\left(\frac{\widehat{s}}{\Lambda^2}\right)^2\left(1+\frac{v}{3}\right)\left(1-\frac{m^2_{e^*}}{\widehat{s}}\right)^2\left(1+\frac{m^2_{e^*}}{\widehat{s}}\right) \tag{3.5}$$

$$\widehat{\sigma}(q\bar{q} \to l^*\bar{l}^*) = \frac{\pi\widetilde{v}}{12\widehat{s}}\left(\frac{\widehat{s}}{\Lambda^2}\right)^2\left(1+\frac{\widetilde{v}^2}{3}\right) \tag{3.6}$$

where

$$v = \frac{\hat{s} - m_{e^*}^2}{\hat{s} + m_{e^*}^2} \quad , \quad \tilde{v} = \left(1 - 4\frac{m_{e^*}^2}{\hat{s}}\right)^{1/2} \tag{3.7}$$

$\hat{s}$ denotes the Mandelstam variable for the subprocess centre of mass energy and m_{e^*} is the excited electron mass.

Excited electrons can also be produced via gauge interactions (see the effective Lagrangian for the gauge mediated interactions in the next subsection). Gauge interactions can give rise to e^*e^*, ee^*, and $e^*\nu_e$ signatures. The study of such scenario has been carried out in [28]. However, since those processes involve electromagnetic or electroweak couplings they contribute to less than 1% (depending on e^*mass) compared to the excited electron production rate via contact interactions [28]. It is also remarkable to mention that the "charged current" contact term like $ud \to e\nu_e$ is not forbidden by $U(1) \otimes SU(2)_L \otimes SU(3)$ symmetry and can give rise to $e^*\nu_e$ production in contact interactions. This effective Lagrangian is not considered in PYTHIA[31].

3.2.1.2 Decay of excited electrons via gauge mediated interactions

The effective Lagrangian which describes the coupling of excited fermion states and ground states via gauge interactions is given by [27]:

$$\mathcal{L}_{GM} = \frac{1}{2\Lambda}\bar{f}_R^*\sigma^{\mu\nu}(g_s f_s \frac{\lambda^a}{2} G_{\mu\nu}^a + g f \frac{\tau}{2} W_{\mu\nu} + g' f' \frac{Y}{2} B_{\mu\nu}) f_L + h.c. \tag{3.8}$$

where $\sigma^{\mu\nu}$ is the covariant bilinear tensor; $G_{\mu\nu}^a$, $W_{\mu\nu}$ and $B_{\mu\nu}$ are the field strength tensors of the gluon and the SU(2) and U(1) gauge fields with the group generators λ^a (Gell-Mann matrices), τ (Pauli matrices) and Y (weak hypercharge), respectively; the factors f_s, f and f' describe the effective deviations from the SM coupling constants; g_s, g and g' are the corresponding gauge coupling constants. The first term describes the coupling of excited fermions to the QCD gluon field, thus it is not applicable to excited electrons and the effective Lagrangian becomes:

$$\mathcal{L}_{GM} = \frac{1}{2\Lambda}\bar{f}_R^*\sigma^{\mu\nu}(g f \frac{\tau}{2} W_{\mu\nu} + g' f' \frac{Y}{2} B_{\mu\nu}) f_L + h.c. \tag{3.9}$$

Equation (3.9) describes the coupling of excited electrons to both of the $SU(2)$ and $U(1)$ fields, where the physical $W^{\pm}$, gauge bosons are mixed (superposition) states of $W_{\mu\nu}$, and Z and γ are mixed states of W_3 and $B_{\mu\nu}$. An excited electron can then decay via gauge interactions to a gauge boson and a SM electron, where it is assumed that the excited electron has a mass larger than the W and Z boson masses and the main decay mode via gauge interaction will be two-body decays (figure 3.4).

The partial decay width for the gauge mediated interactions is given by [27]:

$$\Gamma_{GM}(e^* \to lV) = \frac{1}{8}\frac{g_V^2}{4\pi}\frac{m_{e^*}^3}{\Lambda^2} f_V^2 (1 - \frac{m_V^2}{m_{e^*}^2})^2 (2 + \frac{m_V^2}{m_{e^*}^2}) \tag{3.10}$$

where V is the gauge boson (γ, W, or Z), and f_V is a parameter that depends on the boson type:

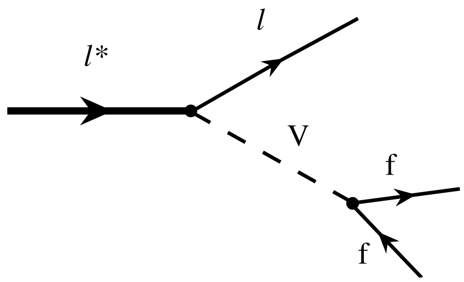

Figure 3.4: Decay of excited lepton (l^*) into a SM lepton (l) and a pair of fermions (f) via gauge interactions mediated by the vector boson (V).

$$
\begin{aligned}
f_\gamma &= f I_3 + f' \frac{Y}{2} \quad , \\
f_W &= \frac{f}{\sqrt{2}} \quad , \\
f_Z &= f I_3 \cos^2\theta_W - f' \frac{Y}{2} \sin^2\theta_W
\end{aligned}
\tag{3.11}
$$

I_3 and Y denotes the third component of the weak isospin and hypercharge of e^*, respectively, and θ_W is the Weinberg angle. Hence the partial widths for the gauge mediated decays are:

$$\Gamma_{GM}(e^* \rightarrow \gamma e) = \frac{\alpha_\gamma}{4} \frac{m_{e^*}^3}{\Lambda^2} f_\gamma^2 \tag{3.12}$$

$$\Gamma_{GM}(e^* \rightarrow W\nu_e) = \frac{\alpha_W}{4} \frac{m_{e^*}^3}{\Lambda^2} f_W^2 (1 - \frac{m_W^2}{m_{e^*}^2})^2 (1 + \frac{m_W^2}{2m_{e^*}^2}) \tag{3.13}$$

$$\Gamma_{GM}(e^* \rightarrow Ze) = \frac{\alpha_Z}{4} \frac{m_{e^*}^3}{\Lambda^2} f_Z^2 (1 - \frac{m_Z^2}{m_{e^*}^2})^2 (1 + \frac{m_Z^2}{2m_{e*}^2}) \tag{3.14}$$

where the structure constants are defined as $\alpha_W = \alpha/\sin\theta_W$ and $\alpha_Z = \alpha_W/\cos\theta_W$. For $m_{e^*} \gg m_W, m_Z$ we can neglect $m_W^2/m_{e^*}^2$ and $m_Z^2/m_{e^*}^2$ terms, and the total width for gauge interaction decay can be obtained as follows:

$$\Gamma_{GM}(e^* \rightarrow \gamma e, W\nu, Ze) \simeq \frac{1}{4} \frac{m_*^3}{\Lambda^2} \left(\alpha_\gamma f_\gamma^2 + \alpha_W f_W^2 + \alpha_Z f_Z^2\right) \tag{3.15}$$

where the parameters f_γ, f_W and f_Z simply reduce to the approximate values -1(0), 0.707(0.707) and -0.269(-0.5) for $f = f' = 1$ ($f = -f' = -1$), respectively [3]. We will consider the case where $f = f' = 1$, but the results can easily be reinterpreted for different values of these parameters, accounting for the change in branching ratio and intrinsic width. Figure 3.5, see equation (3.10), shows the branching ratios (BR) of the three gauge mediated decay modes of excited electron, $e^* \rightarrow e\gamma$ (in red), $e^* \rightarrow \nu_e W$ (in green), $e^* \rightarrow eZ$ (in blue) as a function of the excited electron mass (m_{e^*}) and at a compositeness scale $\Lambda = 5$ TeV. The excited electron decay into the $\nu_e W$ has the highest branching ratio, but W will decay further to lepton + ν_l (with branching ratio equal to $(10.75 \pm 0.13)\%$ [13] in the electron channel) or mostly to hadrons (with branching ratio equal to $(67.60 \pm 0.27)\%$ [13]). Therefore, the decay via photon radiation is the preferred decay mode if a leptonic final state is demanded. This analysis concentrates on the decay mode $e + \gamma$, such that the final state is $ee\gamma$. The Feynman diagram of this final state is shown in figure 3.6. The BR can be renormalized for all possible decays with an electron final state as:

$$BR(e^* \to e\gamma) = \frac{\Gamma(e^* \to e\gamma)}{\Sigma_{V=\gamma,W,Z}\Gamma_{GM}(l^* \to lV)} \tag{3.16}$$

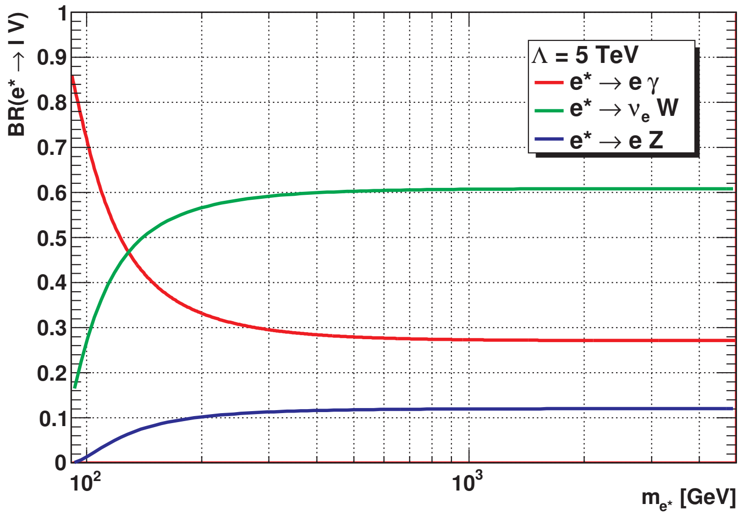

Figure 3.5: Branching ratios of the possible gauge mediated decay modes of excited electron, $e^* \to e\gamma$ (in red), $e^* \to \nu_e W$ (in green), $e^* \to eZ$ (in blue) as a function of m_{e^*} and at $\Lambda = 5$ TeV.

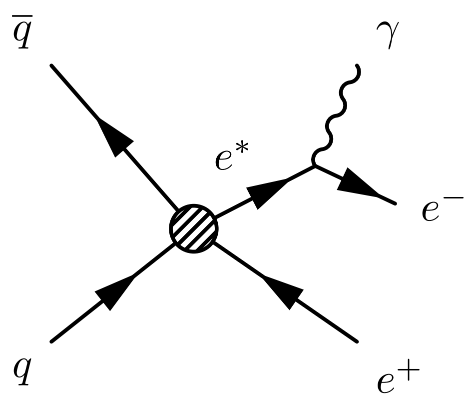

Figure 3.6: Feynman diagram for the process $q\bar{q} \to e^*e \to ee\gamma$.

The decay width of an excited electron via contact interactions (three-body decay) is given by [27]:

$$\Gamma_{CI}(e^* \to ef\overline{f}) = \frac{1}{96\pi} N_C \; S \; \frac{m_{e^*}^5}{\Lambda^4} \tag{3.17}$$

where N_C is the number of colours of the fermion ($N_C = 3(1)$ for quarks(leptons)) and S is an additional combinatorial factor:

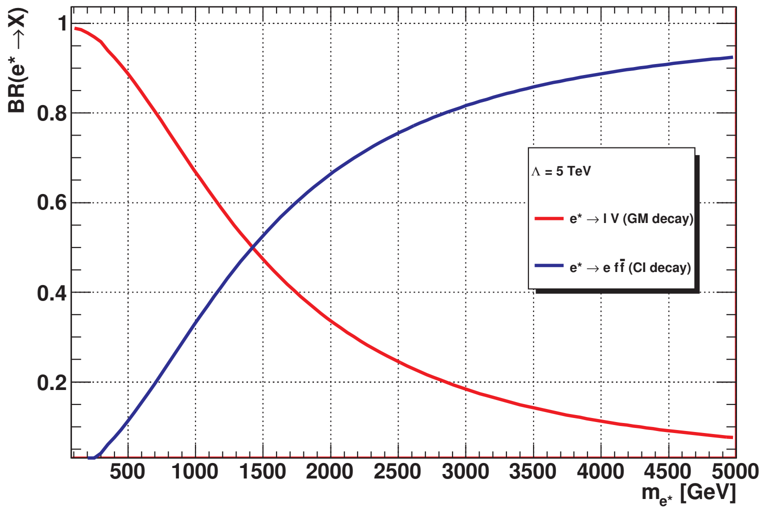

Figure 3.7: Branching fraction of the decay of excited electron (e^*) via contact interaction (in blue) and gauge mediated (in red) as a function of m_{e^*} at $\Lambda = 5$ TeV. The slight kink at $m_{e^*} \simeq 345$ GeV corresponds to the opening of the decay mode $e^{*\pm} \to e^{\pm}t\bar{t}$

$$S = 1 \quad for \quad f = q, l \neq e$$
$$S = 2 \quad for \quad f = e$$

Although decay by contact interaction dominates for $\Lambda = m_{e^*}$, the decay via gauge interaction is proportional to $m_{e^*}^3/\Lambda^2$, equation (3.15), while decay via contact interactions varies as $m_{e^*}^5/\Lambda^4$, equation (3.17). Therefore, the relative importance of the decay mediated by contact interaction on the total decay width will be suppressed by the factor $(m_{e^*}/\Lambda)^2$. This behaviour is clearly illustrated in figure 3.7 which shows the branching fraction of the decay of excited electron (e^*) via contact interaction as well as that of gauge mediated as a function of excited electron mass (m_{e^*}) and at a fixed compositeness scale $\Lambda = 5$ TeV. One can see that (contrary to $\Lambda = m_{e^*}$, that looks unnatural from theoretical point of view) the excited electron decay is dominated by gauge interactions up to $m_{e^*} \sim 1.5$ TeV. However, for $m_{e^*} \geq 3$ TeV the contribution from contact interactions to the total decay width is dominant and cannot be neglected. However, according to equation (3.17), single production of an excited electron followed by the decay via contact interaction produces a final state of at least two electrons and two ordinary (SM) fermions. The SM fermions can also be quarks which would result in two jets in the detector. Such final state, $ee + jj$, is not as easy to analyze as the $ee\gamma$ final state from photon mediated decay mentioned above. In figure 3.7, the slight kink at $m_{e^*} \simeq 345$ GeV corresponds to the opening of the decay mode $e^{*\pm} \to e^{\pm}t\bar{t}$

3.2.2 Previous searches for e^*

Since there is no discovery of e^* (or any other f^*) so far, many experiments that previously searched for excited fermions set limits on the e^*. In most cases the limit is expressed in the form of an excluded region in the (Λ, m_{e^*}) plane. The search for excited leptons started even before the discovery of W and Z bosons[2], one of the first searches for excited lepton

[2] W and Z bosons discovered at CERN in 1983

was done at the PETRA[3] collider [33], in 1982. Since the W and Z had not been discovered yet, they assumed an electromagnetic Lagrangian for the excited lepton production and decay. The limit that was set at PETRA was $M_e* > 58$ GeV for $M_e* = \lambda'$, where λ' is the coupling. The latest experimental previous results are listed below:

- OPAL ***(2002)*** [34]**:** the OPAL collaboration searched for pair and single production of excited leptons ($l = e, \mu, \tau$) by the processes ($e^+e^- \to l^*l^* \to l\gamma l\gamma$), ($e^+e^- \to l^*l \to ll\gamma$) at $\sqrt{s} = 183-209$ GeV. The amount of data used in this analysis was 680 pb^{-1}. Figures 3.8a-c show 95% CL upper limits on the cross-section times branching ratio at $\sqrt{s} = 208.3$ GeV for (a) single and (b) pair production of excited leptons as a function of mass (m_*). The limit obtained for the single production of excited electrons is calculated assuming $f = f'$ (see equation (3.9)). The regions above the curves are excluded. The 95% CL upper limits on the ratio of the excited lepton coupling constant to the compositeness scale, f/Λ, as a function of the excited lepton mass and assuming $f = f'$ are shown in (c). The regions above the curves are excluded by single production searches while pair production searches exclude masses below 103.2 GeV for excited electrons, muons and taus with $\Lambda = 1$ TeV.

- L3 ***(2003)***[35]**:** the L3 collaboration also searched for pair and single production of excited leptons ($l = e, \mu, \tau, \nu_e, \nu_\mu, \nu_\tau$) at $\sqrt{s} = 202 - 209$ GeV. The amount of data used in this analysis was 217 pb^{-1}. They set lower limit at 95% CL of 102.8 GeV (96.6 GeV) for the excited electron mass assuming $f = f'$ ($f = -f'$) for excited electron from the results obtained from pair production searches. In the case of single-production searches, an upper limit on the cross section was set as a function of the excited electron mass. Figures 3.9a-d shows the L3 collaboration 95% CL upper limits on $|f|/\Lambda$, as a function of the excited lepton mass with $f = f'$ for (a) e^*, μ^* and τ^*, (b) ν_{e}^*, ν_μ^* and ν_τ^*, and with $f = -f'$ for (c) e^* μ^* and τ^*, (d) ν_e^*, ν_μ^* and ν_τ^*.

- CDF ***(2005)*** [29]**:** the CDF collaboration searched for single production of excited electrons by the process ($p\bar{p} \to e^*e \to ee\gamma$) at $\sqrt{s} = 1.96$ TeV. The amount of data used in this analysis was 202 pb^{-1}. CDF set a lower limit on the excited electron mass of 209 GeV for both production and decay with GM model assuming $\Lambda/f = m_{e^*}$, see figure 3.10. For the the production via CI model and decay via GM model (similar to the current analysis) the lower mass limit was set to 879 GeV, see figure 3.10. Figure 3.10 also shows CDF cross section $\times$ branching ratio limits for the CI and GM models , compared to the CI model prediction for $\Lambda = m_{e^*}$ and the GM model prediction for $\Lambda/f = m_{e^*}$.

- D0 ***(2008)*** [36]**:** the D0 collaboration searched for single production of excited electrons by the process ($p\bar{p} \to e^*e \to ee\gamma$) at $\sqrt{s} = 1.96$ TeV. The D0 data was interpreted in the context of CI production model and decay via GM model. The amount of data used in this analysis was 1 fb^{-1}. D0 sets a 95% CL upper limit on the production cross section ranging from 8.9 to 27 fb, depending on the mass of the excited electron. A lower mass limit of the excited electron of 756 GeV for $\Lambda = 1$ TeV was set see figure 3.11.

- CMS ***(2011)*** [4]**:** the CMS collaboration searched for single production of excited electrons by the process ($pp \to e^*e \to ee\gamma$) at $\sqrt{s} = 7$ TeV, using 36 pb^{-1} collected in 2010. For $\Lambda = M_{e^*}$, excited electron masses were excluded below 1070 GeV at the 95% confidence level. Figure 3.12 shows the CMS limits.

[3] PETRA (Positron Electron Tandem Ring Anlage) was built between 1975 and 1978 at DESY, Hamburg, Germany. At the time of its construction it was the biggest storage ring of its kind.

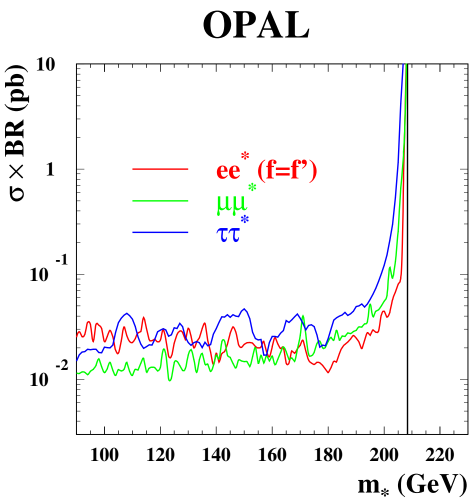

(a) single production

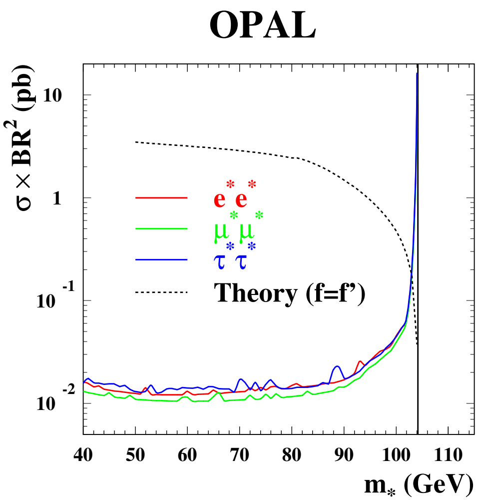

(b) pair production

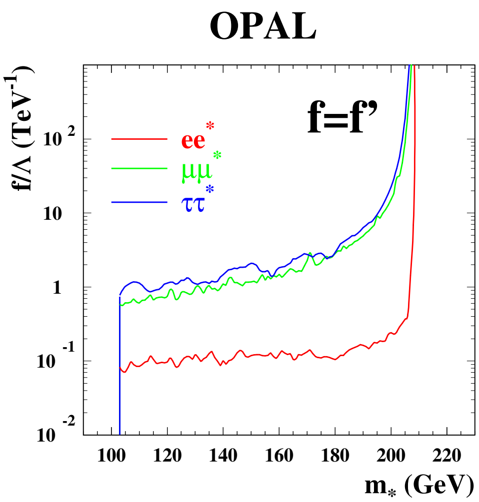

(c) single production

Figure 3.8: OPAL collaboration 95% CL upper limits on the cross-section at $\sqrt{s}$ = 208.3 GeV times the branching fraction for (a) single and (b) pair production of excited leptons as a function of mass (m_*). The theoretical cross-section times the branching fraction squared is also shown in (b). The 95% CL upper limits on the ratio of the excited lepton coupling constant to the compositeness scale, f/Λ, as a function of the excited lepton mass and assuming $f = f'$ are shown in (c).

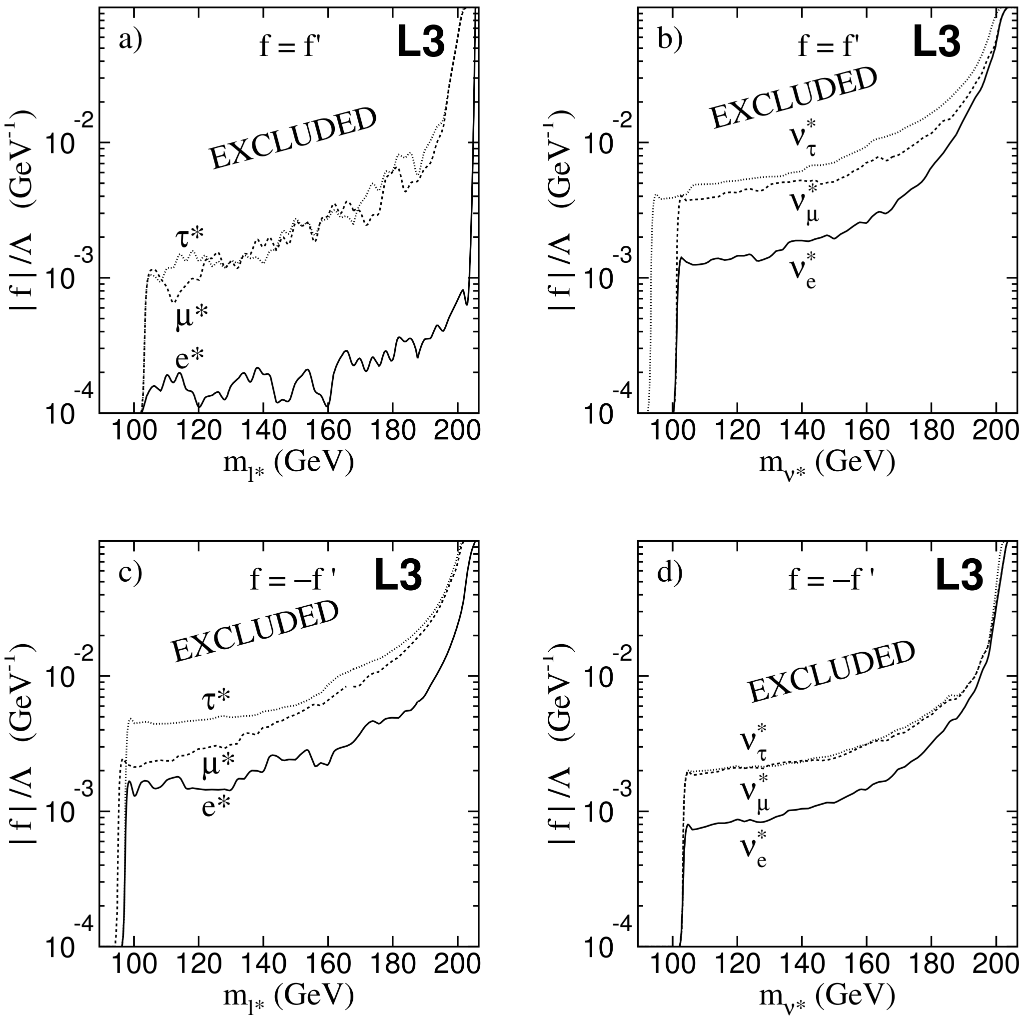

Figure 3.9: L3 collaboration 95% CL upper limits on $|f|/\Lambda$, as a function of the excited lepton mass with $f = f'$ for (a) e^* μ^* and τ^*, (b) ν^*_e, ν^*_μ and ν^*_τ, and with $f = -f'$ for (c) e^* μ^* and τ^*, (d) ν^*_e, ν^*_μ and ν^*_τ.

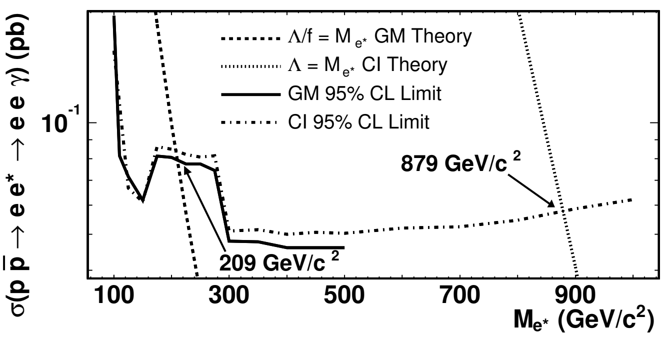

Figure 3.10: CDF collaboration cross section × branching ratio limits for the CI and GM models , compared to the CI model prediction for $\Lambda = m_{e^*}$ and the GM model prediction for $\Lambda/f = m_{e^*}$.The mass limits are indicated.

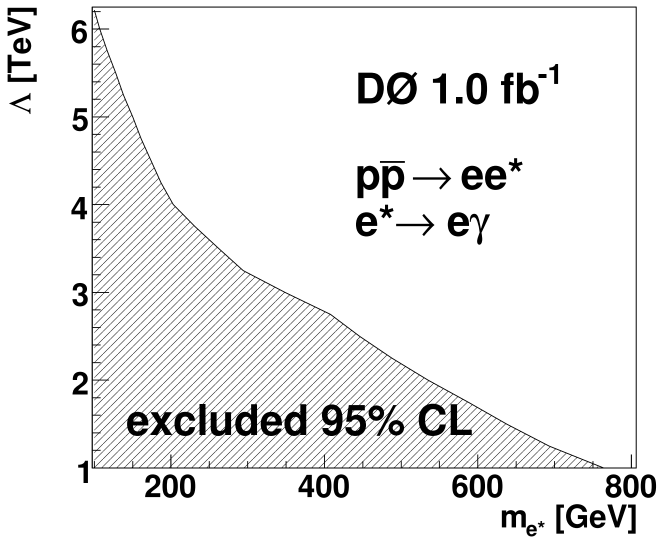

Figure 3.11: The region in the (m_{e^*}, Λ) plane excluded by the D0 experiment.

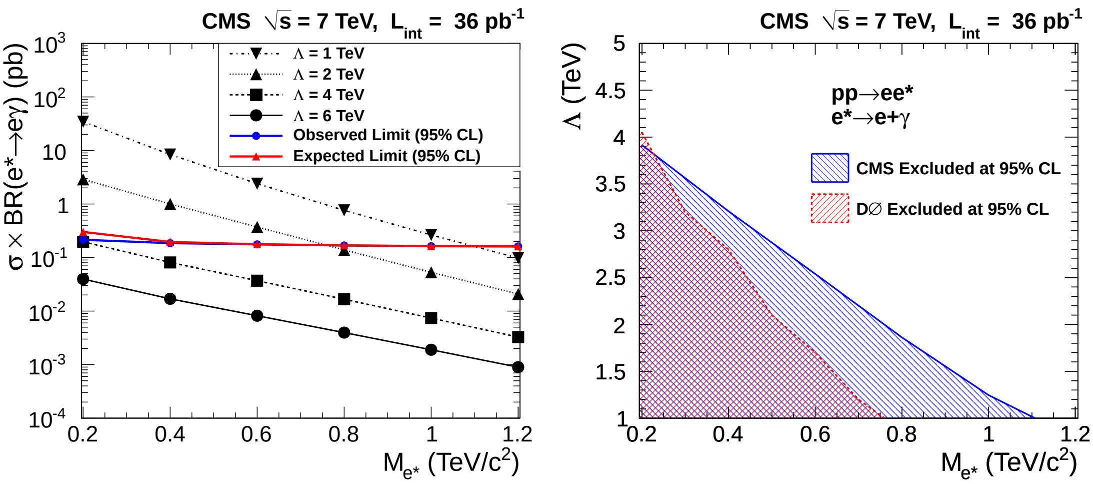

Figure 3.12: Results from CMS collaboration. Left: Observed and expected limits on the excited electron production cross section times branching fraction at 95% CL, as functions of the excited electron mass. The predictions for different Λ values are also shown. Right: The region in the (Λ, M_{e^*}) plane excluded at the 95% CL. The D0 limits are also shown [4].

4

The ATLAS Experiment at LHC

The ATLAS (A Toroidal LHC ApparatuS) [5] detector is one of the two Large Hadron Collider (LHC) general purpose detectors. It is located at one of the four interaction points on the LHC. It is designed to detect the particles that comes out of proton collisions at $\sqrt{s} = 14$ TeV (currently, LHC is running at 7 TeV). The first part of this chapter is dedicated to the LHC, the second is devoted to the ATLAS detector and in the third part ATLAS trigger and data acquisition (DAQ) systems are mentioned.

4.1 The Large Hadron Collider

The LHC is the world's largest and highest-energy particle accelerator. It is a superconducting hadron accelerator and collider that lies in a tunnel 26.7 km in circumference, as much as 50-175 metres beneath the French-Swiss border near Geneva, Switzerland. It is designed to collide opposing particle beams of either protons at an energy of 7 TeV per proton, or lead nuclei at an energy of 574 TeV per nucleus [37]. On the 10^{th} of September 2008, the proton beams were successfully circulated in the main ring of the LHC for the first time [38] but 9 days later operations were halted due to a serious fault [39]. On the 20^{th} November 2009 they were successfully circulated again, with the first recorded proton-proton collisions occurring 3 days later at the injection energy of 450 GeV per beam [40]. After the 2009 winter shutdown, the LHC was restarted and the beam was ramped up to half power, 3.5 TeV per beam [41] (i.e. half its designed energy). On 30 March 2010, the first planned collisions took place between two 3.5 TeV beams, a new world record for the highest-energy man-made particle collisions. The LHC will continue to operate at half power for some years [42].

The LHC is making use of the previous CERN Large Electron Positron collider (LEP) tunnel. The LHC can accelerate protons and heavy ions, here the proton beam acceleration only is considered. The proton trip starts from the bottom of figure 4.1. Firstly, protons are extracted by ionizing hydrogen gas in a Duoplasmatron ion source that is giving up to 300 mA of beam current at 92 keV. Then the proton beam is injected into the pre-injector RFQ (Radio Frequency Quadrupole) that rises the protons energy to 750 keV. The proton beam is then injected into the linear accelerator LINAC2[1] to reach 50 MeV of energy and

[1] In 2007, a replacement of this accelerator was approved. The new LINAC4 accelerator will provide a

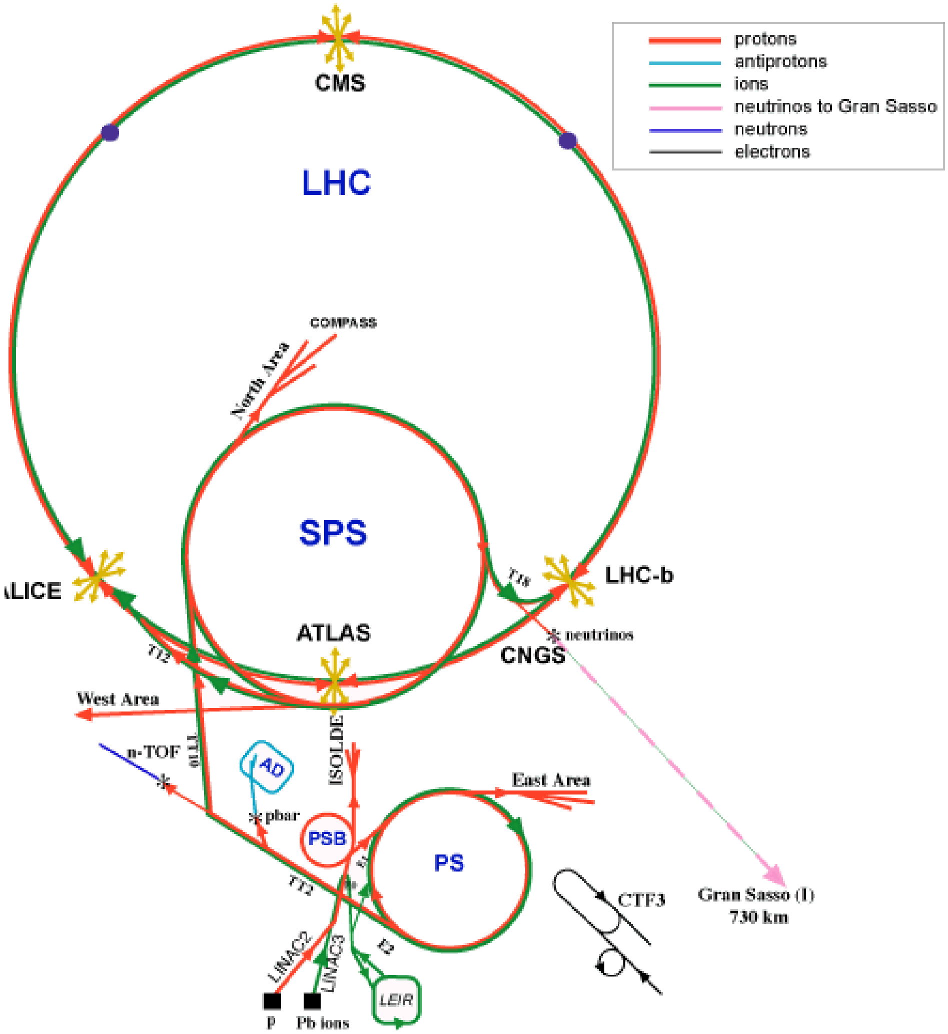

Figure 4.1: Schematic layout of the accelerator complex at CERN.

170 mA of beam current at its end. Then the beam is accelerated in 3 stages before its injection to the LHC with the fellowship of the rings:

- The PSB (Proton Synchrotron Booster), it rises the beam energy to 1.4 GeV.
- The PS (Proton Synchrotron) booster, where the energy reaches about 28 GeV. At this stage the proton beam pulse frequency reaches 40 MHz that is the LHC correct pulse frequency.
- The SPS (Super Proton Synchrotron) is 7 km in circumference. The beam is injected into it after passing through the TT2 and TT10 lines. The SPS rises the beam energy to 450 GeV.

The beam is now ready to be injected into the LHC ring through the transfer lines TI2 (clockwise beam, Beam 1/B1) and TI8 (anticlockwise beam, Beam 2/B2) in two opposite directions. Each of the two beams in LHC at full intensity will contain 2808 bunches, each bunch contains 1.15×10^{11} protons and have a length of a few centimeters with a nominal bunch spacing of 25 ns. The total beam current is about 584 mA that corresponds to a

160 MeV proton beam, firstly as an injector to the PS Booster, and in the future possibly as the front end of a high energy and high duty cycle Super Conducting Proton Linac (SPL).

stored energy of approximately 362 MJ[2] [37]. On the LHC's ring there are four interaction points (1,2,5,8) at each of which the bunches are squeezed into the length of 16 μm in order to increase the probability of collision, that define the size of the interaction regions in each detector. Despite the large number of protons in each bunch, there will only be about 20 *pp* collisions per bunch crossing during a high luminosity run, because of the small cross section of the proton. Although this number seems poor, the fact that the nominal bunch crossing frequency is 40 MHz in the LHC, makes the total number of collisions around 800 million per second.

About 1232 superconducting dipole magnets (each of the length of 14.3 m) are used to deflect the proton beams to keep the circular path along the LHC. Focusing the beam is done with about 858 superconducting quadrupole magnets. There are also about 6200 correction magnets to suppress unwanted resonances in the accelerator. LHC magnets are kept superconducting, by means of a cryogenic system, which uses superfluid helium at the temperature of 1.9^{o}K.

8 superconducting radio frequency (RF) oscillators per beam are used to accelerate the proton beams in the storage ring. The RF provides a resonant electric field that could either accelerate or decelerate the particles depending on when the particles arrive at the oscillation. The RF oscillators are necessary to compensate for the relativistic effects that arise at these high energies. It is important to have bunch frequency and RF oscillators phase matching in order to optimize the protons acceleration. The RF cavities oscillation frequency ($\simeq$ 400 MHz) is increasing somewhat to maintain the resonance as the protons are accelerated and the magnetic field must simultaneously increase to avoid dispersion, thus keeping a constant radius. The RF oscillators are also necessary for keeping the protons within the bunches.

4.1.1 Luminosity

The luminosity describes the beam intensity (both of the two beams) and is defined by the number of particles passing through a cross section of the beam per unit time. In a particle collider like the LHC, the luminosity is given by [43]:

$$L = \frac{N_b^2 n_b f_{rev} \gamma_r}{4\pi \epsilon_n \beta^*} F \quad , \tag{4.1}$$

where N_b is the number of particles per bunch (1.15×10^{11} proton), n_b the number of bunches per beam (2808 bunches), f_{rev} the revolution frequency (11.245 kHz), γ_r the relativistic gamma factor (7461), ϵ_n the normalized transverse beam emittance (3.75 μm rad), β^* the beta function at the collision point (0.55 m at point 1) and F the geometric luminosity reduction factor due to the crossing angle at the interaction point:

$$F = \left(1 + \left(\frac{\theta_c \sigma_z}{2\sigma^*}\right)^2\right)^{-\frac{1}{2}} \quad , \tag{4.2}$$

where θ_c is the full crossing angle at the interaction point (285 μrad), σ_c the RMS bunch length (7.55 cm), and σ^* the transverse RMS beam size at the interaction point (16.7 μm at point 1).

[2] 2808 bunches $\times$ 1.15 10^{11} protons @ 7 TeV each. $= 2808 \times 1.15 \times 10^{11} \times 7 \times 10^{12} \times 1.602 \times 10^{-19}$ Joules = 362 MJ per beam

4.1.2 The LHC experiments

The LHC hosts six experiments four of them placed at the four collision points:

1. ATLAS and CMS (Compact Muon Solenoid) [44] are located at points 1 and 5 respectively. Both are aiming at peak luminosity of $L = 10^{34} cm^{-2}s^{-1}$ for proton operation [37]. ATLAS and CMS are two general purpose detectors. They have a very rich physics program: starting from high precision measurements, searching for Higgs boson, looking for signs of new physics, extra dimensions, and even looking for clues to the nature of dark matter.

2. ALICE (An LHC Ion Collision Experiment) [45] is located at point 2 and is optimized to study quark-gluon plasma, a state of matter wherein quarks and gluons are de-confined. It is aiming at a peak luminosity of $L = 10^{27} cm^{-2}s^{-1}$ for nominal Pb-Pb operation [37].

3. LHCb (LHC beauty) [46] is located at point 8 and is aiming at peak luminosity of $L = 10^{32} cm^{-2}s^{-1}$ with 156 bunches for proton operation [37]. It is dedicated to b-physics, particularly aimed for measuring the parameters of CP violation in the interactions of b-hadrons.

4. LHCf (LHC forward) [47] is a small experiment that is located near from point 1 and is dedicated to measure the energy and numbers of neutral pions (π^0) generated in the forward region of collisions. It consists of two detectors, 140 m on either side of point 1.

5. TOTEM (TOTal Elastic and diffractive cross section Measurement) [48] is sharing point 5 with CMS and is dedicated to measure total cross section, elastic scattering and diffractive processes. It is aiming at peak luminosity of $L = 10^{29} cm^{-2}s^{-1}$ with 156 bunches for proton operation [37].

4.1.3 The Worldwide LHC Computing Grid

The data being collected at the LHC experiments is huge and a single computer farm and storage space is not enough. Thus, a world-wide grid was developed to, firstly, store this data in the various disk and tape storage facilities to make it available to a large number of institutes and, secondly, provide computing resources for data analysis and Monte Carlo production. ATLAS facilities, for instance, follow a computing model [49, 50] that groups the different sites into the so-called Tiers. The central point of this system is the Tier-0, located at CERN. This is where the initial processing of the data takes place, together with calibration and monitoring. The raw data is then copied in parts to each of the ten Tier-1 national centres, scattered all over the world; the first-pass output of the reconstruction are also sent to Tier-1 centres. They are also responsible for reprocessing of the data if new calibration and/or software improvements are available. Attached to each Tier-1 is a collection of Tier-2 centres, which then take care of hosting data formats more oriented towards physics analysis and code development. Finally, the Tier-3 centres are located in various institutions and are devoted to provide resources for physics analysis for their users.

4.2 Overview of the ATLAS detector

ATLAS aims to cover a wide range of physics expected from the LHC. The detector has a cylindrical symmetry around the beam axis. It consists of a barrel part and two end-caps. It is almost perfectly hermetic, leaving only minimal cracks, e.g. between the barrel and the end-caps and the hole of the beam line in the very forward/backward regions. The overall size of the detector is 44 m in length and 25 m in diameter. It has a total weight of 7000 tons [5].

The coordinate system (figure 4.2) of ATLAS is a right-handed coordinate system with the x-axis pointing towards the centre of the LHC tunnel, and the z-axis along the beam pipe, with A-side (toward point 8, i.e. with the direction of beam 2) has a positive z-coordinate. The y-axis is slightly tilted with respect to the vertical because of the general tilt of the LHC tunnel. The azimuthal angle (ϕ) is zero in the positive x-direction and increases clockwise when looking in the positive z-direction. ϕ range is $[-\pi,+\pi]$. The polar angle (θ) is measured from the positive z-axis. The pseudo-rapidity (η) of particles from the primary vertex is defined as

$$\eta = -\ln\left(\tan\left(\frac{\theta}{2}\right)\right) \tag{4.3}$$

hence it is equal to zero in the transverse plane (x-y plane) and increases towards the z-axis. The transverse momentum (p_{T}), transverse energy (E_{T}) and missing transverse energy ($E_{\mathrm{T}}^{\mathrm{miss}}$) are the momentum and energies that are perpendicular to the beam axis. A distance in the $\eta - \phi$ plane is defined as:

$$\Delta R = \sqrt{(\Delta\eta)^2 + (\Delta\phi)^2} \tag{4.4}$$

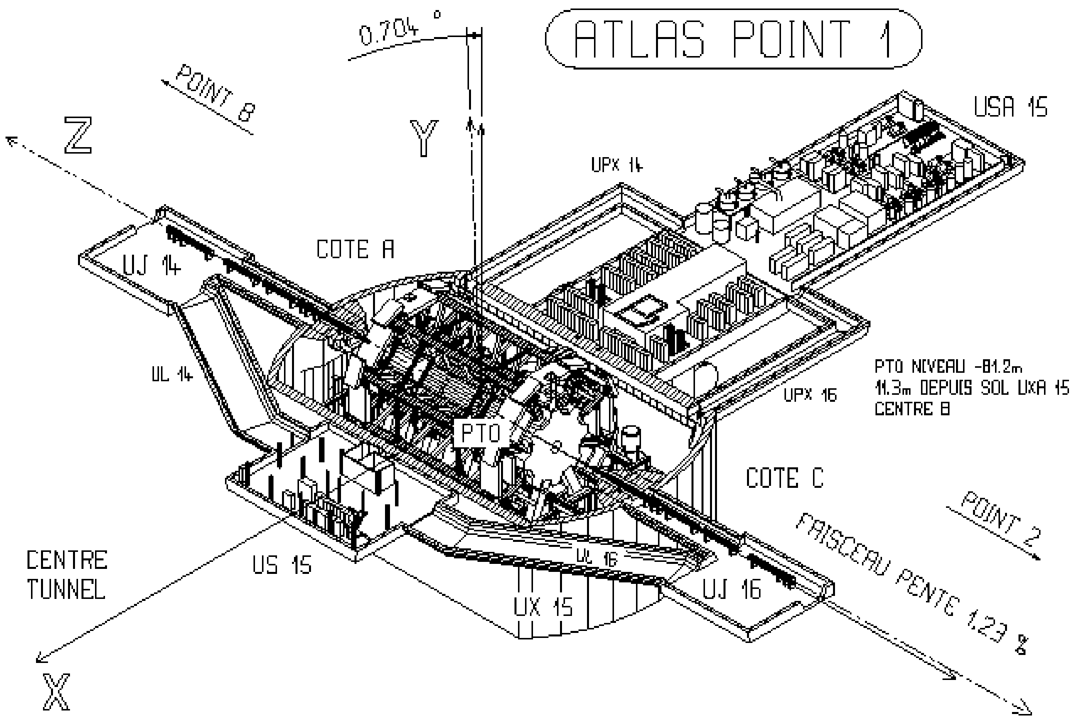

Figure 4.2: The XYZ right-handed ATLAS coordinate system.

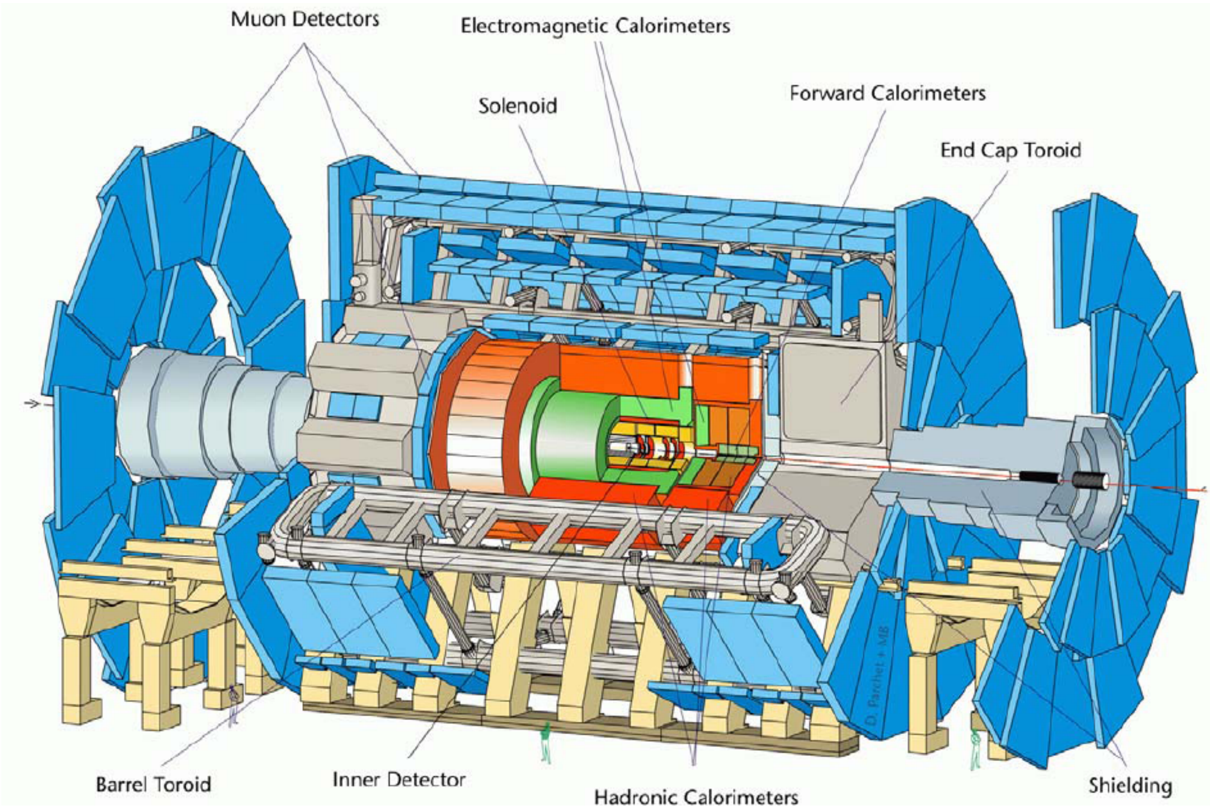

Figure 4.3: An overview of the ATLAS detector.

ATLAS consists of several sub-systems arranged as onion-skins. The innermost shell is the Inner Detector followed by the Calorimeters (Electromagnetic and Hadronic) and the Muon Spectrometer, see figure 4.3. In the following sub-sections, the ATLAS sub-systems are briefly summarized, but before let us have a quick look at the magnet system.

4.2.1 The magnet system

The ATLAS magnet system [5](figure 4.4) is 22 m in diameter and 26 m in length, with a stored energy of 1.6 GJ. The ATLAS magnet system consists of:

- a solenoid which is aligned with the beam axis and provides the inner detector (see section 4.2.2) with at 2 T axial magnetic field, while minimizing the radiative thickness in front of the barrel electromagnetic calorimeter, see section 4.2.3.1;
- a barrel toroid and two end-cap toroid systems, which produce a toroidal magnetic field, for the muon system (see section 4.2.4), of 0.5 T and 1 T in the barrel and end-cap region, respectively. Each toroid consists of eight superconducting coils, equally separated in ϕ. The end-caps have a 22.5^o angle in ϕ with the barrel toroid to provide radial overlap and optimise the bending power in the transition region between barrel and end-cap. The barrel toroid provides a bending power of 2 to 6 T·m in the range $0 < |\eta| < 1.3$ while the end-cap toroids provide 4 to 8 T·m in the range $1.6 < |\eta| < 2.6$.

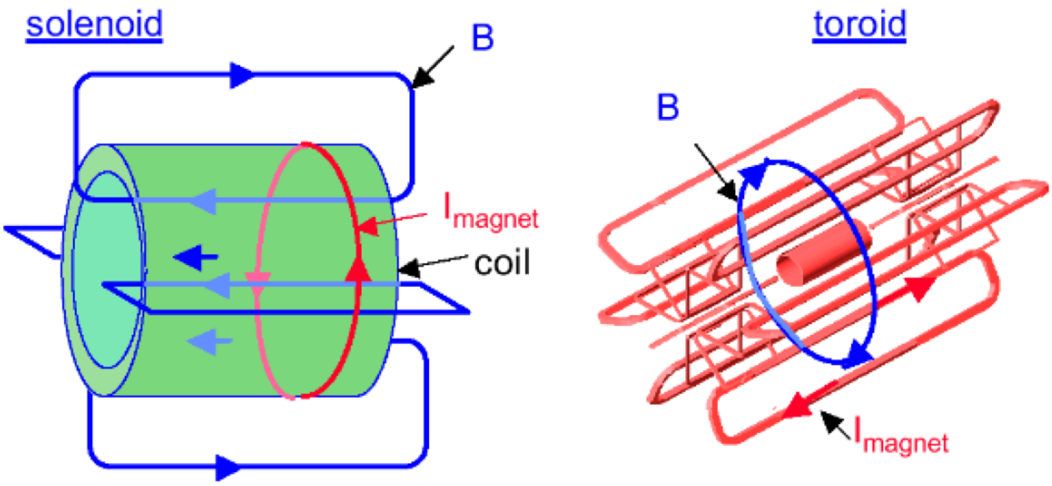

Figure 4.4: The ATLAS magnet system layout.

4.2.2 The Inner Detector

The high instantaneous luminosity and bunch-crossing rate of the LHC (40 MHz) will produce about 1000 particles every 25 ns within $|\eta| < 2.5$. This creates a very large track density in the detector [5]. The Inner Detector is responsible for the tracking of charged particles, i.e. measuring their momentum and the sign of their charge. In order to measure charged particle momentum, the ID is immersed inside a 2 T axial magnetic field (section 4.2.1). The ID provides satisfactory pattern recognition, primary and secondary vertex measurements as well as an exceptional momentum/space resolution for particles within $|\eta| < 2.5$, thanks to its fine granularity [51]. In addition, the inner detector measures the so-called impact parameter and vertex position (both primary[3] and secondary[4]). The ID consists of three sub-detectors (see figure 4.5) the two most inner parts; silicon pixels (Pixel) and micro-strip (known as Semi-Conductor Tracker, SCT) detectors and transition radiation detector (TRT) in the external part.

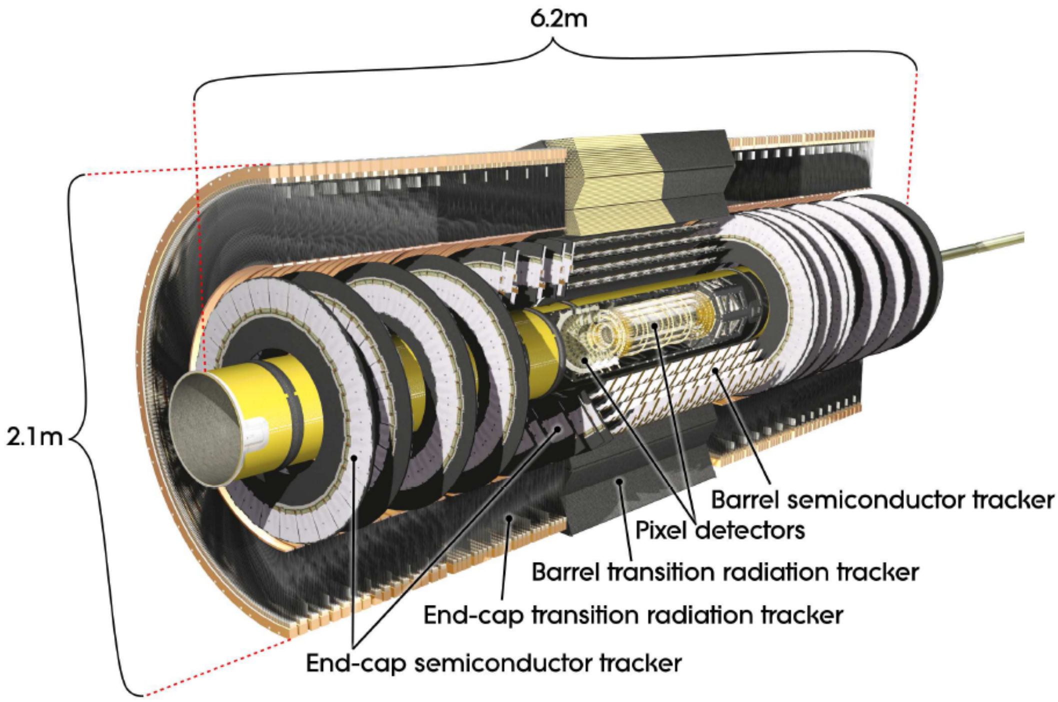

Figure 4.5: Cut-away view of the ATLAS inner detector [5].

4.2.2.1 The Pixel detector

It is the closest sub-detector to the beam pipe in ATLAS. It is is composed of two end-caps and one barrel section. Its barrel part consists of three cylindrical layers at about 50.5 mm, 88.5 mm and 122.5 mm from the z-axis, see figure 4.6, with 22, 38 and 52 silicon staves respectively. The innermost layer of the Pixel detector is known as the b-layer. The end-caps consist of three silicon wheels perpendicular to the beam axis, hence adding three position measurements along the track of a charged particle in the forward region.

The pixel detector covers the region $|\eta| < 2.5$ and it contains about 80.4 million readout channels. In the barrel part, the intrinsic measurement accuracies are 10 μm and 115 μm in the transverse (R-ϕ) plane and in the longitudinal (z) direction respectively, while in the end-caps they are 10 μm and 115 μm in the (R-ϕ) plane and in the longitudinal (R) direction respectively.

4.2.2.2 The Semi-Conductor Tracker (SCT)

The SCT[5] makes use of the micro-strip technology instead of pixels, this reduces the number of readout channels to about 6.3 million readout channels while keeping a good position accuracy of 17 μm in R-ϕ plane and 580 μm in z- (barrel) or R- (end-caps) direction.

[3]the original proton collision point

[4]from a heavy particle decay, like B-meson for example.

[5]a large fraction of the silicon modules, which are the building blocks of SCT, were produced and tested at the University of Geneva.

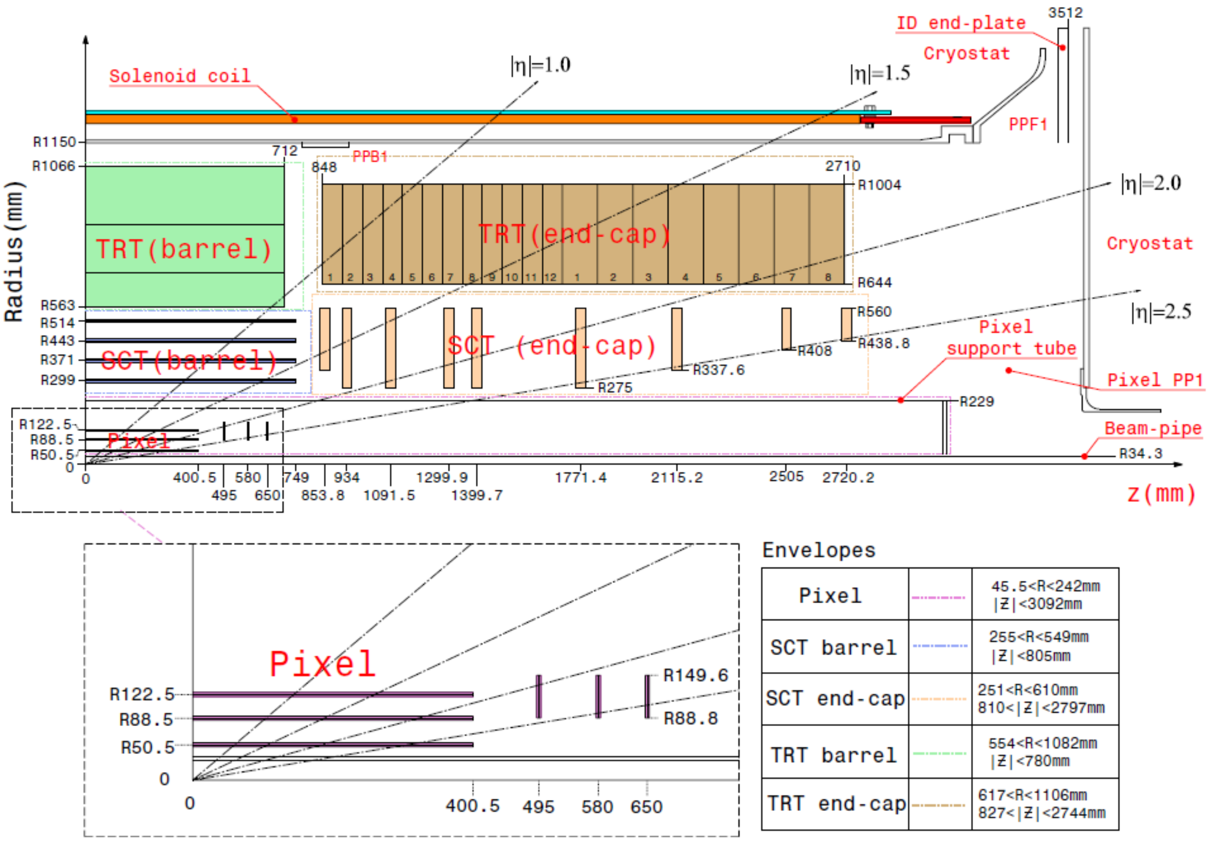

Figure 4.6: Plan view of a quarter-section of the ATLAS inner detector [5].

The barrel part of SCT is made of 4 concentric cylinders mounted at radii of 29.9 mm, 37.1 mm, 44.3 mm and 51.4 mm from the z-axis, see figure 4.6. Each one of the two end-caps is made of nine disks at the distances from the transverse plane that are shown in figure 4.6.

4.2.2.3 The Transition Radiation Tracker (TRT)

The TRT is the outermost part of the ID and is covering up to $|\eta| = 2$. It is made of gaseous[6] 4 mm diameter drift-tubes in the form of straws interleaved with thin foils that provide transition radiation photons which are then detected by the drift-tubes. The TRT only provides R-ϕ information, for which it has an intrinsic accuracy of 130 μm per straw. In the barrel region, the straws are parallel to the z-axis and are 144 cm long, with their wires divided into two halves, approximately at $\eta = 0$. In the end-cap region, the 37 cm long straws are arranged radially in wheels, see figure 4.6. The total number of TRT readout channels is approximately 351,000, each provides a drift-time measurement and two independent thresholds, allowing the detector to differentiate between tracking hits (the low threshold, ~ 200 eV) and transition radiation hits (passing the higher one, ~ 5 keV). An electron typically produce more high threshold hits than a heavier particle at the same energy. A muon with $p_{\mathrm{T}} > 100$ GeV can also produce transition radiation.

[6] 70% Xe, 20% CO_2 and 10% CF_4.

4.2.3 The Calorimeters

Calorimeters are designed to measure the energy and the position of electrons, photons and jets, to give an estimation of the missing transverse momentum and to contribute to the particle identification [5]. Figure 4.7 shows the Calorimeter system in ATLAS which includes Electromagnetic Calorimeters (ECAL) and Hadronic Calorimeters (HCAL). Both the ECAL and HCAL calorimeters consist of a barrel and two end-caps. The forward regions are equipped with a dedicated Forward-Calorimeter (FCAL). All calorimeters used in ATLAS are sampling calorimeters[7].

The ATLAS calorimeter system cover the range $|\eta| < 4.9$, using different techniques suited to the widely varying requirements of the physics processes of interest and of the radiation environment over this large η-range. Over the η region matched to the inner detector, the fine granularity of the EM calorimeter is ideally suited for precision measurements of electrons and photons. The coarser granularity of the rest of the calorimeter is sufficient to satisfy the physics requirements for jet reconstruction and $E_{\mathrm{T}}^{\mathrm{miss}}$ measurements. It is important that the whole shower is contained in the calorimeter system to provide good energy estimation of the interacting particle and to limit punch-through into the muon system. Therefore, it is essential that the total thickness of the EM calorimeter is greater than 22 radiation lengths[8] (X_0) in the barrel and greater than 24 X_0 in the end-caps depending on η. The approximate 9.7 interaction lengths (λ) of active calorimeter in the barrel (10 λ in the end-caps) are adequate to provide good resolution for high-energy jets. Moreover, the calorimeters have to cope with the effect of pile-up as well as the high radiation dose due to the unprecedented luminosity of the LHC.

4.2.3.1 The LAr EM calorimeter (ECAL)

The EM calorimeter is able to reconstruct electrons in the energy range from 1 GeV up to 5 TeV. The lower limit is set by the requirements for b-tagging. Although, b-tagging is mainly done by the ID, a calorimetric identification of low-energy electrons increases the b-tagging efficiency by about 10%. The upper energy limit is set by the possibility to produce new heavy gauge bosons (Z' and W'). The EM calorimeter is divided into a barrel part ($|\eta| < 1.475$) and two end-cap components ($1.375 < |\eta| < 3.2$), each is housed in its own cryostat. The EM calorimeter is segmented in three sections in depth.

- Electromagnetic Barrel calorimeter (EMB): the central solenoid and the LAr calorimeter share a common vacuum vessel, in order to optimise the upstream material by eliminating two vacuum walls. As a consequence, the barrel calorimeter consists of two identical half-barrels, separated by a small gap (4 mm) at z = 0 ($\eta = 0$)[5]. As a sampling calorimeter, the ATLAS EMB calorimeter is built in a way that the shower produced by the incoming particle spreads over many layers of active and passive material. This is done by folding the absorbers (lead) and electrodes (kapton) into an accordion shape with the folds approximately perpendicular to the incoming particle track. The absorbers are interleaved with electrodes and stacked up, leaving liquid argon filled gaps [52]. The accordion geometry provides complete ϕ symmetry without azimuthal cracks [5]. Figure 4.8 shows one module of the EMB, where the accordion geometry as well as the three layers (Front (Strips), Middle, Back) with their granularities in $\eta - \phi$ plane are shown. The second sampling (Middle layer) of

[7] i.e. consists of an active material, where the energy lost by an interacting particle could be measured, and a passive material that is used to make the average density high enough to absorb high-energy particles in a reasonable depth.

[8] Radiation (interaction) length: is the average distance a particle travels before interacting inelastically through electromagnetic (hadronic) interaction.

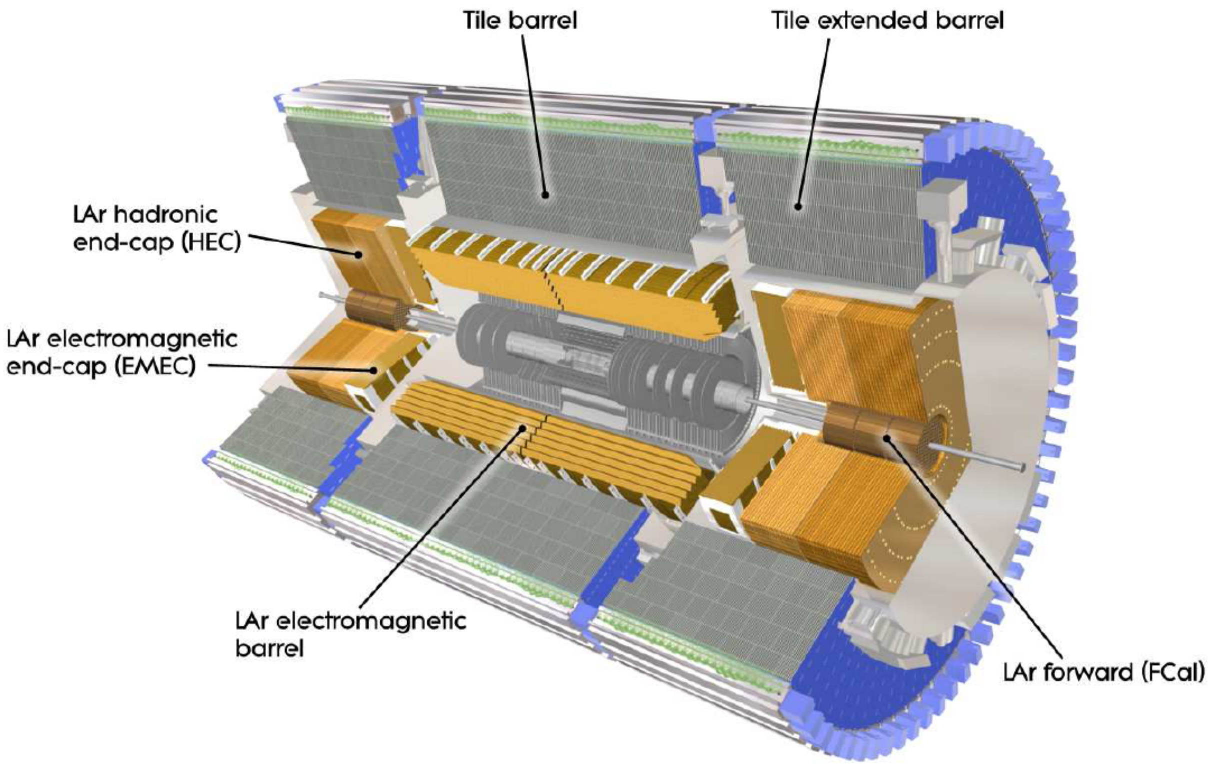

Figure 4.7: Layout of the ATLAS Calorimeters [5].

the EMB contains most of the shower energy, while the first sampling (Front layer) is more finely segmented to precisely measure the incoming particle direction. The third sampling (Back layer) is coarsely segmented and is designed to contain the EM shower.

- Electromagnetic End-Caps calorimeter (EMEC): each end-cap calorimeter is divided into two coaxial wheels: an outer wheel covering the region $1.375 < |\eta| < 2.5$, and an inner wheel covering the region $2.5 < |\eta| < 3.2$. For the end-cap inner wheel, the calorimeter is segmented in two sections in depth and has a coarser lateral granularity than for the rest of the acceptance.

- The PreSampler (PS): in the region of $|\eta| < 1.8$, a forth layer known as the presampler is used to correct for the energy lost by electrons and photons upstream of the calorimeter. The presampler consists of an active LAr layer of thickness 1.1 cm (0.5 cm) in the barrel (end-cap) region.

Beside the small gap at $|\eta| = 0$ there is another one at $1.37 < |\eta| < 1.52$ between barrel and end-caps.

4.2.3.2 The Hadronic Calorimeters (HCAL)

To ensure that the incoming hadrons come close enough to the detector material nucleons and interact strongly with them, the HCAL is quite denser than the ECAL. The hadronic shower is more complicated than the electromagnetic one, as some of the incoming hadrons have electric charge, and so produce showers that are partially electromagnetic beside the hadronic one and moreover leptons can be produced in hadronic decays, making it hard to get a good measurement of the energy of the incoming particle.

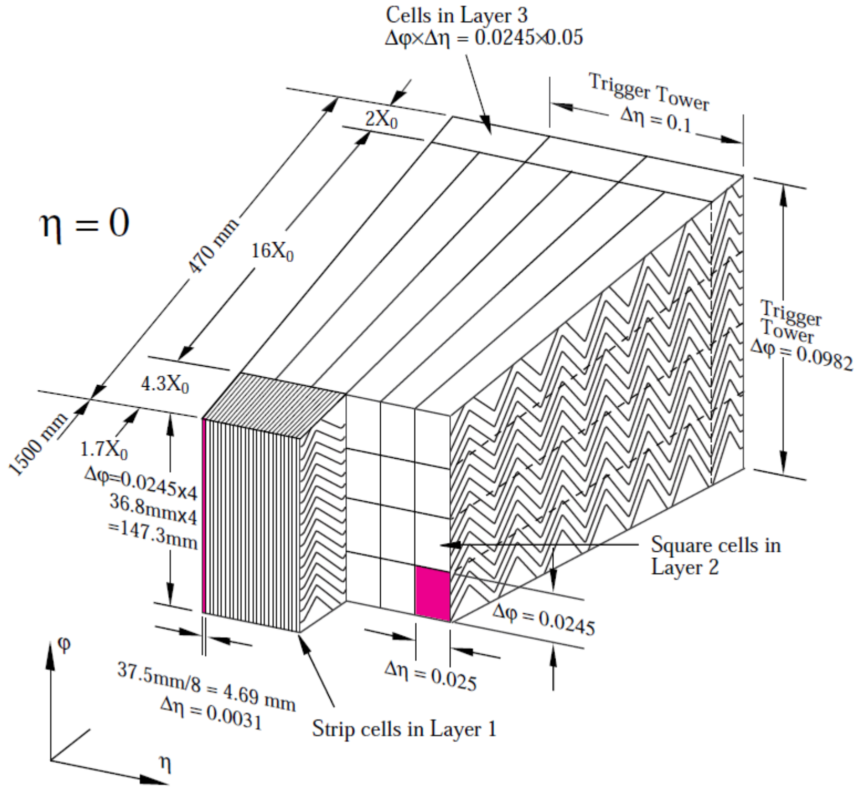

Figure 4.8: A barrel module where the different layers are visible with the ganging in ϕ. The granularity in η and ϕ of the cells of each of the three layers and of the trigger towers is also shown[5].

- Hadronic Barrel calorimeter: the Hadronic Barrel Calorimeter has a large steel absorber tiles equipped with scintillating fibers for readout. Therefore, this calorimeter is also called Tile-Calorimeter. Each scintillator is connected to two photomultipliers by wavelength shifting fibers. There is a central barrel part (Tile barrel) covering the $|\eta| < 1.0$ region and Tile extended barrel on each side that covers η up to 1.7. The gap between the Tile barrel and the Tile extended barrel is used for the cables from the ID and the EM to outside. Scintillators placed in this gap allow a good estimation of the energy lost in this gap.

- Hadronic End-Cap calorimeter (HEC): the HEC uses also liquid argon as the active medium as in the case of ECAL but here the absorbers are flat parallel copper plates instead of accordion-shaped lead. It is placed behind the EMEC in the same cryostat. It covers the ηrange between 1.5 and 3.2.

4.2.3.3 The Forward Calorimeter (FCAL)

The FCAL provides electromagnetic as well as hadronic calorimetry in the very forward region (η ranges from 3.2 to 4.9). It is located in the inner bore of the hadronic calorimeter and around the beam pipe. The first of three forward-calorimeter modules use copper as absorber, the other two are made of tungsten. The FCAL has a much thinner active gap compared to the other LAr calorimeters because of the much higher counting rate.

4.2.4 The Muon Spectrometer

The ATLAS detector is equipped with a high-resolution muon spectrometer, figure 4.9 [5]. For a muon detector, the time resolution is important for the triggering, while the position accuracy is more relevant for tracking. In the barrel region it consists of a large air-core toroidal magnet system (see section 4.2.1), to deflect muon tracks which is needed for momentum measurements, instrumented with Monitored Drift Tube (MDT) chambers to measure the muon trajectory with very high precision in the bending direction and Resistive Plate Chambers (RPC) which provide a stand-alone triggering capability over a wide range of transverse momentum, pseudo-rapidity ($|\eta| \leq 1.05$) and azimuthal angle (ϕ). In the end-cap region, MDTs are also used for muon trajectory and Thin Gap Chambers (TGC) are used as trigger chambers ($1.05 < |\eta| < 2.4$). The very forward region ($2.0 < |\eta| < 2.7$) is instrumented with Cathode Strip Chambers (CSC) instead of MDTs to accommodate the higher counting rates. TGCs have a time resolution better than the 25 ns LHC bunch crossing time spacing, and are used to trigger the acquisition of events with a definite pT cut-off. The magnet system provides a field of 0.5 T. Three layers of precision chambers allow the measurement of three points of the muon trajectory. The RPC has a 10 mm accuracy in z and ϕ with a 1.5 ns time resolution while the TGC

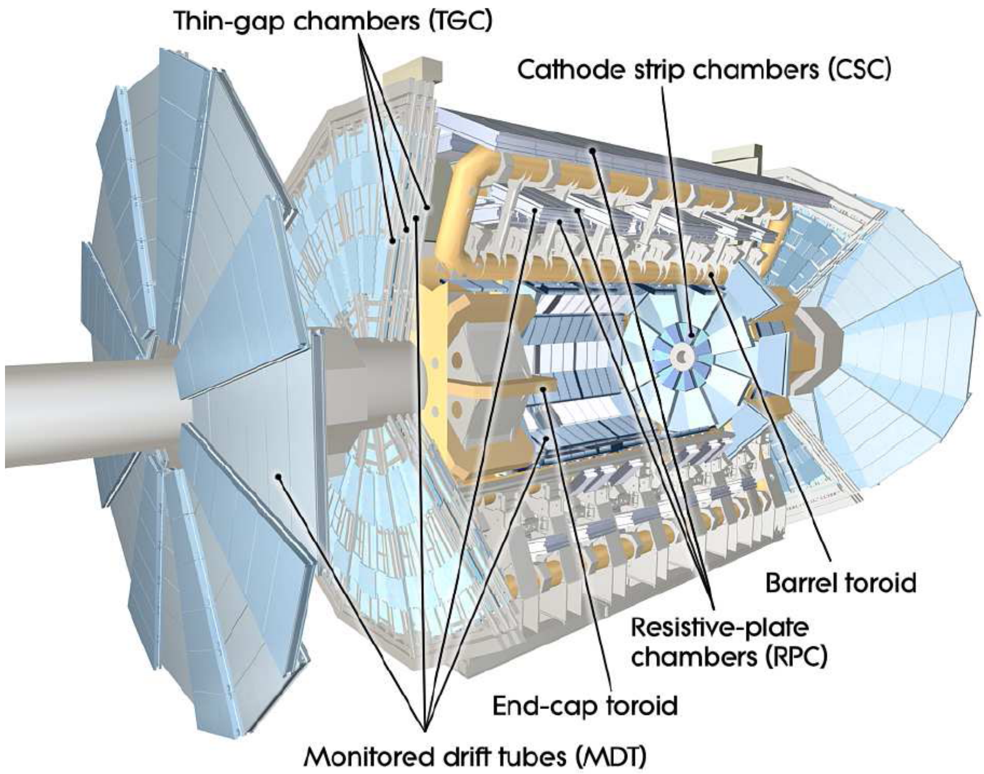

Figure 4.9: The ATLAS Muon Spectrometer [5].

has 26 mm in z, 37 mm in ϕ and a 4 ns time resolution. In comparison, the precision CSC chamber has a 40 mm z, a 5 mm ϕ and a 7 ns time resolution, and the precision MDT has an average resolution of 35 ?m per chamber. The performance benchmark is to measure the momentum of a 1 TeV muon with a resolution $\frac{\Delta p_{\mathrm{T}}}{p_{\mathrm{T}}} \approx 10\%$. Given the magnetic field and the available space, this requires a position resolution of 50μm. For $p_{\mathrm{T}} > 6$ GeV and $\frac{\Delta p_{\mathrm{T}}}{p_{\mathrm{T}}} \approx 1\%$, the expected muon identification efficiency is above 90%.

4.2.5 The Luminosity measurement and the Forward detectors

To determine the recorded luminosity, which may differ from the delivered[9] one by LHC, ATLAS has three dedicated detectors, figure 4.10:

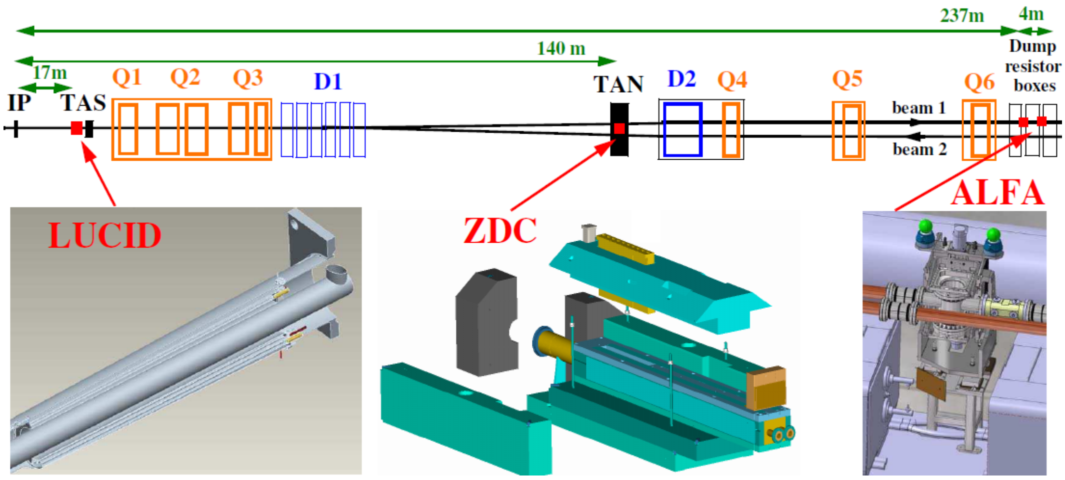

Figure 4.10: The Forward detectors for luminosity measurement [5].

- a LUminosity measurement using Cerenkov Integrating Detector (LUCID): which is a relative luminosity detector. Its main purpose is to detect inelastic *pp* scattering in the forward direction, in order to both measure the integrated luminosity and to provide online monitoring of the instantaneous luminosity and beam conditions [53]. It is placed 17 m from the IP near the Target Absorber Secondaries (TAS), figure 4.10.

- the Absolute Luminosity For ATLAS (ALFA): which measures absolute luminosity by detecting elastic *pp* collisions. ALFA gives the most accurate measurement through the measurement of elastic Coulomb scattering. It detects charged particles using scintillating fibers located inside Roman Pots that are introduced only during stable beam [54]. Its goal is to measure the luminosity with an uncertainty of better than 5%. It is placed about ±240 m from the IP, figure 4.10.

- the Zero Degree Calorimeter (ZDC): its primary purpose is to detect forward neutrons with $|\eta| > 8.3$ in heavy ion collisions. During the start-up phase of the LHC (*pp* collisions with luminosities well below 10^{33} cm^{-2} s^{-1}), the ZDCs will enhance the acceptance of ATLAS central and forward detectors for diffractive processes and provide an additional minimum-bias trigger for ATLAS. It is located ±140 m from the IP, that corresponds to the location where the LHC beam pipe into to separate pipes. It is embedded in the Target Absorber Neutral (TAN), located between the beam pipes just after the split, figure 4.10. The backgrounds from beam-gas and beam-halo effects can be greatly reduced by requiring a tight coincidence from the two arms of the ZDCs, located symmetrically with respect to the interaction point [5].

4.2.6 The Trigger system and Data AcQuisition

Due to the very high interaction rate in the ATLAS detector, a reliable trigger system is needed that can reduce the huge amount of data to be recorded by the Data AcQuisition (DAQ). Interesting events are very rare. In 10^7 events only 1 event is selected and recorded

[9] measured from beam parameters by LHC

for the off-line analysis [55]. The trigger and data acquisition (T/DAQ) system must work in the challenging environment of $\sim 10^9$ interactions per second and the large number ($\sim 10^8$) of readout channels of the ATLAS detector. The initial data stream of 1PB/s must be reduced to ~ 300 MB/s which can be sustained to mass storage, while efficiently retaining a maximum acceptance of physics signatures for offline analysis [6]. The ATLAS T/DAQ system is based on three levels of online event selection [5], figure 4.11. At Level 1 (L1), special-purpose processors act on reduced-granularity calorimeter information and fast readout muon chambers. Level 2 (L2) is a software based which uses full-granularity, full-precision data from the detectors, but, for most triggers, examines only regions of the detector identified by the L1 trigger as containing interesting information (Region of Interest, RoI). At the third trigger level, the Event Filter (EF), the full event data are used together with the latest available calibration and alignment information to make the final selection of events to be recorded for offline analysis. L2 and EF are usually grouped into the so-called High-Level-Trigger (HLT).

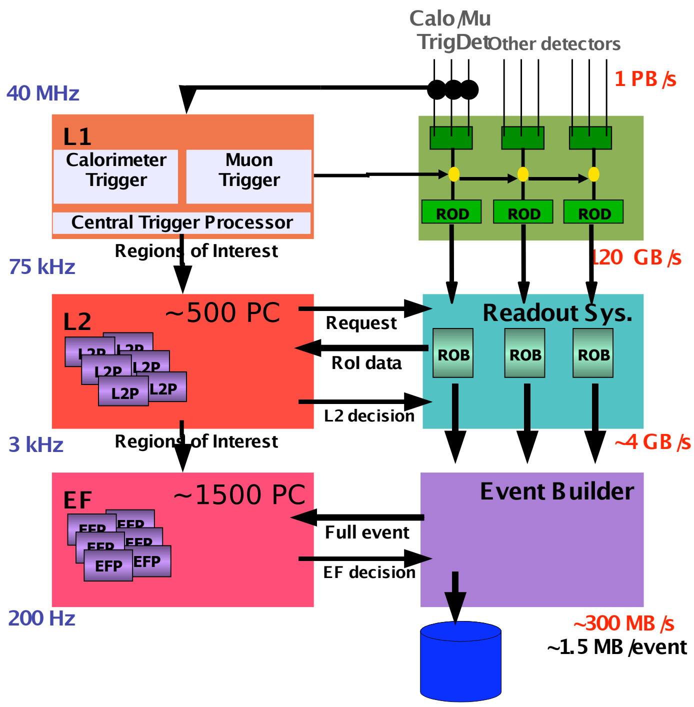

Figure 4.11: Sketch of the ATLAS T/DAQ system. The right side boxes show the data collection infrastructure while the left side shows trigger components. Abbreviations: ROD/ROB - readout driver/buffer respectively, L2P EFP - are L2 processors and EF processes respectively. Multiple boxes are used to express the fact that L2 and EF consist of farms of PCs [6].

4.2.6.1 The Level 1 trigger (L1)

The L1 trigger receives data at 40 MHz (the LHC bunch-crossing rate) providing a decision for each bunch crossing with a latency of ~ 2.5 μs during which all detector data are held in pipeline memories. Its decision is based on relatively coarse data from two subsystems, the calorimeters and dedicated muon trigger stations. Events are selected based on inclusive high-p_{T} objects (muons, electromagnetic/tau/hadronic clusters, jet clusters) plus global event features (the total scalar E_{T} and the $E_{\mathrm{T}}^{\mathrm{miss}}$ vector). There are a number of programmable trigger thresholds for each of these. For accepted events, the geometrical location of the objects, *Regions of Interest* (RoIs), are sent to L2 and the data are then transferred from the pipeline memories to the Read-Out Buffers (ROBs). L1 also specifies which signatures led to the event being selected by the L1 trigger. The L1 trigger reduces the event rate from the initial 40 MHz to about 75 kHz. This maximum accept rate of the L1 trigger (75 kHz) is determined by the capabilities of the sub-detector readout systems. ATLAS requires that it must be possible to upgrade these systems to operate at 100 kHz with a somewhat higher dead time (a few per cent) and, therefore, the DAQ and L2 trigger systems are designed to accept this higher input rate.

4.2.6.2 The High-Level-Trigger (HLT)

The HLT is a software-based trigger, running on farms built from commodity computing and network technology. It is subdivided into L2 and the EF. L2 has a nominal average processing time of ~ 40 ms and should reduce the output rate to around 2 kHz. The L2 trigger uses full-precision information from the inner tracking detectors, the calorimeters and muon detectors. Data from the sub-detectors are combined to provide better particle identification and higher measurement precision than those provided by L1. L2 must retrieve event fragments from the ROBs via Ethernet. To reduce the data transfer to a few percent, it uses only data in RoIs identified by L1. L2 algorithms are highly optimized for speed. If L2 accepts an event, all the fragments from the ROBs are combined and sent to one of the EF processors for further consideration via the event builder.

The EF can take around 4 s and should further reduce the rate to ~ 200 Hz. Like L2, EF has access to the full granularity of all the detector data. It further refines the classification of L2, using the extra time to run more complex algorithms, often based on the same tool set as offline reconstruction. It also benefits from more detailed calibration and alignment than used at L2. The processing at the EF is based mainly on the RoIs however the full detector information can be accessed and this capability is used, for example, in triggers involving missing transverse energy. The EF system can achieve the nominated data-storage rate (~ 300 MB/s) by reducing the event rate and/or the event size. For some triggers the full event data of about 1.5 MB will need to be recorded, while for others a reduced readout is sufficient, allowing a higher event recording rate.

4.2.6.3 The Trigger menu

The overall configuration of the trigger is called a menu. It is composed of building blocks, called trigger chains, which can be considered as the units of selection in that the event is accepted if at least one trigger chain is passed. Examples of trigger chains are the identification 25 GeV electrons or 6 GeV muons etc. This modular structure greatly simplifies the configuration of the trigger and allows for great flexibility as specific chains can be added or removed to the menu easily. The rate can be also controlled chain-wise by the use of prescaling - this means that a given chain is only run for a specified fraction of events chosen randomly, effectively reducing the rate for that chain by the prescale factor. Such decomposition of the whole trigger selection into chains facilitates the tuning of the trigger selection to adapt to the beam and detector conditions as well as to the overall ATLAS experimental program.

Work on the menu is divided into working groups based around the ATLAS sub-detectors and the event-features of interest for trigger selection e/γ, τ, jets, μ, missing-ET, b-jet, B-physics [5]. These groups perform detailed performance optimizations. This work of the individual working groups is integrated into a set of trigger menus adapted to different phases of the experiment. The main consideration for these menus is to provide a full coverage of the physics programme within the limitations of the maximum rate-to-tape which DAQ system can sustain and the offline limitations for data processing and storage. The rates for a given menu is studied by the trigger group by running the trigger selection on a sample of *minimum bias*[10] events.

[10] these are events selected with the loosest possible trigger requirements and which, therefore, represent the main trigger background

5
Monte Carlo Simulation

The simulation software for ATLAS is being used for large-scale production of events on the Worldwide LHC Computing Grid (WLCG), see sub-section 4.1.3. The simulation software chain is generally divided into three steps, though they may be combined into a single job: generation of the event and immediate decays, simulation of the detector and physics interactions, and digitization of the energy deposited in the sensitive regions of the detector into voltages and currents for comparison to the readout of the ATLAS detector. The output of the simulation chain can be presented in either an object-based format or in a format identical to the output of the ATLAS DAQ system (see section 4.2.6). Thus, both the simulated and real data from the detector can be run through the same ATLAS trigger and reconstruction packages. The simulation program is integrated into the ATLAS software framework, Athena [49], and uses the GEANT simulation toolkit [56]. The ATLAS detector geometry used for simulation, digitization, and reconstruction is built from databases containing the information describing the physical construction and conditions data. The latter contains all the information needed to emulate a single data-taking run of the real detector (e.g. detector misalignments or temperatures).

5.1 Simulation framework

The Athena framework [49], uses PYTHON as an object-oriented scripting and interpreter language to configure and load C++ algorithms and objects. Athena releases are divided into major projects by functionality [57], and all of the ATLAS simulation software (including event generation and digitization) resides in a single project. The dependencies of the "simulation" project are the "core" project, which includes the Athena framework, the "conditions" and "detector description" projects, which include all code necessary for the description of the ATLAS detector, and the "event" project, which includes descriptions of persistent objects [7]. Figure 5.1 shows an overview of the ATLAS simulation data flow. Algorithms and applications to be run are placed in square-cornered boxes, and persistent data objects are placed in round-cornered boxes. The optional steps required for pile-up or event overlay are shown with a dashed outline. The simulation software chain main three steps are:

- ***generation of the event and immediate decays*:** a generator is used to produce data in standard HepMC format [58]. These events can be filtered at generation time

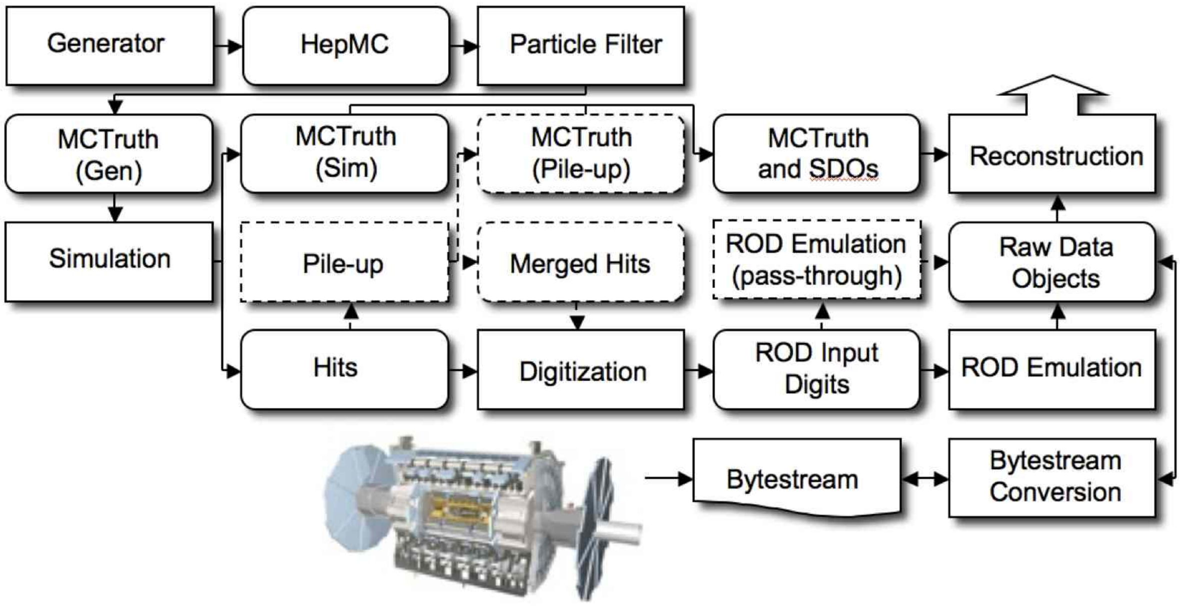

Figure 5.1: The flow of the ATLAS simulation software [7].

so that only events with a certain property (e.g. leptonic decay or missing energy above a certain value) are kept. The generator is responsible for any prompt decays (e.g. Z or W bosons) but stores any "stable" particle expected to propagate through a part of the detector. Because it only considers immediate decays, there is no need to consider detector geometry during the generation step, except in controlling what particles are considered stable. During this step, the run number for the simulated data set and event numbers for each event are established. Event numbers are generally ordered in a single job, though events may be omitted because of filtering at each step. Run numbers for simulated data sets derive from the job options used to generate the sample and mimic real run numbers used during data taking. A record of all particles produced by the generator is retained in the generation output file, MCTruth (Gen), in which the truth is a history of the interactions from the generator, including incoming and outgoing particles.

- ***simulation of the detector and physics interactions*:** the generated events are then read into the simulation. Cuts can be applied to select only certain particles to process in the simulation. Each particle is propagated through the full ATLAS detector by GEANT. The configuration of the detector, including misalignments and distortions, can be set at run time by the user. The energies deposited in the sensitive portions of the detector are recorded as "hits," containing the total energy deposition, position, and time, and are written to a simulation output file, called a hit file. Like event generation, the detector simulation information called "truth" is recorded for each event, MCTruth (Sim). A record is kept for every particle, whether the particle is to be passed through the detector simulation or not. In the simulation jobs, truth tracks and decays for certain particles are stored. This truth contains, for example, the locations of the conversions of photons within the inner detector and the subsequent electron and positron tracks.

- ***digitization*:** in the digitization jobs, Simulated Data Objects (SDOs) are created from the truth. These SDOs are maps from the hits in the sensitive regions of the detector to the particles in the simulation truth record that deposited the hits' energy. The truth information is further processed in the reconstruction jobs and can be used during the analysis of simulated data to quantify the success of the reconstruction software. Also, during the digitization stage, Read Out Driver (ROD) electronics are simulated. At this stage, detector noise is added to the event. The first level trigger, implemented with hardware on the real detector, is also simulated in a "pass" mode. Here no events are discarded but each trigger hypothesis is evaluated. The digitization first constructs "digits," inputs to the read out drivers (RODs) in the detector electronics. The ROD functionality is then emulated, and the output is a Raw Data Object (RDO) file.

In the optional steps required for pile-up or event overlay, the digitization takes hit output from simulated events: hard scattering signal, minimum bias, beam halo, beam gas, and cavern background events. Each type of event can be overlaid at a user-specifed rate before the detector signal (e.g. voltage or time) is generated. The overlay (called "pile-up") is done during digitization to save the CPU time required by the simulation. The output from the ATLAS detector itself is in "bytestream" format, which can be fairly easily converted to and from RDO file format. The two are similar, and in some subdetectors they are almost interchangeable. Truth information is the major exception. It is stripped in the conversion to bytestream.

The simulation software chain, divided in this way, uses resources more effectively than a single-step event simulation and simplifies software validation. Event generation jobs, typically quick and with small output files, can be run for several thousands of events at a time. By storing the output rather than regenerating it each time, it becomes possible to run identical events through different versions of the simulation software or with different detector configurations. The simulation step is particularly slow, and can take several minutes per event [7]. Simulation jobs are therefore divided into groups of 50 or fewer events. Digitization jobs are generally configured to run $\sim$ 1000 events. This configuration eases file handling by producing a smaller number of RDO files. Each step is partially configured based on the input files. For example, the detector geometry used for a digitization job is selected based on the input hit file.

The ATLAS HLT, see sub-section 4.2.6.2, and reconstruction [59] run on the RDO files. The reconstruction is identical for the simulation and the data, with the exception that truth information can be treated and is available only in simulated data. During data taking, the HLT is performed on bytestream files, however all hypotheses and additional test hypotheses may be evaluated by translating the RDOs into bytestream format.

Once the reconstruction is completed, the so-called Event Summary Data (ESD) is produced, together with the Analysis Object Data (AOD) data format, which contain the objects needed in a physics analysis. Various types of Derived Physics Data (DPD) are also available, which contain a combination of the objects available in the ESD and AOD, for specific usage. Different Physics/Performance groups in ATLAS produce their own DPD and/or the so-called D3PD[1]. The TAG format is produced from the AOD which contains event-level metadata, i.e."data about other data", to allow for a fast event selection without reading through the AOD.

In this study two sets of data are used, the first is the 2010 data collected by ATLAS (39 pb^{-1}), the second one is the 2011 data collected before the August technical stop, which represents $\simeq$ 2.05 fb^{-1}. Unless stated otherwise all Monte Carlo (MC) samples are generated, simulated and reconstructed in Athena release 16.0.2.7 for the 2010 data

[1] D3PD is a data format where data is presented as flat ntuples

analysis (see section 7.2), i.e. consistent with the Autumn 2010 reprocessing[2] and release 16.6.X (the so-called MC10b [3]) for the 2011 data analysis which is not compatible with the Autumn reprocessed data. Also, the WZD3PDs[4] are used throughout all this dissertation.

5.2 Z' simulated signals

Z' signal samples are simulated for the Sequential Standard Model (SSM), see section 3.1. PYTHIA [31] is used for event generation, with all interferences (between photon, Z and Z') switched on, to generate a series of Z' masses. MRST2007lomod (also known as LO*) [60] parton distribution functions (PDF) are used. Z' samples also include the Drell Yan contribution above a mass threshold of 0.5 times the pole mass. Tables 5.1 list the characteristics of the Monte Carlo samples for Z'_{SSM} used for the study, where the 1^{st} column is the ATLAS Monte Carlo run number. The 2^{nd} to the 5^{th} columns give the mass, mass threshold, width and electron channel branching fraction. The 6^{th} column is the cross section times branching fraction reported by the generator (gen) and calculated (cal) at QCD NNLO, while the last column gives the number of generated events; the lowest integrated luminosity $L_{\mathrm{int}} = N_{\mathrm{evt}}/(\sigma B)$ is 480 pb^{-1}(for the lowest mass sample).

Table 5.1: Monte Carlo Z' samples used for the study.

Run number	Mass [GeV]	Threshold [GeV]	Γ [GeV]	B($Z' \to e^+e^-$) [%]	σB [fb] gen	cal	N_{evt} [k]
115272	250	125	6.87	3.36	36.4×10^3	41.9×10^3	20
115273	500	250	14.56	3.20	2.63×10^3	2.97×10^3	20
115274	750	375	22.64	3.10	481	534	20
105603	1000	500	30.64	3.06	129	139	20
105549	1250	625	38.60	3.05	40.9	42.6	20
105624	1500	750	46.55	3.04	15.4	15.24	20
105554	1750	875	54.49	3.03	5.99	5.56	20
105409	2000	1000	62.43	3.03	2.55	2.20	20

As the Z' samples also include the Drell Yan contribution (both production and interference), thus, the cross sections displayed in table 5.1 can not be used in the limit computation. Table 5.2 displays the LO Z' cross sections for various models (E_6 and comapried with SSM Z').

In addition to these "usual" (Z'_{SSM}) samples, a "special" SSM sample was generated with an approximately flat mass distribution[5]. This allows to build as many fully simulated "template signals" as needed, by re-weighting the events according to the desired invariant mass shape. For instance, in the E_6 models (see section 3.1), the couplings of Z' to both quarks and leptons are all different, thus the fraction of events stemming from $u\bar{u}$ or $d\bar{d}$ states is different from one model to another. Since the PDFs of the two quark flavors are

[2]https://twiki.cern.ch/twiki/bin/view/AtlasProtected/DataMCForAnalysis

[3]https://twiki.cern.ch/twiki/bin/view/AtlasProtected/AtlasProductionGroupMC10b

[4]the D3PDs that produced by the SM WZ physics group https://twiki.cern.ch/twiki/bin/view/AtlasProtected/ZWD3PDProduction

[5]The procedure is to use a modified version of PYTHIA in which the cross section is multiplied by the inverse Breit-Wigner and divided by an exponential.

Table 5.2: LO order cross sections used in the limit calculation for all Z' models

Mass [GeV]	$\sigma B(Z'_{\mathrm{SSM}})$ [fb]	$\sigma B(Z'_{\mathrm{S}})$ [fb]	$\sigma B(Z'_{\mathrm{N}})$ [fb]	$\sigma B(Z'_{\psi})$ [fb]	$\sigma B(Z'_{\chi})$ [fb]	$\sigma B(Z'_{\eta})$ [fb]	$\sigma B(Z'_{I})$ [fb]
250	2.73e+04	1.47e+04	9.22e+03	8.13e+03	1.59e+04	9.57e+03	1.33e+04
500	2.04e+03	1.08e+03	683	597	1.16e+03	695	952
750	369	189	120	107	210	123	170
1000	94.8	46.9	30.3	26.9	51.8	31.4	41.5
1250	29.6	13.6	9.07	8.17	15.6	9.70	11.9
1500	10.3	4.31	3.00	2.73	5.06	3.23	3.74
1750	3.88	1.44	1.04	9.83e-01	1.75	1.20	1.22
2000	1.58	5.09e-01	3.79e-01	3.71e-01	6.41e-01	4.55e-01	4.22e-01
2250	6.94e-01	1.91e-01	1.44e-01	1.42e-01	2.49e-01	1.78e-01	1.57e-01
2500	3.30e-01	8.03e-02	5.75e-02	5.67e-02	1.04e-01	7.26e-02	6.53e-02

different, the Z' stemming from $u\bar{u}$ are slightly more boosted than those from $d\bar{d}$, and the outgoing electrons tend to have slightly higher pseudo rapidities, hence a slightly lower acceptance for the $u\bar{u}$ events as compared to $d\bar{d}$ ones (see figure 5.2). This effect decreases with the dielectron invariant mass (M_{ee}), because the Z' is produced more and more at rest [8]. This explains the motivation of the generation of such "special" SSM sample to be able to mimic E_6 models with minor approximations (see *Ref.* [8] for more details).

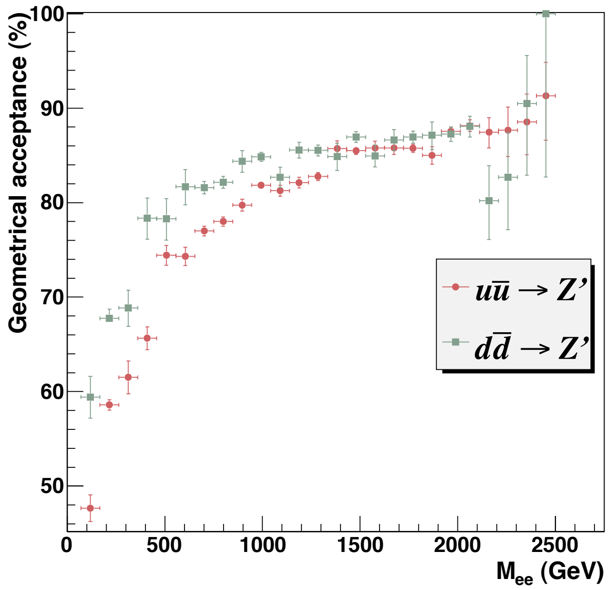

Figure 5.2: Geometrical acceptance as a function of the invariant mass for $u\bar{u}$ and $d\bar{d}$ incoming flavors [8].

NNLO cross sections

It is conventional to assume that all colorless final states have similar QCD radiation in the initial state, and therefore the QCD K-factor derived for the Drell-Yan process can be applied to the Z' signal as well (see subsection 5.4.1.1). For the Z' analysis, the simulation samples have been generated using PYTHIA and the LO* PDFs [60]. Therefore the K^*_{NNLO} is used to weight the simulated Z' signal as a function of the dilepton invariant mass. Some representative values of K^*_{NNLO} are shown in Table 5.3.

Table 5.3: QCD K-factor for several Z' mass points obtained with PYTHIA (LO) and PHOZPR (NNLO) using the central value of MSTW2008 NNLO PDF.

Z' mass [GeV]	250	500	750	1000	1250	1500	1750	2000
$K^*_{\mathrm{NNLO}} = \frac{\sigma_{NNLO}}{\sigma_{LO*}}$	1.149	1.131	1.109	1.080	1.041	0.990	0.929	0.860

5.3 e^* simulated signals

The e^* signal samples are generated using PYTHIA, for four different points in the (M_{e^*}-Λ) plane. In addition to PYTHIA samples another set of e^* samples are generated with CompHEP[30]. As in the case of Z' analysis, the LO* [60] parton distribution functions (PDF) are used. In the current analysis, the excited electron is assumed to be only produced via contact interactions and decay only via gauge mediated interactions (only $e^* \to e\gamma$ channel), see section 3.2.1. Table 5.4 lists the characteristics of the Monte Carlo PYTHIA samples for e^* used in this analysis, where the 1^{st} column is the ATLAS Monte Carlo run number, the 2^{nd} and the 3^{rd} columns give the mass, compositeness scale (Λ), the 4^{th} and 5^{th} columns list the width and the GM decays branching fraction, the 6^{th} column is the cross section time branching fraction reported by the generator (gen), and the last column gives the number of generated events; the lowest integrated luminosity $L_{\mathrm{int}} = N_{\mathrm{evt}}/(\sigma B)$ is 36 fb^{-1} (for the $M_{e^*} = 400$ GeV, $\Lambda = 3000$ GeV sample).

Table 5.4: Monte Carlo PYTHIA samples used for the e^* analysis.

Run number	Mass [GeV]	Λ [GeV]	Γ [GeV]	B(GM decay) [%]	filter eff. [%]	σB [fb] gen	N_{evt} [k]
105636	1000	5000	–	68	96	5.03	20
105098	400	5000	–	92	92	41.16	10
105099	1000	3000	–	44	96	24.85	10
105505	400	3000	–	82	92	280.49	10

In the e^* analysis, it was found that PYTHIA improperly treats the e^* spin. This was confirmed by a dedicated study, see Appendix A. As the compositeness scale Λ is found to have no effect on the kinematics distributions (see sub-section 5.3.1), CompHEP e^* signal samples are generated at fixed Λ (3 TeV) for 22 different e^* masses starting from 200 GeV and up to 2300 GeV with steps of 100 GeV between two successive mass points. To obtain e^* samples with different Λ (other than 3 TeV) for a fixed e^* mass, kinematic distributions are weighted by a scaling factor which gives the proper $\sigma \times$ BR. Table 5.5 lists the characteristics of the Monte Carlo CompHEP samples for the e^* used in this analysis, where the 1^{st} column is the ATLAS Monte Carlo run number, the 2^{nd} and the 3^{rd} columns give the mass, compositeness scale (Λ), the 4^{th} and 5^{th} columns list the width and the GM decays branching fraction, the 6^{th} column is the filter efficiency, the 7^{th} column is the cross section time branching fraction reported by the generator (gen), while the last column gives the number of generated events. Figure 5.3 shows a 2D plot of the total e^* decay width as a function of m_{e^*} and Λ while figure 5.3 shows the generator filter efficiency as a function of the excited lepton mass.

Table 5.5: Monte Carlo CompHEP samples used for e^* analysis.

Run number	Mass [GeV]	Λ [GeV]	Γ [GeV]	$B(e^* \to e\gamma)$ [%]	filter eff. [%]	σB [fb] gen	N_{evt} [k]
119286	200	3000	0.0054	32.4	70.5	758	20
119287	300	3000	0.022	27.4	80.3	468	20
119288	400	3000	0.059	24.1	84.3	302	20
119289	500	3000	0.13	21.7	86.6	200	20
119290	600	3000	0.25	19.4	88.1	133	20
119291	700	3000	0.44	17.3	89.2	88.0	20
119292	800	3000	0.74	15.5	90.1	58.4	20
119293	900	3000	1.18	13.8	90.7	38.9	20
119294	1000	3000	1.81	12.3	91.2	25.9	20
119295	1100	3000	2.70	11.0	91.5	17.3	20
119296	1200	3000	3.92	9.87	91.9	11.6	20
119297	1300	3000	5.55	8.87	92.1	7.79	20
119298	1400	3000	7.69	8.00	92.3	5.25	20
119299	1500	3000	10.5	7.24	92.5	3.54	20
119875	1600	3000	14.0	6.57	92.6	2.40	10
119876	1700	3000	18.5	5.98	92.7	1.62	10
119877	1800	3000	24.0	5.46	92.8	1.10	10
119878	1900	3000	30.8	5.00	92.9	0.75	10
119879	2000	3000	39.2	4.60	92.9	0.51	10
119880	2100	3000	49.2	4.24	93.0	0.35	10
119881	2200	3000	61.3	3.91	93.0	0.24	10
119882	2300	3000	75.6	3.63	93.0	0.16	10

5.3.1 Parton level e^* kinematics

5.3.1.1 Invariant mass properties

In the excited electron search, we look at the electron-photon invariant mass and the three-body (dielectron+photon) invariant mass spectra. Figure 5.5 shows the truth[6] level electron-photon (eγ from e^* decay), invariant mass distributions for points in $M_{e^*} - \Lambda$ plane, which shows a narrow peak. Figure 5.6 shows the three-body (eeγ) invariant mass distributions. These plots are normalized to unit area. The eeγ invariant mass spectra are important when calculating higher order QCD corrections to the LO* cross-sections.

5.3.1.2 Kinematic properties

Figures 5.7, 5.8 show the transverse momentum (p_{T}) distributions of the leading p_{T} electron and the leading p_{T} photon, for different points in $M_{e^*} - \Lambda$ plane. Each plot is normalized to unit area. These figures show that the leading p_{T} electron and the

[6] Truth level means the generator level, i.e. before the detector simulation

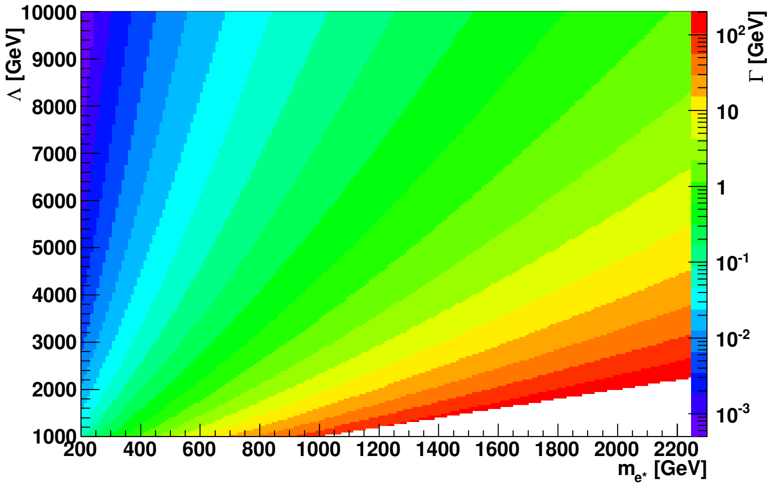

Figure 5.3: The total decay width as a function of m_{e^*} and Λ.

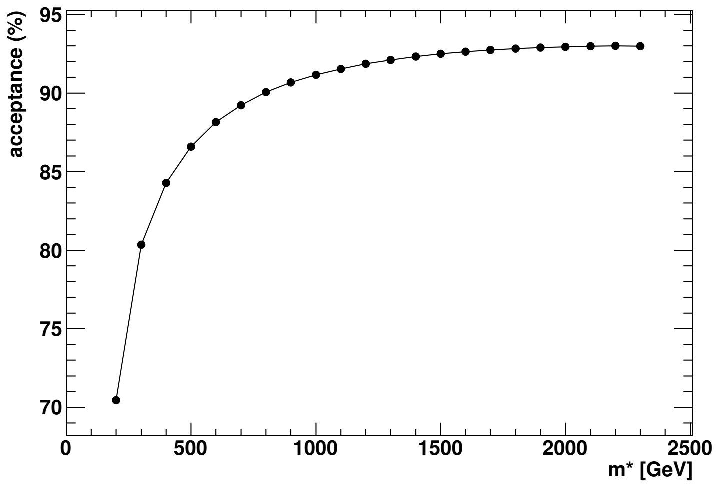

Figure 5.4: The generator filter efficiency as a function of the excited lepton mass.

leading p_T photon have harder p_T distribution as the e^* mass increases, while changing the compositeness scale has no effect on the p_T spectrum for both electrons and photons.

Figures 5.9, 5.10 show the generated pseudorapidity distributions (η) of the leading p_T electron and the leading p_T photon, for different points in $M_{e^*} - \Lambda$ plane. Each plot is normalized to unit area. These figures show that the absolute value of pseudorapidity of the leading p_T electron and the leading p_T photon decreases as the e^* mass increases, i.e. these objects tend to appear in the central region of the detector as the e^* mass increases. As in the case of p_T spectra, changing the compositeness scale has no effect on the η spectrum for both electrons and photons.

The dependence of p_T and η distributions on e^* indicate that the final state particles are easier to be detected in the detector as M_e^* increases. Unfortunately, the cross-section of e* production drops as M_{e^*} increases.

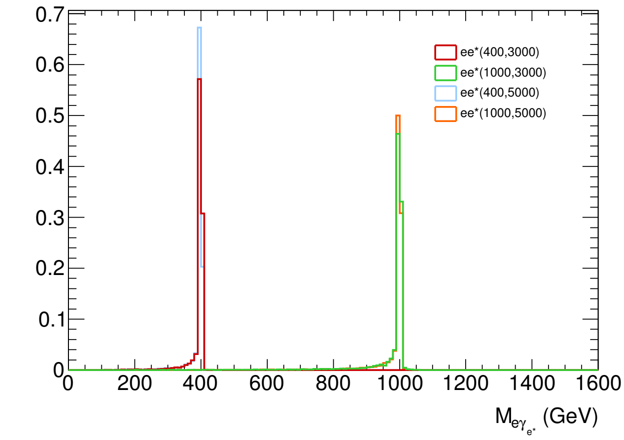

Figure 5.5: Parton (truth) level electron-photon invariant mass spectra for four different points in $M_{e^*} - \Lambda$ plane, normalized to unit area.

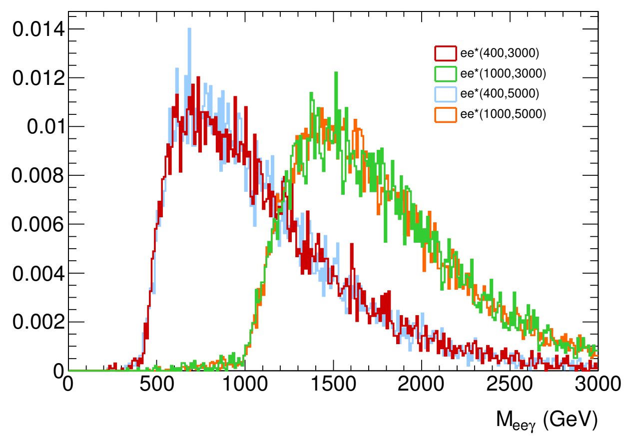

Figure 5.6: Parton level three body ($ee\gamma$) invariant mass spectra for four different points in $M_{e^*} - \Lambda$ plane, normalized to unit area.

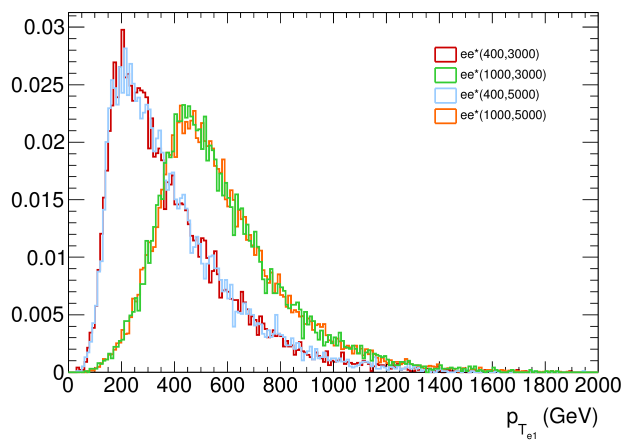

Figure 5.7: Parton level $p_{\rm T}$ distributions for the leading $p_{\rm T}$ electron, normalized to unit area.

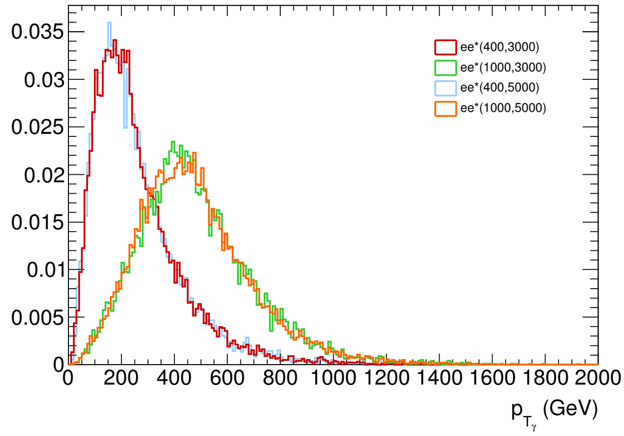

Figure 5.8: Parton level p_{T} distributions for the leading p_{T} photon, normalized to unit area.

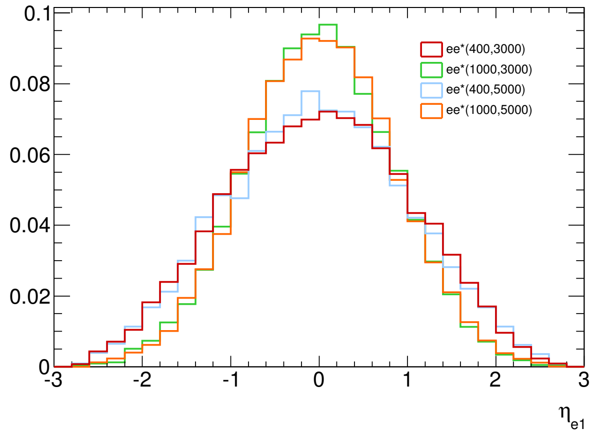

Figure 5.9: Parton level η distributions for the leading p_{T} electron, normalized to unit area.

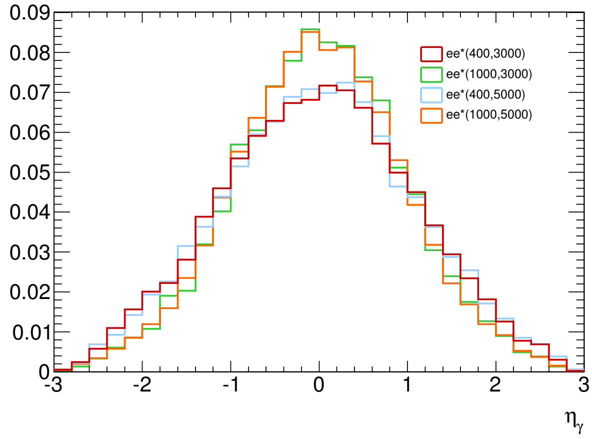

Figure 5.10: Parton level η distributions for the leading p_{T} photon, normalized to unit area.

5.4 Simulated backgrounds

All SM processes giving two or more electrons and/or photons and/or jets are backgrounds for the processes $pp \to Z' \to e^+e^-$ and $pp \to e^*e \to e^+e^-\gamma$. One of the dominant backgrounds consists of the SM Z/γ^* bosons ("Drell Yan" process) decaying to electrons, with the final state photon radiated by either a parton in the initial state (Initial State Radiation, ISR) or from one of the final state electrons (Final State Radiation, FSR) in case of e^* analysis. Other reducible backgrounds are dibosons (ZZ, ZW, WW, $Z\gamma$[7]), $t\bar{t}$ (mainly the purely electronic channel), W plus jet process (in which the jet is misidentified as an electron) and QCD multi-jet production. Also, other negligible background contributions could come from Drell Yan (DY) production of tau pairs with subsequent decay of the taus into an electron. The latter is suppressed by imposing a cut on the invariant mass of the 2 leading electrons M_{ee}.

5.4.1 Drell Yan(ee), $Z\gamma$ production

Drell Yan ($pp \to Z/\gamma^* + X \to e^+e^- + X$), and $Z\gamma \to e^+e^-\gamma$ samples are generated with PYTHIA[31]. For $Z \to ee$ dedicated samples are binned in Z mass and covering masses above 75 GeV to ensure adequate statistics at high invariant mass. In analyzing 2010 data, only for e^* study a dedicated $Z\gamma \to e^+e^-\gamma$ sample, with a photon and multi-lepton filters during event generation [8], were produced to enrich the high mass region with ISR/FSR photons to have adequate statistics at high mass tail for $e^+e^-\gamma$ spectrum. The duplicated events between these three samples are removed by setting the appropriate cuts on the generated Z mass and the ISR photon transverse momentum (p_{T}). Table 5.6 lists the Monte Carlo PYTHIA DY(ee) samples used during 2010 data analysis. The first column gives the mass cut on Z mass in GeV and the 2^{nd} gives the ATLAS Monte Carlo run numbers. The 3^{rd} and 4^{th} columns are the cross section time branching ratios reported by the generator (gen.) and calculated (cal.) at QCD NNLO (see subsection 5.4.1.1). The 5^{th} column is the number of generated events and the last one is the integrated luminosity $L_{\mathrm{int}} = N_{\mathrm{evt}}/(\sigma B)$.

Table 5.6: Monte Carlo PYTHIA Drell Yan samples used during 2010 data analysis.

Process M_Z[GeV]	Run number	σB [pb] gen.	cal.	N_{evt} [k]	L_{int} [fb^{-1}]
$Z \to ee$	106046	856	989	5000	5.
$Z\gamma \to ee\gamma$ [9]	105168	0.694	–	50	72
$Z(75, 120) \to ee$	105466	819.921	948	20	0.02
$Z(120, 250) \to ee$	105467	8.711	9.99	20	2.
$Z(250, 400) \to ee$	105468	0.416	0.461	20	48.
$Z(400, 600) \to ee$	105469	0.0671	0.0729	20	297.
$Z(600, 800) \to ee$	105470	0.0111	0.0118	20	1790.
$Z(800, 1000) \to ee$	105471	0.00275	0.0028	20	7290.
$Z(1000, 1250) \to ee$	105472	0.000919	0.000912	20	21800.
$Z(1250, 1500) \to ee$	105473	0.000249	0.000235	20	80300.
$Z(1500, 1750) \to ee$	105474	0.000077	0.0000687	20	291000.
$Z(1750, 2000) \to ee$	105475	0.000026	0.0000217	20	922000.
$Z(2000,) \to ee$	105476	0.000015	0.0000173	20	1156000.

In 2011 data analysis, the ATLAS excited lepton sub-group decided to use dedicated

[7] Drell-Yan is considered as a separate background for simplicity. In reality the γ, Z (and even Z' if it exists) are all produced by the same process and interfere with each other.

[8] The photon filter requires 1 photon with $|\eta| < 2.5$, $p_{\mathrm{T}} > 15$ GeV while the lepton filter requires 2 leptons with the same η and p_{T} cuts.

[9] only used in 2010 e^* analysis

samples for $Z\gamma$ production that are generated at NLO with SHERPA CTEQ6.6m [61] PDFs, requiring a di-electron masses above 40 GeV. To ensure adequate statistics for energetic photons, these samples are generated with two different photon filters, p_{T}>10 GeV and p_{T}>40 GeV and a cut is applied on the distance between the photon and leptons, requiring the photons to be outside a cone $R = \sqrt{\Delta\eta^2 + \Delta\phi^2}$ =0.5 of the leptons. The overlap between these two samples is removed by rejecting events from the sample with p_{T}>10 GeV cut that have an ISR photon with p_{T}>40 GeV. Table 5.7 lists the Monte Carlo SHERPA $Z\gamma$ samples used in 2011 data analysis. The first column gives the physics process, the second gives the generator level p_{T} cut on the ISR photon, the third is the ATLAS Monte Carlo run numbers, the fourth is the cross section time branching ratios reported by the generator at QCD NLO (see subsection 5.4.1.1), the 5^{th} column is the number of generated events and the last one is the integrated luminosity $L_{\mathrm{int}} = N_{\mathrm{evt}}/(\sigma B)$.

Table 5.7: Monte Carlo SHERPA $Z\gamma$ samples used for the 2011 data analysis.

Process	γ p_{T} cut [GeV]	Run number	σB [pb]	N_{evt} [k]	L_{int} [fb^{-1}]
$Z\gamma \to ee\gamma$	10	126015	16.5150	200	12.11
$Z\gamma \to ee\gamma$	40	126020	0.51932	150	288.8

5.4.1.1 *Cross sections*

Since the Drell Yan process is the main background of both signals (Z' and e^*), we will look at the calculation of its cross section in some more detail. In 2010 data analysis where PYTHIA samples (listed in table 5.6) were used to model $Z+\gamma$ background, both QCD and EW mass dependent K-factors are computed and applied on the generated cross section quoted in the table[10]. In ATLAS MC10 Monte Carlo, the Drell Yan process is simulated using the PYTHIA LO generator and MRST2007LO* PDFs [60]. The normalization and the shape of these differential cross sections are modified when higher-order QCD and electroweak corrections are taken into account. However, next-to-leading order (NLO) or next-to-next-to-leading order (NNLO) generators are typically not available for all the processes of interest. Here, we present how we can add higher order corrections in both cases of QCD and electroweak.

- ***QCD K-factor in the 2010 analysis*:** the usual procedure is to use NNLO QCD calculations of the DY process to compute a mass-dependent K-factor. This mass-dependent K-factor is then used to multiply the LO differential cross section, yielding the NNLO differential cross section as a function of mass.

  The DY cross section has been calculated at NNLO using the PHOZPR [11] program with various PDF sets. These results can be used to correct the PYTHIA data sets to NNLO by applying a K-factor to the PYTHIA cross section.

  The Standard Model group has performed extensive studies of the Drell Yan cross section and associated uncertainties. A selection of the results are presented in the following, see Ref. [62] for details. The differential production cross section

[10]The calculated cross section in table 5.6 has only the QCD K-factor.

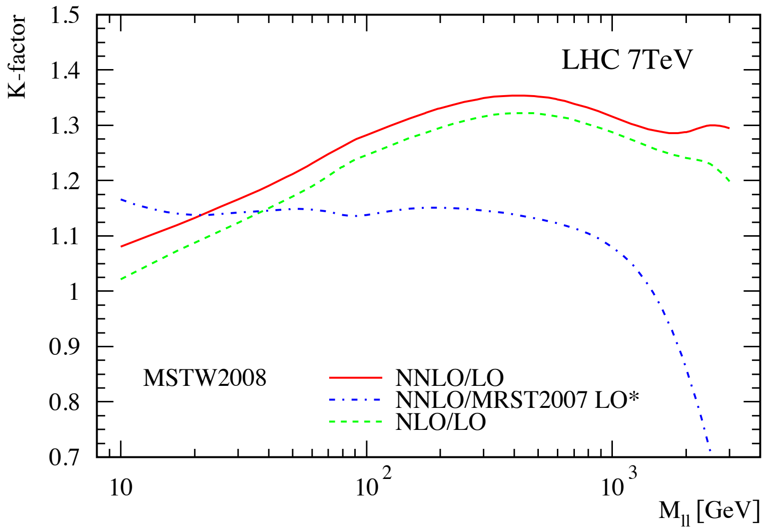

Figure 5.11: Cross section ratios (QCD K-factors) for Drell Yan lepton-pair production as function of dilepton invariant mass $M_{\ell\ell}$, calculated with PHOZPR [8].

$M_{\ell\ell}^2 \frac{d\sigma_{\rm NNLO}}{dM_{\ell\ell}^2}$ calculated at NNLO using the MSTW2008NNLO PDF is given in Table 5.8 for dilepton masses $10\,\mathrm{GeV} < M_{\ell\ell} < 3000\,\mathrm{GeV}$ [8]. Table 5.8 lists also the mass-dependent cross section ratios (K-factors);

$$\begin{aligned}
K_{\rm NLO}(M_{\ell\ell}) &= \frac{d\sigma_{\rm NLO}}{dM_{\ell\ell}^2}(\mathrm{MSTW2008NLO})/\frac{d\sigma_{\rm LO}}{dM_{\ell\ell}^2}(\mathrm{MSTW2008LO}),\\
K_{\rm NNLO}(M_{\ell\ell}) &= \frac{d\sigma_{\rm NNLO}}{dM_{\ell\ell}^2}(\mathrm{MSTW2008NNLO})/\frac{d\sigma_{\rm LO}}{dM_{\ell\ell}^2}(\mathrm{MSTW2008LO}),\\
K^*_{\rm NNLO}(M_{\ell\ell}) &= \frac{d\sigma_{\rm NNLO}}{dM_{\ell\ell}^2}(\mathrm{MSTW2008NNLO})/\frac{d\sigma_{\rm LO}}{dM_{\ell\ell}^2}(\mathrm{MRST2007LO}^*),
\end{aligned}$$

which are shown in figure 5.11 as well. The NLO and NNLO K-factors $K_{\rm NLO}(M_{\ell\ell})$ and $K_{\rm NNLO}(M_{\ell\ell})$, respectively, which are defined based on PDF sets of the corresponding order, increase by approximately 25% for dilepton masses between 10 GeV and 400 GeV. $K^*_{\rm NNLO}(M_{\ell\ell})$, which is based on a LO prediction using the MRST2007* modified LO PDF set [63], has only a modest dependence on $M_{\ell\ell}$ over a wide range of dilepton masses. Since the MRST2007* PDF is used in the ATLAS MC10 production, $K^*_{\rm NNLO}(M_{\ell\ell})$ defines an event specific weight for DY events generated with a LO event generator (e.g. PYTHIA and HERWIG) to obtain a normalization and a dilepton invariant mass shape which is accurate to NNLO.

- ***EW K-factor*:** the electroweak corrections include contributions from final state photon radiation, electroweak loop corrections and processes with initial photons (being part of the proton's structure). For the MC background and signal samples, final state photon radiation (real QED correction) is accurately simulated using PHOTOS [64] and a full detector simulation. Therefore, this contribution needs to be excluded when defining a weight for the simulated samples to account for the remaining electroweak corrections. Similar to the case of QCD K-factors, a mass-dependent electroweak correction is defined to take into account the effects of higher order electroweak effects. The HORACE [65, 66] program is used to calculate

Table 5.8: NNLO Drell Yan lepton-pair production cross section $M_{\ell\ell}^2 \mathrm{d}\sigma_{\mathrm{NNLO}}/\mathrm{d}M_{\ell\ell}^2$ as function of dilepton mass $M_{\ell\ell}$ calculated with PHOZPR [11] and the MSTW2008NNLO PDF set, cross section ratios (K-factors) based on the MSTW2008 LO, NLO, and NNLO and MRST2007* PDF sets, symmetric and asymmetric PDF uncertainties for the NNLO cross section at 68% and 90% C.L., respectively [8].

$M_{\ell\ell}$ [GeV]	$M_{\ell\ell}^2 \frac{\mathrm{d}\sigma_{\mathrm{NNLO}}}{\mathrm{d}M_{\ell\ell}^2}$ [nb] MSTW 2008NNLO	$\frac{\sigma_{\mathrm{NLO}}}{\sigma_{\mathrm{LO}}}$ MSTW 2008NLO/LO	$\frac{\sigma_{\mathrm{NNLO}}}{\sigma_{\mathrm{LO}}}$ MSTW 2008NNLO/LO	$\frac{\sigma_{\mathrm{NNLO}}}{\sigma_{\mathrm{LO}}}$ MSTW/MRST 2008NNLO/2007LO*	Δ_r [%] PDF uncert. 68% C.L.	Δ_r^+ [%]	Δ_r^- [%]	Δ_r [%] PDF uncert. 90% C.L.	Δ_r^+ [%]	Δ_r^- [%]
70	0.665E-01	1.208	1.248	1.144	1.7	1.7	-1.6	3.3	3.5	-3.2
80	0.155E+00	1.225	1.262	1.138	1.7	1.7	-1.6	3.3	3.5	-3.2
91.12	0.113E+02	1.239	1.275	1.136	1.6	1.7	-1.6	3.3	3.5	-3.1
100	0.236E+00	1.246	1.282	1.138	1.6	1.7	-1.6	3.2	3.5	-3.1
125	0.207E-01	1.263	1.299	1.145	1.6	1.7	-1.5	3.2	3.5	-3.0
150	0.784E-02	1.277	1.312	1.149	1.6	1.7	-1.5	3.1	3.5	-3.0
175	0.405E-02	1.287	1.323	1.151	1.6	1.7	-1.5	3.2	3.5	-2.9
200	0.239E-02	1.296	1.331	1.151	1.6	1.7	-1.5	3.2	3.6	-2.9
250	0.104E-02	1.308	1.342	1.149	1.6	1.8	-1.4	3.3	3.7	-3.0
300	0.528E-03	1.316	1.349	1.146	1.6	1.8	-1.5	3.4	3.9	-3.1
400	0.179E-03	1.322	1.354	1.139	1.7	2.0	-1.5	3.6	4.2	-3.3
500	0.750E-04	1.321	1.352	1.131	1.8	2.1	-1.6	3.9	4.5	-3.5
600	0.357E-04	1.316	1.347	1.123	1.9	2.3	-1.7	4.1	4.8	-3.7
700	0.185E-04	1.310	1.339	1.114	2.0	2.5	-1.7	4.4	5.1	-3.8
800	0.101E-04	1.302	1.332	1.104	2.2	2.7	-1.8	4.6	5.5	-4.0
900	0.582E-05	1.295	1.324	1.093	2.3	2.9	-1.8	5.0	6.0	-4.1
1000	0.346E-05	1.288	1.316	1.080	2.5	3.2	-1.9	5.4	6.6	-4.3
1250	0.105E-05	1.271	1.300	1.041	3.2	4.1	-2.3	6.7	8.4	-5.3
1500	0.353E-06	1.257	1.290	0.990	4.2	5.4	-3.2	8.8	11.0	-7.0
1750	0.127E-06	1.247	1.286	0.929	5.5	7.1	-4.4	11.6	14.5	-9.3
2000	0.473E-07	1.241	1.288	0.860	7.3	9.2	-6.1	15.3	19.1	-12.3
2500	0.687E-08	1.230	1.300	0.712	11.9	14.5	-10.7	24.8	30.8	-20.3
3000	0.949E-09	1.199	1.295	0.563	17.2	20.3	-16.2	35.4	43.7	-29.6

the weak K-factor due to virtual gauge boson loops. At this moment the effect of real W and Z boson emission is not included, resulting in a $\sim 2\%$ underestimation of our Drell-Yan background cross section. Cross section weights (correction factors) were defined as function of $\ell^+\ell^-$ invariant mass M as the following ratios of differential cross section predictions [8]:

1. the ratio of the exact $\mathcal{O}(\alpha)$ calculation matched with higher order QED contributions over the prediction including only final state QED radiation in the parton shower approximation (including higher orders) which parameterizes the correction due to electroweak loop contributions (figure 5.12, left),
2. the ratio of the prediction including contributions with initial photons over the one excluding these processes (with both calculations using the exact $\mathcal{O}(\alpha)$ calculation matched with higher order QED contributions) which parameterizes the correction due to the photon contribution of the proton structure (figure 5.12, right),
3. the ratio of the exact $\mathcal{O}(\alpha)$ calculation matched with higher order QED contributions and including contributions with initial photons over the prediction including only final state QED radiation in the parton shower approximation (including higher orders) which is the product of the first two ratios (figure 5.13).

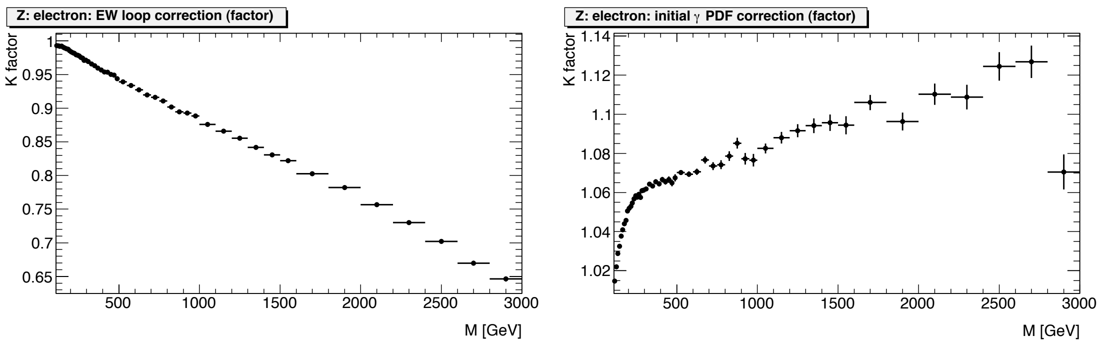

Figure 5.12: Correction factor (event weight) due to electroweak loop contributions (left) and due to photon induced processes (right) [8].

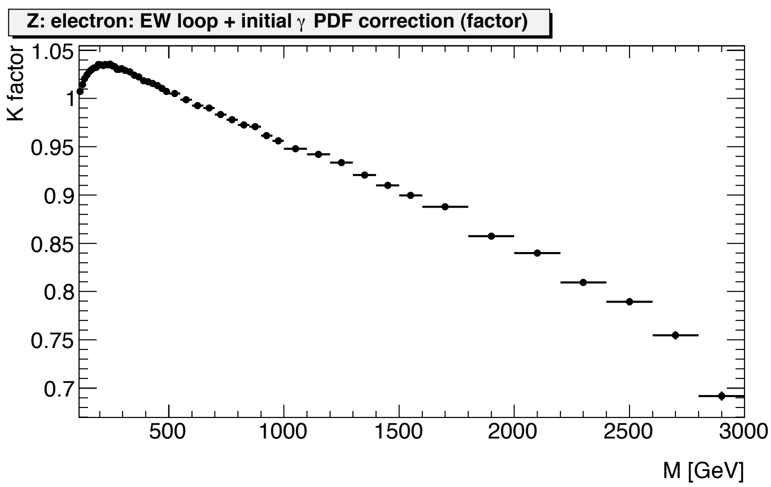

Figure 5.13: Electroweak K-factor (event weight) due to the combination of electroweak loop contributions and photon induced processes [8].

The last ratio (figure 5.13.) can be interpreted as the electroweak K-factor, which can be applied as additional event weight for simulated $Z/\gamma^* \to \ell^+\ell^-$. For convenience, some representative values are shown in Table 5.9. For the differential cross section calculations, the MRST2004QED PDF set [67] is used [8]. This provides a photon distribution function based on photon radiation and splitting kernels, and an electron acceptance of $|\eta_e| < 2.5$ and $p_{T,e} > 20$ GeV. As this acceptance does not properly match the data selection applied, the electroweak K-factor has been recalculated for $|\eta_e| < 2.4$ and $p_{T,e} > 25$ GeV, albeit with lower statistical precision. The ratio of both predictions, which is shown in figure 5.14, agree within ∼0.2%.

Table 5.9: EW K-factor for several ee invariant masses obtained with HORACE using MRST2004QED PDF set [8].

Mass [GeV]	250	500	750	1000	1250	1500	1750	2000
K^*_{EW} (ee)	1.032	1.010	0.986	0.960	0.933	0.905	0.876	0.845

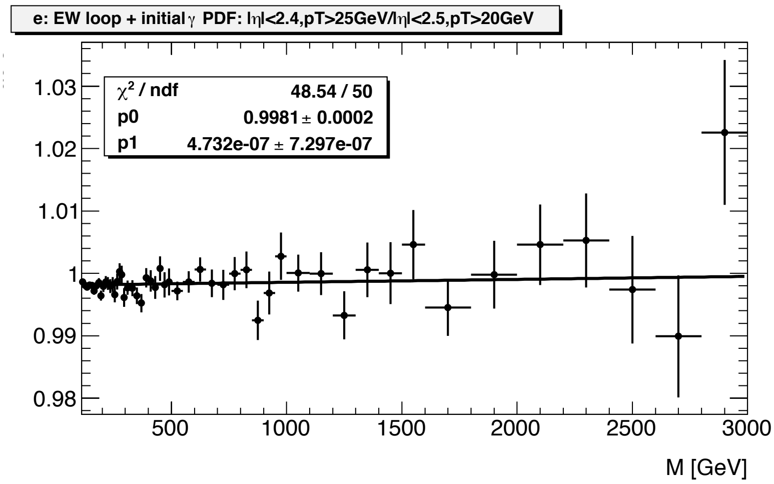

Figure 5.14: Ratio of the electroweak K-factors assuming different lepton acceptances.

In *Ref.* [8] the systematic uncertainty on the electroweak correction is estimated to be 3%, taking into account potential contributions from $\mathcal{O}(\alpha\alpha_s)$ corrections [66], higher order electroweak corrections [68], and an assumed uncertainty of 10% on the contribution from photon induced processes. As we define the correction factors with respect to the predicted cross sections including FSR QED contributions, an additional uncertainty arises, if these contributions modify the total integrated Z/γ^* or Z' cross section. Since we use the G_μ electroweak scheme to calculate the NNLO QCD cross section predictions, which minimizes the correction at low masses [69], this additional uncertainty can be neglected for small invariant masses M. Based on the running of the fine structure constant we estimate the uncertainty to be about 3% for $M \sim 1\,\text{TeV}$. Thus, we obtain a total uncertainty on the expected Z/γ^* and Z' event yields due to electroweak corrections of 4.5%.

Unlike the QCD K-factor, the weak K-factor can not be applied to the Z' signal cross section, since this K-factor depends on the W and Z boson couplings to the Z' boson and is therefore model-dependent. It can not be applied to the e^* signal as well since PYTHIA samples assume only contact interaction production for e^*.

- ***QCD K-factor for the 2011 data analysis*:**

  SHERPA generated samples to model $Z + \gamma$ background includes QCD higher order corrections like the real emission, but it misses virtual corrections and therefore does not give predictions at the NLO accuracy. The Exotic excited lepton sub-group derived a three body mass-dependent $m_{ee\gamma}$ K-factor to scale SHERPA. This scale factors are derived by comparing SHERPA predictions with MCFM [70] calculations which includes the full QCD NLO calculation for the $Z + \gamma$ process. The matrix element photon comes from ISR, FSR, or fragmentation, but unlike in SHERPA samples, there is no ISR or FSR photon in the Z + fragmentation photon contribution. MCFM settings follow the recommendations from the SM group [71]. This calculations were done with the MSTW2008nlo90cl NLO PDF set, in which the fragmentation photons are defined as isolated photons satisfying: $\Sigma_{\Delta R(\gamma,had)<0.4}$ E_{T} (had) $<$ 5 GeV. Matrix element cuts from Sherpa samples have been implemented in MCFM. Figure 5.15 shows the mass-dependent QCD NLO K-factor, computed as the ratio between the differential cross sections from MCFM and SHERPA.

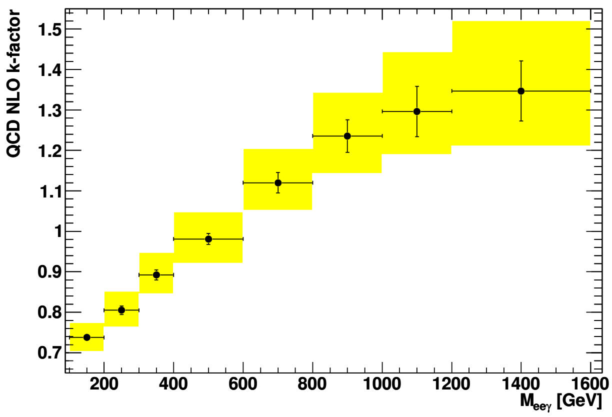

Figure 5.15: Ratio of MCFM to SHERPA differential cross sections with the high mass extension, as a function of $m_{ee\gamma}$

5.4.2 $Z + \text{jets}$ and $W + \text{jets}$ samples

The second important background is the $Z + \text{jets}$ process where Z decays in the electron channel and a jet fakes a high p_{T} photon. The $Z + \text{jets}$ and $W + \text{jets}$ backgrounds are generated with ALPGEN to generate matrix elements, JIMMY to describe multiple parton interactions and HERWIG to describe the remaining underlying event and parton showers. CTEQ6L1 [61] PDFs are used. Table 5.10 shows the MC samples used in the current study; the 1^{st} column lists the physics process and the 2^{nd} is the ATLAS Monte Carlo run number; the 3^{rd} column is the cross section time branching ratio reported by the generator; the 4^{th} column is the number of generated events and the last is the integrated luminosity $L_{\text{int}} = N_{\text{evt}}/(\sigma B)$.

Table 5.10: Monte Carlo $Z+$jets and $W+$jets background samples used for the study.

Process	Run number	σB [pb]	N_{evt} [k]	L_{int} [pb^{-1}]
$Z \to ee$ + 0 parton	107650	830.125	6169	7400
$Z \to ee$ + 1 parton	107651	166.238	1335	8000
$Z \to ee$ + 2 partons	107652	50.282	404	8000
$Z \to ee$ + 3 partons	107653	13.923	110	7900
$Z \to ee$ + 4 partons	107654	3.362	30	8900
$Z \to ee$ + 5 partons	107655	0.942	9	10600
$W \to e\nu$ + 0 parton	107680	8296	3456.5	417
$W \to e\nu$ + 1 parton	107681	1551.6	632.5	408
$W \to e\nu$ + 2 partons	107682	452.5	756	409
$W \to e\nu$ + 3 partons	107683	121.1	202	1669
$W \to e\nu$ + 4 partons	107684	30.4	52	1711
$W \to e\nu$ + 5 partons	107685	8.3	14	1687

Cross sections

The $Z+$jets and $W+$jets cross sections used are LO calculations normalized to inclusive NNLO taken from [71]. The uncertainty of the total cross section (excluding $W+0$ parton, which does not contribute) is 27.6% [72].

5.4.3 Diboson (WW, WZ, ZZ) samples

Diboson samples are generated with HERWIG with a lepton filter requiring at least one lepton with $|\eta| < 2.5$ and $p_{\text{T}} > 15$ GeV. Table 5.11 shows the MC samples used in the current study; the 1^{st} column lists the physics process and the 2^{nd} is the ATLAS Monte Carlo run number; the 3^{rd} and 4^{th} columns are the cross section time branching ratios reported by the generator (gen.) and calculated (cal.); the 5^{th} column is the number of generated events and the last is the integrated luminosity $L_{\text{int}} = N_{\text{evt}}/(\sigma B)$.

Table 5.11: Monte Carlo diboson (WW, WZ, ZZ) background samples used for the study.

Process	Run number	σB [pb] gen.	σB [pb] cal.	N_{evt} [k]	L_{int} [pb^{-1}]
WW	105985	11.49	17.460	250	14300
WZ	105987	3.481	5.430	250	45100
ZZ	105986	0.976	1.261	250	198300

Cross sections

The diboson cross sections used are the NLO calculations taken from [71]. The uncertainty on these cross sections is about 5%.

5.4.4 $t\bar{t}$ samples

$t\bar{t}$ background is generated with MC@NLO to generate matrix elements, and also JIMMY to describe multiple parton interactions and HERWIG to describe the remaining underlying event and parton showers. CTEQ6.6 PDFs are used. The top mass is set to 172.5 GeV. Table 5.12 shows the characteristics of the inclusive MC sample used in this study. In this sample, a filter is applied at the generator level to retain only events with a lepton (e or τ).

Table 5.12: Monte Carlo $t\bar{t}$ background sample used for the study.

Process	M_{ee} [GeV]	Run number	σB [pb] gen.	σB [pb] cal.	N_{evt} [k]	L_{int} [pb^{-1}]
$t\bar{t} \to \ell X$	–	105200	80.2	89.4	1000	11200
$t\bar{t} \to eeX$	30-150	115400	2.7104	3.0240	20	6490
$t\bar{t} \to eeX$	150-300	115401	0.31148	0.34669	20	57300
$t\bar{t} \to eeX$	300-450	115402	0.025219	0.028065	20	713000
$t\bar{t} \to eeX$	450-	115403	0.004321	0.00481	20	4160000

Cross sections

Cross section calculations for $t\bar{t}$ are performed at near-NNLO and described in references [73, 74, 75, 76]. A conservative uncertainty of 9.5% is assigned to this cross section. The generator is already NLO and so no correction for mass dependence is needed.

6

Electrons and photons in ATLAS

6.1 Particle Reconstruction

6.1.1 Electron reconstruction

Three algorithms are used to reconstruct electrons. A standard one, seeded by the EM cluster, is dedicated mostly to high p_T isolated electrons. The standard algorithm has the highest efficiency for the whole tracking η range and a wide range in E_T. A track-based algorithm was developed to find low p_T electrons and electrons in jets. Finally, a specific algorithm exists for forward electrons in the η range where tracking is not available. Because of the limited coverage of the tracking system, no track matching is required for forward electrons. All algorithms reconstruct the same "Electron" object. An overlap-removal procedure is also applied.

6.1.1.1 The calorimeter-seeded algorithm

This algorithm is seeded by an electromagnetic cluster, in the second sampling section of the EM calorimeter, with transverse energy above 2.5 GeV. For a reconstructed cluster, a match is searched for among all reconstructed tracks. The track must be matched to this cluster layer within a $\Delta\eta \times \Delta\phi = 0.05 \times 0.1$ window. If no track is found within a certain $\eta - \phi$ separation, the electron candidate is ignored. Priority is given to tracks with silicon hits over TRT-only tracks, where TRT-only tracks are required to have less than 4 silicon hits (Pixel+SCT). An exception is made for the latter case since η is not measured by the TRT barrel; the track-matching is only performed in ϕ for these tracks. The closest track in $\Delta R = \sqrt{(\Delta\eta)^2 + (\Delta\phi)^2}$ ($\Delta\phi$ in of TRT-only tracks) is kept as the electron track. Tracks without hits in the SCT or Pixel (TRT-only tracks) are considered as more likely to come from conversion. Both prompt electrons and converted photons have an electromagnetic cluster with a track pointing at it. Since calibration differs between electrons and photons, a new clustering step is needed after determination of the EM particle nature. For electrons in the barrel, a 3×7 cluster is built using the Sliding Window[1][77] procedure around the seed positions η_o and ϕ_o. The size in the ϕ direction is larger to accommodate electrons which undergo bremsstrahlung in the ID. In the end-caps, the electron cluster size is 5×5.

[1] The Sliding Window algorithm uses a fixed size cluster and looks for contiguous cells that fulfill certain requirements.

Because of this the electron container is significantly contaminated with converted photons at this point, but high efficiency is assured. The contamination will be dealt with later, when adding electron identification (see the Electron identification sub-section 6.2.1).

6.1.1.2 The track-based algorithm

This algorithm starts with a track that is extrapolated into the electromagnetic calorimeter. This allows to go lower in the seed E_{T}, compared to an EM cluster, which needs a higher threshold to reduce noise. However, the track multiplicity being much higher than the cluster multiplicity in ATLAS, strict preselection requirements on the track are necessary. Therefore, the track p_{T} must be higher than 2 GeV, the algorithm can handle tracks with as little p_{T} as 0.5 GeV, but to enhance the rejection of fakes 2 GeV is used as a lower limit. Also, due to the limited coverage of the transition radiation tracker (TRT), the track $|\eta|$ must be lower than 2. This is crucial for both of tracks preselection and reconstruction. The requirements also include at least 1 b-layer hit, 2 Pixel hits, 7 hits in silicon (Pixel+SCT), 20 hits in the TRT and 1 high-threshold hit in the TRT. The tracks passing these criteria are then extrapolated out to the electromagnetic calorimeter. An EM cluster is then built with the usual cluster size (i.e. 3×7 in the barrel, 5×5 in the end-caps), using the track impact position to the middle layer of the calorimeter as the cluster center. The cluster must have:

- $0.7 < \frac{E}{p} < 4$,
- $\frac{E_1^{cl}(3\times1)}{E^{cl}(core)} > 0.03$,
- and $\frac{E_3^{cl}(3\times3)}{E^{cl}(core)} < 0.5$.

where $E_1^{cl}(3\times1)$ is the energy in 3×1 cells at the center of the front layer (strips), $E_3^{cl}(3\times3)$ is the energy in 3×3 cells at the center of the back layer, and $E^{cl}(core)$ is the sum of layer energies at the core of the EM shower in 3×3 cells in the presampler, 15×3 cells in the front layer, 5×5 cells in the middle layer and 3×5 cells in the back layer.

6.1.1.3 Forward electrons

Due to the tracking absence in ATLAS at $|\eta|$ higher than 2.5, track matching (that is what distinguishes an electron from a photon) to an EM cluster is not applicable here. Physics processes do not set such limit on electrons η, i.e. electrons can come out from any physical process with any η values. Therefore, a third algorithm, the so-called topological clustering algorithm[77], is available for the reconstruction of forward electrons in the region $2.5 < |\eta| < 4.9$. These objects are referred to as forward electrons. In this case, instead of a fixed-size cluster building, a seed cell with an energy significance, i.e signal-to-noise ratio, above a certain threshold is found and neighbouring cells are added to it, given that their significance is above a threshold lower than the seed one. A splitting procedure is implemented to find local maxima and create new topological clusters if needed. With this procedure, the clusters can have a different number of cells and size. Noise suppression is performed during cluster building. The energy of the cluster is computed as the sum of the cluster cells and the direction by their barycenter. A forward electron candidate is reconstructed if a cluster with $E_{\mathrm{T}} > 5$ GeV is found. In order to identify the electron over hadronic background, strict cuts on the shower shape and cluster moments are applied.

6.1.1.4 Electron reconstruction systematic uncertainty

Studies, done by EGamma performance group, indicate that the Monte Carlo reconstruction efficiencies can be used in data with a systematic uncertainty of 1.5%.

6.1.2 Photon reconstruction

The reconstruction of photons follows in its main aspects that of electrons; both objects are treated similarly within an overall reconstruction algorithm. Photons can be classified into two main categories: converted and unconverted photons. Photons reconstructed as converted are characterized by the presence of at least one track matching an electromagnetic cluster originating from a vertex inside the tracker volume, whereas unconverted photons do not have such a matched track. There is an underlying similarity between electrons and converted photons due to the presence of tracks in both objects; this results in a certain amount of ambiguity between the two [78].

6.1.2.1 Reconstruction of unconverted photons

Any cluster that does not have any track (primary or originating from conversion candidate vertices) matched to it, is considered to be an unconverted photon candidate. A generic calibration and some basic corrections are applied in order to compute the cluster energy [79].

Unconverted photon candidates have been identified, at this stage of reconstruction. A significant fraction of unconverted photons (9% in the $H \to \gamma\gamma$ simulated sample) have also been reconstructed as electrons, due to tracks with normally $p_{\mathrm{T}}< 2$ GeV that have been erroneously assigned to electromagnetic clusters.

6.1.2.2 Reconstruction of converted photons

The reconstruction of converted photons includes the initial reconstruction of the conversion vertices inside the tracker, followed by the reconstruction and association of conversion vertices to an electromagnetic calorimeter cluster [80]. The conversion vertices reconstructed by the ID are classified depending on the number of electron tracks assigned to them. *Double-track conversion vertex*: conversion vertex with two tracks which is reconstructed by performing a constrained vertex fit using the track parameters of the two participating electrons under the condition that the photon is a massless particle. *Single-track conversion vertex*: conversion vertices with one electron track assigned to them, this is typically the case when one of the two produced electron tracks failed to be reconstructed either because it is very soft (asymmetric conversions where one of the two tracks has $p_{\mathrm{T}} < 0.5$ GeV), or when the two tracks are very close to each other (symmetric conversions that happen late inside the tracker producing two high-p_{T} tracks) and they can not be adequately separated. In case of conversion vertex with single electron track, a vertex fit can not be performed and the conversion vertex is placed at the location of the first measurement of the participating track, and the original converted photon momentum vector can not be determined.

Almost all converted photons will also end up inside the reconstructed electron collection. This fact is remedied by verifying whether any reconstructed conversion vertex candidate can be matched to a cluster. This matching procedure varies according to the characteristics of the conversion vertex candidate associated to the cluster:

- Single-track conversion vertex candidates associated to the cluster. The track is extrapolated to the second calorimeter sampling from its last measurement. If the impact point on the calorimeter is within a certain window in (η, ϕ) from the cluster center in that sampling, the conversion vertex candidate is considered as matched to that cluster.

- Double-track conversion vertex candidates associated to the cluster, where:

  – one of the two track momenta is much smaller (factor of 4) compared to the other. In this case the original converted photon direction is reconstructed by the two electron track parameters at the vertex returned by the constrained vertex fit. A straight line extrapolation is then performed from the conversion vertex position to the second sampling of the electromagnetic calorimeter. If the impact point is within a certain window in (η, ϕ) from the cluster center in this sampling, the conversion vertex candidate is considered as matched to that cluster.

  – the two track momenta are not very much different (less than a factor of 4) from each other. Each track is extrapolated individually to the calorimeter second sampling, as in the case of the single-track conversion vertex candidates. If both then are matched to the same cluster, the conversion vertex candidate is considered as matched to that cluster too.

A window of size 0.05 on each side of the impact point in η and ϕ is used in all track-to-cluster matches above. It is extended to 0.1 in ϕ on the side where the bremsstralung losses are expected during the track extrapolation.

In case of electromagnetic showers, more than one conversion vertex can exist within a small (η, ϕ) region, thus all of them may point towards the same cluster. In this case all matched conversion vertex candidates are retained and ordered according to the following criteria: double-track conversion candidates have precedence over single-track ones; among double-track conversion candidates, the one with the smallest radial position of the corresponding vertex has precedence over the rest; among single-track conversion candidates, the one with the smallest radial position of the corresponding vertex has precedence over the rest.

All photons (converted and unconverted) that have been reconstructed as electrons need to be recovered. A dedicated procedure, developed by EGamma performance group, is applied after the reconstruction of electrons has been completed.

6.1.3 Electrons and photons authorship

The electron objects created with all algorithms are stored in a common container inside the data file. This is also true for photons. An author bit-word saves the information concerning the algorithm used for a given object. The author values are defined as:

- author = 0: the author of this object is unknown,

- author = 1: electron candidate reconstructed by the calorimeter-seeded algorithm,

- author = 2: soft electron candidate reconstructed by the track-based algorithm,

- author = 3: electron candidate reconstructed by both the calorimeter-seeded and the track-based algorithms,

- author = 4: photon candidate reconstructed by the calorimeter-seeded (standard) algorithm,
- author = 8: forward electron candidate reconstructed by the topological clustering algorithm,
- author = 16: photon candidate that is duplicated with an electron.

6.2 Particle Identification

6.2.1 Electron identification

Identification cuts are needed to reject background more efficiently. IsEM is a flag option that is used for electron and photon identification. It can be set, checking every electron past a selection criteria and then for each return either 0 or 1, for accepted or rejected. The isEM flag can be set to one of three standard states: loose, medium, or tight, with increasing background rejection power. These electron identification cuts are made using rectangular cuts over tracking and shower shape variables that allow a good separation between the isolated electron signal and the hadronic background. The cuts values are optimised in different cluster middle layer η and in cluster E_{T} bins. The η and E_{T} bins used for the identification cuts are shown in Table 6.1; a cut value is defined for each of the 110 combinations. For 2010 data-taking, the list of cuts was optimised to make them more robust for early data- taking [81]. Each cut is applied independently of the others and its result is saved as a single bit in a bit-word, unique for each electron. The three predefined sets of cuts are bit masks which are then compared to the bit-word.

Table 6.1: Identification cuts η and E_{T} bin definitions

η	E_{T} (GeV)
< 0.1	< 5
0.1−0.6	5−10
0.6−0.8	10−15
0.8−1.15	15−20
1.15−1.37	20−30
1.37−1.52	30−40
1.52−1.81	40−50
1.81−2.01	50−60
2.01−2.37	60−70
2.37−2.47	70−80
−	> 80

- *The loose selection:* is a basic selection that includes cuts on shower-shape variables in the middle layer of the EM calorimeter, together with hadronic leakage[2]. The loose selection discriminating variables are[3]:
  - η_{cl}: calorimeter cluster pseudorapidity ($0 < |\eta| \leq 2.47$),
  - R_{had}: ratio of E_{T} of the hadronic calorimeter to that of the EM calorimeter (for $|\eta| < 0.8$ and $|\eta| > 1.37$),

[2]The hadronic leakage refers to the fraction of the cluster energy deposited in the hadronic calorimeter layers beyond the EM calorimeter

[3]The cluster sizes introduced here are in number of cells in η or ϕ.

- R_{had1}: like R_{had} but using only the first layer of the hadronic calorimeter (for $0.8 < |\eta| < 1.37$),
- R_η: ratio in η of energy deposit in 3×7 cluster to that in 7×7 cluster in the middle layer of the EM calorimeter,
- $w_{\eta 2}$: lateral cluster width in η in the middle layer of the EM calorimeter, calculated as: $\sqrt{\frac{\Sigma E_i \times \eta_i^2}{\Sigma E_i} - \left(\frac{\Sigma E_i \times \eta_i^2}{\Sigma E_i}\right)^2}$.

- *The medium selection:* is the loose one plus some additional shower shape cuts on the front layer. The additional variables in the medium selection are:
  - W_{stot}: total cluster width in the front layer which is defined as: $\sqrt{\frac{\Sigma E_i \times (i - i_{max})^2}{\Sigma E_i}}$, where i_{max} is the index of the most energetic strip,
  - E_{ratio}: ratio of the difference between the largest and second largest energy deposit to the sum of these energies in the front layer,
  - n_{pixel}: number of hits in the Pixel detector,
  - $n_{silicon}$: number of hits in the Pixel and the SCT detectors,
  - d_0: transverse impact parameter with respect to the beam position,
  - $\Delta\eta$: track-matching $\Delta\eta$ between the cluster front layer and the track.

- *The tight selection:* is medium one plus some additional cuts. It makes use of the Pixel $b-$layer for conversions/real electron separation and also makes use of the TRT for electron/hadron separation. The additional variables in the tight selection are:
  - $n_{b-layer}$: number of hits in the $b-$layer of the Pixel detector,
  - E/p: ratio of cluster energy to the track momentum,
  - n_{TRT}: number of hits in the TRT detector,
  - n_{hTR}: number of high-threshold hits to the total number of hits in the TRT detector,
  - $\Delta\phi$: track-matching $\Delta\phi$ between the cluster middle layer and the track.

6.2.1.1 Identification efficiency

In the current analysis, the medium electron selection is used. To further reject fakes, the electron track should have a hit in b-layer if expected[4]. In 2011 analysis, an additional isolation cut on the leading electron is added for further rejection of QCD background (see section 6.3).

The measurement of the η dependent medium identification efficiencies is performed by the EGamma group [12]. This measurement is done by the tag-and-probe method using the $Z \to e^+e^-$ as well as the $W \to e\nu$ events from data. In tag-and-probe method: a clean sample of $Z \to e^+e^-$ events, for instance, is selected and using one good electron (the so-called 'tag'), and measuring the efficiency of interest testing the second electron (the so-called probe) from the Z boson decay. If there are more than two electrons after preselection in the event, all possible tag-and-probe pairs are used. The presence of jets faking electrons under the Z-peak in data would result in a mis-measurement of the

[4]The expression if expected is mentioned here, because from time to time there exists some dead module

efficiencies and cannot be neglected. The predicted jet background is subtracted from the probes, separately for *medium* probes and for those passing the additional requirements. This subtraction is done using a sideband subtraction method in which the probes from events in the sidebands (dielectron invariant mass within 60-80 GeV and 100-120 GeV) are required to be from same sign tag-and-probe pairs, while the probes in the middle band (dielectron invariant mass 80-100 GeV) are only considered if they come from opposite signed tag-and-probe pairs. This charge requirement reduces the signal contamination in the sidebands. The background is then linearly interpolated between the lower and upper sidebands. For Monte Carlo measurements, truth matching is applied to find the electrons from the Z boson decay, including electrons from photons radiated by the Z. Scale factors are calculated by taking the ratio of efficiencies measured in data to efficiencies measured in MC. They are used to correct efficiencies in simulated MC samples.

- For the 2010 data, the measurements had been carried out separately in 8 bins in η and 6 bins in E_{T} for medium identification by EGamma group. The η-dependent scale factors are given in table 6.2. The exotic di-electron subgroup extended this tag-and-probe study to measure the efficiencies and corresponding scale factors for *medium* identified electrons to pass the b-layer hit requirement using the $Z \to e^+e^-$ events. Table 6.3 shows the measured efficiencies and scale factors for the b-layer hit with respect to *medium*. The systematic uncertainty is conservatively estimated to be $\pm 2\%$ as recommended by EGamma group [12].

Table 6.2: Scale factors for the *medium* identification efficiencies (plateau values), determined by $Z \to e^+e^-$ as well as $W \to e\nu$ tag-and-probe on both data and MC. Uncertainties listed include statistical and systematic uncertainties [12].

η bin	scale factor	η bin	scale factor
[-2.47,-2.01]	0.983 ± 0.008	[0,0.8]	0.979 ± 0.006
[-2.01,-1.52]	0.981 ± 0.008	[0.8,1.37]	0.980 ± 0.008
[-1.37,-0.8]	0.979 ± 0.007	[1.52,2.01]	0.987 ± 0.007
[-0.8,0.0]	0.976 ± 0.006	[2.01,2.47]	0.979 ± 0.009

Table 6.3: Efficiencies for *medium* electrons to pass the b-layer hit requirement, determined with $Z \to e^+e^-$ tag-and-probe on data and MC, and the corresponding data/MC scale factors. The quoted uncertainties are statistical and systematic [8].

η bin	$\varepsilon_{b-layer(data)}$	$\varepsilon_{b-layer(MC)}$	$\varepsilon_{b-layer(data)}/\varepsilon_{b-layer(MC)}$
[-2.47,-2.01]	0.908 ± 0.023	0.901 ± 0.001	1.007 ± 0.026
[-2.01,-1.52]	0.948 ± 0.021	0.947 ± 0.001	1.001 ± 0.023
[-1.37,-0.8]	0.975 ± 0.020	0.975 ± 0.000	1.001 ± 0.023
[-0.8,0.0]	0.985 ± 0.020	0.977 ± 0.000	1.009 ± 0.021
[0,0.8]	0.983 ± 0.020	0.977 ± 0.000	1.005 ± 0.021
[0.8,1.37]	0.985 ± 0.020	0.977 ± 0.000	1.008 ± 0.021
[1.52,2.01]	0.958 ± 0.021	0.948 ± 0.001	1.011 ± 0.022
[2.01,2.47]	0.922 ± 0.023	0.899 ± 0.001	1.026 ± 0.026

6.2.2 Photon identification

Photon identification in ATLAS relies on rectangular cuts using calorimetric variables which deliver good separation between isolated photons and fake signatures from QCD jets. There are two sets of standard cuts, loose and tight, that have been defined by EGamma performance group. Both predefined sets of cuts are bit masks which are then compared to the isEM bit-word.

- *The loose selection:* for trigger purposes, loose photons share a common set of cuts and cut thresholds with loose electrons [81]. As in loose electron selection case, the loose photon selection includes cuts on shower-shape variables in the middle layer of the EM calorimeter, together with hadronic leakage. This subset of discriminating variables shows relatively small differences for unconverted and converted photons, so using only these variables in the loose selection keeps the two efficiencies for the two types of photon as similar as possible. Because of the sensitivity to the exact amount of material in front of the calorimeter and of the large cross-talk between neighboring cells in the EM calorimeter front layer (strip layer), the discriminating variables obtained from this calorimeter section are not considered robust enough to be used for triggering purposes, especially at the beginning of the LHC data taking. The loose photon selection variables are:
  - R_{had}: ratio of E_{T} of the hadronic calorimeter to that of the EM calorimeter (for $|\eta| < 0.8$ and $|\eta| > 1.37$),
  - R_{had_1}: like R_{had} but using only the first layer of the hadronic calorimeter (for $0.8 < |\eta| < 1.37$),
  - R_η: ratio in η of energy deposit in 3×7 cluster to that in 7×7 cluster in the middle layer of the EM calorimeter,
  - $w_{\eta 2}$: lateral cluster width in η in the middle layer of the EM calorimeter.

- *The tight selection:* include the loose selection plus calorimeter and additional shower shape cuts on the front layer. The additional variables in the tight selection are:
  - η_{cl}: acceptance in η range $|\eta| \leq 2.37$ and $1.37 < |\eta| < 1.52$ excluded (calorimeter crack region),
  - R_ϕ: ratio in ϕ of energy deposit in 3×3 cluster to that in 3×7 cluster in the middle layer of the EM calorimeter,
  - w_{stot}: total lateral shower width in the front layer,
  - w_{s3}: lateral shower width for three strips around the maximum strip,
  - F_{side}: fraction of energy outside core of three central strips but within seven strips,
  - ΔE: difference between the energy associated with the second maximum in the strip layer, and the energy reconstructed in the strip with the minimal value found between the first and second maxima,
  - E_{ratio}: ratio of the energy difference associated with the largest and second largest energy deposits over the sum of these energies.

6.3 Electrons and photons isolation

An additional isolation cut can be applied separately from the standard identification cuts to add more flexibility for analysis needs. The motivation for EM calorimeter isolation cut is to remove efficiently the remaining jet background. The calorimeter isolation variables, EtconeXX, are calculated as a simple sum of calorimeter cell energies of a cone of certain radius around the cluster barycenter, excluding a 5×7 grid of cells in the center of the cone. Two effects, at least, may modify this energy sum:

- Some of the electron (or photon) energy may leak outside this central core, causing the isolation energy to grow as a function of E_{T}.
- Soft energy deposits from pile-up interactions will change the isolation energy depending on the activity of the current event (in-time pile-up) and/or the previous events (out-of-time pile-up).

  The EGamma performance group provides a tool [82] to correct the isolation energy for these effects.

6.4 Cleaning cuts

Any noisy or sporadic noisy channel can sometimes produce a signal with transverse momentum greater than 2.5 GeV and give rise to a sliding window cluster, whose energy is mainly contained in a single cell, producing a fake electron or photon. These channels are masked at the reconstruction level according to a dedicated database for noisy cells [78]. In addition any new problematic channels that may appear and pollute the data before they are identified and tagged for masking, additional cleaning cuts are also applied at the reconstruction level requiring that the fractions of the reconstructed energy in the presampler and in each layer of the electromagnetic calorimeter do not exceed a threshold respectively of 0.9, 0.9, 0.98 and 0.8 [78]. An event by event flag, larError, is used to reject events with calorimeter noise bursts and data integrity errors. larError flag is set to 0, 1, or 2:

- larError ==0 means this is a good event.
- larError ==1 means there is noise burst and the event should be rejected.
- larError ==2 means data integrity errors are present and the event should be rejected.

In addition, on the object level, there is an object quality flag that is used to reject bad quality clusters. This object quality flag is a 32-bit word. For each electron or photon all the cells of the cluster are analyzed and if any important problem is found, then the corresponding bit is set to 1.

Dealing with LAr hardware problems in Monte Carlo to compensate for loss in acceptance is done by using the so-called checkOQ tool provided by the `ATLAS` EGamma performance group [83]. The treatment in 2010 data analysis is different from 2011 data taking and will be described for each case in section 7.2.5 for 2010 data and section 8.2.3 for 2011 data.

6.5 Jet $\rightarrow \gamma$ fake rate

In this section we study the probability of a jet to be misidentified as a photon. The photon fake rate is measured in two steps:

- firstly, the raw fake rate is estimated as the fraction of jets that pass the photon identification cuts,
- the data from which we measure the photon fake rate contain true prompt photons that were classified as jets. These photons pass the selection criteria with high efficiency, thus the raw fake rate mentioned above overestimates the probability of QCD jets faking photons. The prompt photon contamination has to be estimated and then subtracted out from the jet sample.

6.5.1 Raw fake rate (f_{raw})

The QCD data sample from the `JetTauEtMiss` physics stream is used in this fake rate study. The data from run 179710 (start of period D) to run 183963 (period H) makes about 884 pb^{-1} of 2011 data. No trigger requirement is asked to avoid biasing our measurement. The raw fake rate is defined as the probability that a jet matches a photon candidate. Starting from unskimmed `SMWZ D3PDs` data from `JetTauEtMiss` physics stream the event is then asked to pass the following cuts:

- the event is in the Good Runs List (`WZjets` GRL), to ensure sub-detectors involved in the analysis were ready and have no serious hardware problem (see subsection 8.1.1),
- the event has to pass LAr cleaning (see subsection 6.4),
- the event has a primary vertex with at least 3 tracks,
- $E_{\mathrm{T}}^{\mathrm{miss}}$ cleaning: the event is removed if it contains a BadMedium jet with p_{T} greater than 20 GeV as recommended by the JetEtmiss performance group [84],
- the event must have at least one jet with the jet selection mentioned below.

Then each jet is asked to pass the following selection:

- reconstructed with the AntiK_T reconstruction algorithm with radius R=0.4,
- $|\eta| < 2.8$ and $p_{\mathrm{T}} > 20$ GeV,
- pass LArHole[5] cut to avoid bad calorimeter region edge effects [85],
- the jet is removed if it is assigned as BadMedium or Ugly [84].

Photon candidates are selected using the standard tight selection defined in sub-section 6.2.2 with requiring the so-called ambiguity resolver (AR) bit which is used to differentiate electrons from photons. In addition, the photon should be isolated (see subsection 6.3). Therefore jet $\rightarrow \gamma$ fake rate was measured for TightAR+isolation photon selection which is used in analysing 2011 dataset. A jet is considered to be a photon candidate if it matches the photon within $\Delta R < 0.15$. The choice of this ΔR is motivated by figure 6.1 which shows the ΔR distribution between jets and photons. Therefore, for N_j jets considered, if there were N_γ^0 photon matches, the jet to photon raw fake rate is defined as:

$$f_{raw} = \frac{N_\gamma^0}{N_j} \quad . \tag{6.1}$$

Figure 6.2 shows the raw fake rates, f_{raw}, measured as a function of the jet p_{T} for TightAR isolated photons. A coarser binning is used at high p_{T} due to a lack of statistics.

[5]LArHole refers to 6 missing front-end boards (FEBs) in the LAr Calorimeter that were lost during period E and were recovered later (before starting period K) during 2011 data taking

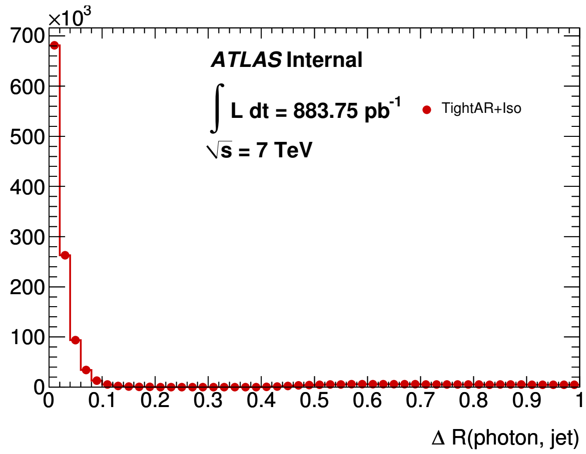

Figure 6.1: ΔR distribution between jets and photons.

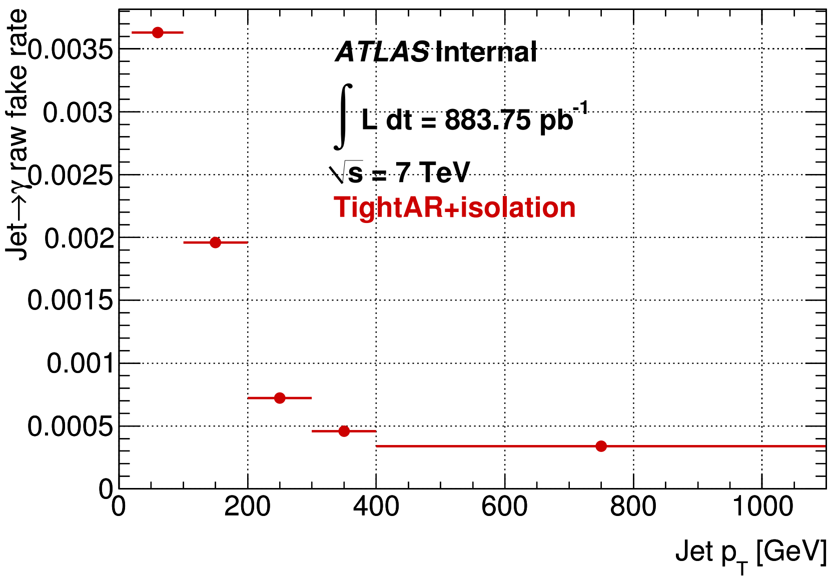

Figure 6.2: Raw jet $\to \gamma$ fake rate as a function of jet p_{T} for TightAR+Isolation photons.

6.5.2 Real photon subtraction

Since the QCD jets sample is contaminated with real photons, the fake rate needs to be corrected. The number of observed photons, N_γ^o, can be sub-divided into: N_γ^{real}, the number of real prompt photons, and N_γ^{fake} the number of faked photons. In order to measure N_γ^{real} in the sample of fake photon candidates N_γ^0, we rely on the converted photons that were recovered with a dedicated algorithm introduced by EGamma group, considering only double track converted photons. Of course not all real photons are converted ones, and to get the total number of real photons N_γ^{real}, the number of double track converted photons N_γ^c has to be divided by the double track conversion probability $P_{conv.}$. Hence,

$$N_\gamma^{real} = \frac{N_\gamma^c}{P_{conv.}} \quad , \tag{6.2}$$

and the corrected (final) fake rate, $f_{corr.}$, is given by:

$$
\begin{aligned}
f_{corr.} &= \frac{N_\gamma^{fake}}{N_j} \\
&= \frac{N_\gamma^o - N_\gamma^{real}}{N_j} \\
&= \frac{N_\gamma^o - \frac{N_\gamma^c}{P_{conv.}}}{N_j} \quad .
\end{aligned} \tag{6.3}
$$

6.5.2.1 Estimation of the number of converted photons (N_γ^c)

To estimate the number of converted photons we use 2 Monte Carlo templates:

- Jet template: using PYTHIA Monte Carlo $pp \rightarrow \gamma + jet$ samples which were generated with a lower cut on photon p_{T} (RunNumbers 108081 to 108084 and 108087, see table 6.4 for more details). The reconstructed photons that pass the following selection are used to define jet template:
  - author equal 4 or 16,
  - $|\eta| < 2.37$ and the crack region ($1.37 < |\eta| < 1.52$) is removed,
  - $p_{\mathrm{T}} > 20$ GeV,
  - not reconstructed in bad calorimeter regions (good Object Quality).
  - pass LArHole (to avoid missing FEBs problem in some data in case we compare this template with real data) and LAr cleaning cuts (no noise burst in the calorimeter).
  - invert photon identification cut: the photon has to fail the hadronic leakage (the so-called HADLEAKETA_PHOTONLOOSE) cut or fail the calorimeter middle layer (the so-called CALOMIDDLE_PHOTONLOOSE) cut to almost ensure it is a jet and not a photon[6].

Table 6.4: Monte Carlo PYTHIA $pp \rightarrow \gamma + jet$ samples used for the jet-to-photon fake rate study.

photon lower p_{T} [GeV]	Run number	σB [pb]	filter efficiency	N_{evt} [k]	L_{int} [pb^{-1}]
17	108087	2.2612×10^5	0.46145	1000	9.5838
35	108081	1.7310×10^4	0.60442	1000	95.7936
70	108082	1.5212×10^3	0.66279	1000	991.831
140	108083	83.547	0.79786	1000	15001.81
280	108084	3.2537	0.85577	1000	359141.4

- Photon template: using the same Monte Carlo samples as for jet templates (listed in table), and selecting reconstructed photons that pass the following selection:
  - author equal 4 or 16,
  - $|\eta| < 2.37$ and the crack region ($1.37 < |\eta| < 1.52$) is removed,
  - $p_{\mathrm{T}} > 12$ GeV, this cut is selected to avoid bias in the fake rate measurement since a 20 GeV cut is used to cut on the jet p_{T}.

[6]For the photon identification cuts definitions, see section 6.2.2

- not reconstructed in bad calorimeter regions (good Object Quality),
- pass LArHole and LAr cleaning cuts,
- pass the photon identification TightAR selection,
- on top of photon identification cut, the photon has be isolated, to estimate the number of converted photons in our TightAR+isolation sample.

Figure 6.3 shows the Monte Carlo templates which are used to estimate the number of photons and the number of jets in our double track converted data sample. This templates represent the ratio between the sum of the conversion tracks transverse momentum, $\Sigma\ p_{\mathrm{T}track}$, and the matched photon cluster transverse momentum $p_{\mathrm{T}cl}$. The photon template shape varies with the photon p_{T} range while the jet template looks similar for all Monte Carlo samples. In figure 6.3 the jet template is shown in blue while the photon templates are shown in pink, light brown, brown and red for 20-50, 50-100, 100-200 and greater than 200 GeV photon p_{T}ranges, respectively[7]. The jet and photon templates are then normalized to data to estimate N_{γ}^{c} and the number of jets N_{jet}^{c} in the double track photon conversion data sample. Figure 6.4 shows the photon and jet template fit to data where data is shown in black and the fit of all templates is shown in green.

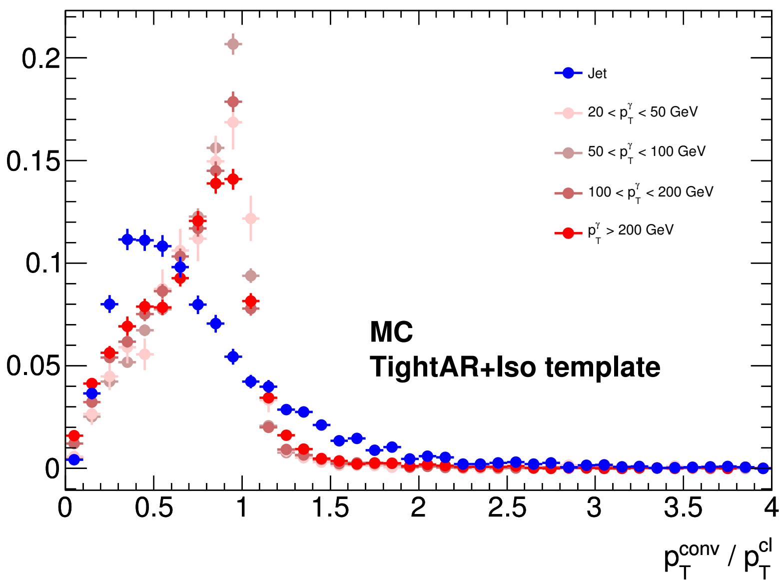

Figure 6.3: Ratio of the sum of the p_{T} of the conversion tracks over the photon cluster p_{T} for jet template (in blue) and 20-50 GeV (pink), 50-100 GeV (light brown), 100-200 GeV(brown), and greater than 200 GeV (red) photon templates for TightAR isolated photons

To ensure a good photon purity in data, we consider only converted photons if they have 0.8< $\Sigma\ p_{\mathrm{T}track}/\ p_{\mathrm{T}cl}$ <1.2. Then the normalized p_{T} distribution of these photons is scaled to the number of double track converted photons N_{γ}^{c} that had been estimated via the template fit.

Figures 6.5(a), and 6.5(b) show the p_{T} distributions of the jets that are matched to converted photons (photons that have 0.8< $\Sigma\ p_{\mathrm{T}track}/\ p_{\mathrm{T}cl}$ <1.2) before (in blue) and after scaling to the total number of double track converted photons N_{γ}^{c} (in dark red, in linear and log scale respectively. These jets are considered to be actually real converted

[7]Templates built with the ratio of vector sum of the conversion tracks momentum over the photon cluster energy, $\Sigma\ p_{track}/E_{cl}$, look similar to that of $\Sigma\ p_{\mathrm{T}track}/\ p_{\mathrm{T}cl}$ templates

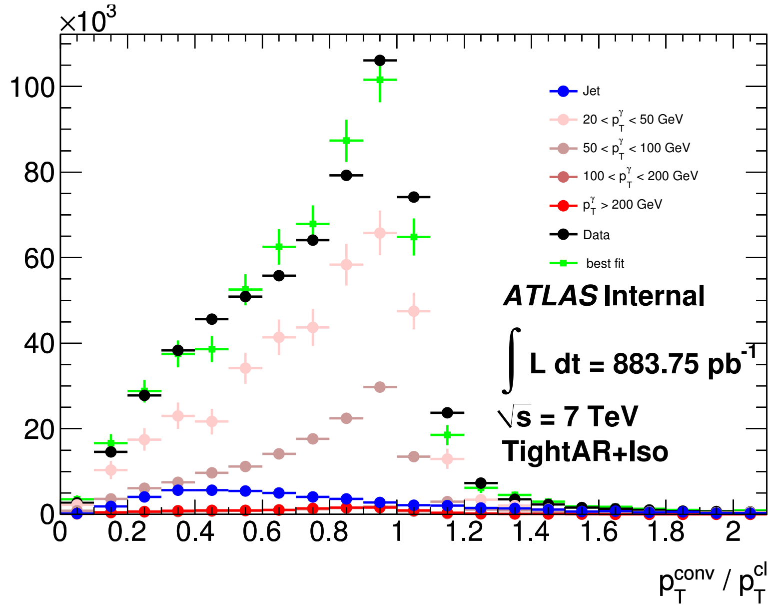

Figure 6.4: Template fit to data for TightAR isolated photons.

photons, N_γ^c, in our multi-jet data sample that we use to estimate the jet to photon fake rate.

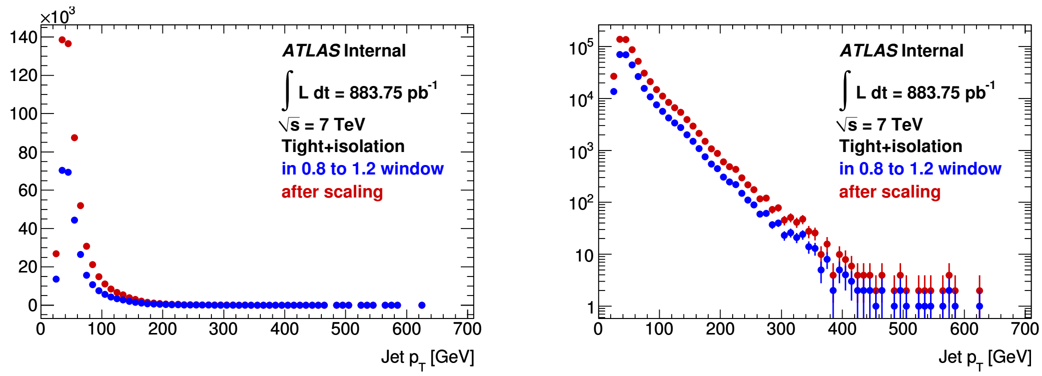

(a) (b)

Figure 6.5: p_{T} distributions of jets matched to photons that have 0.8< $\Sigma\, p_{\mathrm{T}track}/\, p_{\mathrm{T}cl}$ <1.2 before (in blue) and after scaling to the total number of double track converted photons N_γ^c (in dark red): (a) in linear and (b) in log scales.

6.5.2.2 Estimation of the conversion probability ($P_{conv.}$)

The next step is to determine the photon conversion probability, $P_{conv.}$. The conversion probability is determined from data. Photons in data are required to pass the following set of cuts:

- photon has author equal 4 or 16 (see section 6.1.3),
- photon has $|\eta| < 2.37$ and the crack region ($1.37 < |\eta| < 1.52$) is removed,
- has p_{T} > 12 GeV,

- not reconstructed in bad calorimeter regions (good Object Quality),
- pass LArHole and LAr cleaning cuts,
- photon has to pass one of the TightAR identification,
- on top of photon identification cut photon has be isolated for better background rejection.

Let $N_{tightIso}$ be the numbers of photons that pass TightAR+isolation selection. Then, the conversion probability is given by:

$$P_{conv.}^{tightIso} = \frac{N_{tightIso}^{c} - N_{jets}^{c}}{N_{tightIso} - N_{jets}} \tag{6.4}$$

where $N_{tightIso}^{c}$ (N_{jets}^{c}) is the number of converted photons (jets) and N_{jets} is the total number of jets in the data sample. The estimation of the total number of jets in the data sample used to measure photon conversion probability N_{jets} is not straightforward and can be estimated from N_{jets}^{c} by dividing by the jet double track conversion probability $P_{conv.}^{jet}$. The jet conversion probability $P_{conv.}^{jet}$ could be determined from the same dataset with a photon selection similar to the one used for photon conversion probability above but with inverted photon identification cuts: the photon has to fail the hadronic leakage (the so-called HADLEAKETA_PHOTONLOOSE) cut or fail the calorimeter middle layer (the so-called CALOMIDDLE_PHOTONLOOSE) cut to ensure it is almost a jet and not a photon. Figure 6.6 shows the jet double track conversion probability as a function of photon p_{T}, while figure 6.7 shows the jet (photon with inverted ID cuts) p_{T} spectrum after dividing by the jet double track conversion probability N_{jets}. The data points in jet double track conversion probability shown in figure 6.6 is fitted with a simple exponential function $p_0 - p_1 \times exp[-p_2 \times p_{\mathrm{T}}\gamma]$ where the parameters p_0, p_1 and p_2 are determined from the fit to be 0.807±0.0004, 1.081±0.002 and 0.0634±0.0002 respectively, to get rid of the discontinuities arising from the large statistical fluctuation at high p_{T}.

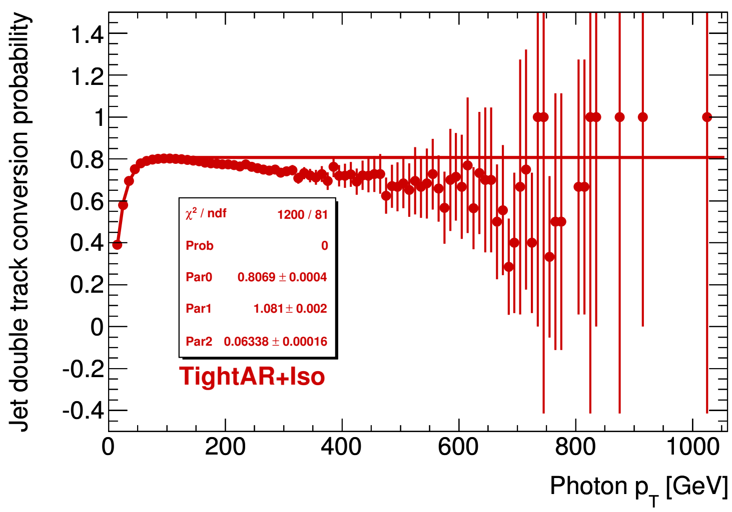

Figure 6.6: Double track jet conversion probability as a function of photon p_{T}.

Then the photon conversion probability as a function of photon p_{T} can be estimated from equation 6.4. Figure 6.8 shows the photon double track conversion probability

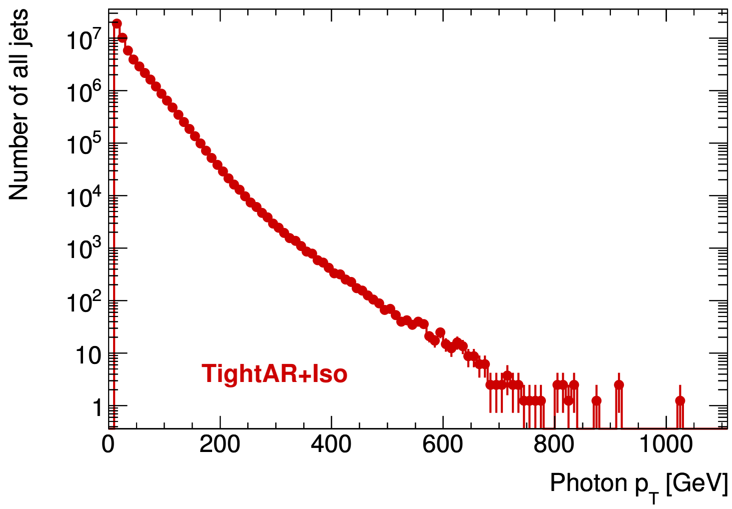

Figure 6.7: p_{T} distribution of photon failing inverted identification cut after dividing by the jet conversion probability N_{jets}.

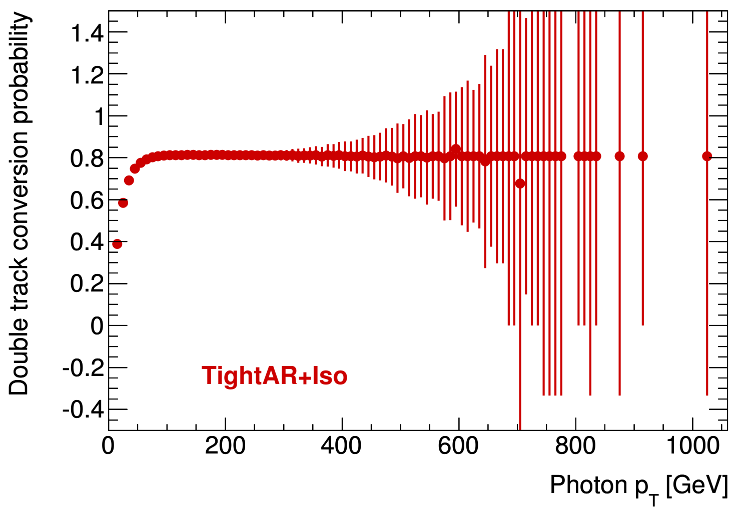

Figure 6.8: Double track photon conversion probability as a function of photon p_{T}.

$P^{tight+Iso}_{conv.}$ as a function of photon p_{T}.

Since the photon fake rate is measured as a function of jet p_{T}, the photon conversion probability must be measured as a function of jet p_{T} as well. Figure 6.9 shows the photon p_{T} versus jet p_{T} for TightAR+isolation photon selection. The profile of this 2D histogram gives the mean value of the jet p_{T} for each photon p_{T} bin. Using this profile, the conversion probability, estimated above as a function of photon p_{T}, can be mapped into jet p_{T}. Moreover, the uncertainty in the profile around each point defines the spread of jet p_{T} around the average value in the 2D original histogram. Figure 6.10 show these profiles of jet p_{T} w.r.t. photon p_{T} in our photon samples.

Using the jet p_{T} profiles the conversion probability can be estimated as a function of jet p_{T}. Figure 6.11 shows the photon double track conversion probability as a function of jet p_{T} that were measured in data. The data points in the photon double track conversion probability is fitted with the function $p_0 - p_1 \times exp[-p_2 \times p_{T\,jet}]$ where the

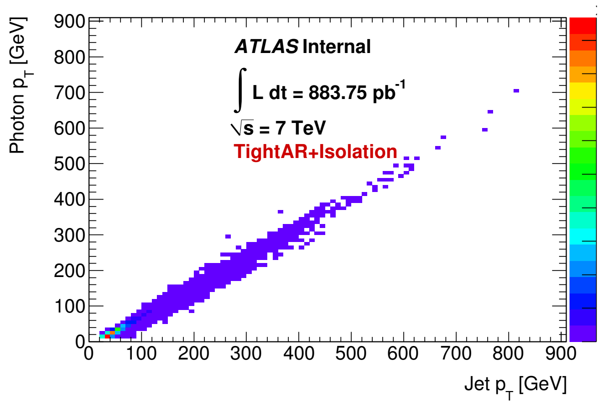

Figure 6.9: 2D-plot of jet p_{T} versus TightAR isolated photon p_{T}.

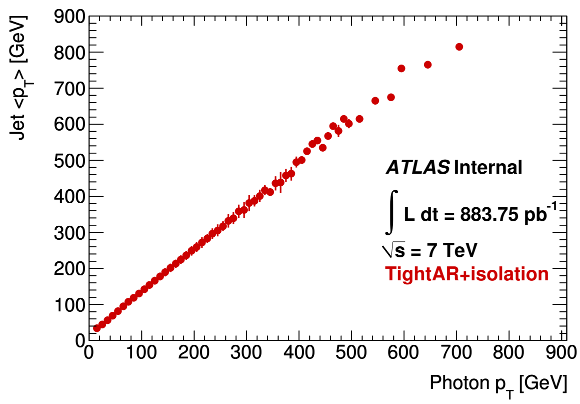

Figure 6.10: Profile of the jet p_{T} as a function of TightAR isolated photon p_{T}.

parameters p_0, p_1 and p_2 are determined from the fit to be 0.8131±0.001, 2.166±0.752 and 0.04965±0.00482 respectively.

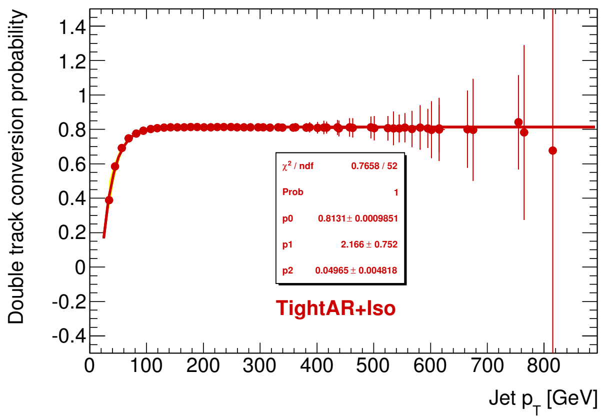

Figure 6.11: Photon double track conversion probability as a function of jet p_{T} as measured using 883.75 pb^{-1} of the 2011 data.

6.5.2.3 Estimation the number of real photons in the multi-jet QCD sample (N_γ^{real})

Now the number of real photons can be determined, see equation 6.2, simply by dividing the jet matched to converted photons shown in figures 6.5(a) and 6.5(b), see sub-section 6.5.2.1, by the photon double track conversion probability fit function shown in figure 6.11 and mentioned above. Figure 6.12 shows the resulting plot for the jets that are matched to real photons which are considered to be the real photons, N_γ^{real}, in the multi-jets QCD sample that we use to estimate the jet to photon fake rate.

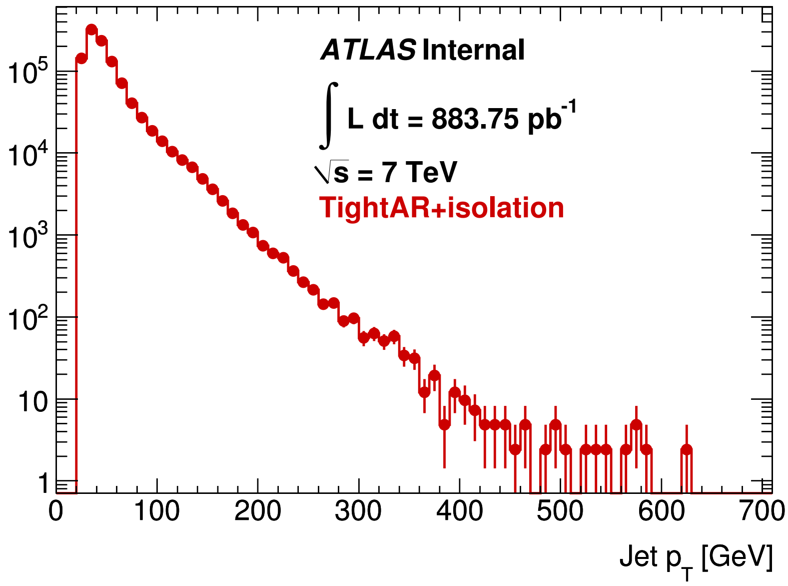

Figure 6.12: p_{T} distribution of jets that are matched to real TightAR isolated photons. These jets are considered as the real photons in the multi-jet QCD data sample.

The real photon contamination, in figure 6.12, in our QCD multi-jet sample can now be subtracted from the jet sample.

Finally, after subtracting real photon contamination, we have all we need to estimate the corrected fake rate, in equation 6.3. Figure 6.13 show the corrected fake rate after subtraction of real photon contamination according to our estimation from photon double track conversions.

6.5.3 Jet p_{T} to γ p_{T} mapping function

The photon matched to a jet contains only a fraction of the jet energy. To apply the fake rate estimated above, one needs to know what photon energy corresponds to a given jet energy. This can be done by using profile of a 2D histogram shows the jet p_{T} versus the photon p_{T} as what was done in sub-section 6.5.2.2. Figure 6.14 shows the profile distribution of $p_{T\gamma}/p_{T jet}$ as a function of the jet p_{T}. The data points of the mapping of jet p_{T} to photon p_{T} is fitted with the function $p_0 + p_1 \times exp[-p_2 \times p_{T jet}] \times p_{T jet}^{p_3}$ where the parameters p_0, p_1, p_2 and p_3 are determined from the fit to be 0.7963±0.038, -2.26±14.25, 0.0077±0.0226, and -0.49±1.819 respectively. The mapping of the jet energy E to photon E shows a similar distribution. Thus, the fit function is used to scale the jet transverse momentum and energy to obtain the corresponding photon quantities.

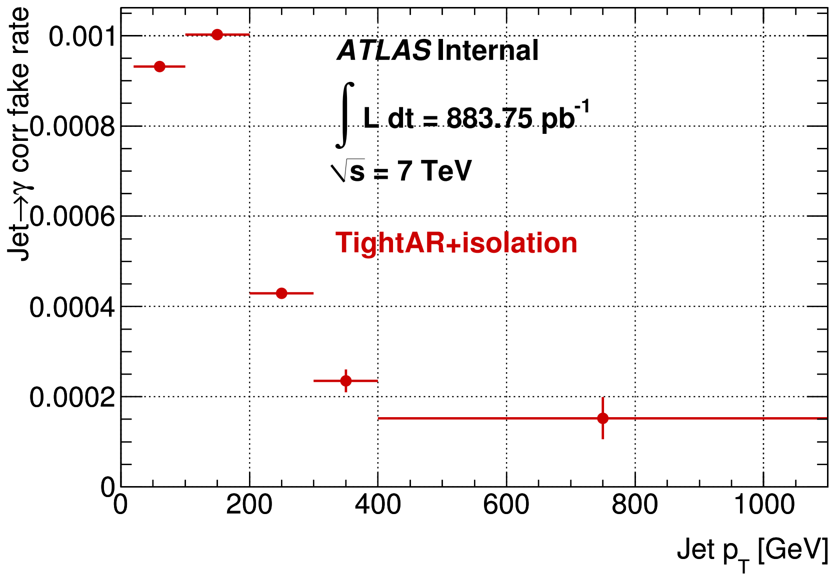

Figure 6.13: Corrected jet $\to \gamma$ fake rate for TightAR isolated photons.

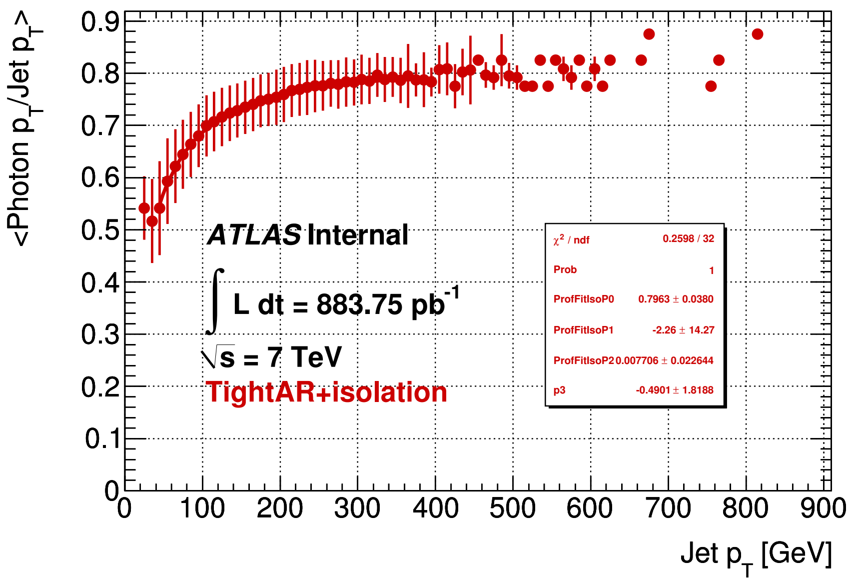

Figure 6.14: The fraction of photon p_{T} over jet p_{T} as a function of jet p_{T}.

7

Z' analysis on 2010 data

This chapter is divided into three sections. The first section is devoted to the collision data that were recorded during 2010 that is equivalent to 39 pb^{-1} of total integrated luminosity. This section starts with the good run list then data format, trigger periods and their corresponding integrated luminosity, and the electron and photon energy scaling in data. The second section is dedicated to the Monte-Carlo simulation and the corrections added to them for better modeling of data. The third section presents the search for heavy neutral gauge boson (Z') decaying to e^+e^-.

7.1 Collision data

7.1.1 Good Run List (GRL)

Atlas data is classified into periods which can be further divided into sub-periods, and are defined by the Data Preparation coordinators. Data periods are designed such that they represent data with a coherent configuration of the detector and the trigger. The naming convention for periods is a single letter (A-Z); they uniquely identify the data when combined with a project tag. The sub-periods are positive integers. The data used for this analysis is that from the 2010 ATLAS run periods D-I[1]. The EGamma combined performance group sets the data quality flags that ensure the relevant parts of the detector were operational. The data quality flags are used to build a Good Run List (GRL). The GRL[2] used in this analysis rely on version 3 (DetStatus-v03-repro05-01) of the data quality flags set by the EGamma group. It ensures that stable beam conditions were existing during data taking, the solenoid was on and stable, the data quality status for each sub-detector relevant to the analysis was good, Level 1 calorimeter trigger and both of electron and photon trigger were operating normally. Also, data quality flags ensure good ID vertexing quality and offline luminosity was properly recorded.

[1] https://twiki.cern.ch/twiki/bin/view/AtlasProtected/DataPeriods

[2] data10_7TeV.periodAllYear_DetStatus-v03-pro05_Eg_standard.xml

7.1.2 Data format

The data is skimmed before analysis by asking each event to have at least 2 container level electrons reconstructed with the standard electron algorithm (author 1, 3, or 8), have $\eta <$ 2.5 and $p_{\mathrm{T}}>$ 15 GeV. Detailed information about the electrons, photons, jets and $E_{\mathrm{T}}^{\mathrm{miss}}$ in those events are kept, as well as some general event level information, such as run number, event number, luminosity block number, flags for LAr noise bursts etc. This information is important for applying GRL and for object quality during analysis. Such selection allows to perform analysis, data driven background estimation, fake rates, and efficiencies studies.

7.1.3 Triggers and Integrated Luminosity

One of the main functions of the L1 trigger (see subsection 4.2.6.1) is to measure the amplitude of the signal from the calorimeter trigger towers, and assign it to the correct bunch crossing[3] (in units of 25 ns). The Bunch Crossing Identification mechanism (BCID) uses a Finite Impulse Response (FIR) filter to extract the signal pulse amplitude, followed by a Peak Finder (PF) algorithm to perform the peak identification in the linear regime. When pulse saturation occurs in the trigger digitization, for transverse energies above $\sim$ 255 GeV, a dedicated algorithm, optimized for the identification of saturated pulses, is used instead. To determine the right bunch-crossing, it uses the leading edge of the pulse, namely the amplitude of the two previous samples, respectively 50 and 25 ns, before the first saturated sample.

During the initial LHC data-taking periods (namely A, B, and C[4]), only FIR and PF algorithms were enabled. In case of highly saturated signals, this led to a wrong assignment of the signal amplitude to the corresponding BCID. Studies based on calibration pulses, performed by EGamma, show that any signal up to a transverse energy of 800 GeV per trigger tower in the EM barrel would be associated to the correct BC in that configuration. Above this limit, the FIR/PF algorithms would most likely incorrectly select the BC 25 ns after the correct one. This had led to a potential loss of high p_{T} electron/photon events. Starting from data-taking period D[5], the additional BCID algorithms, see above, were implemented and were shown to be efficient even in the case of saturated signals. Since the affected sample of data was very small, it was decided not to keep these data.

Starting from period F the ATLAS HLT (see subsection 4.2.6.2) was activated, so two single electron triggers were chosen in this analysis: L1_EM14 and EF_e20_loose, both have been run unprescaled. The L1_EM14 trigger is a L1 trigger that requires an EM cluster with transverse energy above 14 GeV and makes no requirement on the electron (or photon) identification. The EF_e20_loose trigger is an Event Filter trigger that is seeded by L1_EM14 trigger and requires a reconstructed electron with with transverse energy above 20 GeV that satisfies the loose electron identification requirement, isEM::Loose, (see subsection 6.2.1). Table 7.1 shows the integrated luminosity for each trigger period: the first two columns give the ranges of run periods and run numbers, the third gives the triggers and the last the corresponding integrated luminosity.

[3]The term bunch crossing effectively refers to the interaction region where the beams overlap.
[4]Periods A-C are corresponding to about 17 nb^{-1}of good run integrated luminosity
[5]Data taking period D started on 14th of June 2010

Table 7.1: Integrated luminosity for each trigger period in 2010 data.

Run periods	Run numbers	Trigger	L_{int} [pb^{-1}]
D-E	158045-161948	L1_EM14	1.3
F-I	162347-167844	EF_e20_loose	37.7
D-I	158045-167844		39.0

7.1.4 Electron and photon energy scale

In order to precisely measure the energy of electromagnetic clusters, hence electrons and photons, the cluster energy as well as any energy-derived quantity has to be calibrated with energy scale factors that depend on the object location in the EM calorimeter. A dedicated study of the $Z \to ee$ and $W \to e\nu$ events, done by EGamma performance group, using the full 2010 dataset has allowed to measure precisely the electromagnetic energy scale [86]. Energy scale correction factors have been determined in 50 η bins. They are applied to the energy of the real data electromagnetic clusters by means of a tool [87] provided by the EGamma group performance group.

7.2 Monte Carlo simulation

As previously stated in section 5.1, all Monte-Carlo samples were generated and simulated with Athena release 16.0.2. Signals as well as backgrounds properties were mentioned in detail in chapter 5. Several corrections have to be applied to Monte Carlo in order to recreate the environment that was present during data-taking and/or correct for real data/ Monte Carlo discrepancies.

7.2.1 Pile-up simulation

The challenge for ATLAS is to work out which tracks and energy deposits to attribute to which interaction. As the instantaneous luminosity per bunch crossing goes up, the likelihood of additional soft interaction between the constituent quarks and gluons of additional proton-proton pairs increases. On top of this so-called in-time pile-up comes concern about out-of-time pile-up, which refers to events from previous bunch crossings[6].

At the beginning of 2010 data-taking, the LHC ran with only a few tens of well-spaced bunches in the machine, therefore out-of-time pile up was not a concern. But starting from period G, the LHC ran with proton bunches in trains with 150 ns bunch separation, which causes out-of-time pileup in addition.

In this analysis, Monte Carlo samples with both effects simulated (samples with reconstruction tag r_1831) were used. These samples were produced with an average of 2.2 in-time overlaid interactions per event and the following out-of-time configuration: double trains with 225 ns separation (i.e. 9 BC) are simulated, each train having 8 filled bunches with 150 ns bunch separation.

[6]Pile-up is distinct from underlying event in that it describes events coming from additional proton-proton interactions, rather than additional interactions originating from the same proton collision.

The best estimator for the number of additional interactions in one event (i.e. beam crossing) is the number of reconstructed primary vertices, which follows a Poisson distribution with a mean determined from the beam parameters. The Monte Carlo is simulated with a fixed number of primary vertices, whereas the number of primary vertices is varying in the data. Figure 7.1 shows the distribution of the primary vertex multiplicity for data and $Z \rightarrow ee$ Monte Carlo.

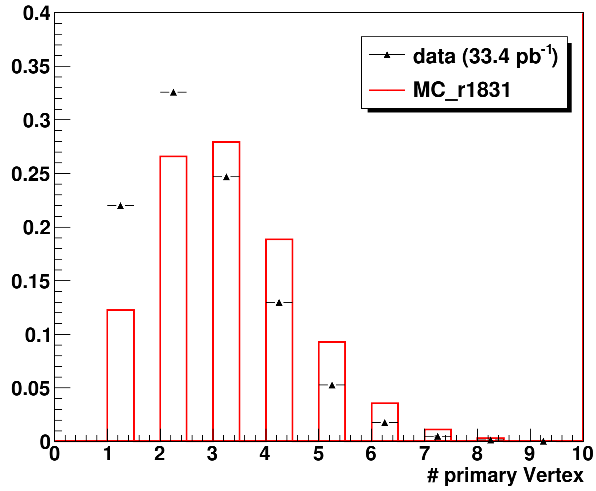

Figure 7.1: Normalized primary vertex multiplicity in periods G-I data (black symbols) and $Z \rightarrow ee$ Monte Carlo (red histogram)[8].

All Monte Carlo samples were re-weighted according to the number of reconstructed primary vertices present in the event after the Good Run List and trigger requirements, see sub-sections 7.1.1 and 7.1.3. Table 7.2 displays the fraction of events with each vertex multiplicity for data and $Z \rightarrow ee$ Monte Carlo as well as the weights applied as a function of primary vertex multiplicity. Figure 7.2 shows these weights as a function of primary vertex multiplicity.

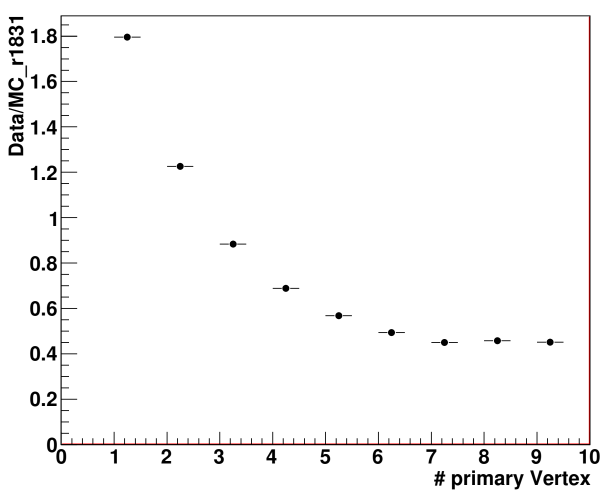

Figure 7.2: Ratio of the normalized primary vertex multiplicity in data periods G-I to that of $Z \rightarrow ee$ Monte Carlo [8].

Table 7.2: Event weights for the $Z \rightarrow ee$ MC samples. The first column is the number of reconstructed vertices, the second and the third columns are the fraction of events with that multiplicity in data and MC, and the fourth column is the MC event weight [8].

# vertices	f_{data}	f_{MC}	Event weight
0	0	0	1
1	0.22011	0.12258	1.79555
2	0.32584	0.26579	1.22591
3	0.24680	0.27936	0.88345
4	0.12991	0.18853	0.68907
5	0.05288	0.09300	0.56863
6	0.01770	0.03579	0.49447
7	0.00506	0.01123	0.45108
8	0.00137	0.00298	0.45830
9	0.00033	0.00073	0.45128
> 9	0.00011	0.00020	0.58095

7.2.2 Trigger simulation

The ATLAS trigger group measured the efficiency of the EF_e20_loose trigger used in this analysis (see sub-section 7.1.3) with respect to reconstructed electrons to be $99 \pm 1\%$ [12]. This efficiency was measured with ATHENA release 15. The trigger simulation was improved in release 16, and the EGamma performance group recommendation is to require the trigger to be fired in the Monte Carlo and to apply an efficiency correction factor of 0.995 ± 0.005.

7.2.3 Electron and photon energy resolution smearing

A study of the $Z \rightarrow ee$ and $W \rightarrow e\nu$ events using the full 2010 dataset has shown that the Monte Carlo simulation does not reproduce exactly the electromagnetic energy resolution [86] observed in the data[7]. At the energies relevant to the current analysis, the resolution is dominated by the constant term, denoted c in the following parametrization: $\sigma(E)/E = a/\sqrt{E} \oplus b/E \oplus c$, where $\oplus$ represents addition in quadrature, and E is the energy in GeV. In physics Monte Carlo samples, a constant term of 0.7% has been introduced. In the data, the constant term is measured to be $(1.1 \pm 0.2)\%$ in the barrel and $(1.8 \pm 0.45)\%$ in the endcaps. The energy of the electromagnetic clusters is smeared in Monte Carlo events to reproduce the resolution measured in data using a tool [87] provided by the EGamma performance group.

7.2.4 Electron identification efficiency scaling

To account for the electron identification efficiency discrepancies observed in data and Monte Carlo, an η-dependent scale factor is applied to each Monte Carlo event which is the product of two scaling factors (see subsection 6.2.1.1):

- *medium* identification selection scale factor provided by EGamma group [12],

[7]Even after applying the energy scale correction which was described in section 7.1.4.

- additional scaling factors computed by the exotic di-electron subgroup to account for the B-layer requirement that is applied on top of the medium selection.

The resulting combined scale factors are displayed in table 7.3.

Table 7.3: Combined scale factor (medium+B-layer) for electron identification efficiency rescaling. Uncertainties listed include statistical and systematic uncertainties [8].

η bin	scale factor	η bin	scale factor
[-2.47,-2.01]	0.990 ± 0.027	[0,0.8]	0.984 ± 0.021
[-2.01,-1.52]	0.982 ± 0.024	[0.8,1.37]	0.988 ± 0.022
[-1.37,-0.8]	0.980 ± 0.022	[1.52,2.01]	0.998 ± 0.023
[-0.8,0.0]	0.984 ± 0.021	[2.01,2.47]	1.005 ± 0.027

7.2.5 Object Quality Maps (OTx)

Due to dying Front End Boards (FEBs) optical readout links, non-nominal high voltage on modules or completely off modules,... etc, the corresponding parts of the electromagnetic liquid argon calorimeter had to be masked. This detector status information was stored in the so-called Object Quality (OQ) Maps (also known as OTx maps). Each time a new hardware problem appears a new map was released. These maps were then used during electrons (or photons) selection. If an electron or photon candidate is located in any of these regions, it is rejected.

7.3 Z' analysis on 2010 data

7.3.1 Electron and event selection

After some preliminary studies, the exotic di-electron subgroup within `ATLAS` converged towards a set of cuts. Preserving potential signal efficiently, while minimizing background processes. The selection criteria include the following set of cuts:

- the event is in the Good Runs List, to ensure the sub-detectors concerned by the analysis were ready and have no serious hardware problem (see subsection 7.1.1).
- the event has at least one primary vertex, with more than two tracks. This cut is used to ensure the lepton that triggered an event was produced in a pp collision.
- the event passes the trigger, L1_EM14 for periods D-E, and EF_e20_loose for periods F-I (see subsection 7.1.3).
- at least 2 electrons:
  - with author 1 or 3, to ensure that the electron candidates are selected by either the standard reconstruction (calorimeter-seeded) algorithm or by both the standard and the soft electron (track-based) algorithms (see section 6.1.3).
  - in the calorimeter acceptance, $|\eta| < 2.47$ excluding the crack region $1.37 < |\eta| < 1.52$ between the barrel and end-caps compartments of the EM calorimeter. The η variable used here is η_{cl}: the electron associated cluster η.

- with transverse momentum $p_\mathrm{T} > 20$ GeV. Following EGamma recommendations, $p_\mathrm{T} = E_\mathrm{T} = E_{cluster}/\cosh\eta$, where η here is the cluster η_{cl} or track η_{track} depending on the track quality.
- having cluster that passes the OTx check (see subsection 7.2.5).
- pass the ISEM *medium* identification selection (see subsection 6.2.1),
- having a B-layer hit, if one is expected.

- The two leading electrons invariant mass must be at least 70 GeV, in order to remove irrelevant low mass events, the Z peak was kept for normalization purposes.

7.3.2 Background estimation

Beside the Drell Yan processes (ee and $\tau\tau$) which are dominant, the expected backgrounds are $t\bar{t}$ and diboson events which also have two real electrons, plus backgrounds in which one (W+jet), or two (QCD multi-jet) jets are misidentified as an electron [8]. All backgrounds are taken from Monte Carlo simulation except the multi-jet QCD which is measured directly with data driven methods.

7.3.2.1 Multi-jet background

The multi-jet QCD background cannot be well predicted by the Monte Carlo simulation and is therefore measured directly from the data as much as possible. The exotics dielectron subgroup developed three deferent methods to estimate the multi-jet QCD background. The first method, 'Reverse identification" technique, is described in detail below and the other two methods are described briefly and for more detail about them see reference [8]:

- "Reverse identification" technique, in this method the amount of residual QCD background in the signal sample is determined by fitting the data to a MC background template and a data-driven QCD template. A sample enriched in QCD events is obtained. Then, a discriminating distribution is chosen: the invariant mass in the region of the Z peak is used. A fit to the invariant mass distribution in the low-mass control region yields both the expected amount of QCD background as well as the normalization of the Drell Yan and other backgrounds taken from MC.

  The QCD sample chosen must be similar to the type of events which pass the entire Z' selection, therefore the Z' selection (see subsection 7.3.1) was applied to the event through the OTx requirement. Then, events with two electrons passing ISEM *loose* selection cuts and the B-layer cut, but failing *medium* cuts were selected. This selection is orthogonal to the one used for signal, which requires the two electrons to pass the ISEM *medium* selection (for ISEM *loose* and *medium* selections see subsection 6.2.1).

  In order to determine the fraction of the QCD background, a fit to two templates was performed. All of the backgrounds from MC (see subsection 7.3.2.2) are combined into a single template according to their cross-sections. The events with two electrons that pass *loose* and B-layer cuts but fail *medium* make up the data-driven QCD template. The MC and data-driven QCD templates are fit to the data using RooFit in the invariant mass from 70-320 GeV. For the corrected calorimeter and track isolation, the shape of the events in the QCD template can be seen in Figure 7.3. The estimated number of events in invariant mass bins are given in Table 7.4.

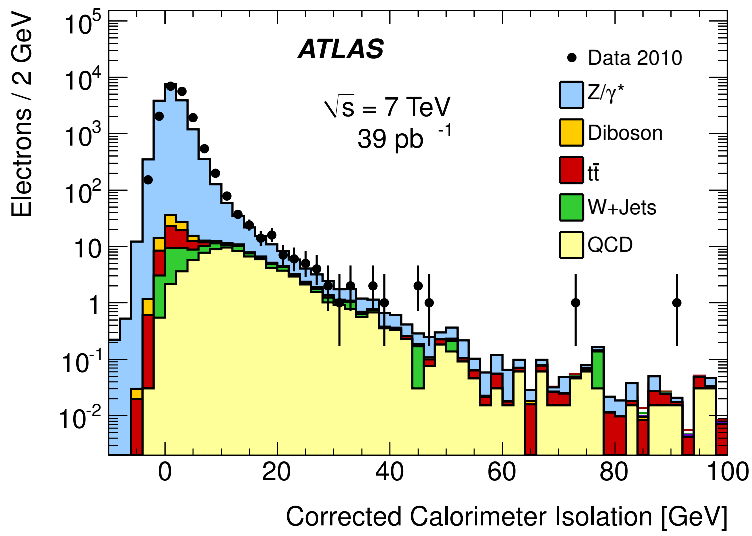

Figure 7.3: Corrected calorimeter isolation after the fit has been performed in the invariant mass. The QCD are from the data-driven reversed identification method, and are less isolated than the Drell Yan, as expected [8].

Table 7.4: QCD background estimates from the reverse identification method [8].

Invariant mass [GeV]	Estimated number of background events
70-110	44.20 ± 19.00 ±1.35
110-130	11.62 ± 5.00 ±0.69
130-150	7.76 ± 3.34 ±0.55
150-300	14.84 ± 6.38 ±1.24
300-800	1.32 ± 0.57 ±0.22
800-2000	0.05 ± 0.02 ±0.04

To understand the level of real electrons contamination in the QCD template, the number of Drell Yan, W+jets and $t\bar{t}$ MC events passing the QCD cuts was measured. For the entire data sample, the QCD template has 5120 events, about 1% of which come from other MC backgrounds: 53.44 events of Drell Yan are expected, 4.29 W+jets, and 0.23 $t\bar{t}$ events. In a later version of the analysis, these signal contributions can be subtracted from the QCD template before fitting, but the small number of events in the smooth QCD shape should not affect the background estimate much in the high-mass tail. If there were more W+jets events than expected from MC, there would be a high-missing E_{T} tail in the QCD template, which is not observed in Figure 7.4.

To test the stability of the QCD estimate, several variations were made. The range of the invariant mass used in the fit was varied around the Z peak with consistent results. In order to evaluate the effect of the particular selection used for the QCD template, several other orthogonal template definitions were tested. For example, some other selections that were checked include events with two electrons that pass *loose* cuts and the B-layer but fail *medium* and fail additional QCD-enriching cuts like $F_{\rm side}$ or a set of other QCD-enriching variables. The differences between the estimates with these alternate selections were within the statistical errors.

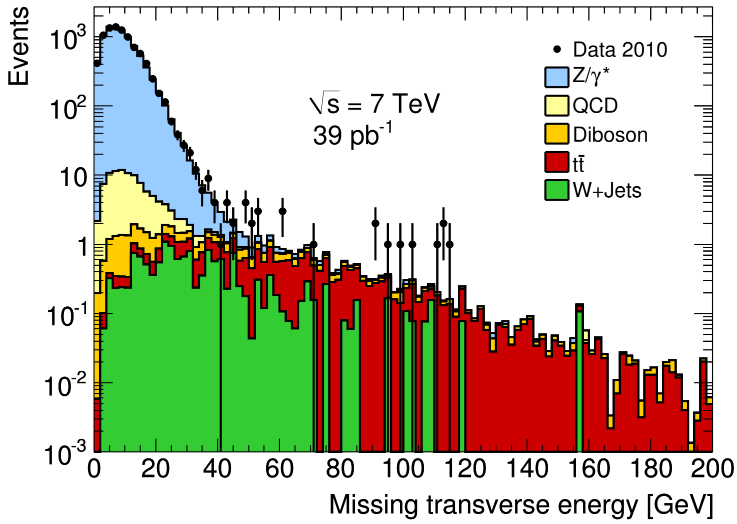

Figure 7.4: Data-driven reversed identification method, QCD template made up of events with low missing $E_{\rm T}$, therefore depleted in W+jets events [8].

In order to evaluate the systematic uncertainties, a number of alternative anti-samples were constructed, and they were all quite consistent with the nominal anti-*medium* selection within their sometimes limited statistics. To get a better handle on the higher mass bins, a higher statistics anti sample was made, where one electron was required to fail *medium* and the other to have: $F_{\rm side} > 0.58$ or abs$(\Delta\eta) > 0.71$ or $\Delta\phi > 0.044$ or $F_{\rm 3core} > 0.035$ or $ptcone30/pt > 2.4$ or $w_{\rm stot} > 6$ (for detailed information about these variables see section 6.2.1). 10,000 pseudo experiments were then generated using the data template from this selection and fit with the nominal two anti-*medium* template to get the bias on the scale. This template was then scaled to the nominal scaling plus this bias and the greater of the difference was taken and the sum of statistical errors between the values in each mass bin between the nominal template and this alternative one. The nominal template has only five events in the highest mass bin, while the modified template has only 2, so there isn't enough information to come up with a sensible systematic for this bin [8].

- "Isolation fits" technique, uses a template fit in "corrected" calorimeter isolation (Etcone40_pt_corrected, see subsection 6.3) to estimate the amount of QCD events. The signal template is relatively independent of the transverse energy of the electron and is thus taken from a high statistics W boson sample in data. The background template is derived using reversed identification cuts on data, and is binned in $E_{\rm T}$, since it shows dependence.
  For more details for this method see reference [8].
- "Matrix" method, relates the measured number of events passing "Loose" and "Tight" selection criteria to the true number of real and fake events in the sample. By inverting a matrix, one can solve for the true quantities in terms of the measured ones, using efficiencies and fake rates measured in data. For more details for this

method see reference [8].

Table 7.5: Estimated numbers of QCD events in the data in bins of $m_{e^+e^-}$ for the three methods used by exotic dielectron subgroup. The first quoted uncertainty is statistical, the second is systematic. The last column shows the combination of the three methods [8].

$m_{e^+e^-}$ [GeV]	Reverse id.	Isolation fits	Matrix	Power law fit
$70-110$	$44.2 \pm 19.0 \pm 2.1$	-	$59.7 \pm 9.5\ ^{+34.8}_{-38.2}$	
$110-130$	$11.6 \pm 5.0 \pm 1.1$	$12.4 \pm 5.3 \pm 2.1$	$6.2 \pm 1.4\ ^{+0.4}_{-2.1}$	$10.1 \pm 1.5\ ^{+0.6}_{-1.8}$
$130-150$	$7.8 \pm 3.3 \pm 0.8$	$9.8 \pm 4.1 \pm 1.7$	$4.7 \pm 1.1\ ^{+0.2}_{-1.2}$	$5.5 \pm 0.7 \pm 0.2$
$150-300$	$14.8 \pm 6.4 \pm 1.5$	$13.4 \pm 5.5 \pm 2.0$	$11.2 \pm 2.2\ ^{+0.2}_{-2.3}$	$9.2 \pm 1.2\ ^{+2.6}_{-0.5}$
$300-800$	$1.3 \pm 0.6 \pm 0.3$	$3.1 \pm 1.7 \pm 2.3$	$2.1 \pm 0.6\ ^{+0.3}_{-0.6}$	$1.3 \pm 0.2\ ^{+0.6}_{-0.3}$
$800-2000$	$0.05 \pm 0.02 \pm 0.04$	-	0.05 ± 0.0	$0.07 \pm 0.02\ ^{+0.03}_{-0.05}$

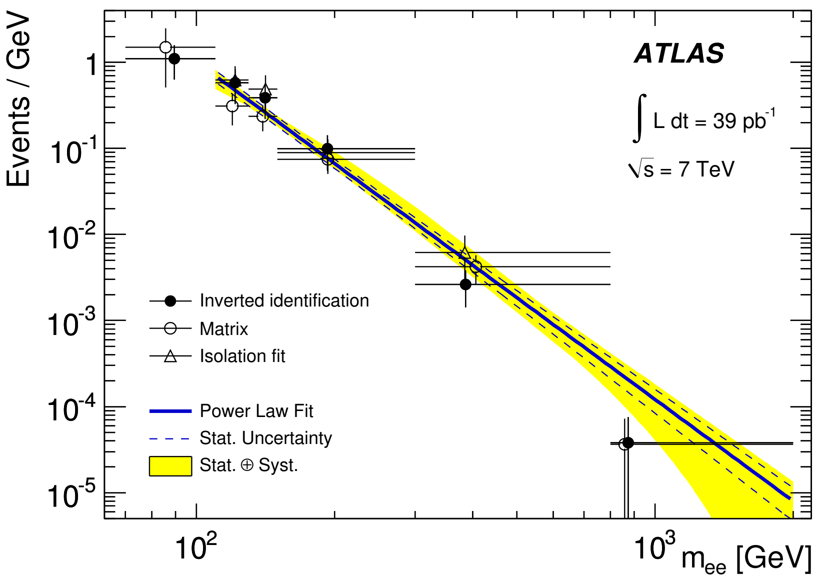

Figure 7.5: QCD background estimates for the reverse identification, isolation fits, and matrix methods as a function of $m_{e^+e^-}$, and combined fit to a power law [8].

The three estimates of the QCD background as a function of $m_{e^+e^-}$ are shown in Figure 7.5 and Table 7.5, and are fairly consistent. A fit is performed for invariant masses above 110 GeV, in order to combine these measurements using a power law:

$$y(x) = p_0 \cdot \frac{-p_1 - 1}{x_0^{p_1+1}} \cdot x^{p_1} \quad , \quad \int_{x_0}^{+\infty} y(x)\mathrm{d}x = p_0 \tag{7.1}$$

where p_0 corresponds to the expected number of QCD events in the mass window $[x_0, +\infty]$, with $x_0 = 110$ GeV. The power law parameters are estimated with a modified χ^2 function:

$$\chi^2(p_0,p_1) = \sum_{bin\ k} \frac{\left(y_k - \frac{1}{x_{k+1}-x_k} \int\limits_{x_k}^{x_{k+1}} y(x)\mathrm{d}x \right)^2}{\sigma^2_{y,k}} \tag{7.2}$$

The statistical uncertainty on the fitted function is obtained by propagating the statistical uncertainty on fitted parameters p_0 and p_1. Two sources of systematic uncertainty are considered: the slight bias introduced when fitting a power law in the low statistics regime, and the choice of the functional form of the fit function (see reference [8] for more details).

7.3.2.2 Backgrounds taken from the Monte Carlo and overall background

For invariant masses above 110 GeV, the QCD background shape and normalization is obtained by combining different QCD estimates as described in subsection 7.3.2.1. For lower invariant masses, only the "Reverse identification" technique has enough statistics, so the distribution from this method is normalized to the combined background estimation in the range 110-300 GeV and its shape is used to estimate the background in the range 70-110 GeV [8].

The Drell Yan, $t\bar{t}$, diboson and W plus jet components are all normalized relatively to each other according to their cross section (given in section 5.4). The final number of expected background events is then obtained from normalizing the invariant mass spectrum in the range 70-110 GeV, fixing the QCD component normalization and letting the second component (all MC backgrounds together) normalization free. Since the latter is dominated by the Drell Yan contribution, this corresponds to normalizing the Monte Carlo to the Z peak in the data, and allows to cancel out the luminosity uncertainty in the σB limit setting. The final number of expected events is displayed in table 7.6 in bins of reconstructed dielectron invariant mass.

The normalization coefficient of the Monte-Carlo samples resulting from the normalization procedure described before (section 7.3.2.2) is 0.975.

Table 7.6: Expected and observed number of events in the dielectron channel. The errors quoted are both statistical and systematic. The systematic uncertainties are correlated across bins and are discussed in the text. Entries of 0.0 indicate a value < 0.05 [8]

$m_{e^+e^-}$[GeV]	70 - 110	110 - 130	130 - 150	150 - 170	170 - 200	200 - 240
Z/γ^*	8498.5 ± 7.9	104.9 ± 3.3	36.8 ± 1.3	19.4 ± 0.7	14.7 ± 0.6	9.5 ± 0.4
$t\bar{t}$	8.2 ± 0.8	2.8 ± 0.3	2.1 ± 0.2	1.7 ± 0.2	1.7 ± 0.2	1.2 ± 0.1
Diboson	12.1 ± 0.9	1.0 ± 0.2	0.7 ± 0.2	0.5 ± 0.2	0.5 ± 0.1	0.4 ± 0.1
$W+$jets	6.0 ± 1.8	3.7 ± 1.2	1.2 ± 0.5	1.3 ± 0.5	1.2 ± 0.4	1.1 ± 0.4
QCD	32.1 ± 7.1	8.4 ± 1.8	5.5 ± 0.8	$3.2\ ^{+0.6}_{-0.4}$	$2.8\ ^{+0.8}_{-0.4}$	$1.9\ ^{+0.8}_{-0.3}$
Total	8557.0 ± 10.8	120.9 ± 4.0	46.4 ± 1.6	$26.2\ ^{+1.1}_{-1.0}$	$20.8\ ^{+1.1}_{-0.8}$	$14.1\ ^{+1.0}_{-0.7}$
Data	8557	131	49	20	18	13

$m_{e^+e^-}$[GeV]	240 - 300	300 - 400	400 - 550	550 - 800	800 - 1200	1200 - 2000
Z/γ^*	6.0 ± 0.3	3.2 ± 0.1	1.3 ± 0.1	0.4 ± 0.0	0.1 ± 0.0	0.0 ± 0.0
$t\bar{t}$	0.9 ± 0.1	0.5 ± 0.0	0.1 ± 0.0	0.0 ± 0.0	0.0 ± 0.0	0.0 ± 0.0
Diboson	0.3 ± 0.1	0.2 ± 0.1	0.1 ± 0.1	0.0 ± 0.0	0.0 ± 0.0	0.0 ± 0.0
$W+$jets	0.3 ± 0.1	0.2 ± 0.1	0.2 ± 0.2	0.0 ± 0.0	0.0 ± 0.0	0.0 ± 0.0
QCD	$1.3\ ^{+0.7}_{-0.2}$	$0.8\ ^{+0.4}_{-0.2}$	$0.4\ ^{+0.2}_{-0.1}$	0.2 ± 0.1	0.1 ± 0.0	0.0 ± 0.0
Total	$8.8\ ^{+0.7}_{-0.4}$	$4.8\ ^{+0.5}_{-0.3}$	2.1 ± 0.2	0.6 ± 0.1	0.1 ± 0.0	0.0 ± 0.0
Data	9	3	0	3	0	0

7.3.2.3 MC background systematic uncertainties

In this subsection, systematic uncertainties associated with the theoretical and experimental modeling are discussed. In addition to the uncertainty on the integrated luminosity, there are "efficiency-like" uncertainties: on trigger, reconstruction and identification efficiencies, on the production models and also on the expected background. Most are common to signal and background; for what concerns the production model uncertainties, this is true only for the dominant background (Drell Yan). In addition, there are "shape" uncertainties, from the energy scale and resolution.

- production model uncertainties: the production model uncertainties arise due to the QCD and EW K-factors, and the PDFs. We assume that the systematic uncertainties grow linearly from the Z boson pole mass to a specified value at a reference mass of 1 TeV.

  The K-factors have been discussed briefly through out chapter 5. The uncertainties on the QCD and EW K-factors are 3% and 4.5% respectively at 1 TeV. The uncertainty in the QCD K-factor is estimated from the difference between the NLO and the NNLO calculations and the uncertainty in the EW K-factor includes the effects of neglecting the running of the coupling and the real gauge boson emission. The PDF uncertainties are evaluated at different masses by using the MSTW2008 set of PDFs, which contains the default as well as 20 variations along the eigenvectors in the PDF parameter space. From 3% at the Z boson pole, the PDF uncertainty is found to grow to 6% at 1 TeV and 9% at 1.5 TeV [8].

- trigger efficiency: the efficiency of the triggers used in this analysis were measured by the `ATLAS` EGamma group [12] to be $\varepsilon = 99 \pm 1\%$ for reconstructed electrons. Given the threshold of 25 GeV on the reconstructed electrons p_{T}, the plateau is reached and the trigger efficiency does not depend on p_{T}. The above efficiency is valid up to about 250 GeV. For higher p_{T}, there are potential inefficiencies due to the saturation of the trigger signals. These inefficiencies are evaluated to be at most 1.6% at low mass and at most 1.9% at 2 TeV (for more details see [8]).

- reconstruction and identification efficiency: the reconstruction efficiency has been shown to be well modeled by Monte Carlo, with a systematic uncertainty of 1.5% which does not depend on p_{T}. The exclusion of the clusters in dead OTx regions was found to add a small systematic uncertainty of 0.3% [8].

- identification efficiency: the efficiency of the electron ISEM *medium* selection was measured by the EGamma group [12] and scale factors were computed as a function of η. The largest uncertainty was 0.9%. The efficiency of the additional B-layer requirement was also measured in data and Monte Carlo using the tag-and-probe method on $Z \to e^{+}e^{-}$ events and additional scale factors were computed as a function of η, see subsection 7.2.4. The resulting *combined* scale factors were applied to all Monte Carlo samples by means of re-weighting each event. The systematic uncertainty on these factors is taken to be the one of the η bin with largest uncertainty, namely 2.7% (see section 7.2.4). These factors are assumed to have reached a plateau and their uncertainty is assumed to be p_{T} independent. The overall uncertainty from reconstruction and identification of one electron is 3.2%, and 4.5%

for an electron pair, assuming they are uncorrelated [8].

- energy scale and resolution: the uncertainty on the electron energy scale is between 0.5% and 1.5% depending on transverse momentum and pseudorapidity, as determined from the energy rescaler tool provided by the `ATLAS` EGamma group [86]. After smearing, the residual uncertainty on energy resolution (0.2% and 0.45% on the constant term respectively in the barrel and endcaps, see section 7.2.3) is negligible [8].

7.3.3 Data-Monte Carlo comparison

The number of expected and observed events in bins of reconstructed dielectron invariant mass is displayed in table 7.6. Figure 7.6 shows the E_{T} distributions of both electrons, leading p_{T} and sub-leading p_{T} separately after Z' final selection (see section 7.3.1). Figure 7.7 displays the η distribution of both electrons after Z' final selection. Figure 7.8 presents the invariant mass ($m_{e^+e^-}$) distribution after Z' final selection. In all these plots, the QCD component is taken from the reverse identification method, (see sub-section 7.3.2.1).

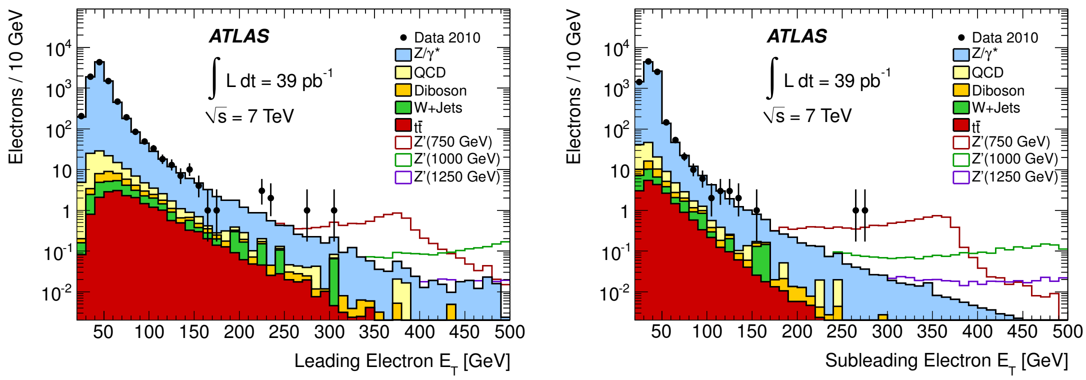

Figure 7.6: E_{T} distributions after Z' final selection. Left: leading electron, right: subleading electron. The QCD component is taken from the reverse identification method, (see sub-section 7.3.2.1) [8].

The consistency of the observed data with the Standard Model prediction is tested using the Bayesian Analysis Toolkit [88], as described in more detail in subsection 7.3.4. The p-value obtained is 0.05, well above the evidence threshold of 1.35×10^{-3}, so consistent with SM expectation.

7.3.4 Z' limits calculation

7.3.4.1 σB limits

As shown in the previous section (7.3.3), the data are consistent with the SM expectation, limits are set on the production cross section times branching ratio (σB) of new gauge bosons. The chosen method is a template shape fit described in reference [89]. Template shape fitting is essentially a counting experiment in many bins of the $m_{e^+e^-}$ distribution and the likelihood function is the product of single bin counting experiment likelihood function. The expected number of events in bin k is $N_k = N_k^{Z'} + N_k^{bg}$, and the observed

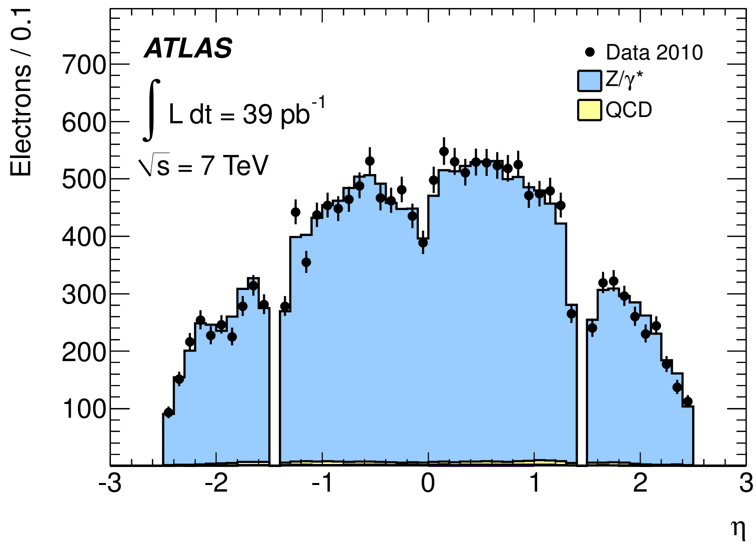

Figure 7.7: Electron (both leading and sub-leading) η distribution after Z' final selection. The QCD component is taken from the reverse identification method, (see sub-section 7.3.2.1) [8].

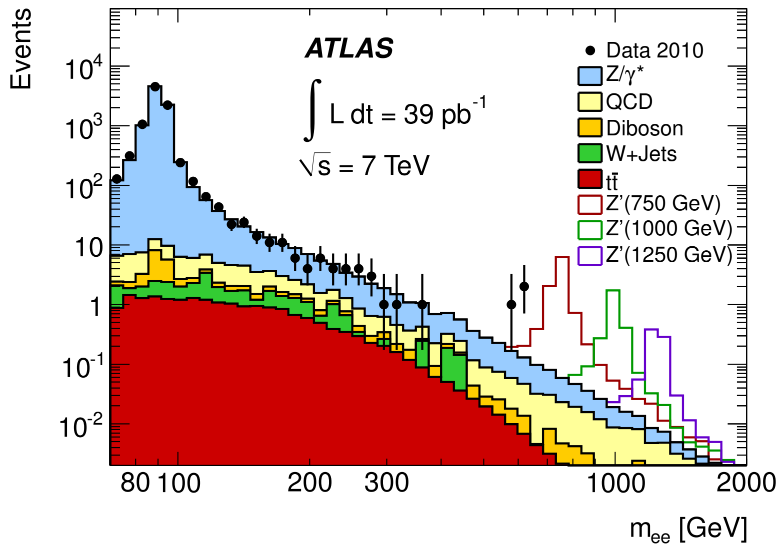

Figure 7.8: Dielectron invariant mass ($m_{e^+e^-}$) distribution after Z' final selection, compared to the stacked sum of all expected backgrounds, with three example Z'_{SSM} signals overlaid (with Z' masses 750, 1000, 1250 GeV). The QCD component is the combination of the three methods. The bin width is constant in $\log m_{e^+e^-}$ [8].

number of events in bin k is denoted by D_k. The binned likelihood function is shown in equation 7.3.

$$\mathcal{L}(N_{Z'}, N_Z|data) = \prod_{k=1}^{N_{bin}} \frac{(N_k)^{D_k} e^{-N_k}}{D_k!} \tag{7.3}$$

This likelihood function can be used to simultaneously fit for the number of Z boson events N_Z and the number of Z' events $N_{Z'}$ which allows to measure the Z boson yield while searching for a Z' at high mass. We normalize the sum of all backgrounds to the data in the mass window $70 < m_{ee} < 110$ GeV, such that:

$$\sigma B(Z') = \sigma B(Z)\frac{N_{Z'}A_Z}{N_Z A_{Z'}}, \tag{7.4}$$

A_Z is the total acceptance times efficiency at the Z boson pole and $A_{Z'}$ is the total acceptance times efficiency for a Z' boson of a certain pole mass. This equation shows that this normalization effectively removes any dependency of this analysis on the integrated luminosity as well as any other mass-independent systematic uncertainty, except from the normalization uncertainty on the Z/γ^* theoretical cross section, which is of 5% [71]. Mass-dependent systematic uncertainties are incorporated as nuisance parameters in the likelihood function. There are two such parameters:

- the theortical uncertainties on the background: QCD and EW K-factors uncertainty, plus PDF uncertainty (section 7.3.2.3). These uncertainties are approximated with a linear dependency on the invariant mass, growing from the Z-pole to a specified value at a reference mass of 1 TeV, and are easily combined. As an extreme alternative, a "step-function" description of the systematic uncertainties versus mass was tried for dielectron mass above the Z-pole. The choice of the functional dependence makes very little difference to the final results, because most of these uncertainties apply to the theory cross section and therefore only the value of the uncertainty near the mass limit matters. These uncertainties are correlated across all bins in the search region of $m_{e^+e^-} > 110$ GeV.

- the QCD background uncertainty, see subsection 7.3.2.1.

The trigger, reconstruction and identification uncertainties are irrelevant since their very small dependence on the invariant mass is negligible.

For a given value of the resonance mass $M_{Z'}$, a signal scan is performed using the likelihood function of equation 7.3. In the absence of a signal, an upper limit is set at the 95% confidence level using the Bayesian approach. This is repeated for a sequence of Z' masses ranging from 0.13 to 2.0 TeV in steps of 40 GeV.

In order to estimate the *a priori* sensitivity, Monte Carlo pseudo-experiments were generated using only standard model processes in proportion to their expected rate. The pseudo-experiments are randomly drawn from Monte Carlo samples of all relevant backgrounds. The 95% C.L. upper limits for each pseudo-experiment is found for each fixed value of $M_{Z'}$. The median of the distribution is chosen to represent the expected limit. The ensemble of limits is also used to find the 68% and 95% envelope of limits as a function of dilepton mass. Figure 7.9 shows the 95% C.L. exclusion limit for the SSM Z' and several E_6 Z'. Table 7.7 also displays the cross section limits given at the mass limit, see subsection 7.3.4.2.

7.3.4.2 Mass limits

The mass limit is computed in the same way as the σB limit, but the signal systematic uncertainties (namely theory uncertainties) are incorporated as nuisance parameters into the likelihood function as well. These uncertainties are correlated between signal and background. Table 7.8 displays the obtained mass limits. The thickness of the theory

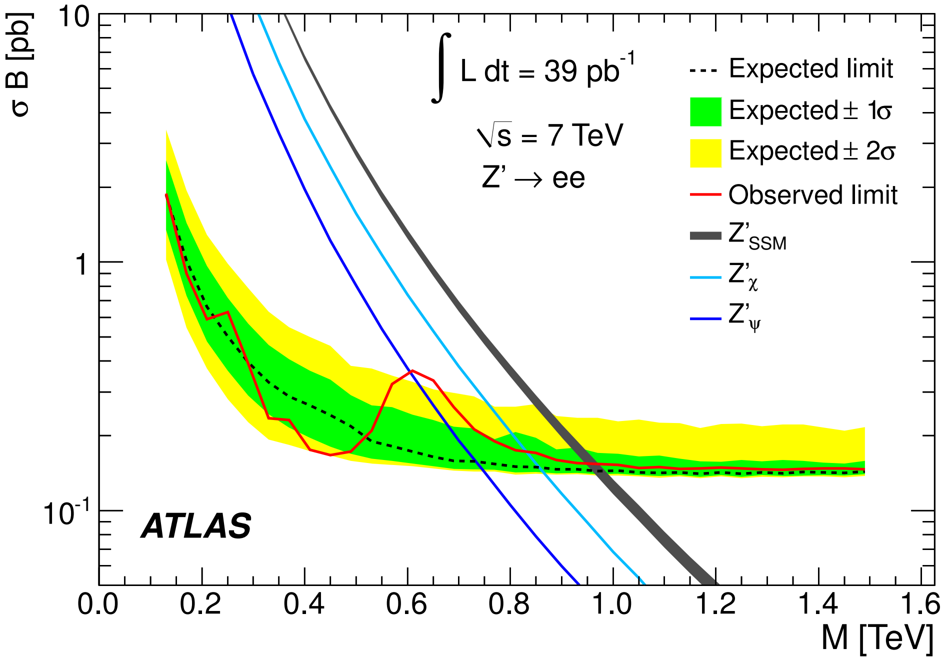

Figure 7.9: Expected and observed 95% C.L. limits on σB and expected cross sections for Z'_{SSM} and the two E_6-motivated Z' models with lowest and highest σB for the dielectron channel. The thickness of the SSM theory curve represents the theoretical uncertainty and holds for the other theory curves [8].

Table 7.7: Expected and observed 95% σB limits for various Z' models.

Model	Z'_{SSM}	Z'_{ψ}	Z'_{N}	Z'_{η}	Z'_{I}	Z'_{S}	Z'_{χ}
Expected limit [pb]	0.145	0.159	0.156	0.156	0.151	0.149	0.148
Observed limit [pb]	0.155	0.362	0.356	0.351	0.187	0.176	0.174

curve in figure 7.9 represents the theortical uncertainty on the signal and is not used in the derivation of the mass limit [8].

Table 7.8: Expected and observed 95% mass limits for various Z' models.

Model	Z'_{SSM}	Z'_{ψ}	Z'_{N}	Z'_{η}	Z'_{I}	Z'_{S}	Z'_{χ}
Expected limit [TeV]	0.967	0.727	0.750	0.756	0.813	0.834	0.854
Observed limit [TeV]	0.957	0.604	0.626	0.633	0.779	0.807	0.829

7.3.5 Comparison with previous searches for Z'

Figure 7.10 shows a comparison of `ATLAS` result with 2010 dataset with the limits from CMS and D0, in which the ratio of the limit to the theortical value of σB, a quantity that is proportional to the square of the coupling strength. The cross section calculations assume standard model couplings for the Z', so that a value of one corresponds to a 95%

C.L. limit on a Z' with those couplings.

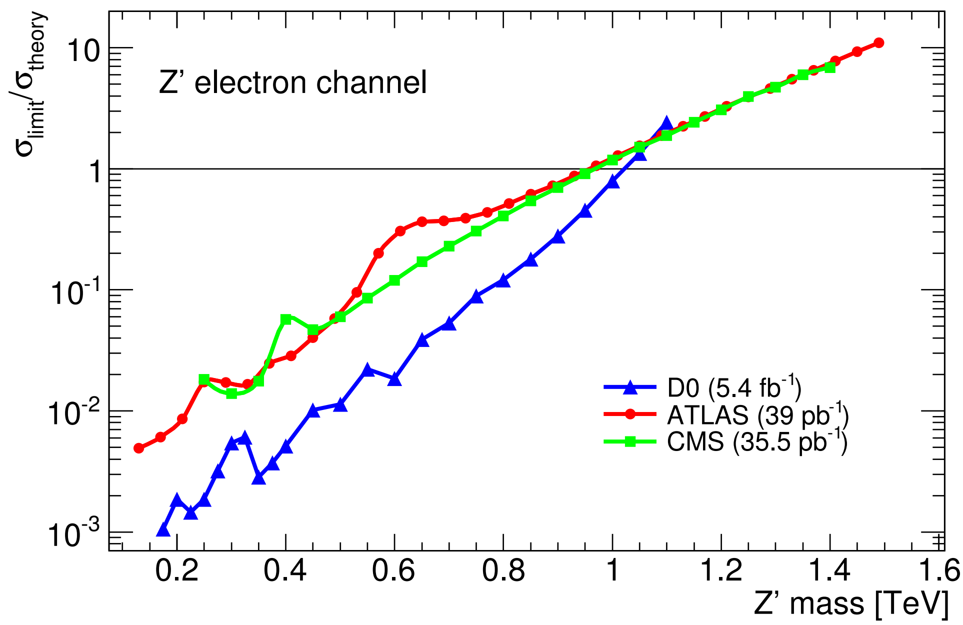

Figure 7.10: $Z' \to e^+e^-$ cross section normalized limits ($\sigma_{\text{limit}}/\sigma_{\text{calculated}}$) as a function of mass for this analysis and those from D0 and CMS. The region above each curve is excluded at 95% confidence level [8].

The result of this Z' search was published in *Phys. Lett. B*, April 2011 [90].

7.3.6 Contribution to the 2010 Z' search

I started to look at data for the first time and doing real physics analysis in the 2010 Z' analysis. My contribution to the 2010 Z' search consisted of preparing D3PDs for some of the Monte-Carlo samples as well as producing 2 electron skims for both data and Monte-Carlo (see section 7.1.2) [91]. I was also a member of Z' data-team to optimise event-selection and comparing cut-flows for data and Monte-Carlo as well as providing data/Monte-Carlo plots with other team members.

8

e* analysis on 2011 data

This chapter describes the search for exotic/excited electron (e^*) produced in association with an electron and decaying to an electron and a photon based on an analysis of 7 TeV pp collision data recorded with ATLAS detector in 2011, which makes about 2.05 fb^{-1} of data.

8.1 Collision data

8.1.1 Good Run List (GRL)

For ATLAS data naming convention see sub-section 7.1.1. The data sample used in this analysis is that from ATLAS run 2011 periods B-K[1] which were collected from March to August, 2011. Instead of using the EGamma Good Run List (GRL) as what was done for the 2010 analysis[2] (see sun-section 7.1.1), the Excited Lepton analysis sub-group[3] decided to use the so-called WZjets GRL. The WZjets GRL are provided by the ATLAS Standard Model WZ physics analysis group which make use of the data quality flags that had been set by the different ATLAS combined performance groups to ensure the relevant parts of the detector were operational.
The GRL[4] used in this analysis rely on version 28 (DetStatus-v28-pro08-07) of the data quality flags. It ensures that stable beam conditions were existing during data taking, solenoid was on and stable, the data quality status for each sub-detector relevant to the analysis was green (good), Level 1 calorimeter trigger and electron, photon, and muon trigger were operating normally. Also, data quality flags ensure good ID vertexing quality and offline luminosity was OK.

8.1.2 Data format 2011

The data in SMWZ D3PD (see section 5.1) format is skimmed before analysis by asking each event to have at least 2 electrons reconstructed with the standard electron algorithm

[1]https://twiki.cern.ch/twiki/bin/view/AtlasProtected/DataPeriods
[2]This is done to have the same GRL for both of excited electron and muon channels
[3]https://twiki.cern.ch/twiki/bin/view/AtlasProtected/ExcitedLeptonAnalysis2011
[4]data11_7TeV.periodAllYear_DetStatus-v28-pro08-07_CoolRunQuery-00-04-00_WZjets_allchannels.xml

(author 1, 3, or 8, see sub-section 6.1.3) and have pseudo rapidity (η) less than or equal 2.5 and have transverse momentum (p_{T}) greater than 20 GeV. Detailed information about the electrons, photons, jets and $E_{\mathrm{T}}^{\mathrm{miss}}$ in those events (that contains at least 2 electrons) are kept, as well as some general event level information, such as run number, event number, luminosity block number, flags for LAr noise bursts etc. This information is important for applying GRL and object quality selection during the analysis. Such selection allows to perform the analysis, data driven background estimation, fake rates, and efficiencies studies.

8.1.3 Triggers and Integrated Luminosity

For detailed information about `ATLAS` High Level and Level1 triggers (see sub-sections 4.2.6.1, 4.2.6.2, and 7.1.3).

Starting from period K[5], a new trigger menu with many changes (so-called 3e33 menu) was used. The single electron trigger EF_e20_medium used in earlier periods was prescaled. Two single electron triggers were chosen in this analysis: EF_e20_medium and EF_e22_medium. The EF_e20_medium (EF_e22_medium) trigger is an EF trigger that is seeded by L1_EM14 L1 trigger and requires a reconstructed electron with transverse energy above 20 (22) GeV that satisfies the *medium* electron identification requirement, see subsection 6.2.1. Table 8.1 shows the integrated luminosity for each trigger period: the first two columns give the ranges of run periods and run numbers, the third gives the triggers and the last the corresponding integrated luminosity.

Table 8.1: Integrated luminosity for each trigger period in 2011 data.

Run periods	Run numbers	Trigger	L_{int} [fb^{-1}]
B-J	177986-186755	EF_e20_medium	1.55
K	186873-187815	EF_e22_medium	0.50
B-K	177986-187815		2.05

8.1.4 Electron and photon energy scale

As for the 2010 analysis (see sub-section 7.1.4), a dedicated study of the $Z \to ee$ and $W \to e\nu$ events[6], using the 2011 dataset has allowed to measure precisely the electromagnetic energy scale [86]. Energy scale correction factors have been determined in 50 η bins. They are applied to the energy of the real data electromagnetic clusters by means of a tool [87] provided by the EGamma group performance group.

8.2 Monte Carlo simulation

As previously stated in section 5.1, all Monte-Carlo samples were generated and simulated with Athena release 16.6.5. Signals as well as background samples properties were mentioned in detail in chapter 5. Table 5.5 lists the characteristics of the Monte Carlo

[5] Data-taking period K started on 4th of Aug. 2011
[6] This study was done by EGamma performance group

CompHEP samples for the various excited electron masses generated and for compositeness scale $\Lambda = 3$ TeV. As can be seen from table 5.5, the decay width is predicted to be narrow for excited leptons with mass $M_{e^*} < \Lambda$. For $M_{e^*} \sim \Lambda$, the width is much larger, at about $\sim 10\%$ of M_{e^*} [10].

For the dominant irreducible $Z+\gamma$ background, the SHERPA samples listed in table 5.7 were used (see section 5.4.1). The second important background $Z+$jets were generated with ALPGEN to generate matrix elements, JIMMY to describe multiple parton interactions and HERWIG to describe the remaining underlying event and parton showers. Table 5.10 lists the $Z+$jets Monte-Carlo samples used in this analysis. To remove overlaps between the $Z+$jets and the $Z+\gamma$ samples, events with prompt energetic photons are rejected if the photons are outside a cone $R = 0.5$ of the electrons.

WW, WZ, ZZ **events:** Another sizable background comes from diboson events. Monte Carlo samples are generated with HERWIG with a filter requiring at least one lepton, section 5.4.3. Finally, $t\bar{t}$ background is generated with MC@NLO to generate matrix elements, JIMMY to describe multiple parton interactions and HERWIG to describe the remaining underlying event and parton showers, for more details see section 5.4.4.

Several corrections have to be applied to Monte Carlo in order to recreate the environment that was present during data-taking and/or correct for real data/ Monte Carlo discrepancies.

8.2.1 Pileup simulation

Since Monte Carlo samples are usually produced before or during a given data taking period, only a best-guess of the data pileup conditions can be put into the Monte Carlo. That's why, there is the need at the analysis level to re-weight the Monte Carlo pileup conditions to that was found during data taking. In the 2010 data (see section 8.2.1), the number of reconstructed vertices was used as a measure of how much pileup there was in a given event. That was in most cases sufficient since it is indicative of the true in-time pile-up [7]. For 2011 data taking, the LHC is running with bunch trains with an in-train bunch separation of 50 ns. Thus, the out-of-time pileup [8] is also present and the number of vertices in a given event is not a good measure any more. Instead, what is needed is the average number of pileup interactions $< \mu >$. A dedicated package was developed by the ATLAS Physics Analysis Tools group (PAT) to calculate the event weight for Monte Carlo events that needs to be applied in order to re-weight the Monte Carlo samples to a given data sample pile-up condition. This package takes as input a histogram, see figure 8.1(a), with the average pile-up distribution for data and another histogram, see figure 8.1(b), with the pile-up distribution for the Monta Carlo. This official package was used for all Monte-Carlo samples pile-up re-weighting.

8.2.2 Trigger simulation

The efficiencies of the 2 single electron triggers used in this analysis, EF_e20_medium and EF_e22_medium triggers, (see sub-section 8.1.3), have been measured by the ATLAS trigger group and the efficiencies of both triggers were found to be similar with respect to reconstructed electrons [12]. This efficiency was measured with ATHENA release 16

[7] The term, in-time pile-up, refers to the number of interactions in the same bunch crossing

[8] the trem out-of-time pile-up refers to the overlapping signals in the detector from other neighboring bunch crossings

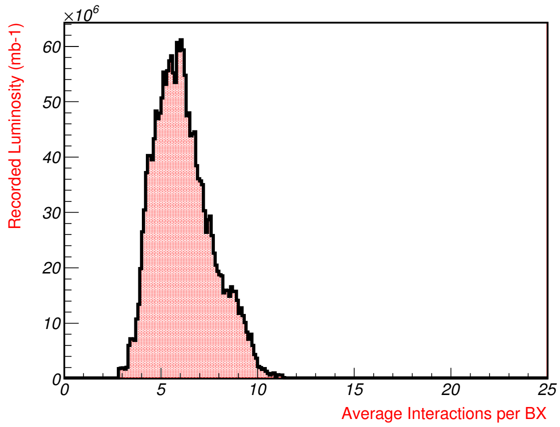

(a)

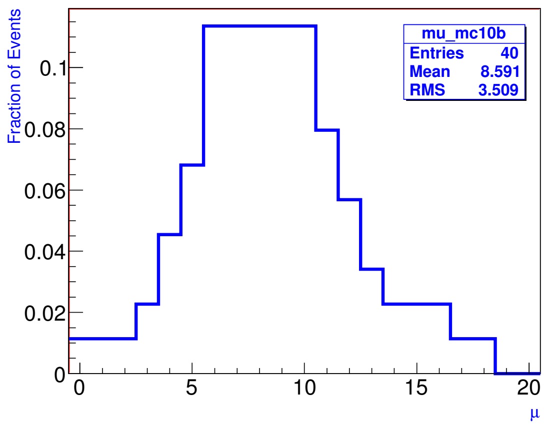

(b)

Figure 8.1: (a) Luminosity weighted average interaction per bunch crossing distributions for the full data sample used in this analysis (2.05 fb^{-1}), and (b) the pile-up distribution in the so-called MC10b Monte Carlo samples used the 2011 analysis.

and the EGamma performance group recommendation is to make the trigger requirement in the Monte Carlo and to apply on Monte Carlo samples an η-dependent trigger scale factor to account for trigger efficiency difference between data and Monte Carlo. Figure 8.2 shows the trigger efficiency as a function of electron E_T measured in data using the tag-and-probe method by the ATLAS EGamma performance group and figure 8.2(b) shows that measured in a 1 TeV Z' MC sample by ATLAS Exotics di-electron sub-group. Table 8.2 displays the η-dependent EF_e20_medium trigger scale factors.

8.2.3 LAr front-end board failure

Starting from run 180614 (period E) till run 184169 (end of period H) that corresponds to about 869.7 pb^{-1} of our 2011 dataset, there were 6 front-end boards (FEBs) in the Liquid Argon calorimeter missing due to hardware problems. The affected region was $\Delta\eta \times \Delta\phi$= 1.4×0.2, centered at η = 0.7 and ϕ = -0.7 which corresponds to 0.8% of the precision coverage. In data, this bad detector region is removed by applying the electron and photon Object Quality flags. In MC, a map is applied on a fraction of events corresponding to the fraction of affected data by means of picking a random run number and pass it to the checkOQ tool [83].

Table 8.2: Official EGamma EF_e20_medium trigger scale. Uncertainties listed include statistical and systematic uncertainties.

η bin	EF_e20_medium scale factor
[-2.47,-2.37]	0.966 ± 0.006
[-2.37,-2.01]	0.974 ± 0.006
[-2.01,-1.81]	0.984 ± 0.004
[-1.81,-1.52]	0.987 ± 0.004
[-1.52,-1.37]	0.978 ± 0.006
[-1.37,-1.15]	0.997 ± 0.004
[-1.15,-0.8]	0.990 ± 0.005
[-0.8,-0.6]	0.985 ± 0.005
[-0.6,-0.1]	0.993 ± 0.004
[-0.1,0.0]	0.991 ± 0.004
[0.0,0.1]	0.993 ± 0.004
[0.1,0.6]	0.992 ± 0.004
[0.6,0.8]	0.997 ± 0.004
[0.8,1.15]	0.991 ± 0.005
[1.15,1.37]	0.996 ± 0.004
[1.37,1.52]	0.990 ± 0.005
[1.52,1.81]	0.998 ± 0.004
[1.81,2.01]	0.978 ± 0.007
[2.01,2.37]	0.979 ± 0.004
[2.37,2.47]	0.979 ± 0.010

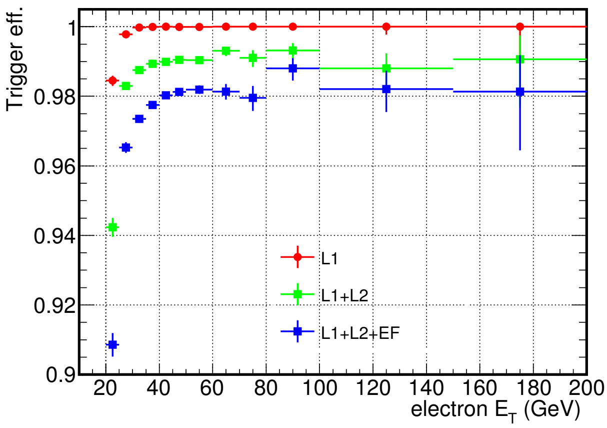

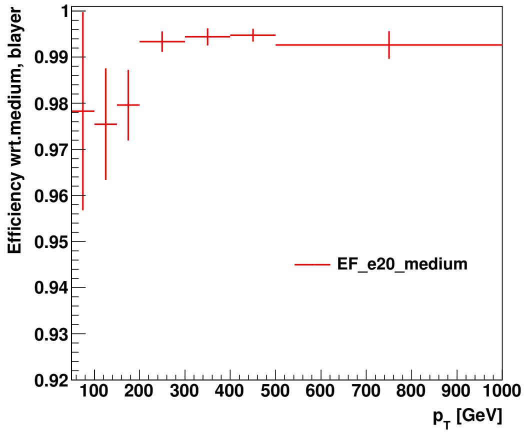

(a)

(b)

Figure 8.2: Trigger efficiency as a function of electron E_T measured in data using the tag-and-probe method (a) and measured in a 1 TeV Z' MC sample (b) [9].

8.2.4 Electron and photon energy resolution smearing

As mentioned in sub-section 7.2.3, a study of the $Z \to ee$ and $W \to e\nu$ events using the full 2010 dataset has shown that the Monte Carlo simulation does not reproduce exactly the electromagnetic energy resolution [86] observed in the data. According to EGamma performance group recommendation, an η-dependent energy scaling on data is applied using the official recommended tool [87]. Moreover, the resolution of the electromagnetic clusters is smeared in Monte Carlo events to reproduce the resolution measured in data using the so-called EnergyRescaler tool [87] provided by the EGamma performance group.

8.2.5 Electron reconstruction efficiency scaling

An η-dependent electron reconstruction scale factor is applied on Monte Carlo samples to account for the reconstruction efficiency discrepancies observed in data and Monte Carlo. Table 8.3 shows the EGamma reconstruction efficiency scale factors.

Table 8.3: Official EGamma electron reconstruction scale factors. Uncertainties listed include statistical and systematic uncertainties.

$\|\eta\|$ bin	reconstruction scale factor
[0.0, 0.8]	0.998 ± 0.007
[0.8, 2.37]	1.009 ± 0.007
[2.37, 2.47]	0.976 ± 0.018

8.2.6 Electron identification efficiency scaling

To account for the electron identification efficiency discrepancies observed in data and Monte Carlo, an η-dependent and p_{T}-dependent scale factor is applied to each Monte Carlo event which is the product of two scaling factors (see subsection 6.2.1.1):

- *medium* identification selection scale factor provided by EGamma group [12],
- additional scaling factors computed by the exotic di-electron subgroup to account for the additional B-layer requirement on the second leading p_{T} electron and the addition B-layer plus isolation requirement on the leading p_{T} electron (see event selection later) on top of the medium selection in the current analysis.

The η-dependent *medium* scale factors and the additional B-layer and B-layer+isolation scale factors are displayed in table 8.4.

Table 8.4: Official EGamma *medium* scale factor, the additional B-layer scale factors applied on second leading p_{T} electron and the additional B-layer+Isolation scale factors applied on the leading p_{T} electron on top of the *medium* identification efficiency. Uncertainties listed are statistical only.

η bin	medium scale factor	B-layer scale factor	B-layer+Isolation scale factor
[-2.47,-2.37]	0.957 $\pm$ 0.008	1.042 $\pm$ 0.008	1.043 $\pm$ 0.008
[-2.37,-2.01]	0.955 $\pm$ 0.015	1.027 $\pm$ 0.002	1.028 $\pm$ 0.002
[-2.01,-1.81]	0.964 $\pm$ 0.008	1.007 $\pm$ 0.002	1.008 $\pm$ 0.002
[-1.81,-1.52]	0.963 $\pm$ 0.005	1.002 $\pm$ 0.002	1.002 $\pm$ 0.002
[-1.52,-1.37]	0.980 $\pm$ 0.010	1.007 $\pm$ 0.002	1.007 $\pm$ 0.002
[-1.37,-1.15]	0.963 $\pm$ 0.007	1.002 $\pm$ 0.001	1.001 $\pm$ 0.001
[-1.15,-0.8]	0.971 $\pm$ 0.006	1.002 $\pm$ 0.001	1.002 $\pm$ 0.001
[-0.8,-0.6]	0.963 $\pm$ 0.007	1.001 $\pm$ 0.001	1.000 $\pm$ 0.001
[-0.6,-0.1]	0.972 $\pm$ 0.006	1.005 $\pm$ 0.001	1.004 $\pm$ 0.007
[-0.1,0.0]	0.979 $\pm$ 0.008	1.003 $\pm$ 0.002	1.004 $\pm$ 0.002
[0.0,0.1]	0.966 $\pm$ 0.008	1.010 $\pm$ 0.001	1.010 $\pm$ 0.002
[0.1,0.6]	0.968 $\pm$ 0.007	1.004 $\pm$ 0.001	1.004 $\pm$ 0.001
[0.6,0.8]	0.971 $\pm$ 0.007	1.003 $\pm$ 0.001	1.003 $\pm$ 0.001
[0.8,1.15]	0.965 $\pm$ 0.006	1.003 $\pm$ 0.001	1.003 $\pm$ 0.001
[1.15,1.37]	0.954 $\pm$ 0.010	1.005 $\pm$ 0.001	1.004 $\pm$ 0.001
[1.37,1.52]	0.980 $\pm$ 0.006	1.003 $\pm$ 0.001	1.004 $\pm$ 0.002
[1.52,1.81]	0.963 $\pm$ 0.005	1.003 $\pm$ 0.002	1.003 $\pm$ 0.002
[1.81,2.01]	0.974 $\pm$ 0.013	1.004 $\pm$ 0.003	1.004 $\pm$ 0.003
[2.01,2.37]	0.958 $\pm$ 0.007	1.020 $\pm$ 0.002	1.020 $\pm$ 0.002
[2.37,2.47]	0.972 $\pm$ 0.014	1.057 $\pm$ 0.008	1.057 $\pm$ 0.008

8.2.7 Photon ID efficiency

The `ATLAS` excited lepton sub-group has used a mixture of all excited muon signal samples, in order to study the efficiency of the photon reconstruction, fudge factors, photon identification, FSR suppression and isolation criteria as function of true photon p_T for photons within the calorimeter acceptance [10]. Figure 8.3 shows the results for the barrel and end-cap regions separately. From these distributions, one can observe that the efficiency of the preselection cuts (fudge factor+loose) are approximately independent of photon E_T, giving confidence in the corrections applied. The FSR suppression requirement is shown to be a safe choice as the photon is well separated from the two signal electrons. The tight selection results in about a 5% (8%) absolute efficiency loss with respect to the loose selection in the barrel (end-cap). A drop in efficiency is also observed for the tight selection of about 3% per TeV. The impact of the isolation cut corresponds to an absolute loss of signal efficiency of about 1-2% with respect to the tight selection, and no significant loss of efficiency is observed as a function of photon E_T.

The fudge factors are meant to take into account the difference in shower shapes between data and Monte Carlo. From figure 8.3, one can see the impact of the fudge factors on the reconstruction: the efficiency improves as a function of photon E_T by about 2%/TeV with respect to the default tight identification. This discrepancy is used later on as a systematic uncertainty on the photon E_T efficiency [10].

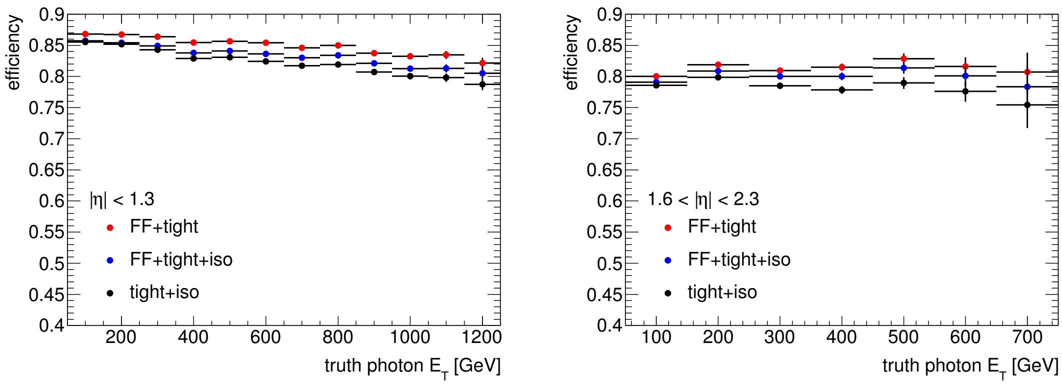

Figure 8.3: Photon reconstruction and isolation efficiencies as a function of the photon momentum for all signal samples. The efficiency for the barrel and end-caps are shown separately, and the crack regions were removed [10].

The photon identification efficiency has been evaluated by running over Monte Carlo samples with additional material. Additional material increases the percentage of the converted photons, which have different shower shapes and hence are optimized separately from unconverted photons. Such samples thus allow to quantify a systematic uncertainty on the identification efficiency due to a different fraction of photons coming from conversions. The difference in absolute value with respect to the nominal event identification efficiency was measured in [92] to be around 1%, and is taken as an additional uncertainty on the photon efficiency. The effect of pileup on the reconstruction efficiency was also investigated in [92] and was shown to be of order 1% per photon.

8.3 Electron, photon and event selection

After some preliminary studies, the `ATLAS` exotic excited electron subgroup converged towards a set of cuts, preserving potential signal efficiently, while minimizing background processes. The selection criteria include the following set of cuts:

- the event is in the Good Runs List, to ensure the sub-detectors concerned by the analysis were ready and no have no serious hardware problem (see subsection 8.1.1),

- no noise burst present in the calorimeter system in the event , i.e. LarError < 1, (see subsection 6.4),
- the event passes the trigger, EF_e20_medium for periods B-J, and EF_e22_medium for period K (see subsection 8.1.3),
- the event has at least one primary vertex, with more than two tracks. This cut is used to ensure the electron that triggered an event was produced in a pp collision.
- at least 2 electrons:
  - with author 1 or 3, to ensure that the electron candidates are selected by either the standard reconstruction (calorimeter-seeded) algorithm or by both the standard and the soft electron (track-based) algorithms (see section 6.1.3).
  - in the calorimeter acceptance, $|\eta| < 2.47$ excluding the crack region $1.37 < |\eta| < 1.52$ between the barrel and end-cap compartments of the EM calorimeter. The η variable used here is η_{cl}: the electron associated cluster η.
  - with transverse momentum $p_{\mathrm{T}} > 25$ GeV. Following EGamma recommendations, $p_{\mathrm{T}} = E_{\mathrm{T}} = E_{cluster}/\cosh\eta$, where η here is the cluster η_{cl} or track η_{track} depending on the track quality.
  - Having cluster that passes the checkOQ requirement [83],
  - pass the ISEM *medium* identification selection (see subsection 6.2.1),
  - having a B-layer hit, if one is expected,
  - $\Delta R = \sqrt{\Delta\eta + \Delta\phi} > 0.1$, if 2 electrons have $\Delta R < 0.1$, the lower p_{T} electron is removed.
- The leading p_{T} electron has to be isolated (EtCone20_ptNPV_corrected < 7 GeV), see subsection 6.3,
- the two leading electrons invariant mass must be at least 70 GeV, in order to remove irrelevant low mass events, the Z peak was kept for normalization purposes,
- at least 1 photon:
  - has author 4 or 6 (see section 6.1.3),
  - is within $|\eta| < 2.37$, and out of crack region $1.37 < |\eta| < 1.52$,
  - has transverse energy $E_{\mathrm{T}} > 20$ GeV
  - has calorimeter cluster that pass the checkOQ and photon clean[9] requirements [83],
  - has $\Delta R = \sqrt{\Delta\eta + \Delta\phi} > 0.7$ from the leading and next to leading electrons selected above, this cut is applied to suppress background from FSR photons associated in $Z/\gamma* \to ee$ decays. A cut of $\Delta R = 0.7$ was also used by the SM $Z\gamma$ and is considered a safe choice. Signal efficiency is not affected as will be shown below.
  - has to be isolated Etcone40_ED_corrected < 10 GeV (see section 6.3),
  - pass the ISEM TightAR selection (see subsection 6.2.2).

[9]The photon cleaning principle is to remove clusters with large amount of energy from bad cells by requiring: $\frac{\sum_{cluster} E_{cell}(Q>4000)}{\sum_{cluster} E_{cell}} > 0.8$.

– In order to take into account the differences in the MC description of the shower shapes, the variables used in the ISEM *tight* identification criteria are shifted in MC by an amount corresponding to the observed difference between a *loose* isolated photon sample selected from 2011 data and a mixed γ + jets MC sample. These shifts, called fudge factors (FF), are provided by the EGamma working group.

– If more than one photon satisfy the above selection, the highest p_{T} photon is used.

8.4 Backgrounds estimation

8.4.1 Drell-Yan control sample

Drell-Yan events (events left after the 2 leading ee invariant mass cut, $ee - selection$) were used to check that Monte Carlo normalization and electron corrections were properly applied and adequate. The $Z+\gamma$, diboson and $t\bar{t}$ Monte Carlo samples were all normalized to the total integrated luminosity according to their cross sections presented in tables 5.7, 5.11 and 5.12.

Figure 8.4 shows the E_{T} distribution of both electrons, leading p_{T} and sub-leading p_{T} separately after $ee - selection$ and prior to applying any photon requirement. Figure 8.5 displays the η distribution of both electrons after $ee - selection$. Figure 8.6 presents the 2 leading electrons invariant mass (m_{ee}) distribution after $ee - selection$. Except for a small excess of data on the low side of the Z-pole mass, a reasonable agreement between data and Monte Carlo is found for both distributions which indicates that the Monte Carlo corrections and normalization are adequate. The excess of data at low dielectron mass is likely coming from W+jets and multijet background faking dielectron events which are not included in this figure. These backgrounds were estimated to be less than 0.2% of the Drell-Yan for $M_{ee} < 110$ GeV, and at most 5% of the total ee yield for the full mass spectrum up to 3 TeV [10]. As we require an additional isolated tight photon, the W+jets and multijet multijet backgrounds are considered negligible and are ignored in this analysis.

8.4.2 Adding TightAR photon ($ee\gamma - selection$)

For the plots after photon requirement, $ee\gamma - selection$, we look at the distribution in the control region for which the $ee\gamma$ invariant mass $m_{ee\gamma} < 300$ GeV. Figure 8.7 shows the E_{T} distribution of both electrons, leading p_{T} and sub-leading p_{T} separately after $ee\gamma - selection$. Figure 8.8 shows the leading and sub-leading electrons isolation (EtCone20_ptNPV_corrected, see subsection 6.3) distributions of both electrons separately, and figure 8.9 displays the η distribution of both electrons. Figure 8.10 shows the photon p_{T}, energy density (ED) corrected isolation (see subsection 6.3), and η distributions after the final selection ($ee\gamma - selection$). Figure 8.11 presents the 2 leading electrons invariant mass (m_{ee}) distribution while figure 8.12 presents the three body invariant mass ($m_{ee\gamma}$) distribution after $ee\gamma - selection$.

Figure 8.13 shows the electron-photon invariant mass for different combinations, namely leading p_{T} electron leading photon, sub-leading electron leading photon, and the highest and lowest mass combinations after ($ee\gamma - selection$).

Our background determination relies on Monte Carlo predictions for the $Z + \gamma$ irreducible background, as well as the diboson and $t\bar{t}$ backgrounds. Z+jets $\rightarrow e^{+}e^{-}$+jets is

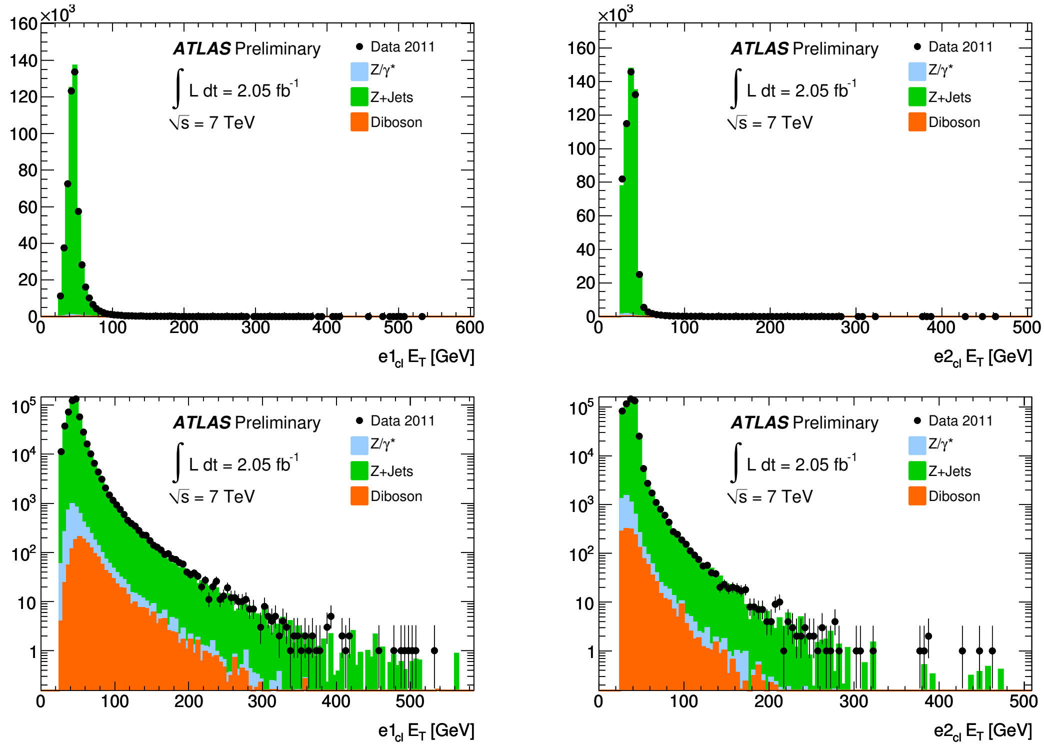

Figure 8.4: E_{T} distributions after $ee - selection$. Left: leading electron, right: subleading electron. The upper plots are in linear scale and the lower ones are in log scale

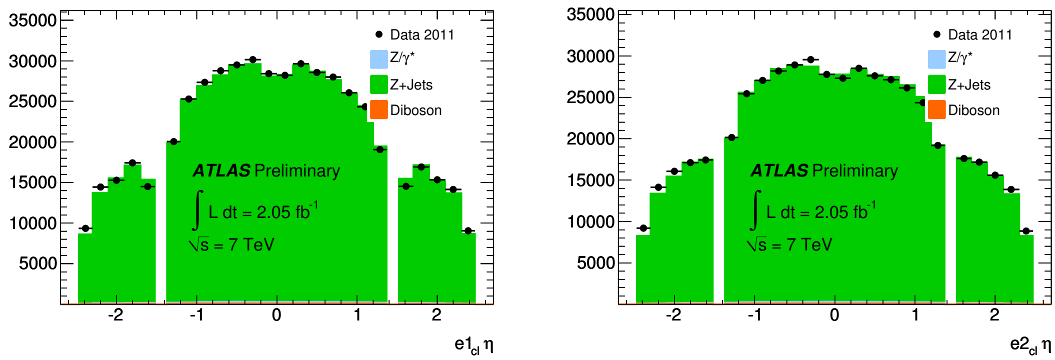

Figure 8.5: η distributions after $ee - selection$. Left: leading electron, right: subleading electron.

the second largest background in this analysis. This background becomes significant when Z boson decays leptonically to two electrons and a jet is mis-identified in the detector as a photon. Although the photon selection criteria are very effective at rejecting jet fakes, a significant fraction of the background arises from $Z+$jets. As can be seen in table 8.5, the jet-to-photon fake rate is not well modeled in the current Monte Carlo simulation. Since the jet to photon fake rate is not well modeled in Monte Carlo, the `Exotic Excited Lepton` sub-group rely on data-driven methods in modeling Z+jets, see sub-section 8.4.4.

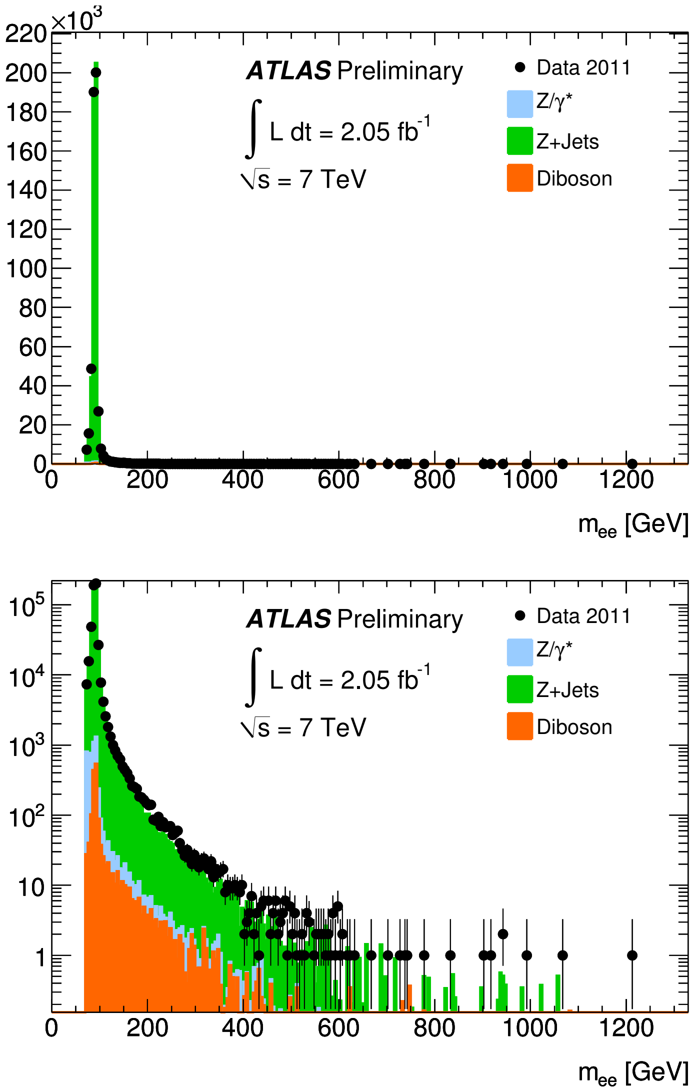

Figure 8.6: Dielectron invariant mass ($m_{e^+e^-}$) distribution after $ee-selection$, compared to the stacked sum of $Z+\gamma$, $Z+njets$ and Dibosons backgrounds. Up: linear scale, down: log scale

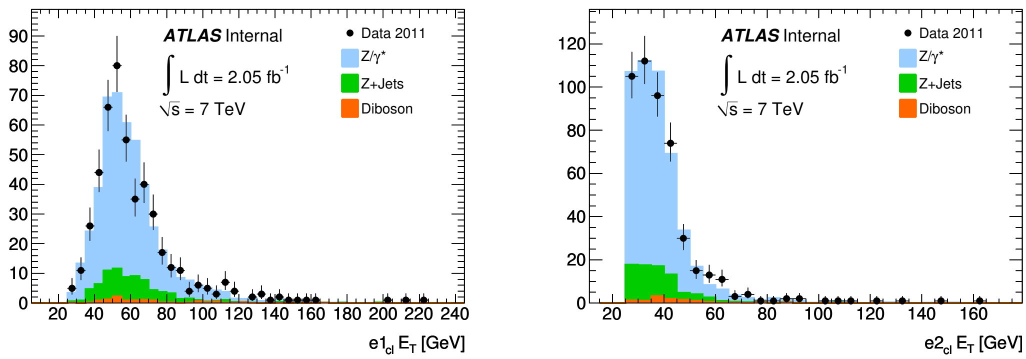

Figure 8.7: E_{T} distributions after $ee\gamma-selection$. Left: leading electron, right: subleading electron.

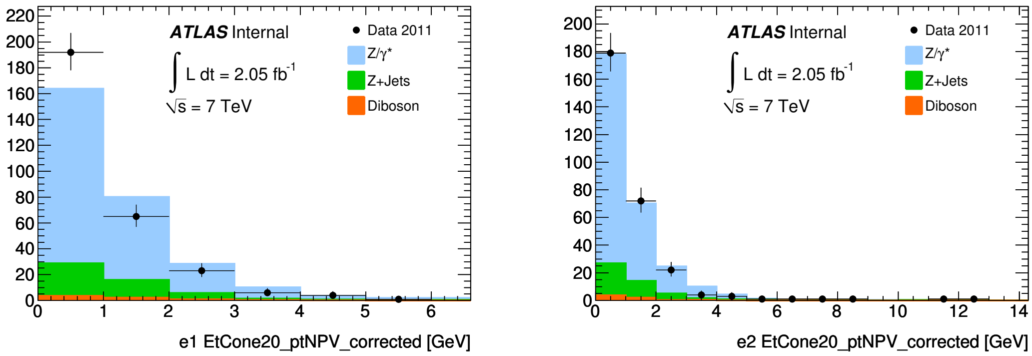

Figure 8.8: Electron isolation distributions after $ee\gamma - selection$. Left: leading electron, right: subleading electron.

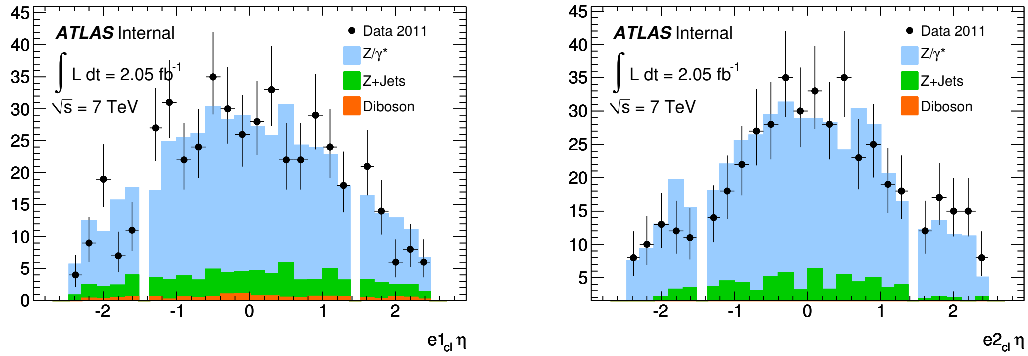

Figure 8.9: η distributions after $ee\gamma - selection$. Left: leading electron, right: subleading electron.

8.4.3 MC backgrounds

8.4.3.1 $Z + \gamma$ background

For the irreducible $Z + \gamma$ background, we rely on Monte Carlo generated with the SHERPA event generator[10].

The expected number of $Z + \gamma$ events integrated in the control region $m_{ee\gamma}$ <300 GeV($m_{ee\gamma}$ graph) is 306±10, where the systematic error considered here is the uncertainty due to data luminosity (other sources will be added) see later.

The primary sources of systematic error in the $Z + \gamma$ background estimation are due to the data luminosity measurement (3.7%) [93], QCD NLO K-factor statistical error, and the NLO cross-section uncertainty due to PDF and scale uncertainties.

- PDF uncertainty: there are 40 PDF error sets of MSTW2008nlo90cl[11]. The Exotic excited lepton group evaluated a combined uncertainty for both α_s and PDF uncertainties. In deriving this combined uncertainty an additional 4 sets are used beside the MSTW2008nlo90cl PDF set, corresponding to shifted values of α_s.
- Scale uncertainty: as mentioned in detail in [10] the nominal value of renormalization

[10]See section 5.4.1, table 5.7 for cross-sections and K-factor used to normalize $Z + \gamma$ to data.
[11]MSTW2008nlo90cl is the NLO PDF set, see section used Z+γ as well as other MC samples, see section 5.4.1.1.

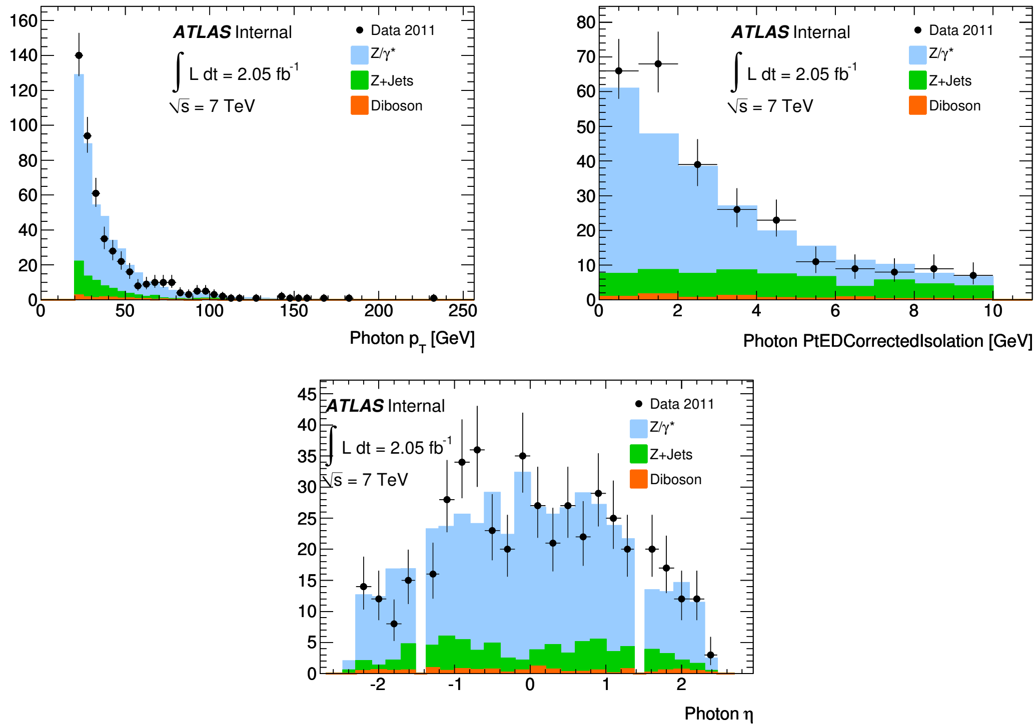

Figure 8.10: Photon p_{T} , isolation (Etcone40_EDCorrected, see subsection 6.3)), and η distributions after $ee\gamma - selection$. Upper left: p_{T}, upper right: isolation, lower: η.

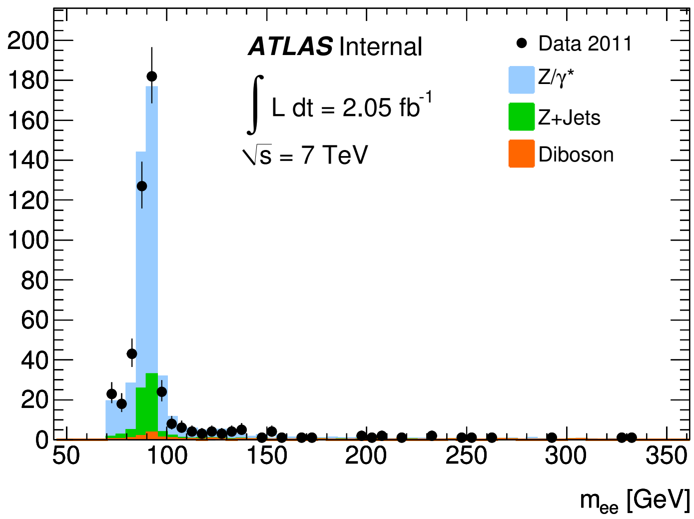

Figure 8.11: Dielectron invariant mass ($m_{e^+e^-}$) distribution after $ee\gamma{-}selection$, compared to the stacked sum of $Z+\gamma$, $Z+njets$ and Dibosons backgrounds.

and factorization scales is chosen to be $\mu_R = \mu_F = m_Z$. In order to estimate the sensitivity of the NLO cross section to missing higher order QCD corrections, one scale is varied up and down by factor of two, and then the other. The maximum deviations are taken as scale uncertainty.

The total uncertainty on the QCD NLO K-factor are obtained by summing in quadrature the statistical uncertainty arising from MCFM and SHERPA differential cross sections (see section 5.4.1), and the scale and $\alpha_s + PDF$ uncertainties on the NLO cross section. Table 8.6 shows these uncertainties as well as the total uncertainty as a function of $m_{ee\gamma}$.

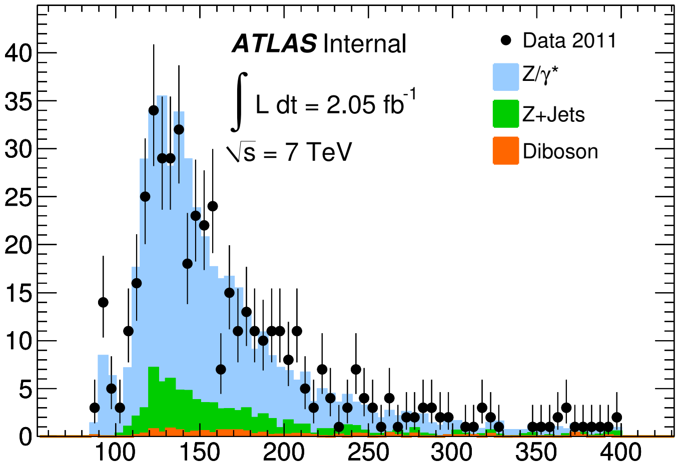

Figure 8.12: The three body invariant mass ($m_{ee\gamma}$) distribution after $ee\gamma - selection$, compared to the stacked sum of $Z+\gamma$, $Z+njets$ and Dibosons backgrounds.

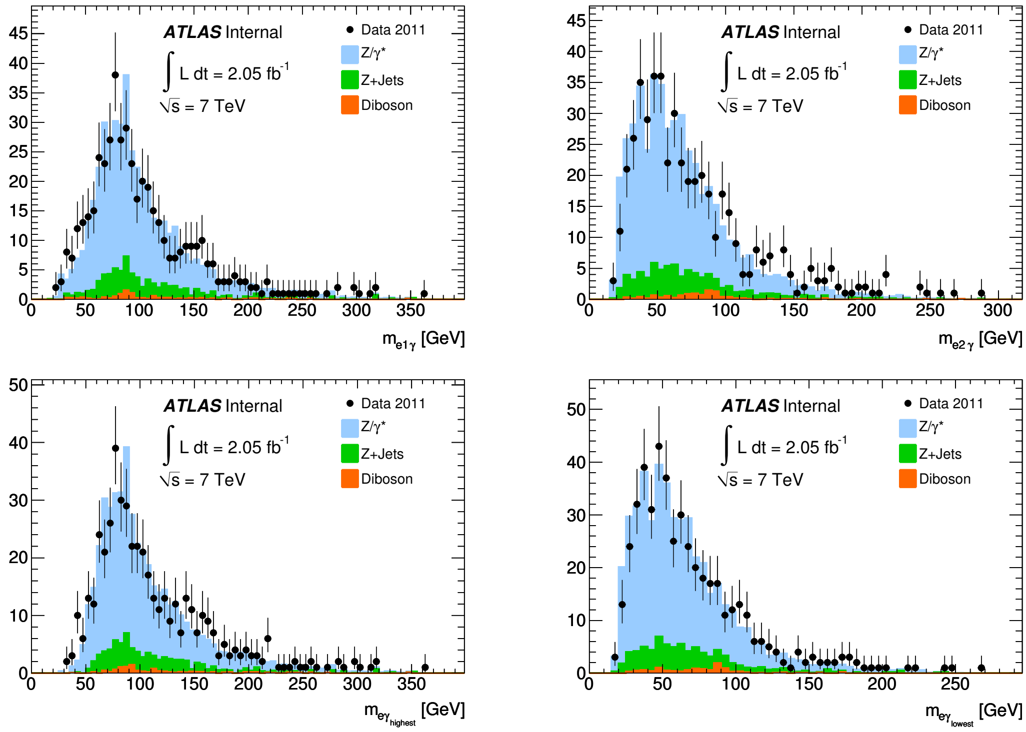

Figure 8.13: Electron-photon invariant mass $m_{e\gamma}$, after the final $ee\gamma - selection$. Upper left: leading p_{T} electron photon, upper right: sub-leading electron photon invariant mass and lower left: electron photon highest invariant mass combination, lower right: electron photon lowest invariant mass combination.

8.4.3.2 Diboson (WW, WZ, ZZ)

In modeling we rely on Monte Carlo HERWIG generated samples, for more details about these samples see section 5.4.3.

Table 8.5: Cut flow for the data and background simulation for the e^* search. For this table, no correction is applied to the $Z+$jets prediction from ALPGEN samples listed in table 5.10. The last row provides the yields in the low $M_{ee\gamma}$ control region described below.

Cuts	$Z+\gamma$	$Z+$jets	$t\bar{t}$	dibosons	total	data
$M_{ee} > 70$ GeV	3228	495393	1121	949	500691	514210
Loose γ	882	64621	361	193	66056	86004
$\Delta R(\gamma, e) > 0.7$	508	7099	230	78	7916	7236
Tight γ	344	339	4.44	9.86	698	515
Iso γ	331	285	2.94	9.01	628	484
$M_{ee\gamma} < 300$	306	269	2.41	8.26	586	455

Table 8.6: QCD NLO k-factor for the $Z+\gamma$ process and associated uncertainties, as a function of $m_{ee\gamma}$ [10].

$m_{ee\gamma}$	K-factor	Δ stat. %	Δ PDF %		Δ scale %		Δ total %	
40-100	0.87	±1.74	+4.69	-4.28	+2.45	-3.28	+5.57	-5.67
100-200	0.74	±0.54	+4.30	-3.79	+2.56	-2.76	+5.03	-4.72
200-300	0.80	±1.31	+4.28	-3.86	+3.82	-3.19	+5.88	-5.17
300-400	0.89	±1.41	+4.34	-3.99	+4.21	-3.17	+6.21	-5.29
400-600	0.98	±1.36	+5.17	-4.98	+4.29	-3.28	+6.85	-6.12
600-800	1.12	±2.25	+5.58	-4.54	+4.61	-3.43	+7.58	-6.12
800-1000	1.24	±3.24	+6.24	-5.81	+5.19	-3.55	+8.74	-7.54
1000-1200	1.30	±4.78	+8.55	-5.49	+5.83	-3.68	+11.40	-8.24
1200-1600	1.35	±5.51	+10.06	-7.22	+5.97	-4.44	+12.93	-10.11

- WW: this background becomes relevant when both W bosons decay to an electron and a neutrino and an extra photon is emitted via ISR or FSR.
- WZ: this background becomes relevant when the W boson decays to an electron and a neutrino and the Z boson decays leptonically to two electrons. The photon can be emitted via ISR or FSR or one of the electrons is misidentified as a photon.
- ZZ: this background becomes relevant when both of the Z bosons decay leptonically to two electrons and the photon can be emitted via ISR or FSR or one of the electrons is misidentified as a photon.

The contribution of these backgrounds is expected to be small, this is why we combine them as a diboson background. The expected number of diboson events integrated over all mass ($m_{ee\gamma}$ graph) is 12.4±0.4 events, while the expected number events integrated in the control region $m_{ee\gamma}$ <300 GeV($m_{ee\gamma}$ graph) is 10.7±0.36 events.

8.4.3.3 $t\bar{t}$ background

Top quark decays almost exclusively to a W boson and a b quark. Thus $t\bar{t}$ events can be a source of background when one of the b quarks radiates a hard photon and both W bosons decay in the electron channel. The $t\bar{t}$ background was estimated using Monte Carlo MC@NLO to generate matrix elements, and also JIMMY to describe multiple parton interactions and HERWIG to describe the remaining underlying event and parton showers (see sub-section 5.4.4).

The expected number of $t\bar{t}$ events integrated over all mass ($m_{ee\gamma}$ graph) is 4.01±0.14 events, while the expected number of events integrated in the control region $m_{ee\gamma}$ <300 GeV($m_{ee\gamma}$ graph) is 3.26±0.11 events.

8.4.4 Estimation of Z+jets background

Three data-driven methods are used to estimate Z+jets background:

- low mass sideband method,
- jet $\rightarrow\gamma$ fake rate method,
- Smirnov transform method,

8.4.4.1 Z+jets background from low mass sideband method

This method is chosen by the `Exotic Excited Lepton` group to be the baseline method to determine the Z +jets events. In this method, a control region in terms of the 3 body invariant mass $m_{ee\gamma}$ after final selection was defined ($m_{ee\gamma}$ <300 GeV). This region was chosen such that it is signal free. In this method all the above mentioned backgrounds taken from Monte Carlo are summed together then the difference between observed data and Monte Carlo background predictions in the control region is then our estimate of the number of Z+ jets events. As shown in table 8.5, the total number of data events in the sideband region ($m_{ee\gamma} < 300$ GeV) is 455, whereas the number of $Z+\ \gamma$, $t\bar{t}$ and diboson events is 317±8. Therefore, the Z+ jets MC ALPGEN[12] prediction is normalized to 455 - (317 ± 8) = 138 ± 8, where the uncertainties are statistical only. The number of Z + jets events after all cuts is 269±16, therefore the Monte Carlo predicted number is scaled down by a ratio 138/269. Systematic uncertainties from this method are fully correlated with the luminosity and $Z + \gamma$ cross section uncertainties (3.7% and 5.5%, respectively), and are evaluated to be ±40 events. Hence, the total Z + jets background is estimated to be:

$$N_{Z\ +jets} = 138 \pm\ 8 \pm\ 40 \tag{8.1}$$

this is the expected number of Z+jets events in our control region.

8.4.4.2 Z+jets background using jet $\rightarrow\gamma$ fake rate

In this data-driven approach, the Z+jets contribution is measured by applying, after $ee-selection$, the photon fake rate evaluated in seb-section 6.5 on a dataset of Z+jets events. The event selection is the same as that for signal search (see section 8.3) up to $M_{ee} > 70$ GeV cut, then adding at least one jet which satisfies the following selection:

- reconstructed with the AntiK_T reconstruction algorithm with radius R=0.4,
- $|\eta| < 2.8$ and p_{T}> 20 GeV,

[12]See section for more details about these Monte Carlo samples.

- pass LArHole[13] cut to avoid bad calorimeter region edge effects [85],
- the jet is removed if it is assigned as BadMedium or Ugly [84].

Each entry in the e^+e^-, $e^+e^-\gamma$, and $e\gamma$ invariant mass plots is weighted by the rate for the jet to fake a photon which is described in details in sub-section 6.5 evaluated at jet p_{T}. In addition, the expected photon E_{T} that is used in the invariant mass calculations is computed from the jet $E_{\mathrm{T}} \to \gamma$ E_{T} mapping function that was described in sub-section 6.5.3 since the energy scale for reconstructing jets is different from the EM scale. The event is removed if the expected photon p_{T} is less than 20 GeV.

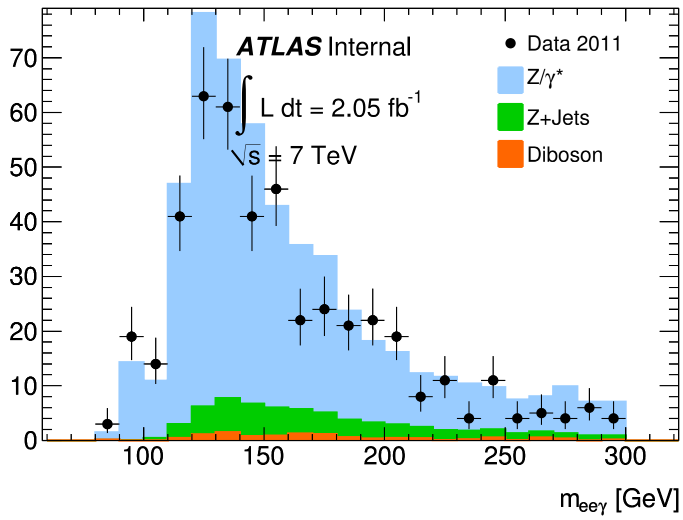

Figure 8.14: The three-body invariant mass ($m_{ee\gamma}$) distribution after $ee\gamma - selection$, compared to the stacked sum of $Z + \gamma$, $Z + njets$ and Dibosons backgrounds. $Z + njets$ shown here comes from the data-driven approach with photon fake rate estimation.

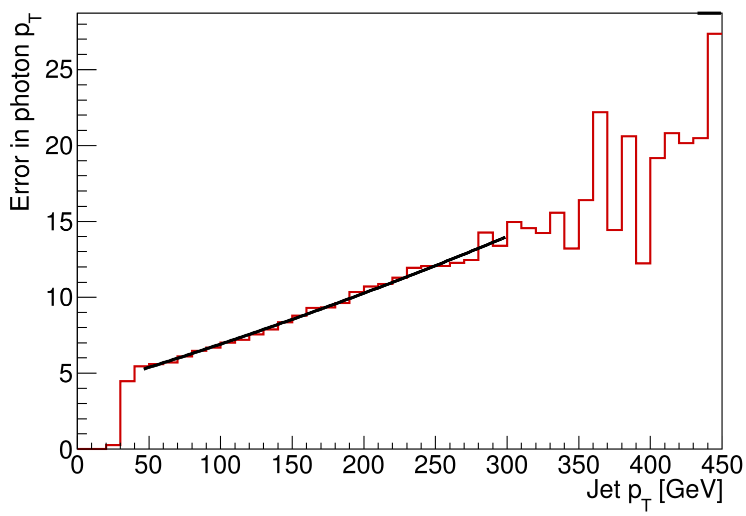

Figure 8.15: Resolution on the photon p_{T} in GeV as a function of jet p_{T}.

[13] LArHole problem refers to 6 missing front-end boards (FEBs) in the LAr Calorimeter that were lost during period E and were recovered later (before starting period K) during 2011 data taking

Table 8.7: Summary of $Z+$jets background determinations with our three data-driven methods.

method	$Z+$jets estimate
Low mass sideband	138 ± 40
Jet fake rate	100 ± 45
Smirnov transform	130 ± 22
Nominal	138 ± 40

Figure 8.14 shows the $M_{ee\gamma}$ distribution from data and all MC with $Z + jets$ coming from the current method. The integrated number from Z+jets $\rightarrow e^+e^-$+jets background is 100 ± 45 (*syst*), which agrees within uncertainty with the number of Z+jets events from the Z+jets background from low mass sideband method. The systematic uncertainty is dominated by the photon p_{T} resolution effects.

8.4.4.3 Smirnov transform method

The Smirnov transform method consists in tuning the jet shower shapes in the Monte Carlo so that they agree with jet shower shapes observed in data. To derive the Smirnov transform for all 12 isEM shower shape variables, the Alpgen $Z+$jets MC sample is compared to a data sample enriched in $Z+$jets events, as described in referance [10]. Once shower shapes are adjusted in the Monte Carlo, the analysis is rerun and results in the following number of $Z+$jets events in the control region: $130 \pm 8\,(\mathrm{stat}) \pm 20\,(\mathrm{syst})$. This is in reasonable agreement with the sideband and jet-fake-rate estimates.

Summary of $Z+$jets estimates

A summary of the $Z+$jets background estimates is provided in table 8.7. The low $M_{ee\gamma}$ sideband region is used to determine the Alpgen $Z+$jets normalization, and a ±40 events uncertainty is assigned to this estimate. The shape from Monte Carlo is then extrapolated to estimate the background for large $M_{ee\gamma}$ (the signal region, $m_{ee\gamma} > 350$ GeV), see section 8.7. In addition to the uncertainty on the fit parameters, a 30% uncertainty is assigned on the normalization as evaluated in the low $m_{ee\gamma}$ sideband region.

8.5 Signal efficiency

Figure 8.16 shows the acceptance times efficiency of the signal selection for all our excited electron simulated samples as a function of the excited electron mass, with and without the correction for the generator filter efficiency. The total acceptance times efficiency is about 56% for $m_{e^*} > 0.7$ TeV. The cutflow for different m_{e^*} with $\Lambda = 5$ TeV is provided in table 8.8.

8.6 Data and background predictions in the signal region ($m_{ee\gamma} > 350$ GeV)

Figure 8.17 shows the electron and leading photon p_{T} distributions without any requirement on $m_{ee\gamma}$. Similarly, the mass of the electron-photon system for the two combinations

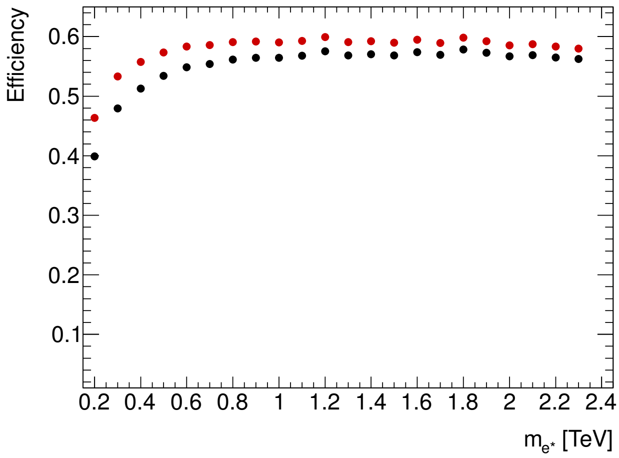

Figure 8.16: Total acceptance times efficiency as a function of the excited electron mass for a compositeness scale $\Lambda = 5$ TeV (in red). The acceptance corrected for the generator filter cuts is also shown (in blue) [10].

Table 8.8: Cut flow for 3 different excited electron masses: 0.5, 1 and 1.5 TeV, for an integrated luminosity of 2.05 fb^{-1}. A compositeness scale of $\Lambda = 5$ TeV was used.

Cuts	$m_{e^*} = 0.5$ TeV	$m_{e*} = 1$ TeV	$m_{e^*=1.5}$ TeV
GRL+LAr	64.32	9.70	1.37
Trigger	64.05	9.66	1.37
Vertex	64.04	9.66	1.37
2 good e	59.50	7.57	1.07
Medium e-ID	52.07	8.01	1.14
B-layer	49.57	7.70	1.09
Iso leading-e	47.24	7.31	1.03
$M_{ee} > 70$ GeV	47.05	7.31	1.03
Loose γ	42.25	6.61	0.93
$\Delta R(\gamma, e) > 0.7$	40.82	6.36	0.90
Tight γ	37.79	5.82	0.81
Iso γ	37.25	5.71	0.79

as well as the mass of the dielectron-photon system are shown in Figure 8.18. Overall, a reasonable agreement is observed between data and background predictions.

8.7 Z veto and final yields

Finally, to suppress both the $Z + \gamma$ and $Z +$ jets backgrounds and thus maximize signal significance, in particular for low m_{e^*}, a Z veto is applied by rejecting events with dielectron mass below 110 GeV. The impact on signal efficiency is of only $\sim 2\%$ for the lowest e^* masses, and is negligible for masses above 500 GeV. As the Monte Carlo statistics become very limited, we fit both the $Z + \gamma$ and $Z +$ jets shapes separately to obtain the background prediction in our signal region using an exponential function $\exp\left(P_0 + P_1 \times m_{ee\gamma}\right)$ as shown in figure 8.19. A log likelihood fit is performed, and the integral of the function in the bin instead of the center of the bin is used. The fit results

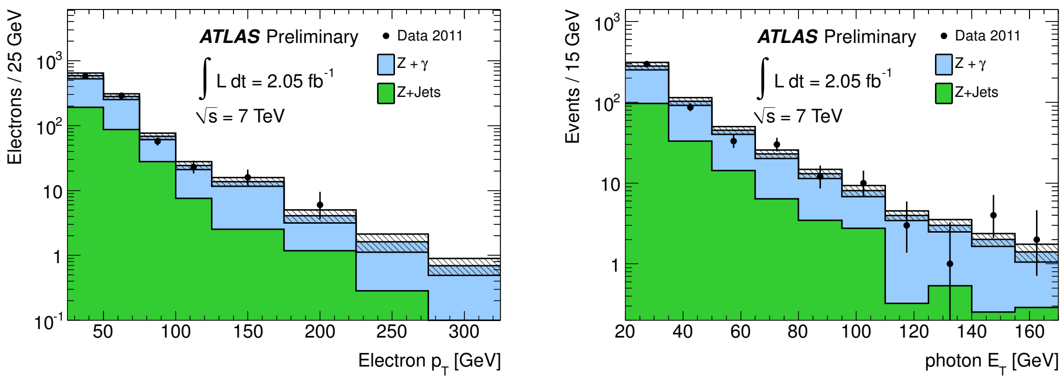

Figure 8.17: Electrons and photons p_{T}. The data are compared to the background sum.

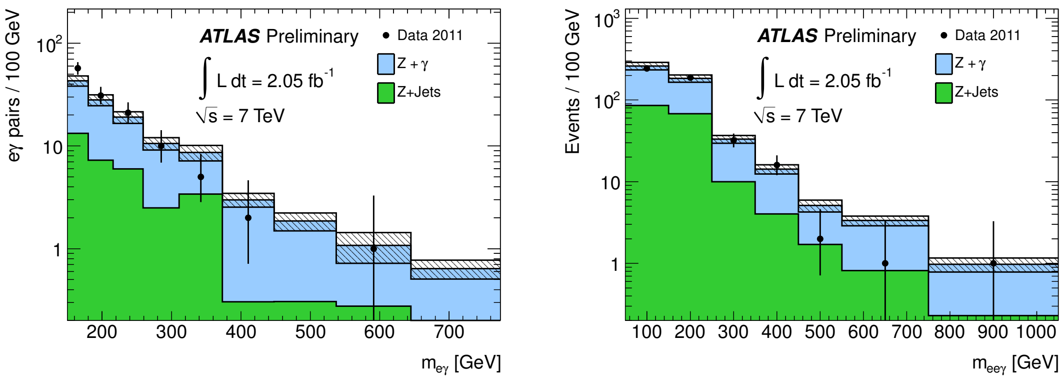

Figure 8.18: Electron-photon invariant mass for both the leading and subleading electrons (left), and invariant mass of the dielectron-photon system (right). The data are compared to the background sum. In the case of the dielectron-photon invariant mass, the $Z+$jets background prediction is obtained by using an extrapolation of the fitted shape.

and uncertainties are displayed in figure 8.19 and summarized in table 8.9. In addition to the uncertainty on the shape of the $Z+$jets, the uncertainty on the scale determined in section 8.4.4 is added in quadrature to obtain the total uncertainty on this background. The total background prediction is then the sum of the $Z+\gamma$ and $Z+$jets shapes and are reported in table 8.11 for different $m_{ee\gamma}$ thresholds.

8.8 Systematic uncertainties

The main systematic uncertainties of this analysis are listed in Table 8.10. The dominant systematic uncertainties on the irreducible $Z+\gamma$ background are from the extrapolation procedure to the signal region discussed in section 8.7. Theoretical uncertainties consist

Table 8.9: Summary of $Z+\gamma$ and $Z+$jets background fits.

background	P_0	P_1 (GeV^{-1})
$Z+\gamma$	5.05 ± 0.64	$(-7.8 \pm 1.6) \times 10^{-3}$
$Z+$jets	3.72 ± 1.34	$(-8.1 \pm 3.5) \times 10^{-3}$

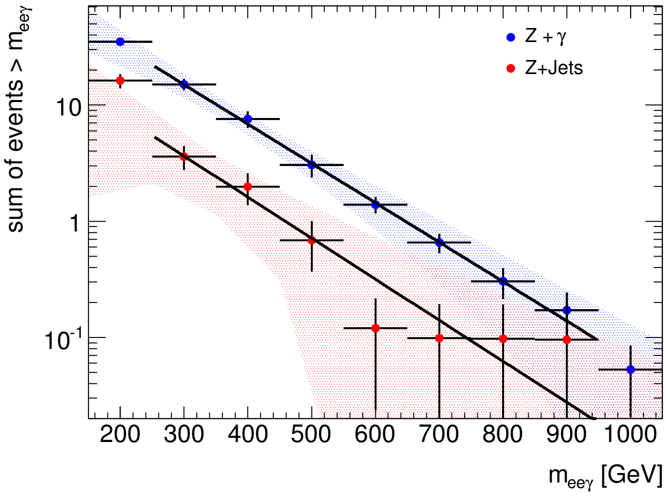

Figure 8.19: $Z + \gamma$ and $Z+$jets background estimates for the signal region. The y-axis provides the integral of the distributions above the $m_{ee\gamma}$ mass. The resulting fit, uncertainties and extrapolation to higher masses are displayed and will be used for the background distribution.

Table 8.10: Summary of dominant systematic uncertainties on the expected numbers of events for a m_{e*} of 0.5 TeV. NA indicates that the uncertainty is not applicable.

Source	m_{e^*}=0.5 TeV	
	signal	background
Luminosity	3.7%	3.7%
PDFs/scale	NA	6.5%
$Z + \gamma$ fit	NA	50%
$Z +$jets fit	NA	15%
Lepton eff	1%	1%
Photon eff	3%	3%
Total	5%	50%

of uncertainties on the QCD NLO K-factor. These were obtained from variations of the renormalization and factorization scales by factors of two around the nominal scales, and from uncertainties on the PDF (see section 8.4.3.1). For $m_{ee\gamma} > 350$ GeV, the resulting uncertainty on the $Z + \gamma$ background is about 6.5%.

Various techniques were used to estimate the reducible $Z +$jets background in the control region $m_{ee\gamma} < 300$ GeV. The uncertainty on the $Z +$jets normalization was determined to be about 35%, which covers the various estimates and their uncertainties. The shape of the $Z+$jets prediction from ALPGEN is then used to estimate the background for $m_{ee\gamma} > 350$ GeV. Uncertainties on the shape result in an additional uncertainty which grows exponentially with $m_{ee\gamma}$. The impact on the total background prediction are about 15%.

On the experimental side, the systematic effects are as follows:

- A 3% systematic uncertainty is assigned on the photon efficiency. These were evaluated by comparing the efficiency with and without the fudge factors (2%), by studying the impact of material mis-modelling in the inner detector (1%) and by studying reconstruction efficiency for various pile-up conditions (1%) [10].
- The average luminosity for the data sample used was of order of 10^{33} cm^{-2}s^{-1}, with

an average of 6 interactions per event. Pileup may then have a non-negligible effect on the primary vertex determination and may affect the photon p_{T} measurement as well. In this analysis, the dilepton (Z) event selection is applied before selecting a good photon, and as such, one expects little contribution from the pileup. Nevertheless, the `Exotic Excited Lepton` group studied the momentum balance between the dilepton p_{T} and E_{T} for all events falling within our signal region and found that the number of events where an imbalance was observed was consistent with the number of $Z+$jets events predicted (see reference [10]). Pile-up is thus assumed to have a negligible impact on this analysis.

- The calorimeter resolution is dominated at large transverse energy by a constant term which is 1.1% in the barrel and 1.8% some regions in the endcaps with a small uncertainty. The simulation was adjusted to reproduce this resolution at high energy and the uncertainty on it has a negligible effect and is therefore neglected. The calorimeter energy calibration uncertainty is between 0.5% and 1.5% depending on transverse momentum and pseudorapidity. The non-linearity of the calorimeter response is negligible according to test beam data and Monte Carlo studies [94]. The uncertainty on the energy calibration has minimal impact on the sensitivity of the search, since its main effect is a shift of a potential peak in electron-photon mass, but it has little effect on the $m_{ee\gamma}$ mass. We assign a systematic uncertainty for the electron efficiency at high p_{T} of 1%. This uncertainty is estimated by studying the lepton efficiency dependence of adding the calorimeter isolation cut.

- Finally an additional 1% systematic uncertainty is assigned to the signal efficiency for the case where $m_{e^*} = \Lambda$. This is the scenario where the excited leptons have the largest decay width, about 0.1 M_{ℓ^*}. This uncertainty was obtained by studying the efficiency of the $m_{ee\gamma}$ requirement at the generator level, by comparing results for various masses and scales Λ. As can be seen in Figure 8.20, for $\Lambda = 5$ TeV, the efficiency is optimal for all excited lepton masses, at near 100% for $M_{\ell^*} \geq 1$ TeV. For $M_{\ell^*} > 1$ TeV and $\Lambda = M_{\ell^*}$ TeV, the efficiency is $\sim 99\%$.

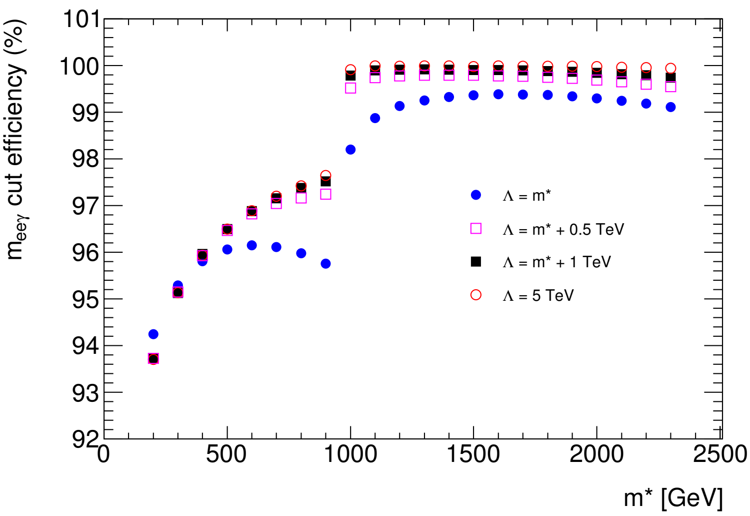

Figure 8.20: Signal efficiency as a function of m_{e^*} and Λ for the signal region defined in the text [10].

8.9 Results

8.9.1 Final yield

The data yield and background expectations as a function of a cut on the $m_{ee\gamma}$ is shown in table 8.11. The uncertainties displayed are the sum of the statistical and systematic uncertainties taken in quadrature. The yield obtained for data is compatible with background expectations.

Table 8.11: Data yield and background expectation as a function of a cut on the $M_{ee\gamma}$. The errors displayed represent the quadratic sum of the statistical and systematic uncertainties. The probability for the background only hypothesis (p-value) is also provided.

Region	$Z+\gamma$	$Z+$jets	diboson	$t\bar{t}$	total bkg	data	p-value
$M_{ee\gamma} > 350$	10.1 ± 1.9	0.65 ± 1.00	0.35 ± 0.13	0.39 ± 0.17	11.5 ± 2.19	8	0.92
$M_{ee\gamma} > 450$	4.64 ± 1.04	0.02 ± 0.56	0.15 ± 0.10	0.27 ± 0.16	5.09 ± 1.18	2	0.83
$M_{ee\gamma} > 550$	2.13 ± 0.73	0.02 ± 0.30	0.10 ± 0.10	0.02 ± 0.02	2.27 ± 0.79	1	0.80
$M_{ee\gamma} > 650$	0.98 ± 0.47	0.01 ± 0.15	0.03 ± 0.03	0.00 ± 0.00	1.02 ± 0.49	1	0.32
$M_{ee\gamma} > 750$	0.45 ± 0.29	0.01 ± 0.08	0.00 ± 0.00	0.00 ± 0.00	0.46 ± 0.30	1	0.16
$M_{ee\gamma} > 850$	0.20 ± 0.16	0.01 ± 0.04	0.00 ± 0.00	0.00 ± 0.00	0.21 ± 0.17	1	0.11
$M_{ee\gamma} > 950$	0.09 ± 0.09	0.01 ± 0.02	0.00 ± 0.00	0.00 ± 0.00	0.10 ± 0.09	1	0.03
$M_{ee\gamma} > 1050$	0.05 ± 0.05	0.00 ± 0.01	0.00 ± 0.00	0.00 ± 0.00	0.05 ± 0.05	0	0.81

8.9.2 Discovery statistics

The significance of a potential excited lepton signal is summarized by a p-value, the probability of observing an outcome of an analysis at least as signal-like as the one observed in data, assuming that a signal is absent. The common convention is that a p-value less than 1.35×10^{-3} constitutes evidence for a signal and a p-value less than 2.87×10^{-7} constitutes a discovery. These are one-sided integrals of the tails of a unit Gaussian distribution beyond $+3\sigma$ and $+5\sigma$, respectively.

Experimental outcomes are ranked on a one-dimensional scale using a test statistic that is used to calculate the p-value. A natural choice for the test statistic is based on the Neyman-Pearson lemma [95] which states that when performing a hypothesis test between two hypotheses - in our case one assuming the presence of signal and background (S+B) and one hypothesis that assumes only SM background (B) - the log-likelihood-ratio (LLR) $LLR = -2ln\frac{L(S+B)}{L(B)}$ is the best test to reject (B) in favor of (S+B). In the Gaussian limit, the LLR corresponds to the χ^2 difference for the two hypotheses under test $\Delta\chi^2 = \chi^2(B) - \chi^2(S+B)$.

In the presence of nuisance parameters to account for systematic uncertainties of each model, the LLR can be written more explicitly as:

$$LLR = -2\ln\frac{\mathcal{L}(data|\hat{N}_{e^*}, \hat{M}_{e^*}, \hat{\theta}_i)}{\mathcal{L}(data|(N_{e^*}=0), \hat{\hat{\theta}}_i)} \tag{8.2}$$

where $\hat{N}_{e^*}, \hat{M}_{e^*}$ are the best-fit values of the e^* normalization and mass and $\hat{\theta}_i$ are the best-fit values of the nuisance parameters which maximize $\mathcal{L}$ given the data, assuming a

e^* signal is present. For the background only hypothesis, $\hat{\hat{\theta}}_i$ are the best-fit values of the nuisance parameters which maximize $\mathcal{L}$ assuming that no e^* signal is present.

The expected distribution of LLR assuming the background only (B) hypothesis is computed numerically performing pseudo-experiments varying all sources of systematic uncertainty as described in section 8.8. The p-value is then:

$$p = p(LLR \leq LLR_{obs}|SM\ only) \tag{8.3}$$

A summary of the p-values are listed in table 8.11. The largest discrepancies observed between data and background predictions correspond to a p-value of 3%. In conclusion, the data is consistent with the SM hypothesis and no significant excess is observed.

8.9.3 Limits

8.9.3.1 Limits on excited electrons

In the absence of a signal, an upper limit on the number of excited lepton events is determined at the 95% confidence level (C.L.) using a Bayesian approach [88] and following closely the method described in [89]. A single bin counting experiment is used to determine the upper limits for each assumed m_{e^*}. The observed number of events are determined from the $m_{ee\gamma}$ distribution above a sliding threshold which varies with the mass hypothesis as presented in section 8.9.1.

8.9.3.2 Likelihood Function

The sum of the number of expected background events and signal events is the total number of expected events μ. Using Poisson statistics, the likelihood to observe N_{obs} events is:

$$\mathcal{L}(\mathrm{data}|N_{e^*}, N_{\mathrm{bkg}}) = \frac{\mu^{N_{obs}} e^{-\mu}}{N_{\mathrm{obs}}!} \quad \text{, where} \quad \mu = N_{e^*} + N_{\mathrm{bkg}} \tag{8.4}$$

We account for the uncertainty in any of the free parameters in the likelihood as nuisance parameters, multiplying by the probability density function (pdf) for that uncertainty. With N_{sys} such nuisance parameters $\theta_1, ..., \theta_N$ we find:

$$\mathcal{L}(\mathrm{data}|N_j, \theta_i) = \frac{\mu^{N_{\mathrm{obs}}} e^{-\mu}}{N_{\mathrm{obs}}!} \prod_{i=1}^{N_{\mathrm{sys}}} G(\theta_i, 0, 1) \quad \text{, where} \quad \mu = \sum_j N_j (1 + \theta_i \epsilon_{ji}) \tag{8.5}$$

where ϵ_{ji} is the relative change in normalization of process j (signal and background) for each source of systematic uncertainty i. $G(\theta_i, 0, 1)$ is the pdf for parameter θ_i which is chosen to be Gaussian.

8.9.3.3 Bayesian Limit

In order to reduce the likelihood to a function that only depends on the parameter of interest (N_{e^*}) we use a marginalization technique employing Markov Chain Monte Carlo as implemented in the Bayesian Analysis Toolkit [88]. This gives us the reduced likelihood:

$$\mathcal{L}'(\mathrm{data}|N_{e^*}) = \int \mathcal{L}(N_j, \theta_1, ..., \theta_N) d\theta_1, ..., d\theta_N \tag{8.6}$$

The reduced likelihood is converted into a posterior probability density using Bayes' theorem by assuming a uniform positive prior in (σB), i.e. $\pi(\sigma B) = 1$. The maximum of the posterior probability density $P(\sigma B|data)$ corresponds to the most likely signal content given the observed data. The 95% Bayesian upper limit $(\sigma B)_{95}$ is obtained by integrating the posterior probability density:

$$0.95 = \frac{\int_0^{(\sigma B)_{95}} \mathcal{L}'(\sigma B)\pi(\sigma B)d(\sigma B)}{\int_0^{\infty} \mathcal{L}'(\sigma B)\pi(\sigma B)d(\sigma B)}. \tag{8.7}$$

Finally, the mass limits are determined using the cross section limits and the theoretical (σB) dependence on the M_{e^*} mass.

8.9.3.4 Mass Dependent Systematic Uncertainty

Mass-dependent systematic uncertainties are also incorporated as nuisance parameters in the likelihood 8.5. The relevant systematic uncertainties are reconstruction efficiency, QCD K-factor uncertainty, lepton resolution smearing and uncertainties in the QCD background estimation. Correlations between signal and background are taken into account. It is assumed that the systematic uncertainty grows linearly to a specified value at a reference mass of 200 GeV.

8.9.4 Signal Templates

As discussed in section 5.3, we generated signal samples for m_{e^*} from 0.2 TeV to 2.3 TeV in steps of 0.1 TeV, which can be varied to arbitrary Λ values. In the absence of a signal at each particular value of the signal mass m_{e^*} we set an upper limit at the 95% confidence level using the Bayesian approach.

8.9.4.1 *A Priori* Sensitivity and Results

We estimate our sensitivity *a priori* for this search by generating pseudo-data drawn from the Standard Model background only distributions. A signal scan is then performed on the pseudo-data, assuming a sum of signal and background. The expected and observed limits on the cross section times branching ratio are shown in figure 8.21. The yellow and green bands show the expected 1 and 2 σ contours of the ensemble of pseudo-experiments. We combine the results for various Λ values and plot the exclusion limits on the $m_{e^*} - \Lambda$ plane in Figure 8.22.

8.10 Conclusion

In conclusion, the ATLAS detector has been used to search for excited leptons with mass above 200 GeV with 2.05 fb^{-1} of proton-proton collision data. No evidence for such excited states are found. In the special case where $\Lambda = m_e^*$, regions below 1.8 TeV are excluded.

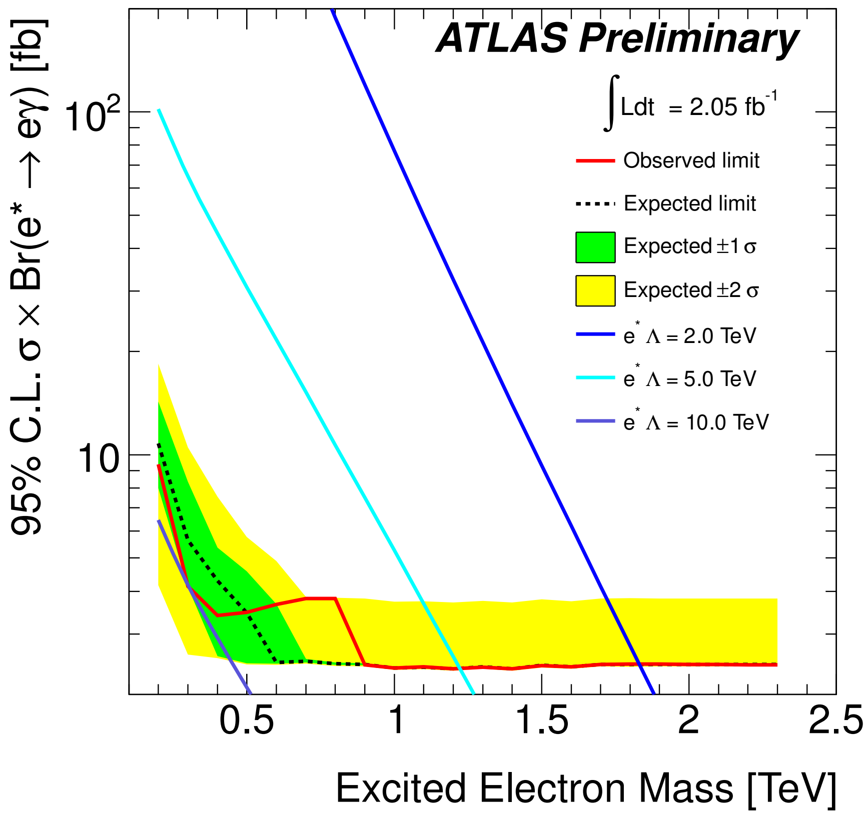

Figure 8.21: Cross section $\times$ branching ratio limits at 95% C.L. as a function of the e^* mass [10].

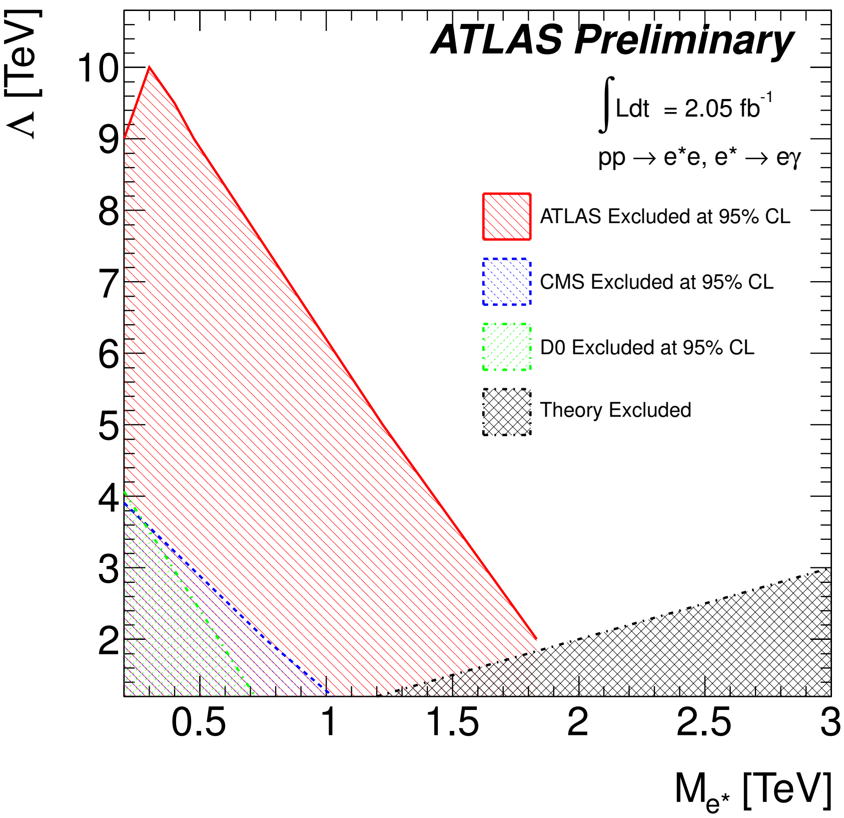

Figure 8.22: Exclusion limits in the $m_{e^*} - \Lambda$ parameters space [10].

Bibliography

[1] The D0 Collaboration, *Search for a heavy neutral gauge boson in the dielectron channel with* 5.4 fb^{-1} *of $p\bar{p}$ collisions at* $\sqrt{s} = 1.96$ TeV, Phys. Lett. B **695** (2011) 88–94.

[2] The CDF Collaboration, *Search for High Mass Resonances Decaying to Muon Pairs in* $\sqrt{s} = 1.96$ TeV *$p\bar{p}$ collisions*, For submission to PRL **000** (2011) 000–000.

[3] O. Cakir, C. Leroy, R. Mehdiyev, and A. Belyaev, *Production and Decay of Excited Electrons at the LHC*, Eur. Phys. J. **C32S2** (2004) 1–18.

[4] The CMS Collaboration, *A search for excited leptons in pp Collisions at $\sqrt{s} = 7$ TeV*, Phys. Rev. **D77** (2011) 091102, arXiv:1107.1773 [hep-ex].

[5] ATLAS Collaboration, *The ATLAS Experiment at the CERN Large Hadron Collider*, JINST **3** (2008) S08003.

[6] T. Bold on behalf of ATLAS TDAQ, *Commissioning ATLAS Trigger*, ICHEP08 (2008) . arXiv hep-ex:0810.3269v1.

[7] ATLAS Collaboration, *The ATLAS Simulation Infrastructure*, Eur. Phys. J. **C70** (2010) 823–874.

[8] Exotics dilepton group, *Search for high mass dielectron resonances at $\sqrt{s} = 7$ TeV*, ATL-COM-PHYS-2011-083.

[9] Exotics dilepton group, *Search for high mass dilepton resonances in pp collisions at $\sqrt{s} = 7$ TeV (2011 update for the EPS conference)*, ATL-COM-PHYS-2011-770.

[10] ATLAS Exotic Excited Lepton Group, *Search for excited leptons in pp collisions at $\sqrt{s} = 7$ TeV with the* ATLAS *detector*, ATL-COM-PHYS-2011-1550.

[11] R. Hamberg, W. L. van Neerven, and T. Matsuura, *A Complete calculation of the order α_s^2 correction to the Drell-Yan K factor*, Nucl. Phys. **B359** (1991) 343–405.

[12] EGamma group, *Efficiency Measurements*, https://twiki.cern.ch/twiki/bin/view/AtlasProtected/EfficiencyMeasurements.

[13] Alvarez-Gaum, et al., *Review of Particle Physics, 2008-2009*, Phys. Lett. B **667** (2008) no. 1-5, 31–92.

[14] S. L. Glashow, *Partial-symmetries of weak interactions*, Nuclear Physics **22(4)** (1961) 579–588.

[15] S. Weinberg, *A Model of Leptons*, Phys. Rev. Lett. **19(21)** (1967) 1264–1266.

[16] *Gargamelle Bubble Chamber*, Available from cern library and archives web page:http://library.web.cern.ch/library/archives/isad/isaggm.html.

[17] Wu, C. S. et al., *Experimental Test of Parity Conservation in Beta Decay*, Phys. Rev. **105(4)** (1957) 1413–1415.

[18] M. Maggiore, *A Modern Introduction to Quantum Field Theory*. Oxford Univ. Press, Oxford, 2005.

[19] F. Garberson, *Top Quark Mass and Cross Section Results from the Tevatron*, Invited talk at the Hadron Collider Physics Symposium (HCP2008), Galena, Illinois, USA (May 27-31, 2008) .

[20] J. Ellis, J.R. Espinosa, G.F. Giudice, A. Hoecker, and A. Riotto, *The Probable Fate of the Standard Model*, Phys.Lett. **B(679)** (Jun. 4, 2009) 369–375.

[21] M. K. Gaillard, P. D. Grannis, and F. J. Sciulli, *The standard model of particle physics*, Rev. Mod. Phys. **71(2)** (Centenary 1999) 96–111.

[22] L. Randall and R. Sundrum, *Large Mass Hierarchy from a Small Extra Dimension*, Phys. Rev. Lett. **83** (Oct. 25, 1999) 3370–3373.

[23] V. BARGER and W. KEUNG, *SEQUENTIAL W AND Z BOSONS*, Phys. Lett. **94B(3)** (Agu. 11, 1980) 377–380.

[24] M. Cvetic and S. Godfrey., *Discovery and Identification of Extra Gauge Bosons*, arXiv:hep-ph/ **9504216v1** (Apr. 1995) .

[25] P. Langacker, *The Physics of Heavy Z' Gauge Bosons*, Rev. Mod. Phys. **81** (2009) 1199–1228.

[26] M. Dittmar, A.-S. Nicollerat, and A. Djouadi, *Z' studies at the LHC: An update*, Phys. Lett. **B583** (2004) 111–120, `arXiv:hep-ph/0307020`.

[27] U. Baur, M. Spira, and P. M. Zerwas, *Excited Quark and Lepton Production at Hadron Colliders*, Phys. Rev. **D42** (1990) 815–824.

[28] O. J. P. Eboli, S. M. Lietti, and Prakash Mathews, *Excited Leptons at the CERN Large Hadron Collider*, Phys. Rev. **D65** .

[29] The CDF Collaboration, *Search for Excited and Exotic Electrons in the e-gamma Decay Channel in p-pbar Collisions at sqrt(s) = 1.96 TeV*, Phys. Rev. Lett. **94** .

[30] CompHEP Collaboration Collaboration, E. Boos et al., *CompHEP 4.4: Automatic computations from Lagrangians to events*, Nucl. Instrum. Meth. **A534** (2004) 250–259.

[31] T. Sjostrand, S. Mrenna, and P. Z. Skands, *PYTHIA 6.4 Physics and Manual*, JHEP **05** (2006) 026.

[32] A. Semenov, *LanHEP - a package for the automatic generation of Feynman rules in field theory. Version 3.0*, Comput. Phys. Commun. **180** (2009) 431–454.

[33] B. Adeva, D. P. Barber, U. Becker, G. D. Bei, J. Berdugo, G. Berghoff, A. Böhm, J. G. Branson, D. Buikman, J. D. Burger, M. Cerrada, C. C. Chang, G. F. Chen, H. S. Chen, M. Chen, M. L. Chen, M. Y. Chen, C. P. Cheng, R. Clare, E. Deffur, P. Duinker, Z. Y. Feng, H. S. Fesefeldt, D. Fong, M. Fukushima, J. C. Guo, D. Harting, T. Hebbeker, G. Herten, M. C. Ho, M. M. Ilyas, D. Z. Jiang, D. Kooijman, W. Krenz, Q. Z. Li, D. Luckey, E. J. Luit, C. Maña, G. G. G. Massaro, T. Matsuda, H. Newman, M. Pohl, F. P. Poschmann, J. P. Revol, M. Rohde, H. Rykaczewski, A. Rubio, J. Salicio, I. Schulz, K. Sinram, M. Steuer, G. M. Swider, H. W. Tang, D. Teuchert, S. C. C. Ting, K. L. Tung, F. Vannucci, Y. X. Wang, M. White, S. X. Wu, T. W. Wu, C. C. Yu, Y. Q. Zeng, N. L. Zhang,

and R. Y. Zhu, *Experimental Limits on the Production of Excited Leptons and Stable Heavy Leptons*, Phys. Rev. Lett. **48** (Apr, 1982) 967–970. `http://link.aps.org/doi/10.1103/PhysRevLett.48.967`.

[34] The OPAL Collaboration, *Search for Charged Excited Leptons in e^+e^- Collisions at* $\sqrt{s} = 183 - 209$ GeV, Phys. Lett. **B544** (2002) 57–72.

[35] The L3 Collaboration, *Search for Excited Leptons at LEP*, Phys. Lett. **B568** (2003) 23–34.

[36] The D0 Collaboration, *Search for Excited Electrons in $p\bar{p}$ collisions at* $\sqrt{s} = 1.96$ TeV, Phys. Rev. **D77** (May 2008) 091102.

[37] L. Evans et al., *LHC Machine*, JINST **3** (2008) S08001.

[38] CERN Press Office (10 September 2008), *First beam in the LHC - Accelerating science*, Press release: http://press.web.cern.ch/press/PressReleases/Releases2008/PR08.08E.html.

[39] Paul Rincon (23 September 2008), *Collider halted until next year*, BBC News: http://news.bbc.co.uk/2/hi/science/nature/7632408.stm.

[40] CERN Press Office (23 November 2009), *Two circulating beams bring first collisions in the LHC*, Press release: http://press.web.cern.ch/press/PressReleases/Releases2009/PR17.09E.html.

[41] CERN Press Office (19 March 2010), *LHC sets new record accelerates beams to 3.5* TeV, Press release: http://press.web.cern.ch/press/PressReleases/Releases2010/PR05.10E.html.

[42] CERN Press Office (31 January 2011), *CERN announces LHC to run in 2012*, Press release: http://press.web.cern.ch/press/PressReleases/Releases2011/PR01.11E.html.

[43] O. S. Brning et al., *The LHC Main Ring*, Tech. Rep. LHC Design Report: Volume I: CERN-2004-003-V-1, CERN, Geneva, May, 2004.

[44] CMS Collaboration, *The CMS experiment at the CERN LHC*, JINST **3** (2008) S08004.

[45] ALICE Collaboration, *The ALICE experiment at the CERN LHC*, JINST **3** (2008) S08002.

[46] LHCb Collaboration, *The LHCb Detector at the LHC*, JINST **3** (2008) S08005.

[47] LHCf Collaboration, *The LHCf detector at the CERN Large Hadron Collider*, JINST **3** (2008) S08006.

[48] TOTEM Collaboration, *The TOTEM Experiment at the CERN Large Hadron Collider*, JINST **3** (2008) S08007.

[49] ATLAS Collaboration, *ATLAS Computing Technical Design Report*, Tech. Rep. CERN-LHCC-2005-022, CERN, Geneva, 2005. See also http://atlas-computing.web.cern.ch/atlas-computing/packages/athenaCore/athenaCore.php.

[50] R. W. L. Jones and D. Barberis, *The ATLAS Computing Model*, J. Phys.: Conf. Ser. **119** (2008) 072020.

[51] T. A. Collaboration, *ATLAS: Detector and physics performance technical design report. Volume 1*, . CERN-LHCC-99-14.

[52] B. Aubert et al., *Construction, assembly and tests of the ATLAS electromagnetic barrel calorimter*, Nucl. Instrum. Methods Phys. **A558** (2006) 388–418. CERN-PH-EP-2005-034.

[53] ATLAS Collaboration, P. Jenni and M. Nessi, *ATLAS Forward Detectors for Luminosity Measurement and Monitoring*, Tech. Rep. CERN-LHCC-2004-010, CERN, Geneva, 2004.

[54] ATLAS Collaboration, P. Jenni, M. Nordberg, M. Nessi, and K. Jon-And, *ATLAS Forward Detectors for Luminosity Measurement of Elastic Scattering and Luminosity*, Tech. Rep. CERN-LHCC-2008-004, CERN, Geneva, 2008.

[55] ATLAS Collaboration, *ATLAS High-Level Triggers, DAQ and DCS Technical Design Report*, Tech. Rep. CERN-LHCC-2000-017, CERN, Geneva, 2000.

[56] S. Agostinelli et al., *Geant4 - a simulation toolkit*, Nucl. Instr. Methods Phys. Res. **A 506** (2003) 250–303.

[57] E. Obreshkov et al., *Organization and management of ATLAS offline software releases*, Nucl. Instr. Meth. **A584** (2008) 244–251.

[58] M. Dobbs and J.B. Hansen, *The HepMC C++ Monte Carlo event record for High Energy Physics*, Comput. Phys. Commun. **134** (2001) 41–46.

[59] V. Boisvert et al., *Final Report of the ATLAS Reconstruction Task Force*, Tech. Rep. ATL-SOFT-2003-010, CERN, Geneva, 2003.

[60] A. Sherstnev and R. S. Thorne, *Parton Distributions for LO Generators*, Eur. Phys. J. **C55** (2008) 553.

[61] P. M. Nadolsky et al., *Implications of CTEQ global analysis for collider observables*, Phys. Rev. **D78** (2008) .

[62] R. Blair et al., *ATLAS Standard Model Cross Section recommendations for 7 TeV LHC running*, https://svnweb.cern.ch/trac/atlasgrp/browser/Physics/StandardModel/xsectf/note/xsectf.pdf.

[63] A. Sherstnev and R. S. Thorne, *Parton Distributions for LO Generators*, Eur. Phys. J. **C55** (2008) 553–575, `arXiv:0711.2473 [hep-ph]`.

[64] Piotr Golonka and Zbigniew Was, *PHOTOS Monte Carlo: a precision tool for QED correction in Z and W decays*, Eur. Phys. J. **C45** (2006) 97–107, `arXiv:hep-ph/0506026 [hep-ph]`.

[65] C. M. Carloni Calame, G. Montagna, O. Nicrosini, and A. Vicini, *Precision electroweak calculation of the production of a high transverse-momentum lepton pair at hadron colliders*, JHEP **10** (2007) 109, `arXiv:0710.1722 [hep-ph]`.

[66] C. M. Carloni Calame, G. Montagna, O. Nicrosini, and A. Vicini, *Precision electroweak calculation of the charged current Drell-Yan process*, JHEP **0612** (2006) 016.

[67] A. D. Martin, R. G. Roberts, W. J. Stirling, and R. S. Thorne, *Parton distributions incorporating QED contributions*, Eur. Phys. J. **C39** (2005) 155–161, `arXiv:hep-ph/0411040`.

[68] TeV4LHC-Top and Electroweak Working Group Collaboration, C. E. Gerber et al., *Tevatron-for-LHC Report: Top and Electroweak Physics*, `arXiv:0705.3251 [hep-ph]`.

[69] S. Dittmaier and M. Kramer, 1, *Electroweak radiative corrections to W-boson production at hadron colliders*, Phys. Rev. **D65** (2002) 073007, arXiv:hep-ph/0109062.

[70] J. M. Campbell, R. K. Ellis, and C. Williams, *MCFM v6.0, A Monte Carlo for FeMtobarn processes at Hadron Colliders, Users Guide*, .

[71] The ATLAS Collaboration, J. M. Butterworth et al., *Single and Diboson Production Cross Sections in pp collisions at* $\sqrt{s} = 7$ TeV, ATL-COM-PHYS-2010-695 (2010) .

[72] Top-group, *TopSystematicUncertainties*, https://twiki.cern.ch/twiki/bin/view/AtlasProtected/TopSystematicUncertainties.

[73] ATLAS Collaboration, *Measurement of the top quark-pair production cross section with ATLAS in pp collisions at* $\sqrt{s} = 7$ *TeV*, arXiv:1012.1792 [hep-ex].

[74] S. Moch and P. Uwer, *Theoretical status and prospects for top-quark pair production at hadron colliders*, Phys. Rev. **D78** (2008) 034003.

[75] U. Langenfeld, S. Moch, and P. Uwer, *New results for* $t\bar{t}$ *production at hadron colliders*, arXiv:0907.2527 [hep-ph].

[76] M. Aliev et al., *– HATHOR – HAdronic Top and Heavy quarks crOss section calculatoR*, Comput. Phys. Commun. **182** (2011) 1034–1046.

[77] W. Lampl, S. Laplace, D. Lelas, P. Loch, H. Ma, S. Menke, S. Rajagopalan, D. Rousseau, S. Snyder, and G. Unal, *Calorimeter Clustering Algorithms Description and Performance*, Tech. Rep. ATL-LARG-PUB-2008-002, CERN, Geneva, 2008.

[78] The ATLAS Collaboration, *Expected photon performance in the ATLAS experiment*, Tech. Rep. ATL-PHYS-PUB-2011-007, CERN, Geneva, 2011.

[79] The ATLAS Collaboration, *Electron and photon reconstruction and identification in ATLAS: expected performance at high energy and results at 900 GeV*, ATLAS-CONF-2010-005 (2010) .

[80] The ATLAS Collaboration, *Reconstruction of Photon Conversions, in Expected Performance of the ATLAS Experiment: Detector, Trigger and Physics, pp. 112-140*, . CERN, Geneva, 2008. CERN-OPEN-2008-020, arXiv:0901.0512.

[81] ATLAS Collaboration, *Expected electron performance in the ATLAS experiment*, Tech. Rep. ATL-PHYS-PUB-2011-006, CERN, Geneva, 2011.

[82] EGamma group, *Calorimeter Isolation Corrections*, https://twiki.cern.ch/twiki/bin/view/AtlasProtected/CaloIsolationCorrections.

[83] EGamma group, *LArCleaningAndObjectQuality*, https://twiki.cern.ch/twiki/bin/view/AtlasProtected/LArCleaningAndObjectQuality.

[84] Jet/EtMiss group, *How to Clean Jets*, https://twiki.cern.ch/twiki/bin/view/AtlasProtected/HowToCleanJets.

[85] Jet/EtMiss group, *Guideline for LAr Hole treatment*, https://twiki.cern.ch/twiki/bin/view/AtlasProtected/HowToCleanJets#Guideline_for_LAr_Hole_treatm

[86] EGamma group, *Energy Scale and Resolution recommendations*, https://twiki.cern.ch/twiki/bin/view/AtlasProtected/EnergyScaleResolutionRecommendations.

[87] EGamma group, *EnergyRescaler*, https://twiki.cern.ch/twiki/bin/view/AtlasProtected/EnergyRescaler.

[88] A. Caldwell, D. Kollar, and K. Kröninger, *BAT - The Bayesian Analysis Toolkit*, Computer Physics Communications **180** (2009) 2197.

[89] A. Abdelalim et al., *Limit Setting and Signal Extraction Procedures in the Search for Narrow Resonances Decaying into Leptons at ATLAS*, Tech. Rep. ATL-COM-PHYS-2011-085, CERN, Geneva, 2011.

[90] The ATLAS Collaboration, *Search for high mass dilepton resonances in pp collisions at $\sqrt{s}$=7 TeV with the ATLAS experiment*, Phys. Lett. B **700** (2011) 163 – 180.

[91] Exotics dilepton group, *ZprimeEarlyAnalysisRelease16*, https://twiki.cern.ch/twiki/bin/view/AtlasProtected/ZprimeEarlyAnalysisRelease16.

[92] Exotics dilepton group, *A Search for Evidence of Extra Dimensions in the Diphoton Final State in $\sqrt{s} = 7$ TeV pp Collisions*, ATL-COM-PHYS-2011-1078.

[93] *The ATLAS Forward Detector project*, .

[94] ATLAS Electromagnetic Barrel Calorimeter Collaboration, M. Aharrouche et al., *Energy linearity and resolution of the ATLAS electromagnetic barrel calorimeter in an electron test-beam*, Nucl. Instrum. Meth. **A568** (2006) 601–623.

[95] Neyman and Pearson Phil. Trans. of the Royal Soc. of London A (1933) .

A

Comparison between Pythia and CompHEP predictions

As previously stated in sub-section 3.2.1, in Pythia excited electrons can be singly produced via contact interaction, but the pair production is not allowed, neither the gauge-mediated production. Also for decay modes, in Pythia excited electrons can decay into $e\gamma, eZ, \nu_e W$ but 3-body decays via contact interaction are not simulated in Pythia[1]. Results are reported in table A.1 for a few benchmark points, and show a very good agreement. However, $\sigma(pp \to ee^*) \times BR(e^* \to e\gamma)$ (shown in tables 5.4 and 5.5) cannot be compared because of the missing decay modes in Pythia.

m_{e^*} [TeV]	Λ [TeV]	σ_{Pythia} [fb]	$\sigma_{CompHEP}$ [fb]
0.40	3.00	1256.8	1256.8
0.40	5.00	162.4	162.9
1.00	3.00	210.5	210.7
1.00	5.00	27.48	27.31

Table A.1: Total production cross-sections computed with Pythia and CompHEP for different sets of (m_{e^*}, Λ). Statistical uncertainties on CompHEP results are below the percent level, and are not available for Pythia.

Figure A.1 shows generator-level kinematic distributions as predicted by CompHEP and Pythia for $m_{e^*} = 1$ TeV and $\Lambda = 5$ TeV. Leading electron distributions show a reasonable agreement, contrary to the next-to-leading electron and photon distributions. The treatment of the e^* spin was suspected to be the source of the discrepancy, which was confirmed by a dedicated study, see Ref. [10], which is described below.

Given the Lagrangian $\mathcal{L}_{CI}$, defined in equation 3.2, particles produced in the hard interaction are in a chiral eigenstate. In case of e^{*-} production (resp. e^{*+}), q and e^{*-} (e^-) are left-handed while $\bar{q}$ and e^+ (e^{*+}) are right-handed. Assuming quarks and electrons are massless, they are also produced in a pure helicity state: negative for q, e^{*-}, e^-, positive for $\bar{q}, e^{*+}, e^+$. Because of its mass, the situation is a priori different for e^*. Both negative

[1] For a fair comparison, gauge-mediated production has not been considered in CompHEP.

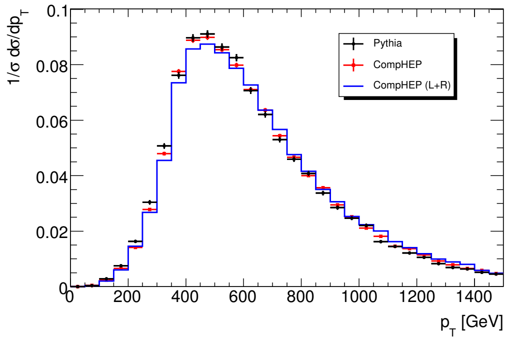

(a) Leading electron p_{T}.

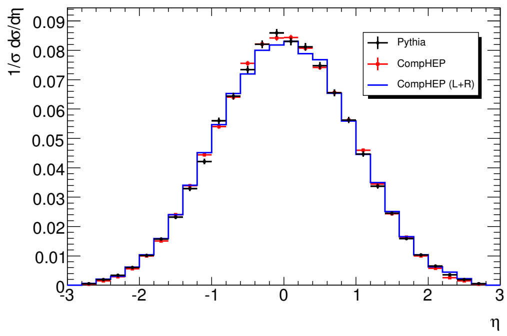

(b) Leading electron η.

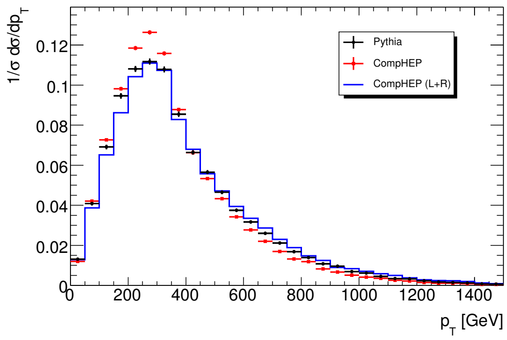

(c) Next to leading electron p_{T}.

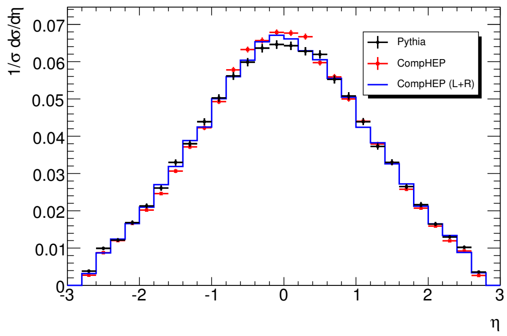

(d) Next to leading electron η.

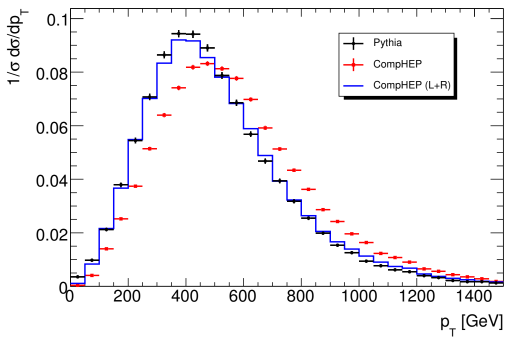

(e) Leading photon p_{T}.

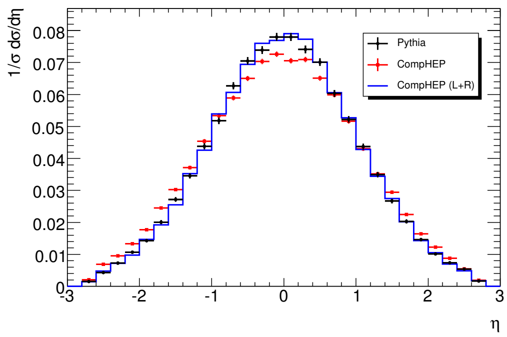

(f) Leading photon η.

Figure A.1: Kinematic distributions of the final state electrons and photon for PYTHIA and COMPHEP at generator level. The "COMPHEP (L+R)" is defined in equation [10].

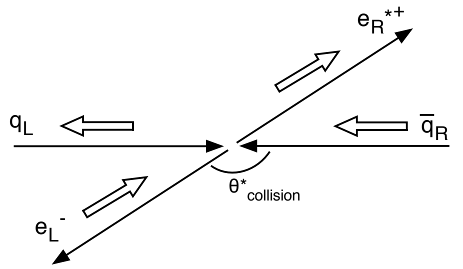

(a) $q\bar{q} \to e^- e^{*+}$ in the collision rest frame. Favored configuration: $\cos\theta^*_{collision} \simeq 1$.

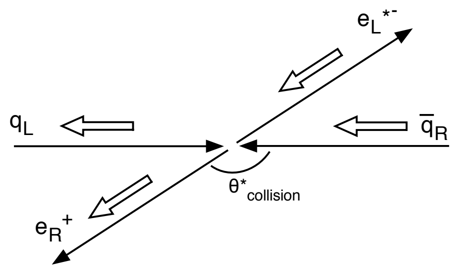

(b) $q\bar{q} \to e^+ e^{*-}$ in the collision rest frame. Favored configuration: $\cos\theta^*_{collision} \simeq -1$.

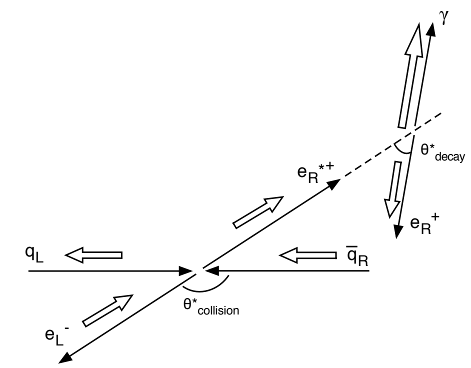

(c) $q\bar{q} \to e^- e^{*+} \to e^+ e^- \gamma$ spin correlations. Favored configuration: $\cos\theta^*_{decay} \simeq 1$.

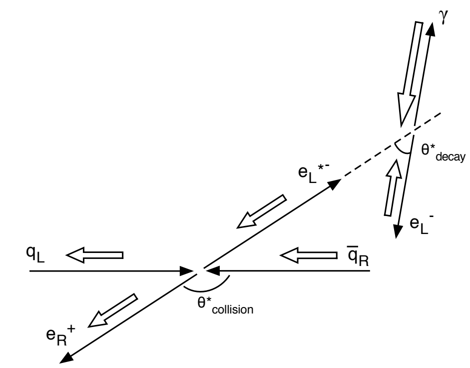

(d) $q\bar{q} \to e^+ e^{*-} \to e^+ e^- \gamma$ spin correlations. Favored configuration: $\cos\theta^*_{decay} \simeq 1$.

Figure A.2: Schematic view of helicity states involved in production and decay. The $\theta^*_{collision}$ variable defined as the angle between the incoming quark and the outgoing $e^\pm$ momenta is not an observable, as one cannot know from which beam the quark comes from, and it is used for Monte Carlo studies only. The angle θ^*_{decay} between the e^* flight direction and the electron momentum is computed in the e^* rest frame.

and positive helicity states are expected to contribute to the ${e_L^*}^-$ chiral state, with respective weights of $\frac{1}{2}\left(1+\frac{|\overrightarrow{p}|}{E+M}\right)$ and $\frac{1}{2}\left(1-\frac{|\overrightarrow{p}|}{E+M}\right)$, and vice versa for ${e_R^*}^+$. However, the excited electron recoils against a massless electron with a well defined helicity. As the total helicity should be conserved in a given frame, ${e_L^*}^-$ and ${e_R^*}^+$ can only be produced in negative and positive helicity states respectively in the collision rest frame. As for the e^* decay, the magnetic-moment transition from $\mathcal{L}_{trans}$ flips the fermion chirality: ${e_R^*}^- \to e_L^-\gamma$, ${e_L^*}^+ \to e_R^+\gamma$. Because the electron is approximately massless, it should also be produced with a well-defined helicity [10].

Figure A.3 shows the $\cos\theta^*$ distribution in the e^* rest frame as a function of $\cos\theta^*$ in the partonic collision rest frame. The "$\left(\frac{1}{2}\right)_L \otimes \left(\frac{1}{2}\right)_R \to \left(\frac{1}{2}\right)_L \otimes \left(\frac{1}{2}\right)_R$" spin structure can be seen along the x axis for both generators. Along the y axis, the photon is preferentially emitted in the e^* flight direction in CompHEP, while the Pythia sample exhibits a flat dependence, as if the $e^* \to e\gamma$ decay was isotropic. This explains why the photon p_{T} spectrum is harder in CompHEP.

For further check that the discrepancy comes from an improper treatment of the e^* spin in Pythia, Feynman rules dictating the e^* decay have been modified in LanHEP + CompHEP in an attempt to flatten the $\cos\theta^*_{decay}$ distribution. The Lagrangian $\mathcal{L}_{trans}$ has been replaced with $\mathcal{L}_{trans}^{(L+R)}$ where chiral projectors have been removed:

$$\mathcal{L}_{trans}^{(L+R)} = \frac{1}{2\Lambda}\bar{f}^*\sigma^{\mu\nu}\left[g\frac{\tau^a}{2}W^a_{\mu\nu} + g'\frac{Y}{2}B_{\mu\nu}\right]f + h.c. \tag{A.1}$$

Even if a flat $\cos\theta^*$ distribution cannot be reached in a $\frac{1}{2} \to 1 \otimes \frac{1}{2}$ decay, it is now symmetric w.r.t. 0. Kinematic distributions of the "CompHEP (L+R)" sample are displayed in figures A.1 and A.3. As expected, they are in a good agreement with Pythia distributions [10].

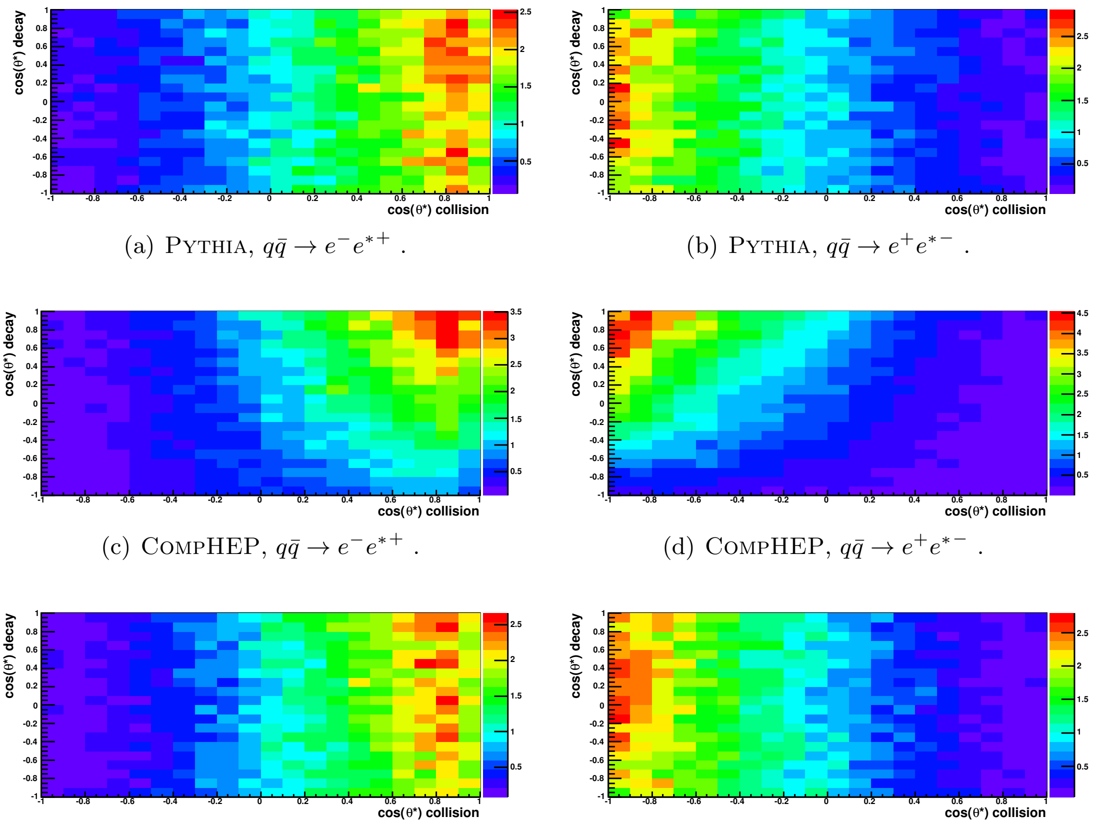

(a) Pythia, $q\bar{q} \to e^- e^{*+}$.

(b) Pythia, $q\bar{q} \to e^+ e^{*-}$.

(c) CompHEP, $q\bar{q} \to e^- e^{*+}$.

(d) CompHEP, $q\bar{q} \to e^+ e^{*-}$.

(e) CompHEP (L+R), $q\bar{q} \to e^- e^{*+}$.

(f) CompHEP (L+R), $q\bar{q} \to e^+ e^{*-}$.

Figure A.3: $\cos\theta^*_{decay}$ in the e^* rest frame as a function of $\cos\theta^*_{collision}$ in the $q\bar{q}$ rest frame. Angular conventions are described in figure A.2 [10].